NIKOLAI-SVEN STROHFELDT

HYDROGEN IN METAL NANOPARTICLES

UNDERSTANDING AND APPLYING THERMODYNAMIC PROPERTIES OF METAL-HYDROGEN NANOSTRUCTURES

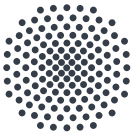

Universität Stuttgart

Hydrogen in metal nanoparticles

Understanding and applying thermodynamic properties of metal-hydrogen nanostructures

Von der Fakultät Mathematik und Physik
der Universität Stuttgart zur Erlangung der Würde
eines Doktors der Naturwissenschaften (Dr. rer. nat.)
genehmigte Abhandlung

vorgelegt von

Nikolai-Sven Strohfeldt
aus Waiblingen

Hauptberichter:	Prof. Dr. Harald Giessen
1. Mitberichter:	Prof. Dr. Sebastian Loth
2. Mitberichterin:	Prof. Dr. Na Liu
Prüfungsvorsitzender:	Prof. Dr. Christian Holm

Tag der münlichen Prüfung: 15.11.2017

4. Physikalisches Institut der Universität Stuttgart
2017

Nikolai-Sven Strohfeldt: *Hydrogen in metal nanoparticles – Understanding and applying thermodynamic properties of metal-hydrogen nanostructures*, 2017

Für meinen Vater (1936–2017)

Be yourself,
everyone else is taken!

— Oscar Wilde

ABSTRACT

The mobility sector is undergoing a fundamental change from fossil fuels through electricity to hydrogen. However, for hydrogen technology to be successful, the storage devices need to be pushed forward. Currently, the most promising path is to employ nanotechnology in metal hydride storage systems.

This thesis presents different methods and material systems exploring the interaction of metallic nanoparticles and hydrogen. It aims to expand the limited literature knowledge about size dependent effects on thermodynamic and optical properties at the nanoscale. Several analytical and numerical models are developed and compared to own experimental data as well as existing literature.

The experimentally investigated structures are palladium square patches, palladium-gold disk stacks, and yttrium nanorods. All structures throughout the thesis are characterized using plasmonic extinction spectroscopy, an optical measurement technique employing localized oscillations of the conduction electrons as a sensitive tool for structural and electronic changes in nanoparticles. The palladium square-patch investigations show a hydrogen loading pressure that is increasing with nanoparticle size, whereas the hydrogen induced in-plane expansion is decreasing with size. In the yttrium rod antenna studies, a drastic but reversible hydrogen induced elimination of the plasmonic resonance is observed, rendering the structure a highly interesting plasmonic switch. A sensitive plasmonic gas sensor is realized combining palladium nanoparticles with gold antennas. Through palladium-gold disk nanostacks that plasmonically behave as one superstructure, large hydrogen induced peak shifts of comparatively narrow resonances are demonstrated.

Complementing the experimental findings, analytical models are developed for the isotherms of palladium nanoparticles and the plasmonic resonances of square nanopatches. The isotherm model reveals a coherent loading mechanism of palladium nanoparticles. In contrast, the unloading mechanism and the general bulk behavior follow incoherent transitions with a reduced hysteresis. The developed plasmon resonance model illustrates a method for obtaining broadband dielectric data of nanoparticles without prior knowledge of any material properties besides the particle geometry and the plasmon resonance wavelength.

The findings presented in this thesis will be helpful to develop more efficient energy storage systems and powerful hydrogen sensors through well designed nanostructured devices.

ZUSAMMENFASSUNG

Mit der Verdrängung klassischer Verbrennungsmotoren durch elektrische Antriebe mit Batterie- oder Brennstoffzellentechnologie ist ein weltweiter fundamentaler Umbruch im Automobilsektor im Gange. Um die Brennstoffzellentechnologie jedoch zu einem langfristigen Erfolg zu führen, sind Innovationen in der Wasserstoffspeicherung notwendig. Eine Schlüsselrolle sollen dabei neue hocheffiziente Wasserstoffspeicher auf Metall-Hydrid Basis spielen.

In dieser Dissertation werden metallische Nanopartikel und ihre Interaktion mit Wasserstoff mit Hilfe unterschiedlichster Methoden und auf Basis mehrerer Materialsysteme untersucht. Das Ziel ist dabei das begrenztes Wissen über größenabhängige Effekte thermodynamischer und optischer Eigenschaften auf der Nanoskala zu erweitern. Zu diesem Zweck werden unter anderem mehrere analytische und numerische Modelle entwickelt und mit eigenen experimentellen Daten sowie Literaturdaten verglichen. Experimentelle Studien, durchgeführt an Palladium Nanoquadraten, Palladium-Gold Nanoscheiben-Stapeln und Yttrium Nanostäben mit Hilfe von plasmonischer Extinktions-Spektroskopie, zeigen optische, elektronische und strukturelle Eigenschaften der jeweiligen Systeme und die dazugehörige wasserstoffabhängige Dynamik.

So zeigt sich bei den untersuchten Palladium Nanoquadraten, dass der Wasserstoff Ladedruck mit zunehmender Größe der Teilchen zunimmt, während die wasserstoffinduzierte laterale Größenzunahme mit der Teilchengröße abnimmt. Die Untersuchungen an Yttrium Stabantennen zeigen ein drastisches aber reversibles wasserstoffabhängiges Ausschalten der plasmonischen Resonanz, was die Strukturen zu einem interessanten Kandidaten für einen plasmonischen Schalter machen. Des Weiteren wurde ein plasmonischer Wasserstoffsensors bestehend aus einer Kombination von Palladium und Gold Nanoscheiben realisiert und charakterisiert. Dabei zeigten sich abhängig

von der Anordnung relativ große wasserstoffinduzierte Resonanzverschiebungen und gutes dynamisches Verhalten.

Komplementär zu den durchgeführten experimentellen Studien wurden analytische Modelle für die Isothermen von Palladium Nanopartikeln, die Wasserstoffdiffusion in Yttrium Nanostäben und die plasmonischen Resonanzen in Palladium Nanoquadraten entwickelt. Das Isothermen Model offenbart, dass Palladium Nanopartikel bis zu einer gewissen Größe während der Wasserstoffabsorption einem kohärenten Phasenübergang folgen, während die Desorption von einem inkohärenten Phasenübergang begleitet wird, wie es bei großflächigem Palladium üblich ist. Das neuentwickelte Modell für plasmonische Resonanzen von Nanoquadraten kann dazu verwendet werden die dielektrische Funktion von Nanostrukturen über einen breiten Wellenlängenbereich experimentell zu bestimmen - nur durch Kenntnis der Geometrie und plasmonischen Resonanz der Strukturen aber ohne spezielle Annahmen über das Material zu machen.

All die Erkenntnisse dieser Thesis können als kleine aber erkenntnisreiche Schritte zur Entwicklung effizienterer Energiespeicher und leistungsstarker Wasserstoffsensoren auf Nanostrukturbasis betrachtet werden.

AUSFÜHRLICHE ZUSAMMENFASSUNG

Im Angesicht der zunehmenden weltweiten Umweltschäden und Gesundheitsprobleme, mitverursacht durch Abgase der heutigen Verkehrssysteme sowohl im privaten, öffentlichen als auch im gewerblichen Sektor, ist es notwendig saubere und praktikable Alternativen zu finden. Viel diskutierte Alternativen sind synthetische Kraftstoffe, klassische Batterien in Kombination mit Elektromotoren und die Brennstoffzellen-Technologie, bei welcher Wasserstoff in elektrische Energie umgesetzt wird. Die entscheidende Fragestellung für all diese Technologien ist, genügend hohe Energiedichten zu erzeugen um vergleichbare Reichweiten zu herkömmlichen Kraftstoffen zu realisieren. Da Batterien (z.B. Lithium-Polymer Akkus) nie derart hohe Energiedichten erreichen können, werden sich rein elektrische Verkehrssysteme nur in Kurzstreckenanwendungen oder einer Infrastruktur mit ständig verfügbarem Strom durchsetzen können. Brennstoffzellen-Technologie bietet dagegen eine Möglichkeit des vollständigen Ablösens von Verbrennungsmotoren durch deutlich erhöhte Energiedichten und 100 % Emissionsfreiheit.

Als Wasserstoffspeicher bieten sich besonders sogenannte Metall-Hydrid Systeme an, bei denen der Wasserstoff (meist reversibel) in Metallgitter aufgenommen wird. Magnesium kann z.B. bis zu 7,6 % seines Gewichts in Wasserstoff aufnehmen und dabei die Energiedichten von herkömmlichen Batterien und Wasserstoffdruck- oder Flüssigwasserstofftanks deutlich überbieten. Diese Formen der Energiespeicherung erreichen jedoch immer noch keine Energiedichten ähnlich fossiler Brennstoffe. Eine Möglichkeit diese Differenz zu überbrücken bietet die Nanostrukturierung der jeweiligen Metall-Hydride. Zur Thermodynamik von nanostrukturierten Metall-Hydriden gibt es jedoch aufgrund experimenteller Herausforderungen bisher nur sehr

wenige Studien. Daher ist es sinnvoll das einfachste mögliche Metall-Wasserstoff System zu betrachten und anschließend die dort gewonnenen Erkenntnisse auf die komplexeren Materialsysteme zu übertragen. So sind in den letzten Jahren einige experimentelle und theoretische Arbeiten zu Palladium Nanostrukturen und ihrer Interaktion mit Wasserstoff entstanden. Jedoch sind viele Aspekte, wie z.B. die mikroskopische Beschreibung des Phasenübergangs, Änderungen in der kritischen Temperatur, Oberflächeneffekte, sowie Lade- und Entladedrücke, immer noch umstritten. Dies lässt sich auf die Unterschiedlichkeit der Experimente und die experimentellen Beschränkungen in Temperatur- und Größenvariation zurückführen, welche das Treffen allgemeingültiger Aussagen erschweren.

In dieser Arbeit wird zunächst versucht die Literatur zu einem einheitlichen thermodynamischen Modell zusammenzuführen. Darauf aufbauend dienen eigene experimentelle Erkenntnisse dazu das Bild zu vervollständigen und die Forschung voran zu bringen. In Kapitel 4 wird ein größenabhängiges analytisches Modell für die Isothermen von Palladium Nanopartikeln entwickelt. Die dabei entscheidenden freien Parameter werden anhand von Literaturdaten mehrerer Studien bestimmt. Die Resultate zeigen, dass einfache Modifikationen an einem physikalisch motivierten Gitter-Gas Modell zu einem Nanopartikel-Modell führen, welches die von unterschiedlichsten Gruppen an Nanopartikeln gewonnenen Erkenntnisse hervorragend reproduziert. Dabei wird gezeigt, dass sich Palladium Nanopartikel mit Größen zwischen 2 nm und 100 nm in ihrem Wasserstoffladeverhalten von ausgedehnten Palladium Festkörpern unterscheiden. Die Ladedrücke sind teilchengrößenabhängig. So durchlaufen kleine Nanoteilchen einen vollständig kohärenten Ladevorgang bei welchem der maximal mögliche Ladedruck, ohne dass sich spannungsreduzierenden Versetzungen bilden. Je größer die Teilchen werden desto früher bilden sich jedoch Versetzungen, welche den Ladedruck reduzieren. Der Entladevorgang orientiert sich dagegen eher an dem für Palladium Festkörper üblichen Maxwell-Druck. Bei diesem wird durch Bildung von Versetzungen und Domänen zum frühestmöglichen Zeitpunkt der Phasenübergang von β- zu α-Phase eingeleitet und dadurch Gitterspannungen reduziert. Damit folgen Palladium Nanoteilchen eher einer sogenannten vollen spinodalen Isotherme. Ob

sie jedoch vollständig versetzungsfrei beladen werden oder die Spannungen groß genug werden, dass sich β-Phasen-Domänen ausbilden können, hängt nicht nur von der Teilchengröße, sondern auch der Temperatur ab. Je wärmer es ist, desto größer ist die Wahrscheinlichkeit zur Bildung von Versetzungen. Die theoretische Grenze für einen vollständig kohärenten Ladevorgang liegt bei 35 nm großen Teilchen ungefähr bei Raumtemperatur.

Eine Möglichkeit das thermodynamische Verhalten von metallischen Nanoteilchen zu untersuchen ist die Plasmonik. Das (Leitungs-) Elektronengas eines Nanopartikels kann mit Hilfe elektromagnetischer Strahlung zu lokalisierten Oszillationen (den sogenannten Plasmonen) angeregt werden Diese weisen eine für das Material, die geometrische Dimension und die dielektrische Umgebung des Teilchens, charakteristische Eigenfrequenz auf. Diese Resonanzen eignen sich dazu Veränderungen auf der Nanoskala spektroskopisch und mikroskopisch in Echtzeit zu verfolgen. Denn die Resonanzen für Nanopartikel mit Größen zwischen 50 nm und 1000 nm liegen im sichtbaren und nah-infraroten Frequenzbereich und erzeugen einen partiell drastisch erhöhten Absorptions- und Streuquerschnitt.

Diese Methode wird hier (siehe Kapitel 3 und 5) durch Bildung eines analytischen Modells für die Plasmonenresonanz quadratischer Platten (Quader mit $a = b > c$) verfeinert. Durch Separation der einzelnen Faktoren in materialabhängige und geometrieabhängige Größen, wird dabei eine Methode zur Bestimmung der dielektrischen Funktion von Nanoteilchen geschaffen wurde. Hierfür wird ein bekanntes analytisches Modell für oblate Sphäroide auf experimentell einfach zu realisierende quadratische Platten übertragen. Die dabei entstehenden freien Parameter (der geometrische Konversionsfaktor m und der angepasste Depolarisationsfaktor N_x) werden mit eigenen experimentellen Studien an Goldstrukturen bestimmt und durch theoretische Überlegungen plausibilisiert. Das vollständige Modell erlaubt es, den dielektrischen Faktor E (eine Kombination aus Real- und Imaginärteil der dielektrischen Funktion und dem Brechungsindex der Umgebung) einzig aus der plasmonischen Resonanzfrequenz und den Abmaßen

der Nano-Platte zu bestimmen. Bei Hinzunahme der Resonanzbreite ergibt sich daraus die vollständige dielektrische Funktion. Die Bestimmung stellt keine Anforderungen an die Form der dielektrischen Funktion, sondern beruht nur auf dem Vergleich von Strukturen verschiedener Ausmaße (mit jedoch der gleichen plasmonischen Resonanzposition). Damit ist das Modell, bei ausreichender Datenbasis, in der Lage selbst dynamische Größenänderungen von Nanostrukturen zu errechnen. In dieser Arbeit wird diese Methode bei der Bestimmung und Einordnung der dielektrischen Funktionen von Gold und Palladium unter Beweis gestellt und auf Palladium-Hydrid Nanostrukturen angewandt. Erstmals wird dabei die dielektrische Funktion von Wasserstoff-beladenem Palladium in nah-infraroten Wellenlängenbereich bestimmt. Da die plasmonischen Resonanzen sehr sensitiv auf Größenänderungen der Nanostrukturen reagieren, kann die horizontale sowie laterale wasserstoffinduzierte Ausdehnung der Palladium-Hydrid Nanostrukturen ebenfalls errechnet werden.

Für den langfristigen Erfolg der Wasserstoff-Wirtschaft sind nicht nur effiziente Speichertechnologien von Bedeutung, sondern auch die Sicherheit in der gesamten Verwertungskette, von der industriellen Produktion, über den Transport, bis hin zum Einsatz im Auto (oder Zug, oder Schiff). Eine wichtige Komponente dafür ist ein möglichst sicherer, kompakter, günstiger und einfach verfügbarer Wasserstoff-Detektor. In Kapitel 6 folgt aus diesem Grund eine andere Anwendung des Palladium-Wasserstoff Systems als Wasserstoff-Sensor, welche die zuvor gewonnenen Erkenntnisse zum thermodynamischen und optischen Verhalten von Palladium Nanostrukturen verwertet. Für den erfolgreichen Einsatz als optischer (Wasserstoff-) Sensor, sollte das System folgende Eigenschaften aufweisen:

- Eine monotone, konzentrationsabhängige Änderung der optischen Eigenschaften,
- eine hohe Selektivität, d.h. möglichst keine Querempfindlichkeiten durch Reaktion auf andere Stoffe,
- hohe Sensitivität, d.h. eine eindeutige Reaktion auf schon geringste Konzentrationen, möglichst im ppm Bereich,

- schnelles Ansprechverhalten mit Reaktionszeiten im Sekunden-Bereich,

- hohe Stabilität und Reversibilität mit möglichst geringer permanenter Schädigung des Materials durch das Messverfahren oder generelle Alterung.

In der Literatur sind Palladium-basierte Wasserstoffsensoren länger bekannt und es wurden schon unterschiedlichste Konzepte, von einfachen Dünnfilmschichtsystemen über Nanopartikel-Ensembles, bis hin zu Palladium-Gold Hybridsystemen vorgestellt. Genau diese Hybridstrukturen sind von besonderem Interesse, da sie die Vorteile von Palladium als Wasserstoff-sensitivem Material mit denen von Gold als plasmonische Antenne höchster Güte kombinieren. Um diese Vorteile von hybriden Strukturen mit den industriellen Anforderungen, einer einfachen und großflächigen Fabrikationsmethode in Einklang zu bringen, werden in Kapitel 6 vertikal gestapelte Gold und Palladium Nanoscheiben vorgestellt, welche durch kolloidale Lochmaskenlithographie kostengünstig, großflächig (>1 cm^2) und mit hoher, reproduzierbarer Qualität hergestellt werden können. Mit den so hergestellten Nano-Stapeln wird der Frage nachgegangen, welche Stapelreihenfolge den bestmöglichen Sensor hervorbringt. Gleichzeitig werden numerische Simulationen zur Klärung der physikalischen Hintergründe herangezogen. Die Untersuchungen, bei welchen Pd-Au, Au-Pd und Au-Pd-Au Stapel miteinander verglichen wurden, ergaben, dass alle System im Fernfeld reagieren, als bestünden sie aus einem einzigen plasmonischen Nanoteilchen. Jedoch ist die optische Antwort dieses Gesamtteilchens bei allen drei Geometrien sehr unterschiedlich. Das System mit der Palladiumscheibe als unterster Schicht (direkt auf dem Substrat) weist dabei die größte Wasserstoff-abhängige Reaktion auf (ca. 34 nm spektrale Verschiebung), hat aber auch die breiteste Resonanz. Dieser sogenannte Substrat-Effekt lässt sich auch durch numerische Simulationen bestätigen. Das Substrat mit Brechungsindex $n_s > n_{\mathrm{Air}}$ sorgt dafür, dass durch das Plasmon in der unteren Scheibe höhere optische Ströme und höhere elektrische Felder induziert werden als in der oberen Scheibe (relativ zu den vom Material verursachten Strömen). Das Pd-Au System reagiert also ähnlich einer dicke Palladium-Scheibe mit hoher Wasserstoffsensitivität, die

Au-Pd und Au-Pd-Au Stapel verhalten sich dagegen eher goldähnlich (mit schmaler Resonanz und geringer Wasserstoffempfindlichkeit). Interessanterweise zeigt sich bei den Reaktionszeiten ein umgekehrtes Bild. Dort hat das Au-Pd System das schnellste Ansprechverhalten und das Pd-Au das langsamste. Dieser Effekt, welcher sich auf die höhere relative freie Oberfläche zurückführen lässt, zeigt dass beide Systeme ihre Anwendung finden können. Je nachdem ob die Anwendung eher zeitkritisch ist, oder eine hohe Sensitivität fordert, werde Au-Pd und der Pd-Au Stapel eingesetzt.

Palladium eignet sich aufgrund seiner graduellen Änderung der dielektrischen Funktion und folglich auch der Reflektivität und der plasmonischen Resonanzwellenlänge, besonders gut als Material für Wasserstoffsensoren. Andere Metalle wie Magnesium oder Yttrium zeigen ein komplexeres, aber nicht weniger interessantes Wasserstoffabhängiges Verhalten. Yttrium durchläuft, bei erstem Kontakt mit Wasserstoff, einen (unter normalen Bedingungen) irreversiblen Phasenübergang von Yttrium (Y) zu Yttrium-Dihydrid (YH_2), wobei es ein Metall (mit sogar leicht erhöhter Leitfähigkeit) bleibt. Weitere Aufnahme von Wasserstoff führt zu einem unter Normalbedingungen reversiblen Phasenübergang von YH_2 zu Yttrium-Trihydrid (YH_3). Dieser Phasenübergang führt zu einer drastischen Änderung des elektronischen und strukturellen Verhaltens. Aus dem Metall YH_2 wird der transparente Isolator YH_3. Diese Eigenschaft macht Yttrium zu einem (fast) einzigartigen palsmonischen Material. In Kapitel 7 wird gezeigt, dass es möglich ist aus Yttrium mit Hilfe von Elektronenstrahl-Lithographie Nanoantennen herzustellen. Diese können mit Wasserstoff in YH_2 Antennen übertragen werden, welche eine plasmonische Resonanz im nah-infraroten Wellenlängenbereich aufweisen. Weitere Hydrogenisierung führt zu einem drastischen Einbruch der Plasmonenresonanz, welche sich durch Entfernen des Umgebungswasserstoffes langsam wieder zurückentwickelt. Dieses reversieble Verhalten macht Yttrium zu einem plasmonischen Schalter, mit dem die Transmission selektiv an frei wählbaren Wellenlängen im nah- und mittel-infraroten Wellenlängenbereich geschaltet werden kann. Zur genauen Charakterisierung dieses Verhaltens wurde hier ein Diffusionsmodell entwickelt, welches das (schnelle) Schalten von Metall auf

Dielektrikum und das (langsame) Zurückschalten von Dielektrikum perfekt wiedergibt.

All diese gewonnenen Erkenntnisse sind ein kleiner aber nicht unbedeutender Schritt zur Entwicklung einer umfassenden Theorie zu Wasserstoff in metallischen Nanoteilchen. Durch neue Messmethoden werden wir bald hoffentlich in der Lage sein auch komplizierte Metall-Hydrid Systeme auf der Nanoskala zu untersuchen und damit sowohl der Wasserstoffspeicher- als auch die Wasserstoffsensor-Technologie den notwendigen Durchbruch zu verschaffen.

PUBLICATIONS

JOURNAL PUBLICATIONS

Parts of this thesis have been published in the scientific journals:

P1 N. Strohfeldt, A. Tittl, M.Schäferling, F. Neubrech, U. Kreibig, R. Griessen and H. Giessen,
"**Yttrium Hydride Nanoantennas for Active Plasmonics**"
Nano Letters **14**(3), 1140-1147 (2014).

P2 N. Strohfeldt, J. Zhao, A. Tittl, and H. Giessen,
"**Sensitivity engineering in direct contact palladium-gold nano-sandwich hydrogen sensors [Invited]**"
Optical Materials Express **5**(11), 2525-2535 (2015).

P3 R. Griessen, N. Strohfeldt, and H. Giessen,
"**Thermodynamics of the hybrid interaction of hydrogen with palladium nanoparticles**"
Nature Materials **15**(3), 311-317 (2016).

P4 N. Strohfeldt, R. Griessen, and H. Giessen,
"**Retrieving Dielectric Properties of Plasmonic Nanostructures - A direct Approach**"
In preparation.

P5 N. Strohfeldt, F. Sterl, R. Griessen, and H. Giessen,
"**Palladium Nanopatches - Size-dependent Hydrogen Kinetics**"
In preparation.

Other publications that are not directly part of this thesis:

P6 N. Strohfeldt, A. Tittl, and H. Giessen,
"**Long-term stability of capped and buffered palladium-nickel thin films and nanostructures for plasmonic hydrogen sensing applications**"
Optical Materials Express **3**(2), 194-204 (2013).

P7 F. Sterl, N. Strohfeldt, R. Walter, R. Griessen, A. Tittl, and H. Giessen,
"**Magnesium as Novel Material for Active Plasmonics in the Visible Wavelength Range**"
Nano Letters **15**(12), 7949–7955 (2015).

P8 L. Gui, S. Bagheri, N. Strohfeldt, M. Hentschel, C. M. Zgrabik, B. Metzger, H. Linnenbank, E. L. Hu, and H. Giessen,
"**Nonlinear Refractory Plasmonics with TiN Nanoantennas**"
Nano Letters **16**(9), 5708–5713 (2016).

P9 S. Bagheri, N. Strohfeldt, F. Sterl, A. Berrier, A. Tittl, and H. Giessen,
"**Large-Area Low-Cost Plasmonic Perfect Absorber Chemical Sensor Fabricated by Laser Interference Lithography [Invited]**"
ACS Sensors **1**(9), 1148–1154 (2016).

P10 T. Teutsch, N. Strohfeldt, F. Sterl, A. Warsewa, E. Herkert, D. Paone, H. Giessen, and C. Tarín
"**Mathematical Modeling of a Plasmonic Palladium-Based Hydrogen Sensor**"
Submitted, (2017).

P11 F. Sterl, H. Linnenbank, T. Steinle, F. Mörz, N. Strohfeldt, and H. Giessen,
"**Nanoscale hydrogenography of individual magnesium nanoparticles**"
Submitted, (2017).

P12 S. Bagheri, N. Strohfeldt, A. Berrier, G. Richter, and H. Giessen,
"**Niobium as Alternative Material for Refractory Plasmonics and Hydrogen Sensing**"
In preparation.

Conference contributions as presenting autor:

C1 N. Strohfeldt, A. Tittl, M. Hentschel, and H. Giessen, "**Hydrogen sensing with palladium alloy nanostructures**", *Advanced DPG Physics School "Nanoantennas and Hybrid Quantum Systems", Bad Honnef*, Germany (2011), poster presentation.

C2 N. Strohfeldt, A. Tittl, and H. Giessen, "**Systematic Study of the Hydrogen Sensing Performance of Buffered and Capped Pd and PdNi Layers for Plasmonic Applications**", *Spring Meeting of the German Physical Society (DPG), Berlin*, Germany (2012), oral presentation.

C3 N. Strohfeldt, A. Tittl, F. Neubrech, U. Kreibig, and H. Giessen, "**Plasmonic Sensing using Hydrogen induced Phase Transitions in Yttrium Nanoparticles**", *Spring Meeting of the German Physical Society (DPG), Regensburg*, Germany (2013), oral presentation.

C4 N. Strohfeldt, A. Tittl, and H. Giessen, "**Long-term Stability of Capped and Buffered Palladium-nickel Thin Films and Nanostructures for Plasmonic Hydrogen Sensing Applications**", *7th International Conference on Materials for Advanced Technologies (ICMAT), Singapore*, Singapore (2013), oral presentation.

C5 N. Strohfeldt, A. Tittl, M. Schäferling, F. Neubrech, U. Kreibig, R. Griessen, and H. Giessen, "**Nanoantennas for reconfigurable plasmonics**", *551st WE-Heraeus-Seminar: Active Nanoplasmonics and Metamaterial Dynamics, Bad Honnef*, Germany (2014), poster presentation.

C6 N. Strohfeldt, A. Tittl, M. Schäferling, F. Neubrech, U. Kreibig, R. Griessen, and H. Giessen, "**Yttrium hydride nanoantennas for reconfigurable plasmonics**", *Spring Meeting of the German Physical Society (DPG), Dresden*, Germany (2014), oral presentation.

C7 N. Strohfeldt, A. Tittl, M. Schäferling, F. Neubrech, U. Kreibig, R. Griessen, and H. Giessen, "**Yttrium hydride nanoantennas for reconfigurable plasmonics**", *Gordon Research Seminar and Conference on Plasmonics (GRS/GRC), Newry*, USA (2014), oral and poster presentation.

C8 N. Strohfeldt, A. Tittl, M. Schäferling, F. Neubrech, U. Kreibig, R. Griessen, and H. Giessen, "**Yttrium hydride nanoantennas for Active plasmonics**" *SPIE Optics + Photonics Conference, San Diego*, USA (2014), oral presentation.

C9 N. Strohfeldt, J. Zhao, A. Tittl, and H. Giessen, "**Sensitivity engineering in direct contact Au@Pd nanosandwich hydrogen sensors**", *Spring Meeting of the German Physical Society (DPG), Berlin*, Germany (2015), poster presentation.

C10 N. Strohfeldt, F. Sterl, R. Griessen, and H. Giessen, "**Hybrid Thermodynamics for Hydrogen in Palladium Nanocubes and Nanoparticles for Active Plasmonics**", *SPIE. Micro + Nano Materials, Devices, and Applications Conference, Sydney*, Australia (2015), invited oral presentation.

C11 N. Strohfeldt, R. Griessen, and H. Giessen, "**Thermodynamics of Hydrogen in Palladium Nanoparticles**", *Spring Meeting of the German Physical Society (DPG), Regensburg*, Germany (2016), oral presentation.

C12 N. Strohfeldt, R. Griessen, and H. Giessen, "**Hybrid Thermodynamics for Hydrogen in Palladium Nanoparticles**", *MRS Spring Meeting & Exhibit, Phoenix*, USA (2016), oral presentation.

C13 N. Strohfeldt, R. Griessen, and H. Giessen, "**Hybrid Thermodynamics of Palladium Hydride Nanostructures**", *Gordon Research Conference on Plasmonics and Nanophotonics, Newry*, USA (2016), poster presentation.

C14 N. Strohfeldt, F. Sterl, R. Griessen, and H. Giessen, "**Palladium Nanopatches - Size-dependent Hydrogen Kinetics**", *Spring Meeting of the German Physical Society (DPG), Dresden*, Germany (2017), oral presentation.

Selected conference contributions as co-author:

C15 A. Tittl, N. Strohfeldt, and H. Giessen, "**Systematic Study of the Hydrogen Sensing Performance of Buffered and Capped Pd and PdNi Layers for Plasmonic Applications**", *European Materials Research Society 2012 Spring Meeting (E-MRS), Strasbourg*, France (2012).

C16 J. Zhao, N. Strohfeldt, A. Tittl, and H. Giessen, "**Hybrid plasmonic oligomer for large-area low-cost nano-size direct contact hydrogen**

sensors", *Spring Meeting of the German Physical Society (DPG), Dresden*, Germany (2014).

C17 R. Griessen, N. Strohfeldt, A. Tittl, and H. Giessen, "**Origin of the huge asymmetry in ab- and desorption kinetics of hydrogen in capped films**", *MH2014: Fundamentals and Applications, Manchester*, UK (2014).

C18 V. Manninen, N. Strohfeldt, F. Sterl, and H. Giessen, "**Plasmonic copper nanodisks for monitoring electrochemical redox-reactions**", *Spring Meeting of the German Physical Society (DPG), Berlin*, Germany (2015).

C19 F. Sterl, N. Strohfeldt, R. Walter, A. Tittl and H. Giessen, "**Magnesium as a novel material for active plasmonics in the visible**", *The 7th International Conference on Surface Plasmon Photonics (SPP7), Jerusalem*, Israel (2015).

C20 S. Bagheri, N. Strohfeldt, A. Tittl, and H. Giessen, "**Large-Area Low-Cost Plasmonic Perfect Absorber Sensor Fabricated by Laser Interference Lithography**", *SPIE Optics and Photonics, San Diego*, USA (2015).

C21 L. Gui, H. Linnenbank, S. Bagheri, N. Strohfeldt, C. Zgrabik, B. Metzger, M. Hentschel, E. Hu, and H. Giessen, "**Nonlinear Refractory Plasmonics with TiN Nanoantennas**", *CLEO, San Jose, California*, USA (2016).

C22 J. Karst, N. Strohfeldt, M. Hentschel, H. Giessen, and N. Liu, "**Circular Dichroism Spectroscopy on Individual Plasmonic Nanoparticles**", *Spring Meeting of the German Physical Society (DPG), Regensburg*, Germany (2016).

C23 Q. Ai, D. Paone, N. Strohfeldt, S. Ristok, and H. Giessen, "**Strong coupling of surface plasmons and whispering gallery cavity**", *Spring Meeting of the German Physical Society (DPG), Regensburg*, Germany (2016).

C24 R. Griessen, N. Strohfeldt, and H. Giessen, "**Hydrogen in Palladium Nanocubes and Nanoparticles for Active Plasmonics**", *The 15th International Symposium on Metal-Hydrogen Systems (MH2016), Interlaken*, Switzerland (2016).

C25 F. Sterl, N. Strohfeldt, R. Griessen, and H. Giessen, "**Observing nanoscale hydrogen diffusion in plasmonic Mg particles**", *The 6th International Topical Meeting on Nanophotonics and Metamaterials (NanoMeta), Seefeld*, Austria (2017).

C26 D. Paone, M. Mayer, N. Strohfeldt, F. Sterl,, T. König, and H. Giessen, "**Hydrogen Sensing using Chemically Grown Plasmonic Nanorods in a Dust-on-Film Geometry**", *Spring Meeting of the German Physical Society (DPG), Dresden*, Germany (2017).

C27 T. Teutsch, A. Warsewa, N. Strohfeldt, F. Sterl, E. Herkert, H. Giessen, and C. Tarín, "**Modeling of Pressure-Composition Isotherms and Diffusion Dynamics of a Plasmonic Palladium Sensor for Hydrogen Detection**", *IEEE Conference of Advanced Intelligent Mechatronics (AIM), Munich*, Germany (2017).

C28 F. Sterl, H. Linnenbank, T. Steinle, F. Mörz, N. Strohfeldt, and H. Giessen, "**Nanoscale Hydrogenography of Individual Magnesium Nanoparticles**", *MRS Fall Meeting, Boston*, USA (2017).

CONTENTS

ACRONYMS

AFM	atomic force microscopy
Ar	argon
Au	gold
CaF_2	calcium fluoride
CST	CST Microwave Studio
ECS	extinction cross section
EELS	electron energy loss spectroscopy
FEM	finite element method
FTIR	Fourier-transform infrared spectrometer
FWHM	full width at half maximum
H_2	hydrogen
INPS	Indirect NanoPlasmonic Sensing
LHS	left-hand side
LSPR	localized surface plasmon resonance
MLWA	modified long-wave approximation
MOF	metal-organic framework
Pd	palladium
PdH	palladium hydride
PMMA	Poly(methyl methacrylate)
RHS	right-hand side
SEM	scanning electron microscope
SNOM	scanning near-field optical microscopy
TEM	transmission electron microscope

LIST OF FIGURES

LIST OF TABLES

1

INTRODUCTION

Worldwide health problems and environmental issues due to aerosols, combustion gases (NO_x) and greenhouse gases (CO_2, methane, etc.) attracted a lot of attention in recent years [1]. Governmental institutions and private organizations are starting to realize the importance of preventing further damage to the environment and human health by developing strategies for reducing or eliminating hazardous emissions, especially in the mega cities of Asia and South America. Our current fossil fuel based mobility, including private, public and commercial transportation, is the main contributors to air pollution [2]. There are basically three strategies to replace the current transportation systems by the use of cleaner technologies [3, 4]:

- Classical batteries (e.g. lithium polymer, nickel-metal-hydride cells) in combination with electrically powered engines for cars, trains and (small) ships [5]. This technology is already fully developed but lacks sufficient energy densities for long range use.

- Synthetic fuels synthezised using electricity from renewabel energy sources. These can be used in conventional engines and they are due to their high energy densities highly interesting as replacement for cerosin in airplanes. Through chemical conversion from cabon monoxide and hydrogen (using the Fischer Tropsch conversion) they can reach energy densities higher then convetional fuels, have a cleaner combustion process and do not consume fossile resources [6].

- Fuel-cell based electrical engines with hydrogen storage devices can be employed in cars, trains and ships [7]. This technology perfectly complements the battery powered mobility options, since it essentially uses the same engine, but provides

a much better range due to the enhanced energy density of hydrogen storage devices. Long-term stability issues with the fuel cells, safety concerns of using hydrogen as fuel and a lack of efficient high density hydrogen storage devices prevent this technology from taking off.

All these developments show that the most important goal for developing clean mobility is finding renewable energy sources with volume and mass energy densities comparable with crude oil based fuels [8]. Hydrogen is one of the simplest molecules, with the highest accessible specific energy (not counting radioactive materials) of 142 MJ/kg. However, the volumetric energy density of pressurized and even liquefied hydrogen is very poor compared to gasoline or other crude oil based fuels. Figure 1.1 shows the different ways to store hydrogen, with the goal to enhance the volumetric energy density without significantly reducing the mass energy density of hydrogen. At the same time the hydrogen needs to be accessible for fast loading and unloading. Since, the development potentials for pressurized tanks or liquefied hydrogen storage are limited, other approaches need to be considered for further development.

The reversible storage of hydrogen in metal lattices is a well estabilshed way to enhance the volumetric energy density of hydrogen, since a metal latice is the densest way to pack hydrogen atoms (except strongly bound chemical compounds). The material development in recent years led to storage devices with over 7 wt % (weight percent) hydrogen (H_2) storage capacitiy (e.g. $LiNH_2$ or MgH_2) [9].

For a succesful use hydrogen storage technologies and hydrogen in chemical plants (producing synthetic fules), safety is a top priority. Hydrogen strongly reacts with oxygen through the highly excotermic oxyhydrogen reaction at a wide range of concentrations (betwenn 4 % and 75 % in Air). For preventing any accidents, a constant monitoring for leaks or miscarried reaction is necessary. Thus there is a demand for cheap, reliable and mobile hydrogen sensors, monitoring hydrogen powered transportation and industrial production (e.g. ammonia production, synthetic fuel production, steel production and hydrogen

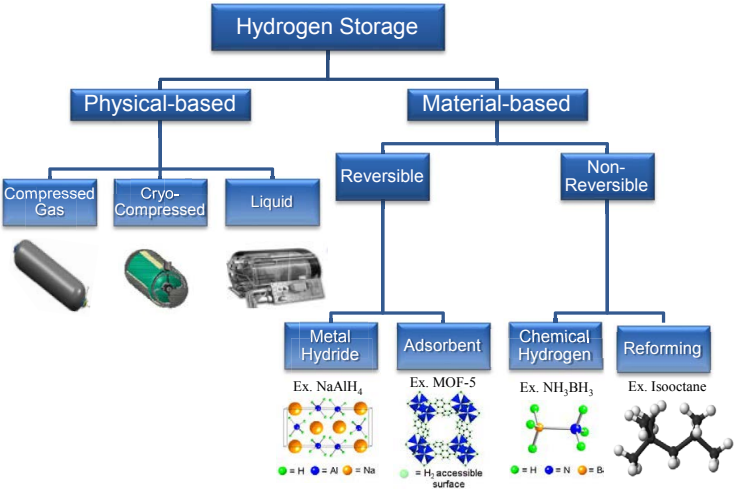

FIGURE 1.1. Overview of the potential hydrogen storage materials. Reprinted from the *Hydrogen Storage Technical Team Roadmap* of the U.S. Department of Energy [12].

electrolysis) [10, 11]. Standard hydrogen sensors are for example explosimenters, using resistance measurements at Wheatstone bridges. They are bulky and need to be well protected to prevent triggering explosions themselves. Other commercial sensors sense hydrogen electrochemically. The disadvantage of such a device is that the electrolyte consumes itself during the sensing procedure, reducing the sensor lifetime. A third way, is using mass spectroscopy, unfortunately a very bulky and expensive sensing technology. Therefore, an alternative optical hydrogen sensors based on reflectivity changes in hydrogen absorbing metals has emerged in recent years.

For both, hydrogen storage and hydrogen gas monitoring devices, understanding the mechanisms defining the particular metal hydrogen system is highly relevant. This involves knowledge of catalytic hydrogen splitting, physi- and chemisorption on the metal's surface and subsurface sites as well as the diffusion of hydrogen atoms through the lattice until equilibrium is reached.

In the last century, the study of metal-hydrogen systems, and especially the prototypical palladium-hydrogen system, was well established, making it one of the best understood solid solution systems [13, 14]. However, the effects of nanostructuring the materials could only be studied in the last decade, opening up a whole new field of research. Palladium is the simplest and well-behaved material in the class of hydrogen absorbing metals. It is catalytically active and able to split hydrogen at room temperature. It does not oxidize under normal conditions and undergoes a reversible and non-destructive phase transition, forming $PdH_{0.71}$. (with weight fraction). Unfortunately palladium only stores 0.93 wt % hydrogen in its lattis, making it a bad candidate for hydrogen storage. Other materials such as MgH_2 with 7.3 wt% or $NaAlH_4$ with about 5 wt% are much better suited candidates [15]). Nevertheless, it is a perfect model system to study the effects that are relevant for the more complex metal hydride systems [16].

The room temperature and reversible hydrogen absorption, makes palladium additionally a promissing hydrogen sensor material that can be used in electrical, electrochemical and optical hydrogen monitoring devices [11]. Hydrogen detection is most relevant in hazardous environments, therefore the use of electrical devices, high temperatures or intense light is undesirable. Consequently, optical sensors are a suitable solution. They can be used in fiber networks and only require low light intensities, leading to a considerable amount of research on palladium based optical hydrogen sensors in recent years [17–27].

1.1 OUTLINE

The thesis is combining the research of thermodynamic processes in nanosized metal hydride material systems with modern nanoscale lithography methods and optical metrology.

To give the reader the necessary theoretical background for understanding the material system and the optical characterization methods, namely plasmonics, **Chapter 2** gives a short introduction on the basic concepts and properties, used in the following chapters.

In **Chapter 3**, a new method for determining the optical properties of nanosized metals is introduced. An analytical model for the plasmonic resonances of square-nanopatches is developed and applied to experimentally obtained extinction spectra of gold and palladium nanostructures. The resulting dielectric functions are compared to literature data and a path is illustrated to generalize the findings for many other materials and geometries.

Chapter 4 provides an overview of experimental and theoretical studies on the thermodynamics of nanosized palladium hydride. The hydrogen ab- and desorption dynamics of palladium nanocubes is studied in detail. To gain a coherent picture of all the available fragmentary data, a size-dependent thermodynamic model is developed and fitted to the available experimental data. Finally, unambiguous conclusions about the hydrogen ab- and desorption mechanisms in nanosized palladium are drawn. This chapter is adapted from the manuscript, *'Thermodynamics of the hybrid interaction of hydrogen with palladium nanoparticles'* [28].

A way to close the gap between the thermodynamic behavior of bulk and nanosized palladium discussed in Chapter 4, is attempted in **Chapter 5**. Here, the model developed in Chapter 3 is applied, to study the hydrogen loading dynamics of palladium square-patches using plasmonic metrology. Knowledge about the size-dependent expansion and the dielectric function of palladium hydride nanoparticles are a result of this study.

In **Chapter 6** that I adapted from my publication, *'Sensitivity engineering in direct contact palladium-gold nano-sandwich hydrogen sensors'* [29], an application of palladium nanostructures for hydrogen sensing schemes is illustrated. The findings on thermodynamic and optical properties of palladium hydride, described in Chapters 2, 4 and 5 together with experimentally obtained extinction data, are used to qualify different hydrogen sensor systems of vertically stacked palladium and gold nanodisks regarding their sensitivity and response time.

Chapter 7 transfers the knowledge about nanosized metal hydrogen systems from palladium to yttrium. The chapter shows that the optical response of yttrium nanorods can be switched reversibly on and off, using hydrogen gas exposure. To characterize the material system we performed experimental studies together with theoretical modeling. The modeling is applied to the thermodynamic as well as the spectral response. The concepts of this chapter are published in *'Yttrium Hydride Nanoantennas for Active Plasmonics'* [30].

Chapter 8 gives a short summary of the covered topics and draws conclusions on how to use the gained knowledge on metal hydride nanoparticles in further research and illustrates possible applications.

2

THEORETICAL BACKGROUND

For a complete picture of the matters discussed in this thesis it is worth to have a short introduction into the main topics of the following chapters, namely the theory of plasmonics and the thermodynamics of the metal (especially palladium) hydrogen system.[1] To begin with, the theory of plasmonics and its basic principles will be presented.

2.1 LIGHT MATTER INTERACTION

For understanding plasmonics and its applications it is of crucial importance, to know about the theoretical background of light matter interaction.

2.1.1 *Maxwell's Equations*

The basic concept of light matter interaction can be understood by having a closer look at the macroscopic Maxwell equations[2]:

$$\begin{aligned} \nabla \cdot \boldsymbol{D} &= \varrho_{ext} \qquad \nabla \cdot \boldsymbol{B} = 0 \\ \nabla \times \boldsymbol{E} &= -\frac{\partial \boldsymbol{B}}{\partial t} \quad \nabla \times \boldsymbol{H} = \boldsymbol{j}_{\boldsymbol{ext}} + \frac{\partial \boldsymbol{D}}{\partial t} \end{aligned} \tag{2.1}$$

These equations give relations between the dielectric displacement $\boldsymbol{D}$, the electric field $\boldsymbol{E}$, the magnetic field $\boldsymbol{H}$ and the magnetic induction

1 The following sections are adapted in part from my Diploma Thesis [31].

2 In SI units, following the line of argument and the notation of "Plasmonics: Fundamentals and Applications", by Stefan A. Maier [32]

$\boldsymbol{B}$ and link them with the external charges ϱ_{ext} and current densities $\boldsymbol{j_{ext}}$.

To be able to find solutions to Eq. (2.1) it is necessary, to have two more equations that link $\boldsymbol{D}$ with $\boldsymbol{E}$ and $\boldsymbol{H}$ with $\boldsymbol{B}$. In general, these vectors are linked via the polarization $\boldsymbol{P}$ and the magnetization $\boldsymbol{M}$ by:

$$\boldsymbol{D} = \varepsilon_0 \boldsymbol{E} + \boldsymbol{P} \tag{2.2}$$

$$\boldsymbol{H} = \frac{1}{\mu}\boldsymbol{B} - \boldsymbol{M} \tag{2.3}$$

In linear and isotropic media it is possible to find the following linear relations:

$$\boldsymbol{D} = \varepsilon_0 \varepsilon \boldsymbol{E} \tag{2.4}$$

$$\boldsymbol{B} = \mu_0 \mu \boldsymbol{H} \tag{2.5}$$

With that the electric and magnetic response of a medium can be described completely via the relative permittivity ε and the relative permeability μ plus the electric and magnetic constants.

In the context of this thesis, only non-magnetic metals are considered, so from now on μ is set equal to 1 and the magnetic field and induction can be treated similarly up to a prefactor μ_0.

The relative permittivity $\varepsilon\left(\boldsymbol{K}, \omega\right)$, as a function of the wave vector $\boldsymbol{K}$ and the angular frequency ω, can also be related to the conductivity $\sigma\left(\boldsymbol{K}, \omega\right)$ through the fundamental equation:

$$\varepsilon\left(\boldsymbol{K}, \omega\right) = 1 + \frac{i \cdot \sigma\left(\boldsymbol{K}, \omega\right)}{\varepsilon_0 \cdot \omega} \tag{2.6}$$

In the limit of spatially local response, meaning the wavelength in the material is much larger than the electron mean free path, $\boldsymbol{K}$ can be set to zero, resulting in $\varepsilon\left(\boldsymbol{K} = 0, \omega\right) = \varepsilon\left(\omega\right)$. The relative permittivity $\varepsilon\left(\omega\right)$ is normally called dielectric function and is, in general, a complex number.

This complex $\varepsilon\left(\omega\right) = \varepsilon_1\left(\omega\right) + i\varepsilon_2\left(\omega\right)$ can also be related to the complex refractive index $\tilde{n}\left(\omega\right) = n\left(\omega\right) + i\kappa\left(\omega\right)$ by:

$$\tilde{n}\left(\omega\right) = \sqrt{\varepsilon\left(\omega\right)} \tag{2.7}$$

The real part n of the complex refractive index $\tilde{n}$ can be identified with the normal refractive index of a material, defining the dispersion of the material. The imaginary part κ determines the absorption of electromagnetic waves in a material. By the relation:

$$\alpha_B(\omega) = \frac{2 \cdot \kappa(\omega) \cdot \omega}{c} \tag{2.8}$$

κ can also be associated with the absorption coefficient α_B from Beer's law describing the exponential intensity decay of a beam traveling through a medium ($I(z) = I_0 \cdot \exp(-\alpha_B z)$).

By putting the definitions of $\tilde{n}$ and ε into Eq. (2.7), one can find expressions relating the refractive index n, the extinction coefficient κ and the real and imaginary part of ε:

$$n^2 = \frac{\varepsilon_1}{2} + \frac{1}{2} \cdot \sqrt{\varepsilon_1^2 + \varepsilon_2^2} \tag{2.9}$$

$$\kappa = \frac{\varepsilon_2}{2n} \tag{2.10}$$

These two equations show the complexity of the relations between ε and $\hat{n}$. There is no generally applicable simplification to these relations. Nevertheless, it can be said that the absorption κ of a medium is mainly determined by the imaginary part of ε, whereas the change of phase velocity in a medium ($\sim n$) mostly determined by the real part of ε.

2.1.2 *Optical Properties of Metals*

After becoming acquainted with the nature of the light matter interaction in general, the first step to a predictive model of real metals is to find an expression for the dielectric function $\varepsilon(\omega)$.

The simplest model of a metal is a free electron gas. Here, the electrons are allowed to move freely, against the fixed positively charged ion core background. This very simple model works surprisingly well

for a lot of metals up to visible frequencies and for alkali metals even into the ultraviolet frequency range.

To find an expression for the dielectric response to an external electric field we assume that the electrons act as driven oscillators with an oscillating external filed ($\boldsymbol{E}(t) = \boldsymbol{E}_0 \cdot \exp(-i\omega t)$) exciting them:

$$m_e^* \cdot \frac{d^2\boldsymbol{x}}{dt^2} + m_e^* \cdot \gamma \cdot \frac{d\boldsymbol{x}}{dt} = -e \cdot \boldsymbol{E}(t) \tag{2.11}$$

Here m_e^* is the effective optical mass of an electron that can differ from the electron rest-mass to account for the band-structure of a certain metal. γ represents the damping constant of the metal. The ansatz to solve the second order linear differential Eq. (2.11) is:

$$\boldsymbol{x}(t) = \boldsymbol{x}_0 \cdot \exp(-i\omega t) \tag{2.12}$$

Putting Eq. (2.12) into Eq. (2.11) and solving for $\boldsymbol{x}(t)$ leads to:

$$\boldsymbol{x}(t) = \frac{e}{m_e^*\omega^2 + im_e^*\gamma\omega} \cdot \boldsymbol{E}(t) \tag{2.13}$$

Using the relation $\boldsymbol{P} = -n_e e\boldsymbol{x}$ where n is the number of electrons and $\boldsymbol{x}$ the displacement from Eq. (2.13), we get:

$$\boldsymbol{P} = -\frac{n_e e^2}{m_e^*\omega^2 + im_e^*\gamma\omega} \cdot \boldsymbol{E} \tag{2.14}$$

Combining this result with the relation of Eq. (2.2) and comparing it with Eq. (2.4), one get's an equation determining the dielectric function of a (free electron gas) metal:

$$\varepsilon(\omega) = 1 - \frac{\omega_p^2}{\omega^2 + i\gamma\omega} \tag{2.15}$$

Here, $\omega_p^2 = \left(n_e e^2\right) / \left(\varepsilon_0 m_e^*\right)$ is the characteristic plasma frequency. By using $\gamma = 1/\tau$, where τ is the lifetime of the oscillations, Eq. (2.15) can be split into real and imaginary part:

$$\varepsilon_1(\omega) = 1 - \frac{\omega_p^2\tau^2}{1 + \omega^2\tau^2} \tag{2.16}$$

$$\varepsilon_2(\omega) = \frac{\omega_p^2\tau}{\omega\left(1 + \omega^2\tau^2\right)} \tag{2.17}$$

Metals only retain their metallic character for frequencies $\omega < \omega_p$, otherwise they are transparent. For most (noble) metals the plasma frequency is in the ultraviolet regime and therefore the condition $\omega < \omega_p$ is fulfilled for the phenomena discussed in this thesis. In the case $\omega\tau \gg 1$ where ω is close to the plasma frequency, the imaginary part of $\varepsilon(\omega)$ vanishes and the real part simplifies to:

$$\varepsilon(\omega) = \varepsilon_1(\omega) = 1 - \frac{\omega_p^2}{\omega^2} \tag{2.18}$$

This equation is only valid for metals that do not show any interband transitions within a given frequency domain. In the case of gold, the free electron model brakes down for energies above 2 eV (or wavelengths below 620 nm). This is illustrated in 2.1 where the real and imaginary part of the measured dielectric function of gold (red dots) are compared with the free electron model (Drude model).

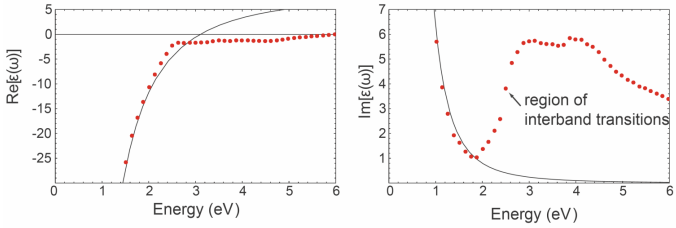

FIGURE 2.1. Dielectric function for a free electron gas compared to the measured gold data of Johnson and Christy, 1972 [33]. The plots are taken out of [32].

The free electron gas model can also be identified with the Drude model [34]. According to Drudes theory, electrons are ballistic particles with momentum $\boldsymbol{p}$ and that scatter randomly with other particles after a characteristic time τ. The Drude equation of motion for electrons in metals is therefore:

$$\frac{d\boldsymbol{p}}{dt} = -\frac{\boldsymbol{p}}{\tau} - e\boldsymbol{E} \tag{2.19}$$

With $\boldsymbol{p} = m_e^* \cdot d\boldsymbol{x}/dt$ this can be identified with Eq. (2.11), leading to the free electron gas dielectric function of Eq. (2.15).

So far, we have dealt with $\varepsilon(\omega)$ in the regime $\omega < \omega_p$ where metal reflects electromagnetic radiation and therefore shows the characteristic metallic shine. For $\omega > \omega_p$ metals are transparent and the propagation of radiation through them follows the equation:

$$\omega^2 = \omega_p^2 + K^2 c^2 \tag{2.20}$$

with K being the incoming wave vector. This equation is only valid for $\omega > \omega_p$, therefore, transverse electromagnetic waves with $\omega < \omega_p$ cannot travel through a metal. In the special case $\omega = \omega_p$, we have $\boldsymbol{K} = 0$ and so called volume plasmons can be excited. These plasmons are collective longitudinal electron oscillations in the whole metal. However, the condition $\boldsymbol{K} = 0$ forbids an excitation with electromagnetic radiation. Therefore, the only way to create volume plasmons is through impact of other particles (e.g. electrons).

There are also other ways to excite resonant electronic oscillations in a metal that can be excited optically and that reveal many interesting properties about the metal and its surroundings. Namely surface plasmons and localized surface plasmons that will be the focus of the following sections.

2.2 SURFACE PLASMONS

Surface plasmons are electronic excitations that propagate along interfaces between metallic and dielectric media [32]. They are confined to the surface of the metal, decaying exponentially in the volume. Since the surface plasmon dispersion curve does not cross the light line in a dispersion diagram, surface plasmons cannot be excited directly by incident light. Nevertheless, there are several schemes to excite these surface plasmon polaritons. They can either be excited by other particles, like electrons, or by light in an indirect excitation geometry like the so-called Kretschmann or Otto configuration. In the Kretschmann configuration [35], a thin metal film is put onto one side

of a prism. Then the prism is illuminated under an angle of total internal reflection so that only an evanescent wave enters the metal. That way a surface plasmon wave is excited in the metal traveling parallel to the surface. This is possible because the surface plasmon is excited at the metal air interface by light with a wave vector characteristic for SiO_2 (material of the prism). Now that the SiO_2 light line and the metal-air interface surface plasmon dispersion curves cross, the excitation can be performed as long as the metal film is thin enough to allow the evanescent wave of the prism to reach the outer surface of the film. If the resonance condition is fulfilled, the reflectivity of the prism is reduced. In this way the plasmon resonance can be detected by an angle-resolved measurement of the reflected light. For a more detailed discussion concerning surface plasmon resonances and their applications see S. Maier, '*Plasmonics: Fundamentals and Applications*' [32] or a review article about surface plasmon sensors [36].

2.2.1 *Localized Surface Plasmons*

In contrast to surface plasmons, localized surface plasmons are not propagating. They occur in metallic particles that are smaller than the wavelength of visible light. Nevertheless, they can be excited by it. Especially noble metal nanoparticles have very distinct resonances, where the resonance wavelength is not only dependent on the metal but also on the nanoparticle's shape and size. These resonances, especially in gold and silver particles, produce very brilliant colors and, therefore, they were used in many applications for the last 3 thousand years.

Even though, the Romans did not know about the physical background of surface plasmon resonances, solutions of gold and silver particles were already used in the 4th century AD to color glass. The Lycurgus Cup shown in Fig. 2.2 is a very impressive example for the art of glass coloring using noble metal nanoparticles. Many church windows were also colored with glasses containing these particles, because of their vibrant colors.

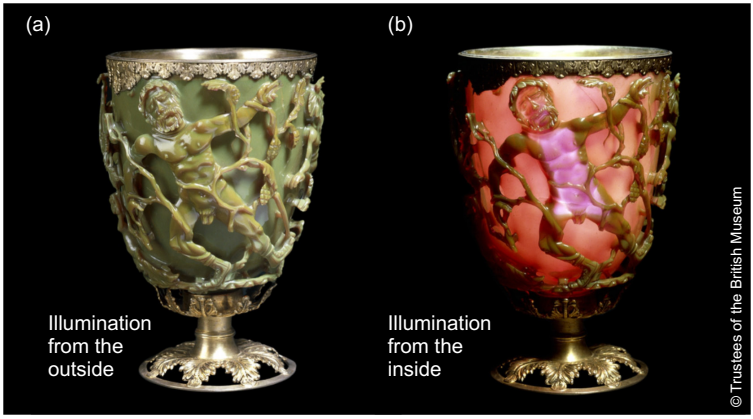

FIGURE 2.2. Roman Lycurgus Cup from the 4th century AD. The cup contains gold and silver nanoparticles that show a surface plasmon resonance. (a) Cup, illuminated from the outside. The reflected light makes the cup appear green. (b) Cup, illuminated from the inside. The transmitted light is mostly red. The difference comes from the resonant metal particles in the green wavelength region. Therefore, the scattered light is green and the transmitted light is mostly red. Both photographs are used with kind permission of the British museum.

The physics of these localized surface plasmon resonance (LSPR) are best explained by calculating the electric fields for a small metallic sphere. The sphere (see Fig. 2.3) is much smaller than the wavelength of the incident light ($a \ll \lambda$). Therefore, the electric field is almost constant over the whole sphere and can be approximated by an electrostatic field $\boldsymbol{E} = E_0\hat{\boldsymbol{z}} = E_0 \cos\theta$. This approximation is valid for particles smaller than 100 nm.

The normal modes of the electric field ($\boldsymbol{E} = -\nabla \cdot \Phi$) of such a geometry can be derived by solving the Laplace equation:

$$\nabla^2 \Phi = 0. \tag{2.21}$$

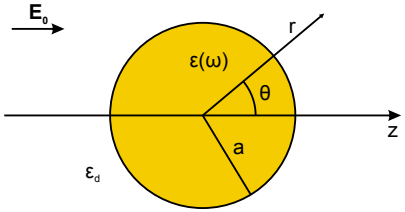

FIGURE 2.3. Sketch of the metallic sphere placed in a uniform electric field. The sphere has a radius a and a dielectric function $\varepsilon(\omega)$ and is surrounded by a material with dielectric constant ε_d. The whole system is exposed to an electrostatic field $\boldsymbol{E_0}$ with a field vector parallel to the z-direction.

The general solution for a sphere is [32]:

$$\Phi(r,\theta) = \sum_{l=0}^{\infty} \left[A_l r^l + B_l r^{-(l+1)} \right] P_l(\cos\theta) \tag{2.22}$$

where A_l and B_l are coefficients that need to be determined by boundary conditions and $P_l(\cos\theta)$ are the Legendre Polynomials of order l. Furthermore, the Potential can be split into the potential in and outside of the sphere. Additionally, the field has to be finite for $a \longrightarrow 0$ and at the same time resemble the incoming field for $r \longrightarrow \infty$. By applying the boundary condition that the tangential components of the electric field and the normal components of the displacement field have to be the same for the inner and the outer potential at $r = a$, we get the solutions for both Φ_{in} and Φ_{out}:

$$\Phi_{in} = -\frac{3\varepsilon_d}{\varepsilon(\omega) + 2\varepsilon_d} \cdot \boldsymbol{E}_0 r \cos\theta \tag{2.23}$$

$$\Phi_{out} = -\boldsymbol{E}_0 r \cos\theta + \frac{\varepsilon(\omega) - \varepsilon_d}{\varepsilon(\omega) + 2\varepsilon_d} \cdot \boldsymbol{E}_0 \cdot a^3 \cdot \frac{\cos\theta}{r^2}. \tag{2.24}$$

It is insightful to have a closer look at Φ_{out}. The first part is the incoming field. This second part can be written as dipole, located at the sphere's center:

$$\Phi_{out} = -\Phi_0 + \frac{\boldsymbol{p} \cdot \boldsymbol{r}}{4\pi\varepsilon_0\varepsilon_d r^3} \tag{2.25}$$

$$\boldsymbol{p} = 4\pi\varepsilon_0\varepsilon_d a^3 \frac{\varepsilon(\omega) - \varepsilon_d}{\varepsilon(\omega) + 2\varepsilon_d}\boldsymbol{E}_0. \tag{2.26}$$

This means that the incoming field induces a dipole moment inside the sphere. That dipole moment can be written in terms of the polarizability α through

$$\boldsymbol{p} = \varepsilon_0\varepsilon_d\alpha\boldsymbol{E}_0 \tag{2.27}$$

with α being:

$$\alpha = 4\pi a^3 \frac{\varepsilon - \varepsilon_d}{\varepsilon + 2\varepsilon_d}. \tag{2.28}$$

Equation (2.28) is very interesting in terms of surface plasmon resonance. For wavelength regions with vanishing imaginary part of ε the absolute value of the polarizability is resonantly enhanced at

$$\mathfrak{Re}\left(\varepsilon(\omega)\right) = -2\varepsilon_d, \tag{2.29}$$

hence, the frequency where the denominator $|\varepsilon + 2\varepsilon_d|$ has a minimum. This relation is also called Fröhlich condition for a dipole surface plasmon. This resonance is very sensitive to changes in ε_d and therefore the dielectric surrounding of the nanoparticle, giving rise to the many applications LSPR has today. Equation (2.29) also shows that the resonance red-shifts when ε_d is increased. For a Drude metal sphere in air the resonance condition is met if $\omega = \omega_p/\sqrt{3}$.

We now can derive the electric fields in and outside of the spherical particle from the potential of Eq. (2.23) and Eq. (2.25).

$$\boldsymbol{E_{in}} = \frac{3\varepsilon_d}{\varepsilon + 2\varepsilon_d}\boldsymbol{E_0} \tag{2.30}$$

$$\boldsymbol{E_{out}} = \boldsymbol{E_0} + \frac{3\boldsymbol{n}\left(\boldsymbol{n}\cdot\boldsymbol{p}\right) - \boldsymbol{p}}{4\pi\varepsilon_0\varepsilon_d} \cdot \frac{1}{r^3} \tag{2.31}$$

From the equations it becomes clear that both the electric field in and outside of the sphere gets resonantly enhanced if Eq. (2.29) is matched.

The scattering and absorption cross sections crucially depend on α and therefore both are resonantly enhanced when the condition in Eq. (2.29) is matched. This is also the reason why nanoparticles that are smaller than the wavelengths of visible light can still be made visible under, for example, a dark-field microscope. The brilliance of window paint, containing metal nanoparticles, can be explained by this as well.

If we want to calculate the resonances more accurately, we need to consider the oscillating time-dependent behavior of the electric and the magnetic field that penetrates the particle. This is especially important if the particles get larger and their size comes close to the visible wavelength ($d > 100\,\text{nm}$). One way to solve these issues is by applying Mie theory. It is a full electrodynamic approach that expands the fields in normal modes to solve for the resonance conditions. A more detailed discussion can be found, for example, in the book '*Absorption and Scattering of Light by Small Particles*' [37].

The calculations for shapes other than spheres can even be more challenging and mostly require numerical calculation methods to estimate the electric fields or even the resonance position. However, in Chapter 3 I present a method to calculate the resonances of cuboids based on an analytical model.

Nevertheless, the most important physical insights are already visible in the simple example of a sphere in a dielectric environment. Especially the strong dependence of the electric field on the dielectric function ε_d of the environment is extremely important, for example for refractive index sensing.

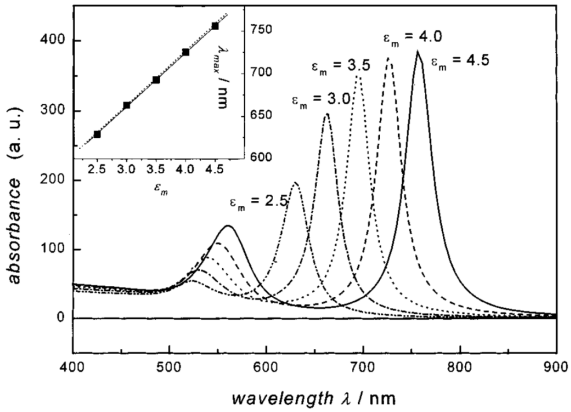

FIGURE 2.4. Influences of the surrounding refractive index on the surface plasmon resonance. Simulated are the LSPR spectra for gold nano-rods with an aspect ration of 3.3 and a surrounding dielectric with ε_m (called ε_d in the rest of the thesis) varying from 2.5 to 4.5. The plot is adapted from Link et al. [38].

2.2.2 *Refractive Index Sensing*

Localized surface plasmons or particle plasmons are very sensitive to changes in the dielectric function of both, the dielectric environment and the metal itself. Most dielectrics have a predominantly real and positive $\varepsilon(\omega)$ with a negligible ω-dependence in the visible region. Thus, the dielectric response of the material can be reduced to a constant refractive index $n = \sqrt{\varepsilon_1} = \sqrt{\varepsilon_d}$.

Figure 2.2 shows the ε_d-dependence of the plasmon peak position and amplitude. The amplitude increases and the plasmon resonance red-shifts when the dielectric constant increases. To some degree, this shift is even linear (see inset in Fig. 2.4). This makes it possible to use the plasmon peak to identify shifts in a dielectric environment.

The effects can be utilized in different sensing schemes. If one brings a fluid or gas with a slightly different refractive index in the vicinity of the metal particle, the plasmon resonance is shifted according to the refractive index of the fluid or gas. Only refractive index

changes in the direct vicinity of metal particle influence the plasmon peak position. Therefore, it is sufficient to change the environment in a radius of several hundred nanometers around the nanoparticle. All changes that happen at greater distances do not influence the plasmonic behavior.

This feature is used in many plasmonic bio-sensing schemes. After bio-functionalization of the metal particle surface only certain biomolecules are able to get close to the particle and bind to it. Therefore, the functionalization makes the plasmonic sensor selectively sensitive to the concentration of the molecules in question [39].

A slightly different scheme is used for plasmonic gas sensing. Since the refractive index change induced by concentration changes in the gaseous environment is very small, a change of the plasmon resonance cannot be observed directly. The refractive index of hydrogen, oxygen, air or pure nitrogen only deviates in the 4th decimal from $n = 1$ (e.g. $n_{H_2} = 1.00013875$ at 650 nm [40]). Instead, the gases can influence other materials that in turn change their refractive index in a measurable fashion. If this material is made a plasmonic antenna, once can use the dielectric change in the antenna itself, instead of the dielectric environment. Only materials with losses low enough that plasmonic resonances can still be excited can be used in that scheme. However, another possibility is to place a gas-absorbing material very close to the plasmonic antenna so that it is part of the dielectric environment. A prominent example is palladium, serving as sensitive material for detecting hydrogen. Palladium can serve as dielectric environment for a plasmonic nanoparticle [41] as well as plasmonic particle itself [42].

2.3 THE METAL-HYDROGEN SYSTEM

So far we examined the light-matter interaction, plasmonic resonances and their application in refractive index sensing. In the following,

we have a closer look on the materials and their optical and thermodynamic properties. Palladium and other transition metals like vanadium, yttrium, but also magnesium, nickel and iron all react to hydrogen, and form more or less stable metal-hydride compounds. These compounds have very interesting optical, electronic and thermodynamic properties and have already been studied intensively in the last 50 years [43]. Of special interest among all these hydrides is the palladium hydride PdH_x. It is the only metal the can split and absorb gaseous hydrogen at room temperature in significant amounts. It is a model system for all other metal hydrogen compounds and therefore, discussed in most detail in the following chapters.

2.3.1 *Hydrogen*

The hydrogen atom is the simplest and smallest element in the periodic table. It consists of one proton and one electron in an 1s orbital. Therefore, it is the only atom whose quantum mechanical wavefunction can be determined analytically. The natural form of hydrogen are molecules with two protons and two electrons. These molecules have a binding energy of $E_0 = 4.748\,\text{eV}$ [43]. At room temperature, hydrogen forms a gas that is lighter than air. It is a flammable colorless gas that ignites in air at a wide range of concentrations between 4 and 74 % [44]. This is due to a exothermic reaction with oxygen to water:

$$2H_2 + O_2 \longrightarrow 2H_2O + 572\,\text{kJ} \tag{2.32}$$

This reaction makes hydrogen a very powerful explosive. However, the energy of this reaction can be harnessed in hydrogen fuel cells to produce electric energy, safely. Since the only by-product of the reaction is water, hydrogen fuel cells have a great potential to substitute petroleum in the near future [45]. Making cheap and reliable hydrogen detection schemes indispensable.

2.3.2 *Palladium*

The material that is mostly used for hydrogen detection is palladium. Palladium is a transition metal with the atomic number 46. The crystallographic structure is a face centered cubic lattice with a lattice constant of 3.88 Å. It has a shiny silver color and is a strong catalyst like most of the other platinum group metals. As a consequence, its powder is used in industrial processes like in hydrogenation and dehydrogenation of other materials or in speeding up petroleum cracking processes. Nevertheless, the main applications of palladium are related to hydrogen.

2.3.2.1 *Palladium and hydrogen*

One of the unique properties of palladium is its ability to absorb an enormous amount of hydrogen. The density of hydrogen atoms stored in palladium can be up to 935 times higher than that of pure hydrogen gas at ambient pressure [46]. Due to the palladium's catalytic properties, the hydrogen molecules split up into atoms at the Pd surface and than diffuse into the volume. The power of splitting, absorbing and storing hydrogen in its lattice makes palladium the ideal model system for studying the processes important for hydrogen storage as well as sensing applications [16]. The number of hydrogen atoms that are actually absorbed closely depends on the temperature and the partial pressure of the surrounding H_2 gas. The pressure diagram of Fig. 2.5 shows the form of the dependence.

Figure 2.5 looks very similar to a classical phase diagram. Indeed, palladium undergoes a phase-change when incorporating hydrogen. For temperatures below the critical temperature $T_C = 293\,°\mathrm{C} = 566\,\mathrm{K}$, there are three distinctive regimes. First, the so-called α-phase (or solid solution), where the hydrogen/palladium atomic ratio slowly increases for increasing H_2 partial pressure. In this phase the hydrogen uptake follows Sieverts law [43]:

$$\sqrt{p} = K_s x. \tag{2.33}$$

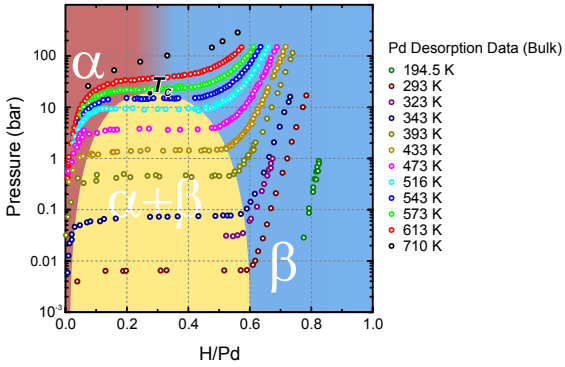

FIGURE 2.5. Pressure-composition diagrams of bulk palladium at different levels of H_2 pressure and for different temperatures. The red colored area represents the α-phase, the yellow colored area the phase coexistance region and the blue shaded area the β-phase. The plotted data is from Manchesters '*Phase Diagrams of Binary Hydrogen Alloys*' [47].

Where p is the hydrogen partial pressure, K_S the Sieverts constant and x the ratio of hydrogen to palladium atoms. This law generally holds for hydrogen uptake in metals at low hydrogen pressures and can be derived from the fact that the H_2 molecules are dissociated into atoms at the metal's surface while getting dissolved in the volume.

At higher pressures the palladium enters the regime of α and β-phase coexistence. If the gas exceeds a critical pressure, the hydrogen uptake increases rapidly. This critical pressure is highly dependent on the temperature. For higher temperatures the critical pressure is increased, while the region of phase coexistence is getting smaller. This is true until a critical temperature, above which the coexistence region vanishes and the transition between α and β-phase becomes smooth.

At low temperatures the coexistence region covers a large part of the x-axis. This makes the system very unstable, when approaching the critical pressure. Since most of the change in the palladium happens within a very narrow pressure corridor, small variations in the hydrogen pressure can have a large impact on the whole system.

The third region in Fig. 2.5 is called β-phase or palladium hydride. This is again a region where the hydrogen concentration inside the palladium slowly varies with increasing pressure. The hydrogen concentration in the palladium increases until the maximum value ($x = 0.82$) is reached. Even for very high pressures the composition does not exceed this value [13].

It is also instructive to monitor the palladium lattice constant going through the different phases of hydrogen uptake. As showed by Khanuja *et al.* [48], the lattice constant of palladium stays almost constant while being in the α-phase. It only changes from 0.3889 nm to 0.3893 nm, an increase of about 0.1 %. However, when the hydrogen pressure exceeds the critical value and the palladium is in its β-phase, the lattice constant rises sharply to a value of 0.4023 nm. This corresponds to an increase of 3.4 % in length and an increase of 10.7 % in the palladium molar volume.

Not only the volume changes when hydrogen is absorbed into the palladium lattice, but also its dielectric and conductive properties.

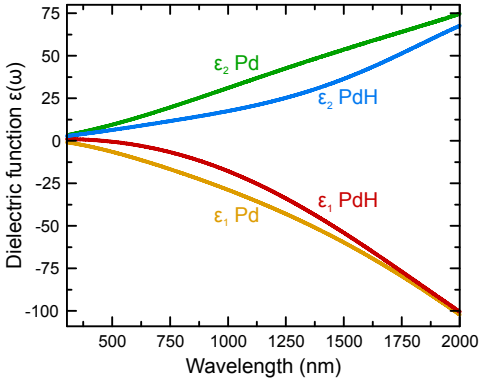

FIGURE 2.6. Real part (ε_1) and imaginary part (ε_2) of the Pd and PdH dielectric function. Calculated from the optical constants n and κ measured by Von Rottkay *et al.* [49] on a 10 nm Pd film.

Figure 2.6 shows the real and imaginary part of the palladium's dielectric function in the visible and near-infrared region. In black and

green for pure palladium and in red and blue of palladium hydride ($PdH_{0.82}$). It can be seen that the hydration of palladium lowers the absolute value of the dielectric function, especially in the region between 700 and 1500 nm. Combined with the change of the dielectric function, the conductivity changes for the PdH case. At high hydrogen concentrations palladium even becomes a semiconductor [46].

In plasmonic applications, the difference in the dielectric function of Pd and PdH can also be very interesting. Going from Pd to PdH would lead to an red-shift in the plasmon resonance peak. This can be easily explained with the argument of Section 2.2.1. In the case of a metal sphere, the resonance condition is $\Re\mathrm{e}\left[\varepsilon(\omega)\right] = -2\varepsilon_d$. This condition can be visualized by drawing a constant line with y-value $-2\varepsilon_d$ into Fig. 2.6 ($\varepsilon_d > 0$). The point where the line intersects with the black line (ε_1 Pd) is the resonance wavelength for palladium. Whereas the intersection with the red PdH line would represent the resonance wavelength in palladium hydride. This is a very basic calculation for the plasmon peak wavelength, but nevertheless the qualitative statement is valid.

3

DIELECTRIC PROPERTIES OF METALLIC NANOSTRUCTURES

In this chapter, a way to determine dielectric functions of metallic nanoparticles that does not involve any assumptions about the material, except that it supports plasmonic resonances, will be proposed. It is realized through deriving an accurate analytical relation for the plasmonic peak wavelength of spheroids and square patches without any assumption about the dielectric function. The resulting expressions enable us to determine the dielectric properties, as well as structural parameters of nanosized materials, by making use of plasmonic resonances and their highly sensitive dependence on electronic and geometric parameters. Exemplary, gold (Au) and palladium (Pd) square nanopatches are studied. Their dielectric function ε, the depolarization factor N and the geometric parameter m, linking square patches to the plasmonic response of oblate spheroids are determined and compared to literature data. All this is obtained by analyzing plasmonic resonance peak position data of square nanopatches with various side lengths and three different sample thicknesses. The procedure is very general and can be applied to a variety of stable and unstable nanomaterials in the future that do not allow for reliable ellipsometric studies. In Chapter 5, the method is applied to hydrogenated Pd nano-patches, giving a unique opportunity to study the geometric and dielectric behavior of the material in-situ.

3.1 INTRODUCTION

Knowledge of a materials response to light and electromagnetic waves in general is a crucial ingredient in modern technology and many

scientific discoveries. The most powerful and widely used way to describe such a response is the frequency-dependent complex dielectric function $\varepsilon(\omega)$. For linear and isotropic media it relates the dielectric displacement $\boldsymbol{D}$ to the electric field $\boldsymbol{E}$ (see Section 2.1.2). All electric properties of a material can be derived from the dielectric function, from the DC conductance, over the interplay with RF fields to the optical response.

The most common method to determine the dielectric properties of a material, especially for optical frequencies, is the use of ellipsometry. In ellipsometry the angle-dependent transmitted and reflected electromagnetic polarization of a sample of known dimensions and surface properties are measured [50]. The obtained reflectance ratios cannot be converted straightforward into the complex dielectric function ε (or sometimes the complex refractive index $\tilde{n} = n + i\kappa$ where $\varepsilon = \tilde{n}^2$). A model, either containing information on the materials behavior (Drude metal, etc.), or several free parameters is required to be fitted to the measured data. The Forouhi-Bloomer model is a prominent fitting method used to determine the complex refractive index for thin amorphous [51] or crystalline films [52]. It uses a set of five physically based parameters (or in the case of crystalline structures a series of these parameters) to fully describe the frequency dependent complex refractive index. Modern ellipsometers use more complex models also correcting for surface roughness, grain size or impurities. However, all these models depend on small changes in the reflectance (or transmittance), which crucially depends on the quality of the film and especially of the films surface.

To determine the optical properties of a material that cannot be processed to a thin film with good (or at least well known) surface quality, other techniques than ellipsometry are necessary. Especially for nanoparticles, the possibilities for obtaining the dielectric properties are limited. Since the enhanced scattering and excitation of localized modes, such as localized surface plasmon resonance (LSPR), strongly change the reflectance and transmittance, and thus, render standard methods like ellipsometry to be impossible. Therefore, bulk dielectric data are mostly used to derive or simulate the optical properties of such nanoparticles. However, the hugely altered surface-to-volume

ratio in nanostructures also alters the optical response of the structures, generating the need to directly determine the dielectric properties of such structures.

There is no straightforward general technique to describe all optical properties of different kind of nanoparticles. However, many metallic nanoparticles support localized oscillations of their electron gas that absorb and scatter light, depending on their material properties and geometry (namely LSPR, see Chapter 2). These resonances, hence, are a measure for the dielectric properties of the particle in the region around the resonance frequency. By producing many different sizes of particles with the same material properties, it is, theoretically, possible to determine the optical properties over a wide range of frequencies using plasmonic resonances (depending on the material, approximately for $\omega < 600\,\mathrm{THz}$). Unfortunately, for most particle geometries the relation between resonance wavelength λ_{res} and dielectric properties is very complex and cannot be described analytically (what would be required for an easy inversion $\lambda_{res}(\varepsilon) \rightarrow \varepsilon(\lambda)$). For some simpler geometries, such as spheres and spheroids, it is possible to derive analytical equations, as we show in the following sections. However, full spheroidal structures are very challenging to fabricate with such accuracy. By making a few simple assumptions about the conversion of geometry related factors for spheroid samples, we are also able to find an accurate description for flat rectangular prisms with quadratic base (cuboids with $a = b > c$ that in the following are called *square patches*). The description for square patches is necessary to use the model for well-defined nanostructures on a substrate, manufacturable using lithography techniques.

3.2 ANALYTICAL EXPRESSION FOR THE PLASMON RESONANCE

In the following sections, the theoretical groundwork for our method is demonstrated. First, we derive an accurate expression for the plasmon peak position for the ideal case of oblate spheroids. This is necessary to determine the functional form of the dependencies on geometry and epsilon. Secondly, the same functional forms will be used for square patches but with appropriately scaled parameters.

In the electrostatic approximation, the polarizability of an oblate spheroid with major axis $a = b$ and minor axis c and the dielectric function $\varepsilon\left(k\right)$, where k is the wave-vector, in a medium with refractive index $n = \sqrt{\varepsilon_d}$ is given by [53]

$$\alpha\left(k, \varepsilon_d\right) = \frac{4\pi a^2 c}{3} \frac{\varepsilon\left(k\right) - \varepsilon_d}{\varepsilon_d + N_i \cdot \left(\varepsilon\left(k\right) - \varepsilon_d\right)}. \tag{3.1}$$

Here, N_i with $i = x, y, z$ is the geometric depolarisation factor [54] for an oblate ellipsoid $\left(a = b > c\right)$, given by [55, 56]

$$N_z = \frac{1 + e^2}{e^3}\left(e - \arctan e\right) \tag{3.2}$$

$$N_x = N_y = \frac{1}{2}\left(1 - N_z\right) = \frac{\left(1 + e^2\right)\arctan e - e}{2e^3} \tag{3.3}$$

with the eccentricity

$$e = \sqrt{\left(\frac{a}{c}\right)^2 - 1}. \tag{3.4}$$

In the case of light impinging on the structures along the z-axis, one only needs to consider the polarizability along the x- and y-axis and thus $N_x = N_y$. The metallic nano- and micro-structures studied in the following sections have lateral dimensions between 150 nm and

5000 nm while having thicknesses ranging from 30 nm to 100 nm. This results in eccentricities e between 0 and 200. Within this range Eq. (3.3) is well represented by

$$N_x = \frac{1}{1.2718 \cdot \frac{a}{c} + 1.6499}. \tag{3.5}$$

For ratios $a/c > 1.5$ the difference between Eq. (3.3) and Eq. (3.5) is well below 1 % (and even below 0.1 % for $a/c > 5$).

When analyzing square-patches instead of oblate spheroids, in the following chapters the geometrical depolarization factor has to change, too. Therefore, we propose the general form

$$N_x = \frac{1}{\alpha \cdot \frac{a}{c} + \beta}. \tag{3.6}$$

With $\alpha = 1.2718$ and $\beta = 1.6499$ Eq. (3.6) reduced to Eq. (3.5). We assume that for a general form with symmetry in x and y and with characteristic length in z direction smaller than in x and y ($l_x = l_y > l_z$) (e.g. a square-patch), the general form for N_x in Eq. (3.6) is preserved. Therefore, we will be able to determine a set of parameters α and β for each kind of geometry. For simplification, and due to the fact that we will only deal with N_x, we set $N_x \equiv N$.

We are interested in finding a model for plasmonic resonances of structures with characteristic dimensions below or close to the wavelength of the impinging light. Therefore, the quasi-static approximation for the polarizability in Eq. (3.1) needs to be expanded to get a realistic model. The so-called modified long-wave approximation (MLWA) is a way to deal with retardation in particles (to first order) and therefore leads to a much more accurate expression for the polarizability [57–60]. For a particle within a medium of real-valued dielectric constant, ε_d reduces to the real-valued factor $\varepsilon_d = n^2$. With the impinging light wave-vector $k = 2\pi/\lambda$, the radius a (parallel to the electric field) and electrostatic polarizability $\alpha\left(k\right)$, the modified polarizability is given by

$$\alpha\left(k, n\right)_{MLWA} = \frac{1}{\frac{1}{\alpha\left(k,n\right)} - \frac{n^2}{4\pi a}k^2 - i\frac{n^3}{6\pi}k^3}. \tag{3.7}$$

The quadratic term in the denominator is due to radiation damping and the cubic term originates in the dynamical depolarization.

3.2.1 *Scattering and Absorption Cross-sections*

Using the polarizability Eq. (3.7) we can calculate the extinction and scattering cross-sections for ellipsoid as [53]

$$c_{scatt}\left(k\right) = \frac{k^4}{6\pi}\left|\alpha\left(k,n\right)_{MLWA}\right|^2 \tag{3.8}$$

and

$$c_{abs}\left(k\right) = k\Im\left\{\alpha\left(k,n\right)_{MLWA}\right\}. \tag{3.9}$$

As the dielectric function of a metal is complex, we can write

$$\varepsilon\left(k\right) = \varepsilon_1\left(k\right) + i\varepsilon_2\left(k\right). \tag{3.10}$$

Introducing Eq. (3.10) and Eq. (3.1) into Eq. (3.7), we get the full polarizability

$$\begin{aligned}\alpha\left(k,n\right)_{MLWA} =& \left[\frac{3}{4\pi a^2 c}\left(E\left(k\right)+N\right) - \frac{n^2}{4\pi a}k^2\right.\\ &\left. - i\left(\frac{n^3}{6\pi}k^3 + \frac{3}{4\pi a^2 c}F\left(k\right)\right)\right]^{-1}\\ =& \frac{4\pi a^2 c}{3}\left[\left(E\left(k\right)+N\right) - \frac{acn^2}{3}k^2\right.\\ &\left. - i\left(\frac{2a^2 cn^3}{9}k^3 + F\left(k\right)\right)\right]^{-1}\end{aligned} \tag{3.11}$$

with the dielectric expressions $E\left(k\right)$ and $F\left(k\right)$, defined as

$$E\left(k\right) = \frac{n^2\left(\varepsilon_1 - n^2\right)}{\left(\varepsilon_1 - n^2\right)^2 + \varepsilon_2^2} = \frac{n^2}{\left(\epsilon_1 - n^2\right) + \frac{\epsilon_2^2}{\left(\epsilon_1 - n^2\right)}} \tag{3.12}$$

and

$$F\left(k\right) = \frac{n^2\epsilon_2}{\left(\epsilon_1 - n^2\right)^2 + \epsilon_2^2}. \tag{3.13}$$

It is worth having a closer look onto Eq. (3.11), since it nicely separates all macroscopic and extrinsic parameters (k, a, c, n, N) from the microscopic material parameters, as the dielectric function of the material appears only in the expressions $E\left(k\right)$ and $F\left(k\right)$.

The polarizability in Eq. (3.11) makes it possible to calculate the full extinction cross section (ECS) c_{ext} for a spheroidal particle

$$c_{ext} = c_{abs} + c_{scatt} \tag{3.14a}$$

with

$$c_{abs} = \frac{4\pi a^2 c}{3} \frac{\left(\frac{2a^2cn^3}{9}k^4 + kF\right)}{\left(E + N - \frac{acn^2}{3}k^2\right)^2 + \left(\frac{2a^2cn^3}{9}k^3 + F\right)^2} \tag{3.14b}$$

and

$$c_{scatt} = \frac{8\pi a^4 c^2}{27} \frac{k^4}{\left(E + N - \frac{acn^2}{3}k^2\right)^2 + \left(\frac{2a^2cn^3}{9}k^3 + F\right)^2}. \tag{3.14c}$$

3.2.2 *Zeroth Order Approximation*

The plasmonic resonance of a nanoparticle is equivalent to the maximum of the ECS Eq. (3.14a). A zeroth order estimate is given by the pole of the real part of the polarizability in Eq. (3.11). Thus

$$E\left(k\right) + N - \frac{acn^2}{3}k_0^2 \equiv 0 \tag{3.15}$$

with $k_0 = 2\pi/\lambda_0$, the 0^{th} order approximation of the plasmon resonance wavelength.

To simplify the notation we set

$$A \equiv \frac{acn^2}{3} \tag{3.16}$$

and then

$$k_0^2 = \left(\frac{2\pi}{\lambda_0}\right)^2 = \left(\frac{E\left(k\right)+N}{A}\right) \tag{3.17}$$

$$\lambda_0 = 2\pi\frac{\sqrt{A}}{\sqrt{N+E\left(k\right)}} = 2\pi n\sqrt{\frac{ac}{3\left(N+E\left(k\right)\right)}} \tag{3.18}$$

Equation (3.18) is typically 10 % accurate. Important is that λ_0 can be expressed only in terms of geometrical parameters (a, c, N) and the dielectric factor E.

Rearranging Eq. (3.15) we, thus, have to lowest order

$$E_0\left(\lambda\right) = \frac{4}{3}\pi^2 ac\frac{n^2}{\lambda_0^2} - N. \tag{3.19}$$

3.2.3 *First Order Estimate of the Peak Position*

To get a more accurate description of the peak position, we consider the scattering cross-section c_{scatt} in the form

$$c_{scatt} = \left(\frac{8\pi a^4 c^2}{27}\right)\frac{1}{\left(\frac{(E+N)}{k^2} - \frac{acn^2}{3}\right)^2 + \left(\frac{2a^2cn^3}{9}k + \frac{F}{k^2}\right)^2}. \tag{3.20}$$

Note that the denominator is the same as for the absorption cross-section. Therefore, the treatment is valid for both cross-sections.

The last term $\frac{F}{k^2}$ is in general small and can be neglected. This is explicitly demonstrated for typical spheroids in Fig. 3.1.

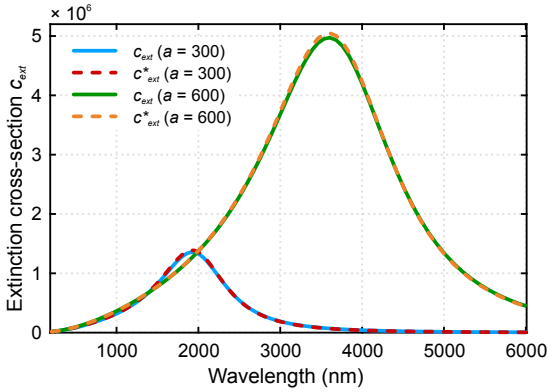

FIGURE 3.1. ECS for two exemplary spheroids ($a = 300\,\text{nm}$ & $600\,\text{nm}$, $c = 25\,\text{nm}$, $n = 1.25$). The solid lines show the full ECS c_{ext} calculated, using Eqs. (3.14b) and (3.14c). The dashed lines (c^*_{ext}) are calculated with the same formula but setting $F = 0$. All spectra use literature dielectric data for Au from [61].

The maximum of c_{scatt} occurs, when

$$\frac{d}{dk}\left(\left(\frac{\left(E\left(k\right)+N\right)}{k^2}-\frac{acn^2}{3}\right)^2+\left(\frac{2a^2cn^3}{9}k\right)^2\right)\equiv 0. \tag{3.21}$$

More compactly when

$$\frac{d}{dk}\left(\left(\frac{\left(E\left(k\right)+N\right)}{k^2}-A\right)^2+\left(B\cdot k\right)^2\right)=0 \tag{3.22}$$

with A from Eq. (3.16) and

$$B\equiv\frac{2a^2cn^3}{9} \tag{3.23}$$

Equation Eq. (3.22) implies

$$\left(B^2k^6-2\left(E+N\right)^2+2A\left(E+N\right)k^2\right)\approx 0, \tag{3.24}$$

if we assume that the k-dependence of $E\left(k\right)$ is very week, meaning $d/dk\left(E\left(k\right)\right) \approx 0$.

As shown in Eq. (3.18), to lowest order the resonance is found at

$$\left(\frac{E\left(k\right)+N}{A}\right) = k_0^2. \tag{3.25}$$

To find the next best approximation we set

$$k = k_0\left(1+x\right). \tag{3.26}$$

Introducing Eq. (3.26) into Eq. (3.24), one finds

$$\begin{aligned} B^2\left(k_0\left(1+x\right)\right)^6 - 2\left(E+N\right)^2 \\ +2A\left(E+N\right)\left(k_0\left(1+x\right)\right)^2 = 0. \end{aligned} \tag{3.27}$$

Keeping only linear terms in x we obtain

$$\begin{aligned} B^2k_0^6\left(1+6x\right) - 2\left(E+N\right)^2 \\ +2A\left(E+N\right)k_0^2\left(1+2x\right) = 0, \end{aligned} \tag{3.28}$$

resulting in

$$\begin{aligned} B^2\left(\frac{E+N}{A}\right)^3\left(1+6x\right) - 2\left(E+N\right)^2 \\ +2A\left(E+N\right)\left(\frac{E+N}{A}\right)\left(1+2x\right) = 0, \end{aligned} \tag{3.29}$$

using the definition of k_0 in Eq. (3.25) and by dividing through $\left(E+N\right)^2$, we finally get

$$\frac{B^2}{A^3}\left(E+N\right)\left(1+6x\right) + 4x = 0. \tag{3.30}$$

The solution to Eq. (3.30) is simply:

$$x = -\frac{1}{6+4\frac{A^3}{\left(N+E\right)B^2}}. \tag{3.31}$$

Using the definitions for A and B in Eqs. (3.16) and (3.23), we find

$$x = -\frac{1}{6 + \frac{3c}{(N+E)a}} \tag{3.32}$$

and

$$k = k_0 (1 + x) = \frac{1}{n}\sqrt{\frac{3(E+N)}{ac}}\left(1 - \frac{1}{6 + \frac{3c}{(N+E)a}}\right). \tag{3.33}$$

As

$$k = \frac{2\pi}{\lambda} \approx \frac{2\pi}{\lambda_0}(1 + x) \tag{3.34}$$

we can use the fact that $x << 1$ and obtain a relation for the peak wavelength

$$\begin{aligned} \lambda = \lambda_0 (1 - x) &= \lambda_0 \left(1 + \frac{1}{6 + \frac{3c}{(N+E)a}}\right) \\ &= 2\pi n \sqrt{\frac{ac}{3(N+E)}}\left(1 + \frac{1}{6 + \frac{3c}{(N+E)a}}\right). \end{aligned} \tag{3.35}$$

The expression Eq. (3.35) is quite accurate (better than 2 %). For example, for a spheroid with $n = 1.25$, $a = 300$ nm and $c = 25$ nm the pole of the real part of the denominator vanishes at $\lambda_0 = 1806.3$ nm. Then the correction factor is

$$\left(1 + \frac{1}{6 + \frac{3c}{(N+E)a}}\right) = 1.08841 \tag{3.36}$$

so that the approximate peak position is at

$$\lambda = 1806.3 \cdot 1.08841 = 1966.0\,\text{nm}, \tag{3.37}$$

compared to 1986.6 nm for the exact calculation (see Fig. 3.1). In this case, the error is $20.6/1986.6 \simeq 1.04$ %. This means that we can safely use Eq. (3.35) for further calculations.

3.2.4 *Determination of E(λ) to First Order*

In the previous section, we derived a relation for the plasmon resonance wavelength that only depends on geometrical parameters and the E-factor, containing all material-dependent information. Therefore, by solving Eq. (3.35) for E we will be able to determine material parameters, containing the dielectric function of nanomaterial with the plasmonic resonance wavelength and the particle geometry as sole input. Our aim is to find a closed relation for E of the form

$$E\left(\lambda\right) = f\left(\lambda, a, c, n\right). \tag{3.38}$$

Introducing

$$L\left(\lambda\right) = \frac{\sqrt{3}\lambda}{2\pi n a} \tag{3.39}$$

and

$$y = \sqrt{\frac{\left(N+E\right)a}{c}} \tag{3.40}$$

into Eq. (3.35), we obtain

$$6Ly^3 - 7y^2 + 3Ly - 3 = 0 \tag{3.41}$$

This equation can be solved exactly and leads to

$$\sqrt{\frac{\left(N+E\right)a}{c}} = W + \frac{\frac{49}{324L^2} - \frac{1}{6}}{W} + \frac{7}{18L} \tag{3.42}$$

and thus

$$E\left(\lambda\right) = \frac{c}{a}\left(W + \frac{\frac{49}{324L^2} - \frac{1}{6}}{W} + \frac{7}{18L}\right)^2 - N \equiv \frac{c}{a}M - N \tag{3.43}$$

with

$$W = \sqrt[3]{\sqrt{\frac{167}{15\,552L^2} + \frac{343}{11\,664L^4} + \frac{1}{216}} + \frac{11}{72L} + \frac{343}{5832L^3}}. \tag{3.44}$$

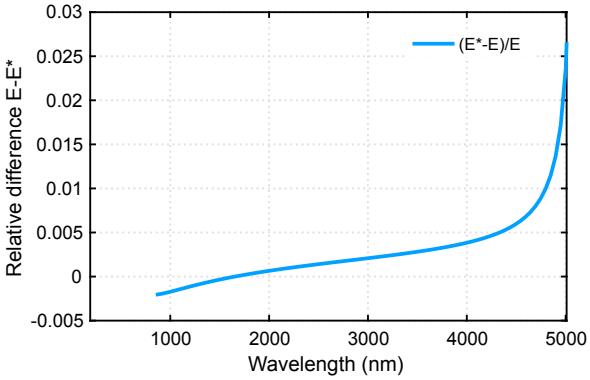

FIGURE 3.2. Difference between full solution and simplified E, demonstrated by calculating E^* using the approximate expression in Eq. (3.46) and E using the exact solution in Eq. (3.43) and plotting the difference normalized to the exact solution. For this example an Au spheroid with $a = 300\,\text{nm}, c = 25\,\text{nm}, n = 1.25$ is used. Over the full wavelength range, the two methods differ less than 3 %.

The complicated expression for M in Eq. (3.43) simplifies in the ranges of a and λ considered in this thesis to:

$$M = \left(W + \frac{\frac{49}{324L^2} - \frac{1}{6}}{W} + \frac{7}{18L} \right)^2 \simeq \frac{1.251}{L^{2.14}} = 19.717 \left(\frac{na}{\lambda} \right)^{2.14}. \quad (3.45)$$

Introducing Eq. (3.45) into Eq. (3.43), we obtain

$$\begin{aligned} E\left(\lambda, a, c, n\right) &= 19.717 \frac{c}{a} \left(\frac{na}{\lambda} \right)^{2.14} - N\left(a, c\right) \\ &= 19.717 c a^{1.14} \left(\frac{n}{\lambda} \right)^{2.14} - N\left(a, c\right) \\ &= 19.717 c a^{1.14} \left(\frac{n}{\lambda} \right)^{2.14} - \frac{1}{1.2718 \frac{a}{c} + 1.6499}. \end{aligned} \quad (3.46)$$

This simple expression $E\left(\lambda, a, c, n\right)$ is very powerful, since it gives us the possibility to predict the dielectric properties of a material, only knowing the geometry and the plasmonic resonance position. However, in real experiments it is almost impossible to study oblate spheroids. Therefore, in the next section, we will translate the results, obtained so far for oblate spheroids, to experimentally realizable geometries, namely square patches.

3.3 RESONANCES OF SQUARE NANOPATCHES

Square patches are rectangular prisms with quadratic base, side-length S and height t with $S > t$. Due to the similarities to oblate spheroids with major axis $a = b$, minor axis c and $a = b > c$, we postulate that a scaling factor m exists so that

$$a = m \times S \tag{3.47}$$

and

$$c = m \times t. \tag{3.48}$$

Consequently, the relevant equations for λ and E developed before for spheroids (namely, Eqs. (3.35), (3.43) and (3.46)) for square patches are

$$\lambda = 2\pi nm\sqrt{\frac{St}{3\left(N+E\right)}}\left(1+\frac{1}{6+\frac{3t}{(N+E)S}}\right), \tag{3.49}$$

$$E\left(\lambda, S, t\right) = \frac{t}{S}\left(W + \frac{\frac{49}{324L^2}-\frac{1}{6}}{W} + \frac{7}{18L}\right)^2 - N\left(S, t\right) \tag{3.50}$$

with

$$W = \sqrt[3]{\sqrt{\frac{167}{15\,552L^2}+\frac{343}{11\,664L^4}+\frac{1}{216}}+\frac{11}{72L}+\frac{343}{5832L^3}} \tag{3.51}$$

and with

$$L\left(\lambda\right) = \frac{\sqrt{3}\lambda}{2\pi nmS}. \tag{3.52}$$

and the simplified form for E

$$E\left(\lambda, m, S, t, n\right) = 19.717tS^{1.14}\left(\frac{mn}{\lambda}\right)^{2.14} - N\left(S, t\right). \tag{3.53}$$

The depolarization factor N very sensitively depends on the geometry of the structure. Hence, we cannot assume Eq. (3.5) to hold true, in the case of square patches. However, as mentioned before, a general form of the depolarization factor (see Eq. (3.6))

$$N\left(S, t\right) = \frac{1}{\alpha\frac{S}{t} + \beta} \tag{3.54}$$

could be able to provide a combination of α and β that is valid for square patches.

It is not a straightforward to determine N theoretically for the structures with non-spherical geometry and sharp edges, the best approach is to determine the value by using experimental data of known structures[1].

3.3.1 *The Square Patch Polarization Factor N*

To obtain the optimal values of α and β, without prior knowledge of m, n and E, it is necessary to find a set of equations where theses parameters drop out.

Therefore, we assume to have a set of experimental data of metallic square-patch structures with S varying over a wide range of sizes

1 In a private communication Prof. Dr. Tim Davis attempted to derive an accurate expression, based on geometrical considerations. This attempt, however also included the discretization of the geometry to form a mesh that could be used to numerically solve for N. The results, unfortunately, strongly depend on the selected mesh, and thus they are not robust enough to be used in our calculations.

and three different thicknesses t_i, t_j, t_k. When determining the plasmonic resonance wavelength $\lambda_{res}(S)$ for different side-lengths S and one specific t_i, we get the (monotonic) relation

$$\lambda_{res}(S) = g(S, t_i) \tag{3.55}$$

The plasmonic resonance wavelength changes differently with varying S and t. Therefore, at a chosen wavelength λ^0_{res}, which corresponds to a certain pair S_i and t_i, we can find other pairs S_j, t_j and S_k, t_k that fulfill the condition

$$\lambda^0_{res} = g(S_i, t_i) = g\left(S_j, t_j\right) = g(S_k, t_k), \tag{3.56}$$

as we assume that the physical properties (e.g. the dielectric function) do not depend on the size of the sample.

For three thicknesses t_i, t_j, and t_k and the same resonance wavelength λ^0_{res}, we obtain, according to Eq. (3.38),

$$\begin{aligned} E\left(\lambda^0_{res}\right) &= f\left(\lambda^0_{res}, m \cdot S_i, m \cdot t_i\right) \\ &= f\left(\lambda^0_{res}, m \cdot S_j, m \cdot t_j\right) \\ &= f\left(\lambda^0_{res}, m \cdot S_k, m \cdot t_k\right). \end{aligned} \tag{3.57}$$

This set of equations is the basis of all following calculations.

From Eq. (3.53) and Eq. (3.57) and the size-triples $\{S_i, t_i\}, \{S_j, t_j\}$ and $\{S_k, t_k\}$ we arrive at

$$N_j - u \cdot t_j \frac{\left(S_j\right)^{1.14}}{(\lambda)^{2.14}} = N_i - u \cdot t_i \frac{(S_i)^{1.14}}{(\lambda)^{2.14}} \tag{3.58}$$

$$N_j - u \cdot t_j \frac{\left(S_j\right)^{1.14}}{(\lambda)^{2.14}} = N_k - u \cdot t_k \frac{(S_k)^{1.14}}{(\lambda)^{2.14}} \tag{3.59}$$

using

$$u = 19.717 \cdot (mn)^{2.14}. \tag{3.60}$$

After rearrangement, we obtain

$$N_j - N_i = \frac{u}{(\lambda)^{2.14}} \left(t_j \left(S_j \right)^{1.14} - t_i \left(S_i \right)^{1.14} \right) \tag{3.61}$$

$$N_j - N_k = \frac{u}{(\lambda)^{2.14}} \left(t_j \left(S_j \right)^{1.14} - t_k \left(S_k \right)^{1.14} \right). \tag{3.62}$$

Taking the ratio of both equations the factor $u/(\lambda)^{2.14}$ is eliminated and we arrive at the simple relation

$$\frac{N_j - N_i}{N_j - N_k} = \frac{\left(t_j \left(S_j \right)^{1.14} - t_i \left(S_i \right)^{1.14} \right)}{\left(t_j \left(S_j \right)^{1.14} - t_k \left(S_k \right)^{1.14} \right)}. \tag{3.63}$$

The right-hand side (RHS) of this equation can be easily determined in experiments, whereas the left-hand side (LHS) is a sole function of the depolarization factors of the corresponding square patches. Therefore, we can use a fitting algorithm, varying α and β, to get the optimal solution that fulfills Eq. (3.63). For example, using Au and Pd square nanopatches with thicknesses $t_i = 30\,\text{nm}, t_j = 50\,\text{nm}, t_k = 100\,\text{nm}$, we find that over the entire range of sizes S and for both materials the RHS is approximately

$$\frac{N\left(S, 50\,\text{nm}\right) - N\left(S, 30\,\text{nm}\right)}{N\left(S, 50\,\text{nm}\right) - N\left(S, 100\,\text{nm}\right)} \approx -0.4. \tag{3.64}$$

as one can see in Fig. 3.4 (blue circles for Au and green diamonds for Pd).

Figure 3.3(a) shows that there are several combinations of α and β that fulfill the condition in Eq. (3.63). Therefore, we need to impose another condition to find the correct values for α and β. Apart from Eq. (3.50), one can also determine the factor E using known dielectric data ε_1, ε_2 and n in Eq. (3.12). For a known material with known dielectric function both equations need to give the same value of E (assuming our procedure is valid). Au is a theoretically and experimentally well-studied plasmonics material [62, 63]. Therefore, we know

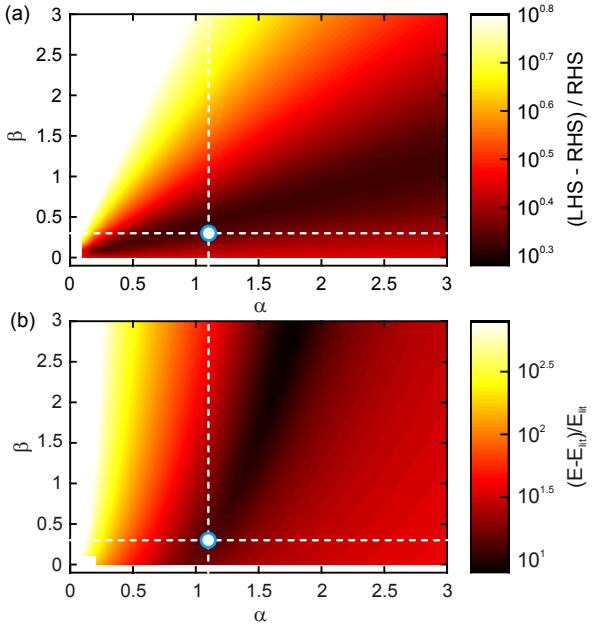

FIGURE 3.3. Optimal α and β for square patches. (a), Colorplot for the relative difference between RHS and LHS of Eq. (3.63), summed over all experimentally available λ_{res} and normalized to the RHS that is independent of α and β. (b), Colorplot for the relative difference between E calculated using Eq. (3.43) and E_{lit} calculated using Eq. (3.38) with literature data from [61], summed over all experimentally available λ_{res} and normalized to E_{lit} that is independent of α and β. In both (a) and (b), experimental values for Au square patches with $t_{i,j,k}$ = 30 nm, 50 nm and 100 nm and 150 nm $\leq S \leq$ 4000 nm are used.

that Au plasmonic resonances of nanoparticles with sizes down to 50 nm can be described using literature dielectric data from Johnson and Christy [33] or Rakic *et al.* [61]. Thus, the values of E determined from experimentally measured plasmonic resonance positions using Eq. (3.50) and the values determined using Eq. (3.12) and literature dielectric data, should be equal.

If one also imposes the condition $E - E_{lit} = 0$ (see Fig. 3.3(b)), an optimal set of α and β can be obtained, with

$$\alpha = 1.1 \tag{3.65}$$

and

$$\beta = 0.3. \tag{3.66}$$

This leads to

$$N_{sq}(S,t) = \frac{1}{1.1\frac{S}{t} + 0.3}. \tag{3.67}$$

The corresponding ratios $\left(N_j - N_i\right) / \left(N_j - N_k\right)$ are shown in Fig. 3.4, for both Au and Pd samples. Since, the technique using Eq. (3.63) in many different nanopatches and imposing the correct E factor for well-known Au nanostructures, is very general, the resulting Eq. (3.67) holds true for all square patch nanostructures. It will be used from now on for all further calculations.

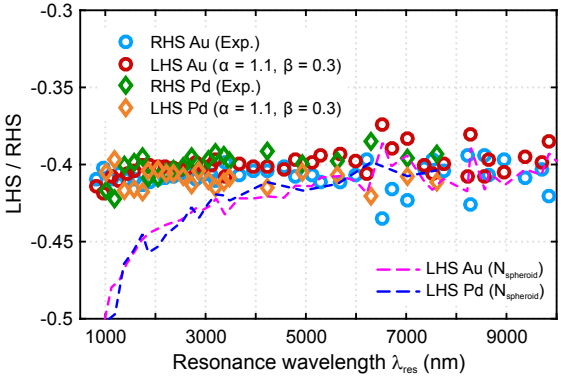

FIGURE 3.4. LHS and RHS of Eq. (3.63) for Pd and Au square patches. The LHS is calculated using N_{sq} from Eq. (3.67) (colored dots for Au and diamonds for Pd). For comparison, the LHS using N_{sp} is displayed as dashed lines.

It is important to note that if we had used the standard spheroid expression

$$N_{sp}(S,t) = \frac{1}{1.2718\frac{S}{t} + 1.6499}, \tag{3.68}$$

we would have obtained a very different result that does not fulfill Eq. (3.63) and contradicts the experiment (see dashed lines in Fig. 3.4).

3.3.2 *Determining the Size-ratio m for Square Patches*

After having determined the depolarization factor N in the previous section, it is straightforward to identify the size-ratio m, linking the major and minor half-axis of a spheroid (a, c) to the side-length and height of a square-patch (S, t), defined in Eqs. (3.47) and (3.48). We again use the fact that for a certain resonance wavelength λ_{res} one finds different pairs of parameters $\{t_i, S_i\}$ and $\{t_j, S_j\}$ that fulfill the condition

$$E\left(\lambda^0_{res}, m \cdot S_i, m \cdot t_i\right) = E\left(\lambda^0_{res}, m \cdot S_j, m \cdot t_j\right), \tag{3.69}$$

which is the same as in Eq. (3.57) for only two parameters i and j. Therefore, we can now use Eq. (3.61) and solve it for m.

$$u = 19.717 \cdot (nm)^{2.14} = \lambda^{2.14} \frac{N_j - N_i}{t_j \left(S_j\right)^{1.14} - t_i \left(S_i\right)^{1.14}} \tag{3.70}$$

$$m = 2.483 \times 10^{-1} \left(\frac{\lambda}{n}\right) \sqrt[2.14]{\frac{N_j - N_i}{t_j \left(S_j\right)^{1.14} - t_i \left(S_i\right)^{1.14}}}. \tag{3.71}$$

By calculating Eq. (3.71) for many different samples and for both Au and Pd structures, one finds $m \approx 0.56$ (as we see in Section 3.5.4 it is not constant but slowly decreasing from ≈ 0.7 to ≈ 0.56).

This is a very interesting result since, when one imposes that for having the same resonance condition, the base area $A_{spheroid}$ of the

spheroid and A_{cuboid} of the square-patch (cuboid) should be equal, one finds

$$A_{spheroid} \equiv A_{cuboid} \longrightarrow \pi a^2 = \pi m^2 S^2 = S^2 \tag{3.72}$$

$$m_A = \sqrt{\frac{1}{\pi}} \approx 0.5642, \tag{3.73}$$

which is very close to the result we get from our model together with the experimental data for the larger square patches.

If one would instead imposes that the volume $V_{spheroid}$ of the spheroid and V_{cuboid} of the square-patch should be equal, one finds

$$V_{spheroid} \equiv V_{cuboid} \longrightarrow \frac{4\pi}{3} a^2 c = \frac{4\pi}{3} m^3 S^2 t = S^2 t \tag{3.74}$$

$$m_V = \sqrt[3]{\frac{3}{4\pi}} \approx 0.62. \tag{3.75}$$

This is slightly higher but close to the experimental results for smaller square patches.

A third possibility would be to impose equal surface areas U for both systems

$$U_{spheroid} \equiv U_{cuboid}$$

$$2\pi a^2 \left(1 + \frac{1-e^2}{e} \tanh^{-1} e\right) = 2\left(S^2 + 2St\right) \tag{3.76}$$

$$m_U = \sqrt{\left(\frac{1 + 2t/S}{\pi\left(1 + \frac{1-e^2}{e} \tanh^{-1} e\right)}\right)} \tag{3.77}$$

with

$$e^2 = 1 - \frac{c^2}{a^2} = 1 - \frac{t^2}{S^2}. \tag{3.78}$$

In this case, m is not constant but varies slowly with the parameter t/S showing the same trend as the experimental data, as we see Fig. 3.12 of Section 3.5.4). Hence, the values we get for m using this simple model and the conditions from Eqs. (3.47) and (3.48) match our physical understanding of plasmonic resonances.

3.4 RETRIEVING THE DIELECTRIC FUNCTION

Using the results for N from Section 3.3.1 and m from Section 3.3.2 we are able to determine E for square patches of any material that supports plasmonic resonances using Eq. (3.53). For a more detailed analysis and to be able to retrieve the full dielectric function $\varepsilon(\omega)$ of a nanosized material, it is insightful to study the physical meaning of E in more detail.

Using Eqs. (3.12) and (3.13) we can write $\varepsilon_1(\omega)$ and $\varepsilon_2(\omega)$ in terms of E and F:

$$\varepsilon_1(\omega) = E(\omega) \cdot \frac{n^2}{E(\omega)^2 + F(\omega)^2} + n^2 \tag{3.79}$$

and

$$\varepsilon_2(\omega) = F(\omega) \cdot \frac{n^2}{E(\omega)^2 + F(\omega)^2}. \tag{3.80}$$

From Eqs. (3.79) and (3.80) it is evident that the approximation $F \approx 0$ used in Section 3.2.3 is equivalent with $\varepsilon_2 \approx 0$ and

$$\varepsilon_1(\omega)\big|_{F\approx 0} = \frac{n^2}{E(\omega)} + n^2 \propto \frac{1}{E(\omega)}. \tag{3.81}$$

From Eq. (3.81) and Fig. 3.5, we see that E is proportional to $1/\varepsilon_1$, when F is small. Thus, knowing E, we have a valid first estimate for ε_1 of a material. ε_1 represents the dispersion of a material and, when negative, provides information about the metallicity and the conductance. Hence, E can be used to compare two plasmonic materials and give an estimate for their dispersion. ε_2 is closely related to the absorption of a material. Therefore, the approximation $\varepsilon_2 \approx 0$ is only valid for metals with a relatively high conductivity and low absorption at frequencies below the plasma frequency ω_p (defined in Section 2.1.2). In the case of Pd and Au, this is the case for frequencies below 500 THz (wavelengths above 600 nm).

The construction of E and F enables us to determine reasonably good values (see Fig. 3.5) solely using $E(\omega)$ and Eq. (3.81). If one also

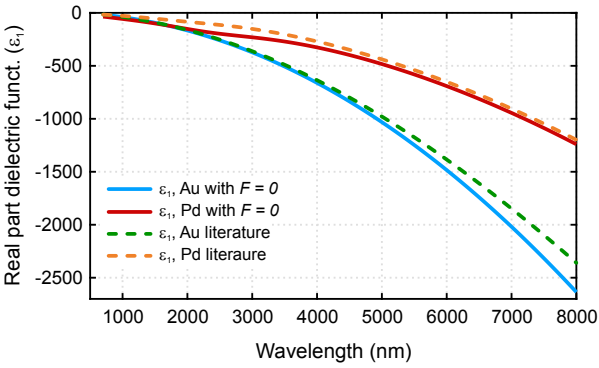

FIGURE 3.5. Real part of the dielectric function of Au and Pd using literature dielectric data [61] (green and orange dashed line) and the calculated real part using $F = 0$ and otherwise the same dielectric data (red and blue solid line). In both cases setting $F = 0$ has only small consequences. For Au only above wavelengths of 5 µm differences are visible. The Pd data, in contrast, shows the influence of F already in the lower wavelength region.

needs to determine the imaginary part of the dielectric function ε_2 or if one is inclined to have a more accurate value for ε_1 in regions with higher absorption, a method to also determine $F(\omega)$ is necessary.

3.4.1 *Determining F*

In the previous sections, we have seen that $F(\omega)$ is closely related to the imaginary part of the dielectric function ε_2. We also verified in Figs. 3.1 and 3.6 that the resonance frequency (or wavelength) is virtually not influenced by $F(\omega)$. Therefore, it is not feasible to use the plasmonic resonance frequency to determine $F(\omega)$. For materials and wavelength ranges where F does influence the resonance, as it is the case for Pd in the NIR wavelength region, the resonance width and amplitude clearly change with F (compare Fig. 3.1 with Au resonances showing no influence of F to Fig. 3.6 with Pd resonances that clearly differ in amplitude when F is set to zero). Consequently, we

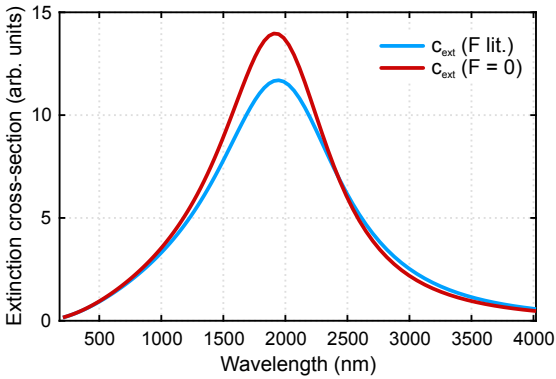

FIGURE 3.6. Calculated Pd resonance ECS ($S = 500\,\text{nm}$, $t = 50\,\text{nm}$, $\alpha = 1.1$, $\beta = 0.3$, $n = n_{CaF_2}$ and $m = 0.68$) with literature values [61] for E and F (blue line) and with $F = 0$ (red line). The resonance width and amplitude show a clear difference (higher amplitude and smaller width for $F = 0$), whereas the resonance wavelength only differs marginally (1.1 %).

can use the experimental data on the resonance width to determine the corresponding value of F at a certain wavelength.

The procedure is the following:

- From Section 3.3.2 and Section 3.4 we can determine m and E as a function of wavelength, solely using the resonance wavelength.

- Using the formula for the extinction of a square-patch (combination of Eqs. (3.14a) to (3.14c) with Eqs. (3.47) and (3.48) and Eq. (3.67))

$$C_{ext}^{\square} = \frac{A \cdot \left(\frac{2^7 \pi^5 m^6 S^4 t^2 \left(1+n^3\right)}{3^3 \lambda^4} + \frac{2^3 \pi^2 m^3 S^2 t F}{3\lambda} \right)}{\left(E + N - \frac{2^2 \pi^2 m^2 S t n^2}{3\lambda^2} \right)^2 + \left(\frac{2^4 \pi^3 m^3 S^2 t n^3}{3^2 \lambda^3} + F \right)^2} \tag{3.82}$$

  with the known values of $m\,(\lambda)$, $E\,(\lambda)$, square-patch size S and height t, surrounding refractive index n, depolarization factor

$N = N(S,t)$ and wavelength λ, a fitting procedure with only two free parameters (the amplitude A and the factor F that we are looking for) can be applied.

- In general, the factor $F = F(\lambda)$ is a function of the wavelength λ. Using Eq. (3.82), we will only get a scalar $F = F(\lambda_{res})$ that represents the F value at the resonance position of one square-patch with $S_i, t_i, \lambda_i^{res}$. To get the full function $F(\lambda)$, one needs to fit the full set of data $\left[S_i, t_i, \lambda_i^{res}\right]_{i=1,2,\ldots,n}$.

With this procedure, we can obtain values of $F(\lambda)$ for every square patch size S.

Finally, this enables us to determine the full dielectric function $\varepsilon(\lambda)$, using E, F and Eqs. (3.79) and (3.80). As we have already seen in the difference between Fig. 3.1 and Fig. 3.6, the influence of F on the spectrum can be either negligible (in the case of Au structures) or highly relevant (in the case of smaller Pd structures). The determination of F relies on an additional fitting procedure using experimentally obtained spectral data. Therefore, only materials with larger ε_2 show enough contrast to determine F reliably. For all other materials, we can safely assume $F = 0$ and use Eq. (3.81) to obtain values for ε_1.

It is also worth mentioning that it one does not always have to determine the full dielectric function of a material to determine its optical properties. As see in Fig. 3.6, knowing only E can give a very good estimate for a plasmonic resonance. Therefore, a plasmonic scientist does not necessarily want to know ε_1 and ε_2 for simulating the optical response of nanostructures, but can take E (and in some cases F) to determine resonances.

3.5 EXPERIMENTAL RESULTS FOR AU AND PD SQUARE PATCHES

After the theoretical groundwork for determining the dielectric properties of nanosized materials is established, we first demonstrate the procedure with the most commonly used and best studied metal in

plasmonics, i.e. Au. Additionally, we fabricated Pd nano-squares to verify the conclusions and lay the groundwork for using the model later on in Chapter 5 for studying so far inaccessible thermodynamic parameters of nanosized palladium hydride (PdH).

3.5.1 *Square Nanopatch Sample Design*

All samples are produced on 10 mm × 10 mm × 1 mm {111} calcium fluoride (CaF_2) substrates to ensure a wide transmission window from 400 nm to 10 000 nm. On the substrate, the metal nanostructures are patterned by electron beam lithography using a 2 layer PMMA resist mask (200 K 3.5 % Poly(methyl methacrylate) (PMMA) + 950 K 1.5 % PMMA baked on a hot plate for 4 min at 160 °C). After development (1:3 MIBK + Propanol) the metal film is evaporated onto the mask with an electron gun evaporator at a rate of 2 Å per second in a vacuum of 10^{-7} mbar. The mask is removed using a lift-off process (80 °C NEP for 1.5 h).

The samples consist of 60 fields of $D_i = 80\,\mu\text{m} \times 80\,\mu\text{m}$ size, placed in an ordered fashion onto the substrate with a distance of 100 µm. All fields consist of quadratic nanopatches with a minimum distance of 200 nm between two structures. They are placed in a completely random way using a random walk algorithm in x and y direction to avoid any unwanted grating effects [64] and collective resonance effects. The number of squares per field is:

$$n_S = \frac{D}{(2S + 200)^2} = \frac{80.000^2}{(2S + 200)^2}. \tag{3.83}$$

This design keeps the substrate coverage per field approximately constant and therefore guaranties an almost equal resonance amplitude for the wide range of square-nanopatch resonances.

The square side lengths S range from 50 nm to 5000 nm with steps of 50 nm until 1000 nm and 100 nm for the larger patches. The different square-patch ensembles $D_{50} - D_{5000}$ are randomly placed into

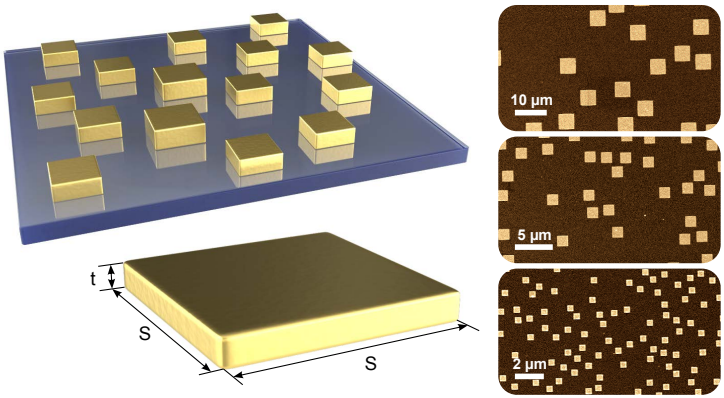

FIGURE 3.7. Sample design for the Au and Pd square patches of sizes S between 150 and 5000 nm, exemplary shown with three colored scanning electron microscope (SEM) pictures. All structures are made of 80 µm × 80 µm fields with randomly arranged square patches to avoid any collective electromagnetic modes influencing the spectra.

a 6 × 10 fields grid to avoid any systematical fabrication or measurement errors.

3.5.2 *Measurement and Data Processing*

All measurements are performed with a Bruker FTIR using a square aperture of 50 µm × 50 µm. For recording the full spectral information, three different measurement types are used:

- Measurements in the VIS and NIR region (800 nm to 1150 nm or 8700 cm^{-1} to 12 500 cm^{-1}) using a silicon diode, a NIR light source and a SiO_2 beam-splitter (Si-VIS).
- Measurements in the NIR spectral region (1000 nm to 3000 nm or 3300 cm^{-1} to 10 000 cm^{-1}) using a nitrogen cooled MCT detector, a NIR light source and a CaF_2 beam-splitter (MCT-NIR).

- Measurements in the MIR region 2000 nm to 10 000 nm or 1000 cm^{-1} to 5000 cm^{-1} using the same nitrogen MCT detector, but MIR Globar light source together a KBr-beam-splitter (MCT-MIR).

After the measurements, the data-set is processed for reading out the information about resonances. Therefore, the raw transmission spectra that are recorded with three different detection schemes over a linear wavenumber-scale are cleaned, stitched and analyzed.

First, an *Adapted Asymmetric Least Squares Smoothing Algorithm* after Eilers and Whittaker is applied to smooth out the vibrational resonances from Water, CO_2 and residual PMMA [65]. The corresponding wavenumbers where the filter is applied are: 5440, 5360, 5230, 3850, 3740, 3620, 2870, 2950, 2350, 1260, 1100 and 1040 cm^{-1} with a span of 25 wavenumbers.

After the elimination of the unwanted vibrational resonances the spectra of the different detectors are stitched to get one spectrum. For the high wavenumber resonances the spectral overlap region 8800 cm^{-1} to 9200 cm^{-1} is used to determine a multiplicative factor to be applied to the Si-diode transmittance data for achieving the largest overlap. Afterwards, the spectra are stitched together using a logistic function to guarantee a smooth transition between two spectral parts. The same procedure is applied between the MCT-detector + NIR- and MIR light-source spectra in the low wavenumber region. The spectral overlap region 4000 cm^{-1} to 5000 cm^{-1} is used for renormalization of the lowest wavenumber spectra that are then stitched via a logistic curve.

The cleaned and stitched spectra are processed to determine the center or resonance wavelength. Therefore, the spectra are converted to extinction spectra ($I_{ext} = -\ln(I_{transm})$). The data around the maximum (+ and −500 wavenumbers) are then interpolated with a 0.05 cm^{-1} resolution and a spline is fitted to determine the maximum position. These data is quite reliable, since the input data is already smoothed through the Eilers filter.

3.5.3 *Determining Size-pairs from Experimental Data*

In order to determine dielectric properties from experimental plasmonic resonance measurements we need to find the three dimension-pairs $[S_i, t_i]$, $[S_j, t_j]$, $[S_k, t_k]$ with the same resonance wavelength λ_{res} introduced in Eq. (3.56). We can only fabricate a limited amount of square-patch sizes, it is not feasible to realize these conditions experimentally. Thus, experimentally one determines the wavelength-thickness pairs $[\lambda_i, t_i]$, $[\lambda_j, t_j]$, $[\lambda_k, t_k]$ for given side-lengths S. Consequently, we need to find a way to convert these experimental results into the necessary parameters entering Eq. (3.56) and Eq. (3.57).

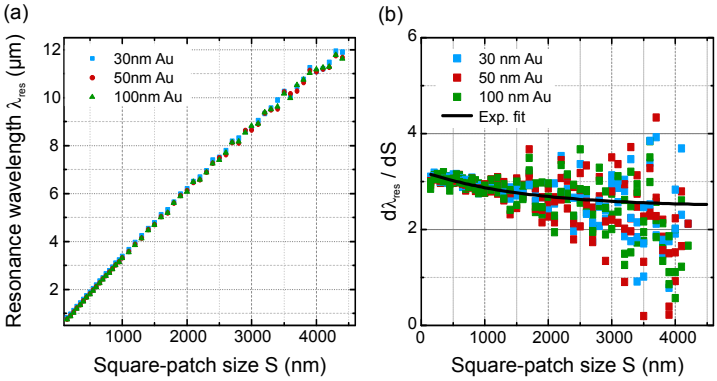

FIGURE 3.8. (a), Resonance wavelengths for Au nanosquares with side lengths S between 150 nm and 4500 nm and thicknesses t of 30 nm (blue squares), 50 nm (red dots) and 100 nm (green triangles). The thickness dependence is very weak. All squares fall approximately on a straight line with slope 3. (b), Slope $d\lambda/dS$ for the same square patches as in (a). The black line is an exponential fit (Eq. (3.84) with $A = 0.743, S_0 = 1578\,\text{nm}, B = 2.478$).

For square nanopatches the function $\lambda_{res}(S)$ for any given t cannot be calculated analytically. However, the slope is slowly varying and in small size and wavelength ranges it can be well approximated by a linear function with the thumb-rule $\lambda_{res}(S) \approx 3 \cdot \lambda_{res}$ (see Fig. 3.8(a)). To be more accurate and to smooth our measurement errors, we first look at the slope $\partial\lambda/\partial S$. Since, the t dependence of the plasmonic

resonance is very week, we find a value for $d\lambda(S)/dS$ independent of t. The slope can be well approximated with a simple exponential decay function (see Fig. 3.8(b))

$$\frac{d\lambda_{res}}{dS} = A \cdot \exp\left(-\frac{S}{S_0}\right) + B, \tag{3.84}$$

where the amplitude A, the limit for $\lambda \to \infty$, B and the size correction factor S_0 depend on the material.

Since, Eq. (3.84) is a good approximation for all thicknesses t, we can use the slope to calculate the pairs $[S_i, t_i]$, $[S_j, t_j]$, $[S_k, t_k]$ for any given $\lambda_j\left(S_j\right)$ using the fact that

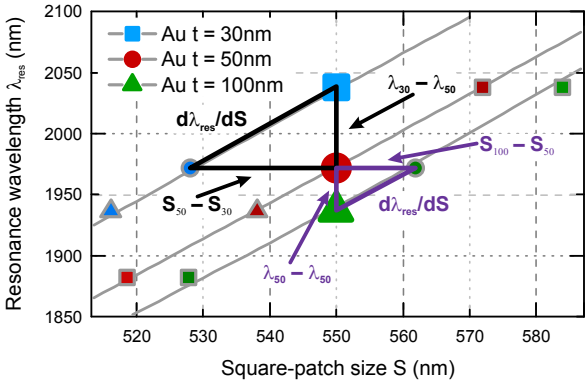

FIGURE 3.9. Illustration of the procedure to determine S_{30} and S_{100} from the measured plasmonic resonance wavelengths λ_{50} ($S = 550\,\text{nm}, t = 50\,\text{nm}$) (large red dot), λ_{30} ($S = 550\,\text{nm}, t = 30\,\text{nm}$) (large green triangle), and λ_{100} ($S = 550\,\text{nm}, t = 100\,\text{nm}$) (large blue square). The grey-framed triangles, squares and dots are the result of the transformation procedure described in Eqs. (3.87) and (3.88).

$$\frac{d\lambda_{res}}{dS} = \frac{\lambda_i - \lambda_j}{S_j - S_i} \tag{3.85}$$

and

$$\frac{d\lambda_{res}}{dS} = \frac{\lambda_j - \lambda_k}{S_k - S_j} \tag{3.86}$$

as illustrated in Fig. 3.9 for experimental results of Au nanosquares with $t_i = 30\,\text{nm}$, $t_j = 50\,\text{nm}$ and $t_k = 100\,\text{nm}$. Consequently, the corresponding sizes $S_i\left(\lambda_j\right)$, and $S_k\left(\lambda_j\right)$ are given by

$$S_i\left(\lambda_j\right) = S_j + \frac{\lambda_i - \lambda_j}{\frac{d\lambda_{res}}{dS}} \tag{3.87}$$

$$S_k\left(\lambda_j\right) = S_j - \frac{\lambda_j - \lambda_k}{\frac{d\lambda_{res}}{dS}}. \tag{3.88}$$

using λ_j. Thus, we have obtained the pairs $\left[S_i\left(\lambda_j\right), t_i\right]$, $\left[S_j\left(\lambda_j\right), t_j\right]$, $\left[S_k\left(\lambda_j\right), t_k\right]$.

3.5.4 *The Dielectric Properties of Au and Pd Samples*

Using the processed experimental data for Au and Pd square patches, one can determine the previously discussed parameters, m, E, F for both materials.

At first, we consider the Au square patches with sizes S between 150 and 4500 nm and heights t of 30, 50, and 100 nm, that yield plasmonic resonances between 700 and 12 000 nm.

A MATLAB code is used to calculate m, by setting

$$\begin{aligned} E\left(\lambda, S_1, t_1 = 30\,\text{nm}\right) &= E\left(\lambda, S_2, t_2 = 50\,\text{nm}\right) \\ E\left(\lambda, S_2, t_2 = 50\,\text{nm}\right) &= E\left(\lambda, S_3, t_3 = 100\,\text{nm}\right) \\ E\left(\lambda, S_1, t_1 = 30\,\text{nm}\right) &= E\left(\lambda, S_3, t_3 = 100\,\text{nm}\right) \end{aligned} \tag{3.89}$$

with E from Eq. (3.50). Solving the equations numerically leads to a wavelength dependent factor m that varies between 0.56 and 0.7 (see Fig. 3.10).

Repeating the same measurements and analysis procedure for Pd square nanopatches with sizes S between 250 and 2500 nm and the

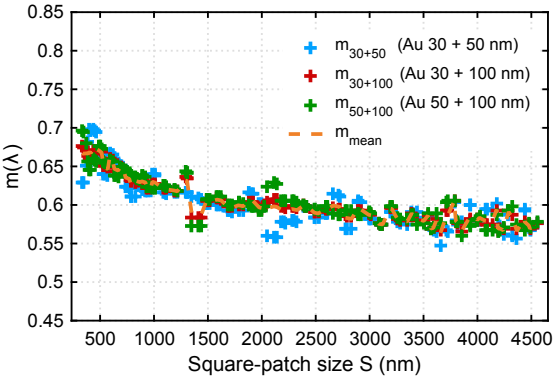

FIGURE 3.10. Size-factor m for Au square patches calculated using $n = \left(n_{Air} + n_{CaF_2}\right)/2$, $\alpha = 1.1$, $\beta = 0.3$ and the three conditions in Eq. (3.89).

same heights as the Au squares, one obtains almost identical results for m (see red dots in Fig. 3.11 in comparison to the blue dots). This strongly supports the hypothesis that the size-factor m is universal, i.e. only depending on the geometry, not the material.

Apart from the excellent overlap of the Pd and Au data, Figs. 3.10 and 3.11 show that m is not really a constant but follows a slow decay with relatively large changes in the low wavelength region (NIR) and almost no changes in the high wavelength region (MIR). There are several effects that can explain this behavior:

- The factor m is designed to be the same for $a \rightarrow S$ and $c \rightarrow t$. This means that it can change with the aspect-ratio S/t. And that is exactly what we see, when the square patches get larger, the aspect-ratio gets larger and therefore, m changes.

- One basic assumption behind the procedure to determine m is its independence on the thickness t. This is in general a very

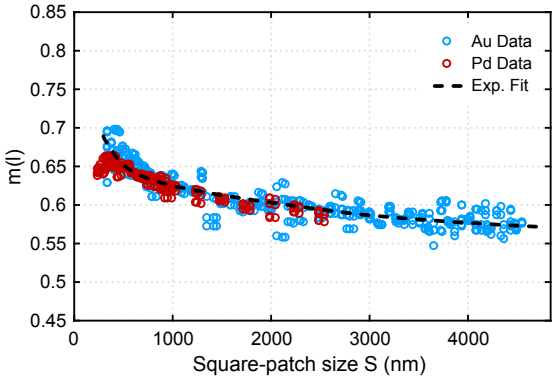

FIGURE 3.11. Size-factor m for Pd (red dots) and Au (blue dots, same as in Fig. 3.10) square patches calculated using $n = \left(n_{Air} + n_{CaF_2}\right)/2$, $\alpha = 1.1$, $\beta = 0.3$. The double-exponential fit (black dashed line) is a guide to the eye.

good approximation, since the plasmonic resonance only weakly varies with changes in t (see Fig. 3.8(a)). However, for smaller square patches with sizes below 500 nm the aspect ratio between length and height becomes very small (e.g. as low as 1.5:1 for $S = 150$ nm and $t = 100$ nm) and, therefore, the influence of changes in t becomes significant.

In general, we can say that the m factor which characterizes the conversion of the internal electric field between a oblate spheroid and a square-patch (square cuboid), is well characterized by simple geometrical considerations. All patches nicely follow the curves assuming equal surface areas (see Eq. (3.77) and green curves in Fig. 3.12). However, the thickness dependence shown in the curves cannot be identified in our data. Since the curves assuming equal base area and equal volume (blue and red lines) are very close to our data, too, the truth lies probably somewhere in between.

After determining the conversion factor m the result can be used to calculate the respective dielectric factor E.

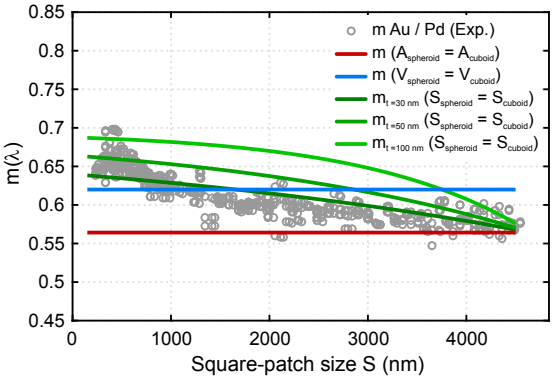

FIGURE 3.12. Comparison between predicted (colored lines) and measured m values (grey dots). The green lines are calculated using equal surface areas (see Eq. (3.77), dark green with $t = 30$ nm, intermediate green with $t = 50$ nm and light green with $t = 100$ nm. The Red line represents equal base-areas (see Eq. (3.73)) and the blue line equal volumes (see Eq. (3.75)).

Figure 3.13 shows the calculated $E(\lambda)$ for the Au and Pd samples, obtained through Eq. (3.50). It is clearly visible (in Fig. 3.13(a) and (b)) that all Au squares (red markers) and Pd squares (blue markers) follow one line, independent of the sample thickness. This demonstrates that the factor E is indeed, truly a material parameter, independent of the particular samples geometry.

There are notable differences between the Au and Pd data. While E_{Pd} is less negative then E_{Au} at wavelengths around 1000 nm, the situation reverses for wavelengths above 2000 nm. Comparing the measured E values to literature data (dashed colored lines), shows an almost perfect overlap. Even though, the parameters for α and β have been optimized using only E_{Au}, the Pd data follow the expected behavior. This is particularly visible in the double-logarithmic plot of $1/E$ in Fig. 3.13(b), showing the functional difference between the almost linear Au and curved Pd data. Since, the inverse of E is a good approximation for the real part of the dielectric function $\mathrm{Re}(\varepsilon) = \varepsilon_1$

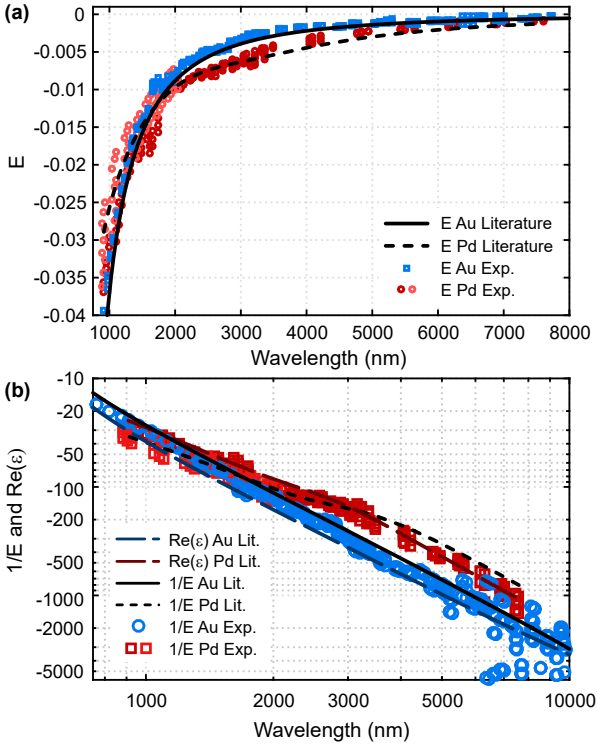

FIGURE 3.13. Factor E for Au and Pd. (a), Factor E calculated from Eq. (3.50) using experimental plasmonic resonance data from several Au (blue squares) and Pd (light and dark red circles) samples. They show almost perfect overlap with E calculated from literature data [61] (black lines). (b), $1/E$ plotted in a double-logarithmic fashion using the same data as in (a). Besides the literature data for $1/E$ (black lines), the original literature values for $\mathrm{Re}(\varepsilon)$ are displayed (long dashed lines).

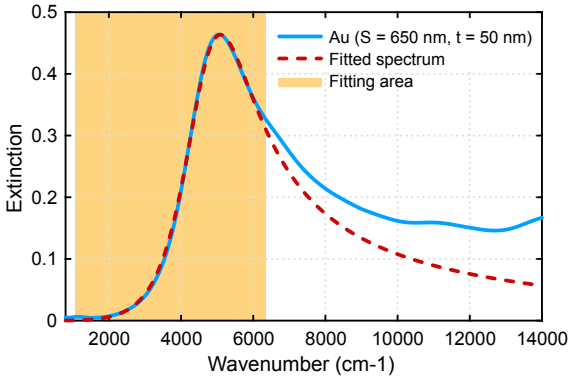

FIGURE 3.14. Exemplary original (blue line) and fitted spectrum (red dashed line) of an Au sample with $t = 50\,\text{nm}$ and $S = 650\,\text{nm}$. The yellow shaded area indicates the interval used for the fitting procedure.

as one can see from the dashed lines in Fig. 3.13(b) that nicely follow the experimental data, too.

As discussed in Section 3.4.1 it is possible to determine the factor F using the plasmonic resonance data that is necessary to retrieve the full dielectric function ε. Fitting Eq. (3.82) as a model for the ECS to the measured extinction spectra one is able to retrieve the factor F for one square-patch size and hence, one wavelength/wavenumber. Figure 3.14 shows that the high wavenumber tail of the spectra exhibit enhanced extinction values compared to the calculated extinction spectra, calculated trough Eq. (3.82). This is probably due to interband transitions and higher order effects not included in the fist order model. However, the resonance itself plus the low wavenumber tail are well represented by the model and thus used for the fitting procedure.

In Fig. 3.15, the resulting F factors are plotted for both, the Au and Pd square patches. The Au values are essentially zero over the whole wavelength range, whereas the F factor for Pd is showing an almost exponential decay. This is already expected from literature, since Pd

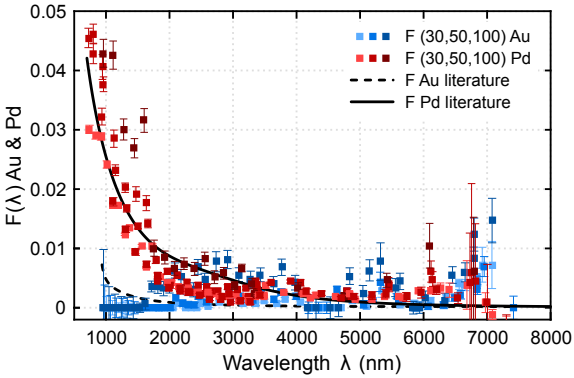

FIGURE 3.15. F calculated for Au and Pd square patches. The factor is calculated from a fitting procedure of the experimental extinction spectra to Eq. (3.82). The red squares are for the Pd data (light red for $t = 30$ nm, red for 50 nm and dark red for 100 nm). The errorbars depict the standard deviation confidence interval from the fit, and the solid black line is the literaure value calculated from Rakic *et al.* [61]. The blue squares depict the Au data (bright to dark colors as for Pd). The comparison to the literature values (dashed line) and the errorbars indicates that all the values are essentially zero, within the error margins.

does have a markedly stronger absorption than Au. The literature values for F in the figure (solid and dashed black lines) confirm this interpretation. Consequently, only for Pd square patches, it is possible to determine F. For Au, the absorption-induced differences in resonance width and hence F is too small to be determined through a fitting procedure (see Fig. 3.1).

Nevertheless, with the calculated E and F factors, the next step is to combine both to obtain the full dielectric function of the material $\varepsilon(\lambda) = \varepsilon_1(\lambda) + i\varepsilon_2(\lambda)$. Taking Eqs. (3.79) to (3.81) together with E, F and

$$n(\lambda) = \left(n_{CaF_2}(\lambda) + n_{Air}\right)/2 \tag{3.90}$$

results in in ε_1 and ε_2 as depicted in Fig. 3.16.

Since, E and F are going to zero in the limit of large wavelengths λ, ε_1, which is depending on the their quotient, highly depends on small errors in the factors E and F. This is especially relevant in the region where F tends to be overestimated by the fitting algorithm and mostly produces noise (see Fig. 3.15). Therefore, it is reasonable to use $F \approx 0$ and Eq. (3.81) instead of Eq. (3.79) to determine ε_1 in the spectral region where $F < 0.08$. This is the case for all values of F_{Au} in Fig. 3.16(a) and F_{Pd} at wavelengths above 4000 nm in Fig. 3.16(b). The blue circles in Fig. 3.16 depict the resultin ε_1, showing excellent agreement to literature data [61] in the case of Au and good agreement for the Pd structures.

Looking at the results for ε_2 (Au) in Fig. 3.16(a) (red circles), it seems to be counter-intuitive that the values for Au are still in reasonably good agreement with the literature data, even though they are calculated using values of F that essentially consist of numerical noise. By performing a tailor expansion of ε_2 for $F \approx 0$

$$\varepsilon_2\big|_{F=0} = \frac{n^2 F}{E^2} - \frac{n^2 F^3}{E^4} + O\left(F\right)^5 \tag{3.91}$$

it becomes clear that ε_2 depends essentially on F/E^2 (compared to $\varepsilon_1 \propto 1/E$, see Eq. (3.81)). Thus, reasonable values of E also contribute to non-zero (and reasonable) values for ε_2, even when F is small and noisy. The imaginary party of the Pd dielectric function in Fig. 3.16(b) shows very good agreement to the literature values, except for very high wavelengths, where again the issue character of noisy F is transferred to a noisy ε_2. Generally good agreement shows that for materials with non-zero E and F, the real and imaginary part of the dielectric function can be well determined using our method. For more examples, see Chapter 5).

3.6 CONCLUSIONS

In conclusion, we have seen in this chapter that it is possible to retrieve the dielectric function of a material using nothing but the plasmonic resonance and the materials geometry as input. This is possible

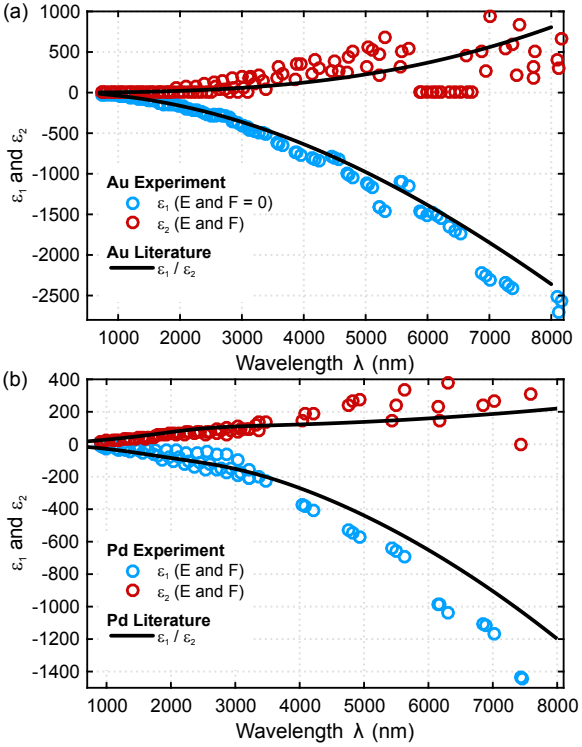

FIGURE 3.16. Calculated dielectric functions. (a), for Au and (b), for Pd, using the E and F data determined by fitting experimental data to our nano-patch model. The imaginary part (red circles) is determined from both, E and F. The real part (blue circles) uses E and F for all values of $F > 0.05$ and $F \approx 0$ otherwise. The black lines are the corresponding literature dielectric functions from Rakic *et al.* [61].

by introducing an analytical model of the plasmonic resonance of a square-patch with known side-length S and height t. The model links the plasmonic resonance wavelength with the nanoparticles size and the dielectric factors E and F that essentially represent the particles material and dielectric environment. The model is developed and tested using Au square patches and then verified for Pd nanostructures.

Since the relations developed in the process are very general, they can be applied to any nanostructurable materials that have size-dependent plasmonic resonances wavelengths. There is no need to fabricate square patches, instead disks, polygons, oblate spheroids, or any flat centrosymmetric geometry can be used. It is only necessary to modify the geometric factor m and the depolarization factor N, using the method introduced in this chapter. In this way, the technique can be applied to determine dielectric properties of chemically synthesized nano-materials that are not suited for ellipsometric measurements. Furthermore, the model offers an easy way to characterizes properties of plasmonic materials that tend to oxidize, like yttrium [30], aluminum [66], or magnesium [67]. For these materials film measurements do not give good estimates for optical properties, as they underestimate the oxidizing effects of the highly surface-dominated nanoparticles. Materials that generally show different properties as bulk or thin films compared to nanosized structures (mostly due to the strongly changed surface-to-volume ratio) can be studies with our technique. In all these cases, ellipsimetry would give results that do not reflect the real material properties and therefore, would lead to inaccurate results in theoretical predictions of these materials using electromagnetic simulation tools. One example for such a material is PdH that will be covered in full detail in Chapters 4 and 5.

4

THERMODYNAMIC MODEL FOR PD AND PDH NANOPARTICLES

Palladium-hydrogen is a prototypical metal-hydrogen system. Therefore, it is not surprisiong that a lot of attention has been devoted to the ab- and desorption of hydrogen in nanosized palladium particles. Several articles on the interaction of H with Pd nanoparticles have been published in recent years [68–76]. Although each article provides detailed data on specific aspects of hydrogen in nanoparticles, neither contains enough information to draw firm conclusions about the mechanisms involved. In this chapter, that was adapted from our publication in ref. [28], we confirm that the available data in literature exhibits general patterns leading to new insight about the processes involved in H absorption and desorption in Pd nanoparticles. On the basis of a robust and simple scaling law for the hysteresis in absorption-desorption isotherms, it is shown that hydrogen absorption in palladium nanoparticles is consistent with a coherent interface model and is thus clearly different from bulk Pd behavior. Nevertheless, H desorption seems to occur fully coherently only for small nanoparticles (typically smaller than 50 nm) at temperatures sufficiently close to the critical temperature. For larger (but still single-crystalline) particles it is partly incoherent as in bulk where dilute α-PdH_x and high concentration β-PdH_x phases coexist.

4.1 INTRODUCTION

Intercalation of small atoms in nanoparticles is relevant for important energy related applications such as electrical batteries [5] and metal-hydrides [77] for electrical and hydrogen storage. In both systems the

large lattice distortion [78] accompanying the absorption and desorption of the solutes plays an essential role in determining the performance of devices. Long-ranged lattice distortions imply that the thermodynamics of solute intercalation is inherently size-dependent [79]. Specifically, the enthalpy and entropy of hydride formation, as well as the critical temperature T_c depend on the size of nanoparticles.

In many systems the relevant temperatures for applications are lower than T_c. Consequently, during absorption at a given hydrogen gas pressure, the metal-hydrogen system transforms from a dilute α-phase to a concentrated β-hydride. As a result of the magnitude of the lattice distortions accompanying this transformation (typically 15 % to 20 % relative volume increase per mole dissolved hydrogen in transition metals such as V, Nb, Ta and Pd), it is not a priori clear whether absorption (and desorption) of hydrogen occurs coherently or incoherently. In a coherent transformation the large spatial hydrogen concentration variations lead to a modulation of the host lattice without disrupting it, and consequently to significant coherency stresses and elastic energy contributions to the enthalpy (see Fig. 4.1). The elastic energy barrier accompanying coherency stresses is proportional to the sample volume and cannot be overcome by thermal fluctuations, unless the particle is sufficiently small.

During absorption, when the external pressure is slowly increased, the system is effectively locked in a meta-stable state until the increase in the chemical potential of the interstitial sites (which is directly related to the chemical potential of the molecules in the surrounding H_2 gas) is sufficiently high to overcome the macroscopic barrier. If the transformation is unlocked, the spontaneous absorption starts [80, 81]. Then, coexistence of the two phases at thermodynamic equilibrium is impossible and a large hysteresis between absorption and desorption pressures occurs at a given temperature. In an incoherent transformation, dislocations are readily created to minimize elastic stresses. Incoherent precipitates of the α-phase nucleate and grow in the β-phase during absorption (see Fig. 4.1), largely reducing the hysteresis.

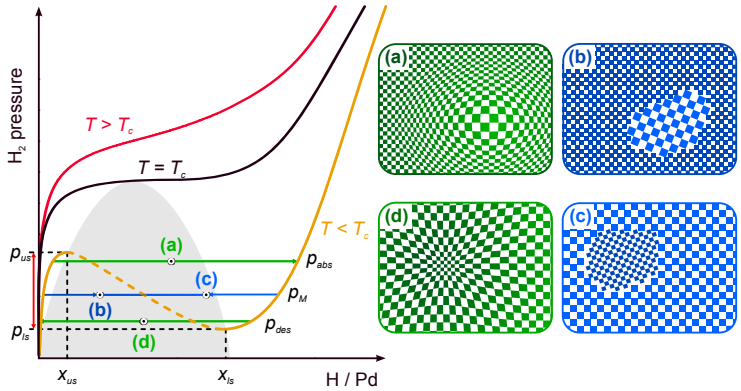

FIGURE 4.1. Schematic pressure-composition isotherms below, at, and above the critical temperature T_c. The upper spinodal pressure p_{us} and the lower spinodal pressure p_{ls} together with the corresponding spinodal concentrations x_{us} and x_{ls} are indicated for the gold isotherm with $T < T_c$. The full-spinodal hysteresis is indicated with the red arrow. The horizontal blue line corresponds to the incoherent plateau pressure obtained by means of the Maxwell construction [82]. In bulk Pd H absorption occurs approximately at the Maxwell pressure p_M and expanded β-PdH$_x$ nucleates incoherently in the dilute α-PdH$_x$ (panel **b**) while during desorption at $p_{des} \approx p_M$ the dilute α-PdH$_x$ nucleates and grows in the β-PdH$_x$ phase [47], leading to a small hysteresis (panel (c)). In case coherent absorption occurs at $p_{abs} \approx p_{us}$ (panel (a)) there is no coexistence of α- and β-PdH$_x$ phases [80, 81]. The gradient in H concentrations leads to continuous spatial variations of the lattice spacing. The same occurs during coherent desorption at $p_{des} \approx p_{ls}$ (panel (d)), leading to a hysteresis comparable to full spinodal hysteresis [81]. The black line corresponds to the critical isotherm at $T = T_c$ and the red line to a supercritical isotherm at $T > T_c$.

4.1.1 *Overview of the Investigated Palladium Nanoparticles*

As measurements of H in Pd nanoparticles are a very challenging task, there is a great diversity in experimental techniques and investigated samples [69–74]. For standard volumetric or gravimetric pressure-composition isotherms large numbers of nanoparticles are required and the data suffer from ensemble averaging and agglomerating effects. Less material is needed for optical measurements based on luminescence from Bardhan *et al.* [69] or for the plasmonic measurements performed by Wadell [73], Wadell *et al.* [72] and Syrenova *et al.* [74]. So far, the most extensive data sets have been obtained by Bardhan *et al.* [69] for dense ensembles of 14 nm to 110 nm nanocubes at temperatures between 295 K and 383 K. It is the first systematic study on the size-dependence of hydrogen ab- and desorption in colloidal ensembles of Pd nanocubes with narrow size distributions. The thermodynamics of hydrogenation was studied using luminescence measurements as a proxy for the hydrogen content. However, whenever laser light is used, heating effects may influence the measurements (see Section 4.5.3 for a more detailed discussion). Additionally, the measured isotherms exhibit sloping plateaus and non-closing hysteresis loops.

The first data on individual, colloidally synthesized and unconstrained nanocubes was obtained by Baldi *et al.* [70] by means of electron energy loss spectroscopy (EELS). The isotherms for their 14 nm to 29 nm nanocubes have flat plateaus but were only measured at one temperature (246 K). For their single nanocube measurements with EELS, there are severe technical constraints, as the pressure in the transmission electron microscope (TEM) must be kept below 1 mbar. In order to be able to load Pd up to the β-PdH_x phase the temperatures need to be sufficiently low. This follows directly from the isotherms in Figs. 4.16, 4.17 and 4.20 and as a consequence all Baldi *et al.* [70] data are taken at 246 K. Very recently Nrayan *et al.* [76] obtained nanocube isotherms for a larger variation of cube sizes (19 nm, 33 nm, 48 nm and 74 nm) using the same setup as Baldi *et al.* used for their experiments. In 2015, Wadell [73] measured isotherms on ensembles of well separated nanocubes with a mean size of 22 nm, 5 nm, 34.1 nm and 65.7 nm

through Indirect NanoPlasmonic Sensing (INPS) [72–74]. They observed completely flat plateaus at temperatures between 303 K and 333 K.

The used methods, namely, luminescence [69], EELS [70] and INPS do not allow for an absolute determination of the hydrogen concentration. Therefore, only the temperature dependence of the plateau pressures can be determined for a given size of nanocubes. Genuine pressure-composition isotherms (i.e. isotherms in which the H concentration is actually measured) have only been determined for Pd clusters smaller than 7 nm by means of electrochemistry [83, 84] and volumetry [68] and for 10 nm nanocubes [71] by volumetry at room temperature.

All these experimental constraints lead to the patchy distribution in Fig. 4.2 showing the size and temperature ranges of the experimental data published so far.

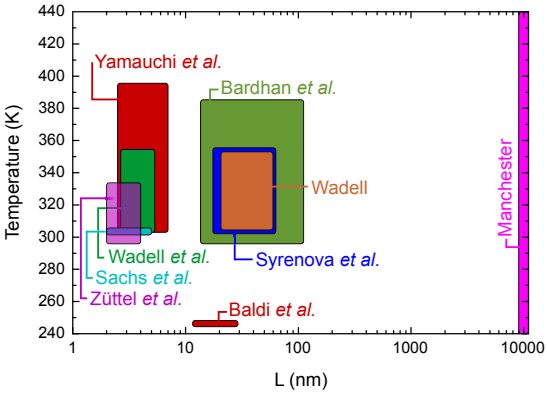

FIGURE 4.2. Size and temperature ranges of experimental works on hydrogen absorption in Pd nanoparticles. The references are Yamauchi et *et al.* [68], Züttel *et al.* [84], Sachs *et al.* [83], Wadell *et al.* [72], Bardhan *et al.* [69], Baldi *et al.* [70] Wadell [73], Syrenova *et al.* [74] and Manchester [47]. Note that Syrenova *et al.* only measured absorption isotherms except at 313 K where both hydrogen absorption and desorption were measured.

On the basis of hydrogen absorption and desorption isotherm measurements on ensembles of 14 nm, 32 nm, 65 nm and 110 nm nanocubes, Bardhan *et al.* [69] concluded that there is a clear size dependence in the thermodynamics of their nanocubes. Comparing their measurements to Monte Carlo simulations (based on the Ising model), they conclude that the size-dependence is a consequence of nanoconfinement of a thermally driven, first-order phase transition where α- and β-phases coexist incoherently. The presence of a large interfacial energy barrier is responsible for the opening of a hysteresis gap.

This is at variance with Baldi *et al.* [70] and Narayan *et al.* [76] who found that in single nanocubes at 246 K, surface stress due to excess hydrogen concentration at the surface of the nanocrystals accounts for the size dependence of the equilibrium absorption pressures. The absorption isotherms of individual nanocrystals are consistent with a coherent absorption process, in which coexistence of two hydride phases is suppressed. In an earlier study Sachs *et al.* [83] suggested that their data for 2 nm to 5 nm Pd clusters were consistent with the theory of Schwarz and Khachaturyan [80, 81] for open, coherent two-phase systems. Evidence of the role of subsurface sites was also found in very small Pd clusters [72, 84].

Although all these pioneering works have still a fragmentary character, there seem to be robust underlying patterns in the existing data mentioned above. To put them into evidence, we consider the following thermodynamic aspects of the PdH system:

- The enthalpy-entropy compensation,
- The ab-and desorption plateau pressures at room temperature,
- Isotherm hysteresis [85].

4.2 ENTHALPY AND ENTROPY COMPENSATION

A collection of enthalpies, ΔH, and entropies, ΔS, of hydrogen ab- and desorption in Pd nanoparticles [68, 69, 73, 74], a free-standing

film [86] and bulk Palladium [47, 87] is shown in Fig. 4.3. The enthalpy ΔH and entropy ΔS are both determined by plotting plateau pressures at fixed concentration as a function of the inverse absolute temperature (see Eq. (4.2)). A remarkably linear correlation between the measured ΔH and ΔS for samples of widely different sizes can be seen in the desorption data. However, there is no clear trend with particle size, as the Bardhan *et al.*'s [69] data is on the less negative ΔH-side of the curve while the Wadell [73] data obtained from measurements on the same type of nanocubes, are on the more negative side.

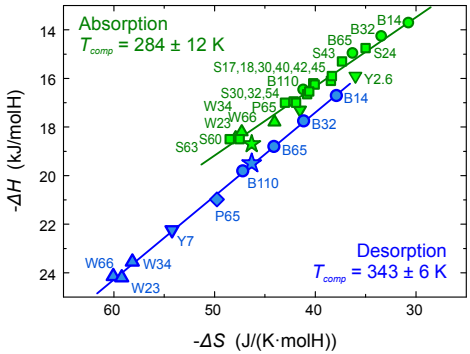

FIGURE 4.3. Enthalpy-entropy correlation for H absorption and desorption in nanosized Pd particles. The labels are as follows: B14 – B65 are for nanocubes from Bardhan *et al.* [69], L23 – L66 are for the 22.5 nm, 34.1 nm and 65.7 nm nanocubes from Wadell [72], Y2.6 and Y7 from Yamauchi *et al.* [68], and S17 – S63 are for single nanocubes from Syrenova *et al.* [74]. The number following the letter is the size of the particles in nm. The stars are from Laesser and Klatt for bulk Palladium [87]. For comparison data for a free standing 65 nm film (P65) are also included [86]. The compensation temperatures T_{comp} are obtained from Eq. (4.1).

The origin of the $\Delta H - \Delta S$ correlation is most likely related to the fact that, for example, the isotherms of Bardhan *et al.* exhibit strongly sloping plateaus and the hydrogen concentration is not measured absolutely. In addition, there are non-closing hysteresis loops and some

of the isotherms are crossing. Consequently, it is not easy to determine accurate values of pressure at a constant concentration for various temperatures. This leads to statistical errors in Van 't Hoff plots which translate into correlated errors in ΔH and ΔS. Hence, a decrease in slope (which is proportional to ΔH) leads automatically to a decrease in the intercept at $1/T = 0$ (which is proportional to ΔS, see Eq. (4.2)).

A direct implication of that effect is the ΔH and ΔS correlation shown in Fig. 4.3. The fact that for essentially the same 65 nm nanocubes the data points of Wadell [73] and Bardhan *et al.* [69] are laying far apart, but on the same line, is a clear indication that most of the discrepancy is of statistical origin. Hence, the conversion of ab- and desorption pressures into the two thermodynamic parameters ΔH and ΔS can be tricky (see Section 4.3.5). For example, if one assumes a perfectly linear $\Delta H - \Delta S$ correlation, it can be written as

$$\Delta H = T_{comp}\Delta S + C \tag{4.1}$$

where T_{comp} and C are the same constants for all samples. The slope $\partial\Delta H/\partial\Delta S$ is the so-called compensation temperature T_{comp}. At T_{comp} all plateau pressures are equal to the same value p_{comp}. This follows directly from the Van 't Hoff relation

$$\frac{1}{2}\ln p = \frac{\Delta H}{RT} - \frac{\Delta S}{R} \tag{4.2}$$

where p is the H_2 gas pressure (in bar), R the ideal gas constant, and T the absolute temperature. Introduction of Eq. (4.1) into Eq. (4.2) at $T = T_{comp}$ gives

$$\ln p_{comp} = \frac{2C}{RT_{comp}} \tag{4.3}$$

which implies that the pressure p_{comp} at T_{comp} is a constant, too. The compensation temperatures obtained from Fig. 4.3 for H absorption ($T_{comp} = 284\,\mathrm{K}$) and desorption ($T_{comp} = 343\,\mathrm{K}$) are very close to the measurement temperatures chosen by Yamauchi *et al.*, Bardhan *et al.*, Wadell *et al.* and Syrenova *et al.* [68, 69, 72–74]. Thus, one expects that the plateau pressures near room temperature are essentially the same in all data.

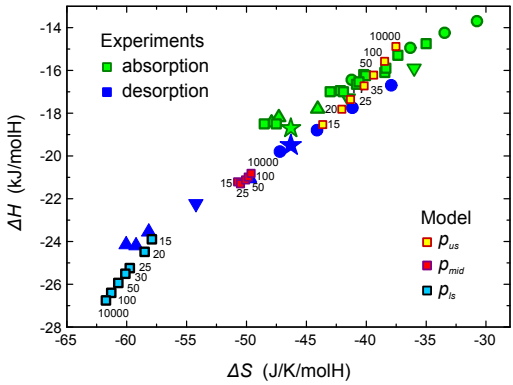

FIGURE 4.4. Comparison of $\Delta H - \Delta S$ correlation calculated with the mean-field model introduced in Section 4.4 for the lower spinodal pressures (p_{ls}, black-blue squares), the upper spinodal pressures (p_{us}, red-yellow squares) and the midpressures (p_M, blue-red squares) for nanocubes in the range 15 nm and 10 000 nm with the experimental data of Fig. 4.3. The numbers indicate the sizes of the calculated nanocubes. The symbols for the experimental data are the same as in Fig. 4.3. Their labeling is omitted for clarity. The compensation temperatures for the calculated cubes are 607 K for absorption and 722 K for desorption.

To quantitatively substantiate this conclusions, we compare enthalpies ΔH and entropies ΔS determined from the Van 't Hoff plots calculated with the mean-field model for nanocubes of various sizes introduced in Section 4.4 with the experimental data in Fig. 4.3. In Fig. 4.4 one can see, a $\Delta H - \Delta S$ correlation for model data, too. However, it is in a much narrower range of entropies and enthalpies than the reported values shown in Fig. 4.3. As expected, the experimental values for bulk are close to the calculated ΔH and ΔS for the midplateau pressures as the measured hysteresis is small. Remarkable is that the Wadell [73] data points W23, W34 and W66 (for $L = 22.5$, 34.1 and 65.7 nm nanocubes) and the Syrenova *et al.* [74] new single nanocube data are consistent with our model values although they were not used in the fitting of the parameters entering the model. The calculated compensation temperatures T_{comp}, 607 K and 722 K for absorption

and desorption are clearly different from the spurious compensation temperatures in Fig. 4.3.

4.2.1 *Plateau Pressures at Room Temperature*

As many existing data have been obtained near room temperature, Fig. 4.5 displays the plateau pressures at 300 K (the plateau pressures are either taken directly from quoted measured values or calculated from quoted enthalpies and entropies by means of Eq. (4.2). The half filled circles are estimated from the data of Baldi *et al.*). Despite the large variation in sample size and shape and different experimental techniques used in the preparation of samples and measurements, clear patterns emerge. The desorption pressures for nanostructures are essentially all equal to that of bulk Pd samples [47, 87]. The absorption pressures of very small particles [68, 83, 86] (typically smaller than 8 nm) are close to the absorption pressure of bulk Pd. In sharp contrast, the absorption pressure of nanocubes larger than $\sim$ 8 nm increases markedly with increasing size L. This increase is bound to stop in large particles when hydrogen absorption breaks them in smaller crystallites (the larges possible single-crystalline nanocubes are around 150 nm in diameter). Even though the data of Wadell [73] are obtained by means of INPS on well separated nanocubes, whereas the data of Bardhan *et al.* [69] is derived from luminescence measurements on dense ensembles of 32 and 65 nm nanocubes, both pressure values are consistent.

The clear difference between the size-dependence of absorption and desorption pressures indicates that the processes occurring during hydrogen absorption are fundamentally different from those during hydrogen desorption. The midpressure p_{mid} (defined as $\ln p_{mid} = 1/2\left(\ln p_{abs} + \ln p_{des}\right)$) considered by Bardhan *et al.* [69] is, therefore, not a suitable parameter for the intrinsic thermodynamics of nanocubes.

Desorption of hydrogen in bulk Pd has been demonstrated to correspond to the one obtained by application of the Maxwell construction

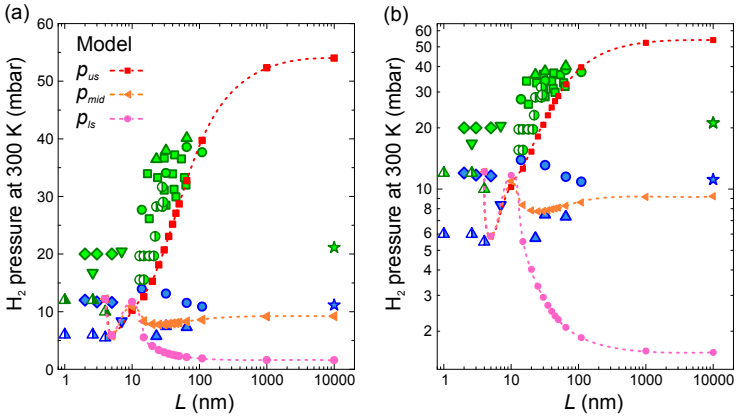

FIGURE 4.5. Experimental and calculated plateau pressures at 300 K for H in Pd nanocubes and nanoparticles. The green symbols represent experimental data for hydrogen absorption and the blue symbols for desorption. Green and blue dots represent data from Bardhan *et al.* [69], Triangles from Wadell [73], Inverted triangles from Yamauchi *et al.* [68], Half-filled triangles from Zuettel *et al.* [84], Diamonds from Sachs *et al.* [83], and Stars from Laesser and Klatt [87]. Half-filled circles are evaluated from the absorption data of Baldi *et al.* [70]. The red squares (upper spinodal pressure p_{us}), pink dots (lower spinodal pressure p_{ls}) and orange triangles (midpressure p_{mid}) are calculated by means of the mean-field model described in Sections 4.4 and 4.5 using the parameters from Eq. (4.86). The size L of the nanoparticles is plotted on a logarithmic scale in order to be able to cover the wide range of sizes ranging from 2 nm to bulk, which is arbitrarily set at 10^4 nm. For better visibility the pressure is plotted in a linear scale in (a) and a logarithmic scale in (b). The rapid variation of the calculated pressures for nanoparticles smaller than 10 nm marks the transition from core-dominated to surface-shell-dominated behavior (see Fig. 4.24). In a 9.7 nm nanocube the surface-shell and core volumes are equal (i.e. $g = 0.5$).

(i.e. to a fully incoherent coexistence [88] of the dilute α-PdH_x and concentrated β-PdH_x phases). Thus, it is tempting to conclude that

this does also happen in nanoparticles. However, the large hysteresis found experimentally in nanoparticles, makes it necessary to postulate that during absorption the concentration of H in α-PdH_x increases until a concentration close to the upper spinodal concentration [89] x_{us} is reached (namely the lowest concentration x for which the pressure-composition isotherms exhibit an extremum, see also Fig. 4.1). These expectations can be substantiated by considering the hysteresis measured during hydrogen absorption-desorption cycles at constant temperature. Considering hysteresis is especially relevant when isotherms exhibit sloping plateaus. In contrast to pressure data and the corresponding Van 't Hoff plots which all critically depend on the chosen concentration in the middle of the plateaus, the hysteresis is much better defined (see Fig. 4.6).

4.3 ISOTHERM HYSTERESIS

The large size dependence of the enthalpy and the entropy found for 14, 32, 65 and 110 nm nanocubes [69] is probably due to several factors:

- Uncertainties in the determination of the critical concentration at which the plateau pressure must be evaluated for the Van 't Hoff analysis,
- the use of the midpressure p_{mid} as representative of the intrinsic thermodynamic properties of PdH_x nanocubes, and
- a relatively narrow temperature range.

As shown in Fig. 4.6, the frist two difficulties can be avoided by considering the isotherm hysteresis. Its magnitude is defined as the logarithm of the ratio of the absorption and desorption plateau pressures ($\ln p_{abs} - \ln p_{des}$). This implies that the y-axis in Fig. 4.7 is well determined and that the critical temperature T_c can be obtained from the temperature-dependent hysteresis (see Section 4.3.3 and Fig. 4.8). The usefulness of hysteresis versus temperature data has been discussed in detail by Pundt and Kircheim [85].

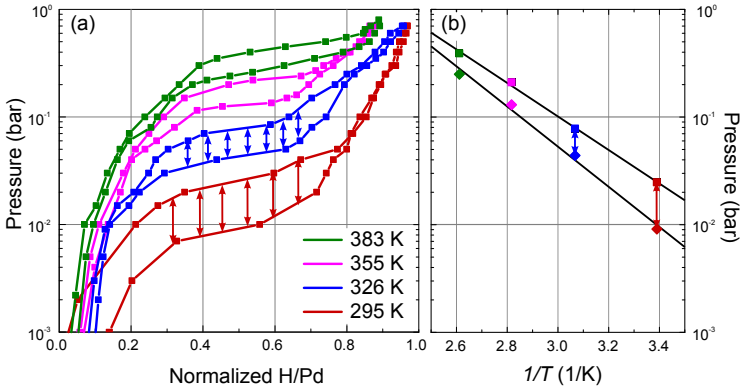

FIGURE 4.6. (a), Illustration the hysteresis. The data are for a 32 nm nanocube ensemble measured by Bardhan *et al.* [69] The arrows of a given color all have the same length. (b), The hysteresis, i.e. the difference $\left(\ln p_{abs} - \ln p_{des}\right)$, does not critically depend on concentration. Nevertheless, it is possible to determine all important thermodynamic quantities (e.g. T_c as the intersection between the two curves) from it.

As the hysteresis vanishes at the critical temperature, one expects a scaling law of the form (see Section 4.3.2)

$$\ln\left(\frac{p_{abs}\left(T,L\right)}{p_{des}\left(T,L\right)}\right) = f\left(\frac{T_c\left(L\right)}{T}\right) \tag{4.4}$$

where $T_c\left(L\right)$ is the critical temperature of a nanoparticle of size L and f is a function such that $f\left(1\right) = 0$. Figure 4.7 shows that the hysteresis of essentially all measured Pd nanocubes falls within the theoretical full-spinodal and half-spinodal hysteresis curves. This is completely different from the behaviour of bulk Pd [87] depicted as black stars in Fig. 4.7. Data for a 50 nm Pd film [90] and a free standing 65 nm film [86] exhibit a behavior intermediate between nanocubes and bulk Pd.

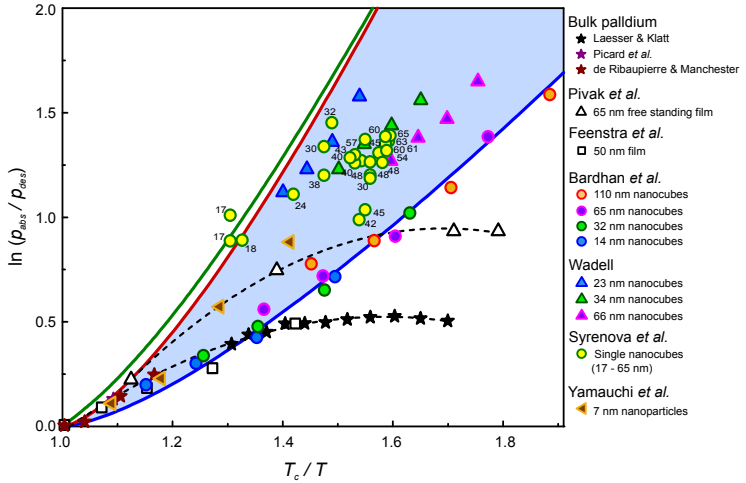

FIGURE 4.7. Scaling law for the hysteresis. The hysteresis is plotted as a function of the inverse absolute temperature T normalized to the critical temperature T_c for Pd nanocubes (Bardhan *et al.* [69], Wadell [73], Yamauchi *et al.* [68], and the single nanocube data of Syrenova *et al.* [74] (the numbers next to the circles indicate the sizes of the respective nanocubes)), Pd films (Feenstra *et al.* [90], and Pivak *et al.* [86]), and bulk Pd [87]. The determination of the critical temperatures is described in Section 4.3.5. The red line corresponds to the full-spinodal hysteresis obtained from Eq. (4.10), the blue line to the 45 %-spinodal and the green line is the full-spinodal hysteresis obtained from a fit to the desorption data of bulk Pd critically analyzed by Manchester *et al.* [47] described in Section 4.4.1. The black dashed lines through the bulk data and the free standing film are a guide to the eye. The shaded blue area is the hysteresis region of the scaling law.

4.3.1 *The Lattice Gas Model*

The full-spinodal line in Fig. 4.7 is calculated as follows. In the simplest mean-field description of a lattice gas [91, 92], for example H in Pd, the isotherms are given by

$$\frac{1}{2}\ln p = \ln\left(\frac{x}{b-x}\right) + \frac{\Delta H_\infty - Ax}{RT} - \frac{\Delta S}{R} \tag{4.5}$$

where $x = \mathrm{H/Pd}$, ΔH_∞ is the enthalpy of hydrogen solution in Pd (i.e., ΔH in the limit $x \to 0$), b is a blocking factor, and A is the magnitude of the long-range effective H-H interaction. The critical temperature is

$$T_c = \frac{Ab}{4R}. \tag{4.6}$$

The spinodal concentrations x_{us} and x_{ls} defined by the condition

$$\left.\frac{\partial \ln p}{\partial x}\right|_T = 0 \tag{4.7}$$

are

$$x_{us} = \frac{b}{2}(1 - z) \tag{4.8}$$

and

$$x_{ls} = \frac{b}{2}(1 + z). \tag{4.9}$$

For temperatures below the critical temperature T_c, the pressure-composition isotherms described by Eq. (4.5) exhibit a local maximum with pressure p_{us} (the upper spinodal pressure) at concentration x_{us} and a local minimum with pressure p_{ls} (the lower spinodal pressure) at concentration x_{ls} (see Fig. 4.1). The calculated curve between x_{us} and x_{ls} is thermodynamically not allowed as the chemical potential (proportional to $\ln p$) decreases with increasing concentration. The maximum hydrogen absorption pressure is p_{us} and the minimum desorption pressure p_{ls}. Consequently, the maximum absorption-desorption hysteresis is $\ln\left(p_{us}/p_{ls}\right)$. The corresponding full spinodal hysteresis is

$$\ln\left(\frac{p_{us}}{p_{ls}}\right) = 8\frac{T_c}{T}z + 4\ln\left(\frac{1-z}{1+z}\right) \tag{4.10}$$

with $z = \sqrt{1 - T/T_c}$. It is noteworthy that the hysteresis $\ln\left(p_{us}/p_{ls}\right)$ only depends on the ratio T/T_c. The full-spinodal hysteresis (red

curve in Fig. 4.7) is the largest possible hysteresis in an absorption-desorption cycle (see Fig. 4.1). It is only realized, if the nanocube remains in a supersatured α-PdH_x phase during hydrogen uptake, until the lower spinodal concentration x_{us} is reached. During hydrogen release the nanocube remains in the concentrated β-PdH_x phase as long as $x > x_{ls}$.

All the measured hystereses $\ln\left(p_{us}/p_{ls}\right)$ in Fig. 4.7 fall between the 100 % spinodal hysteresis (red curve) and the 45 % hysteresis value (blue curve), defined as $0.45 \times \ln\left(p_{us}/p_{ls}\right)$. This, together with the large difference between the absorption and desorption pressures in Fig. 4.5, indicates that hydrogen absorption occurs at $p_{abs} \approx p_{us}$. Whereas the desorption at p_{des} occurs at a pressure intermediate between the Maxwell pressure p_M [82] and the lower spinodal pressure p_{ls}.

One expects that hydrogen absorption proceeds coherently as predicted by the theory of Schwarz and Khachaturyan [80, 81] while an incoherent coexistence of α- and β-PdH_x phases occurs during desorption as is the case in bulk Pd samples [88]. There is, however, a clear tendency towards a full spinodal hysteresis in Fig. 4.7, when T_c/T goes towards 1 (see also Fig. 4.10).

It is noteworthy that the 7 nm nanoparticles of Yamauchi *et al.* [68] and the 22.5, 34.1 and 65.7 nm nanocubes of Wadell [73] are systematically closer to full hysteresis than the Bardhan *et al.* [69] nanocubes. It is unlikely that difference is due to local heating effects as the scaling law is remarkably robust (see Section 4.5.3). For the smallest nanoparticles, Fig. 4.5 indicates that there is still a small hysteresis. It is probably related to the experimental methods used in the publications. As the small width of the '*plateaus*' at 300 K measured by Sachs *et al.* [83] indicates a critical temperature close to or below 300 K. The same applies to the isotherms measured by Wadell *et al.* [72] on 2.7 and 5.3 nm Pd nanoparticles and those of Yamauchi *et al.* [68] on 2.6 nm nanoparticles.

At this point, one might question, whether the simple expression in Eq. (4.10) has any practical relevance. To demonstrate its importance,

a more general mean field model including non-linear H-H interactions fitted to the bulk Pd isotherms is developed in the following sections.

4.3.2 *Hysteresis Scaling Law with Non-linear Effective H-H Interaction*

In Section 4.3 the scaling law for the hysteresis (see Eq. (4.5)) is derived for the simplest possible case: a lattice gas with blocking factor and a linear attractive H-H interaction. In this section, I want to demonstrate that an analytically solvable lattice gas model with a linear attractive (elastic) H-H interaction $-Ax$ and a quadratic repulsive (electronic) H-H interaction Fx^2 results in a similar scaling law. In equilibrium the equality of the chemical potentials is written as:

$$\frac{1}{2}\ln p = \ln\left(\frac{x}{1-x}\right) + \frac{\Delta H_\infty - Ax + Fx^2}{RT} - \frac{\Delta S}{R}. \tag{4.11}$$

Both, A and F are positive.

Similar to the linear case in Section 4.3.1, the critical temperature, pressure and concentration are determined by the following three conditions

$$\left.\frac{\partial \ln p}{\partial x}\right|_{T=T_c} = 0 \tag{4.12a}$$

$$\left.\frac{\partial^2 \ln p}{\partial x^2}\right|_{T=T_c} = 0 \tag{4.12b}$$

$$\left.\frac{\partial^3 \ln p}{\partial x^3}\right|_{T=T_c} \geq 0. \tag{4.12c}$$

From the conditions in Eqs. (4.12a) and (4.12b) follows that

$$RT_c = \left(A - 2Fx_C\right) x_C \left(1 - x_C\right) \tag{4.13a}$$

and

$$RT_c = Fx_C^2 \frac{2\left(1-x_C\right)^2}{1-2x_C}. \tag{4.13b}$$

Equations (4.13a) and (4.13b) lead to the following expression for the critical concentration x_C

$$x_C = \frac{1}{2q}\left(1+2q-\sqrt{1-2q+4q^2}\right) \tag{4.14}$$

with

$$q = \frac{F}{A}. \tag{4.15}$$

If the quadratic H-H interaction term vanishes, i.e., when $F = 0$ then $x_C = 1/2$ and the critical temperature is

$$T_{c_0} = \frac{A}{4R} \tag{4.16}$$

For the general case with $q \neq 0$,

$$T_c = 4T_{c_0}\left(1-2qx_C\right)x_C\left(1-x_C\right). \tag{4.17}$$

A full analytic expression for T_c is obtained by inserting x_C from Eq. (4.14) into Eq. (4.17). Resulting in

$$\begin{aligned}\frac{T_c}{T_{c_0}} = &-\frac{1}{27q^2}\times \\ &\left(2-6q-12q^2+16q^3-\left(2-4q+8q^2\right)\sqrt{1-2q+4q^2}\right).\end{aligned} \tag{4.18}$$

It explicitly shows that T_c/T_{c_0} depends only on the ratio $q = F/A$.

Using these results, we can calculate the upper and lower spinodal pressures p_{us} and p_{ls}. By definition the spinodal compositions x_{us} and x_{ls} are determined by the condition

$$\left.\frac{\partial \ln p}{\partial x}\right|_T = 0 \tag{4.19}$$

Following the same procedure as for Eq. (4.17) we now obtain

$$\frac{T}{T_{c_0}} = 4\left(1 - 2qx_{us/ls}\right) x_{us/ls}\left(1 - x_{us/ls}\right), \tag{4.20}$$

which implies that the spinodal concentrations only depend on q and T/T_{c_0}. For the spinodal hysteresis we consequently have

$$\begin{aligned}\ln\left(\frac{p_{us}}{p_{ls}}\right) =& 2\ln\left(\frac{x_{us}\left(1-x_{ls}\right)}{x_{ls}\left(1-x_{us}\right)}\right) + \\ & 8\frac{T_{c_0}}{T}\left(x_{us}-x_{ls}\right)\left(q\left(x_{us}+x_{ls}\right)-1\right).\end{aligned} \tag{4.21}$$

Using the definitions from Eqs. (4.14), (4.17) and (4.20), Eq. (4.21) implies that

$$\ln\left(\frac{p_{us}}{p_{ls}}\right) = h\left(\frac{T}{T_c}, \frac{T_c}{T_{c_0}}\right). \tag{4.22}$$

The analytic expression for the function h turns out to be rather complicated. For the special case $q = 0$, i.e., when $T_c/T_{c_0} = 1$ it is, however, simply

$$h(z,1) = 8\frac{T_c}{T}z + 4\ln\left(\frac{1-z}{1+z}\right) \tag{4.23}$$

with $z = \sqrt{1 - T/T_c}$. Numerically one can show that the following expression is a very good approximation of the exact analytic result

$$h\left(z, T_c/T_{c_0}\right) \simeq \frac{1}{2}\left(1 + \frac{T_c}{T_{c_0}}\right) h(z,1) \simeq \left(\frac{1}{2} + x_C\right) h(z,1) \tag{4.24}$$

As x_C is typically 0.3 the scaling law is within 20 % the same as in Eq. (4.23).

In Section 4.4.1, the model is used to accurately reproduce the isotherms of bulk Pd over a wide range of temperatures from 194.5 K to 710 K (covering the full thermodynamically relevant range from below to well above the critical point $T_c = 566$ K). The result is displayed in Fig. 4.14. It also shows that the measured desorption plateau pressures are very close to p_M, obtained by applying Maxwell's construction [82] to the calculated isotherms.

Although the model involves a temperature dependent enthalpy of solution, non-linear effective H-H interactions and a temperature and concentration dependent excess entropy, the calculated full-spinodal hysteresis is very close to that predicted by the simple Eq. (4.10) (see Fig. 4.7).

4.3.3 *Spinodal Hysteresis and the Critical Temperature*

The determination of the critical temperature for the Pd-PdH phase transition is crucial for describing the thermodynamics of a given system. However, it can be a very challenging task do so with given experimental constraints. As the hysteresis vanishes at the critical temperature it is tempting to determine T_c from the crossing point of the absorption and desorption Van 't Hoff plots. It only works if

- the experimental data are available for temperatures close to T_c,
- the Van 't Hoff plots are linear,
- or enthalpy and entropy data are available for hydrogen absorption and desorption close to T_c.

In real systems it is not always possible to fulfill these conditions. Therefore, we need alternatives to describe these systems.

4.3.4 *Non-Linearity of Van 't Hoff Plots*

If entropy and enthalpy data close to $T = T_c$ available or if the Van 't Hoff plot are linear in the full temperature range, one can determine the critical temperature simply by using

$$T_c = \frac{\Delta H_{abs} - \Delta H_{des}}{\Delta S_{abs} - \Delta S_{des}}. \tag{4.25}$$

However, this procedure is not valid for systems with a large hysteresis, i.e. with a hysteresis comparable to the full spinodal hysteresis. The Van 't Hoff plots versus $1/T$ are then inherently curved. This can be easily demonstrated by means of the simplest lattice gas model with pressure-composition isotherms given by Eq. (4.5).

The upper and lower spinodal pressures are

$$\ln p_{us} = 2\ln\left(\frac{1-z}{1+z}\right) + 2\frac{\Delta H_\infty - Ab\,(1-z)}{RT} - 2\frac{\Delta S}{R} \tag{4.26}$$

and

$$\ln p_{ls} = 2\ln\left(\frac{1+z}{1-z}\right) + 2\frac{\Delta H_\infty - Ab\,(1+z)}{RT} - 2\frac{\Delta S}{R} \tag{4.27}$$

with

$$z = \sqrt{1 - 4\frac{RT}{Ab}}. \tag{4.28}$$

At the critical point, the two spinodal concentrations and pressures coincide. Thus

$$x_{ls} - x_{us} = 0 \Rightarrow T_c = \frac{Ab}{4R} \tag{4.29}$$

In this case, z can be rewritten as $z = \sqrt{1 - T/T_c}$ and the full spinodal hysteresis given by Eq. (4.10) only depends on the scaled temperature T/T_c.

From Eqs. (4.26) and (4.27) it is evident that Van 't Hoff plots corresponding to the upper spinodal pressure (for absorption) and the lower spinodal pressure (for desorption) are not linear. This is in sharp contrast with the Maxwell plateau pressures given by

$$\ln p_M = 2\left(\frac{\Delta H_\infty}{R} - 2T_c\right)\cdot\frac{1}{T} - 2\frac{\Delta S}{R}. \tag{4.30}$$

The non-linearity of Van 't Hoff plots can have severe effects on the determination of the critical temperature. When determining T_c

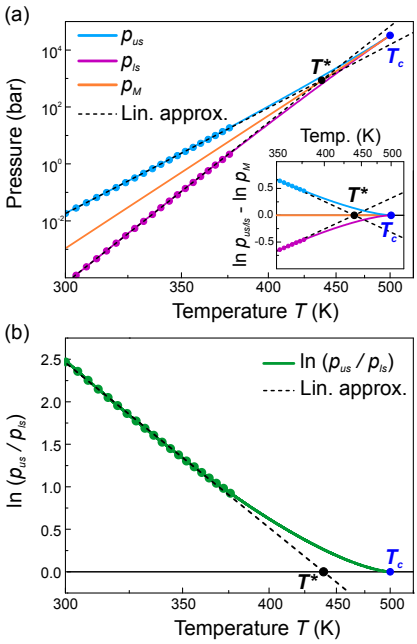

FIGURE 4.8. Spinodal pressures and hysteresis calculated with the simplest mean field model (see Eqs. (4.10), (4.26), (4.27) and (4.30)) with typical thermodynamic values ($\Delta S = -65.39\,\mathrm{J/K/mol}$ (H)). (a), Upper and lower spinodal pressures (p_{us}, p_{ls}, red and pink lines), and the Maxwell pressure (p_M, orange line), plotted on a logarithmic scale versus the reciprocal temperature. The red and pink dots represent data generate using the full-scale model for temperatures between 300 K and 380 K. The black dashed lines are linear fits to these data points. As clearly seen in the inset these two lines cross at a temperature T^* that is much lower (violet dot at $T^* = 439\,\mathrm{K}$) than the true critical temperature $T_c = 500\,\mathrm{K}$. It is noteworthy that the Maxwell pressure p_M behaves perfectly linear. (b), Full spinodal hysteresis (green line) plotted on the same temperature scale as in (a), together with linear fits corresponding to the dashed black curves in (a). In both the underestimation of the critical temperature as is visible.

as the point of intersection of the linearly extrapolated absorption and desorption pressures, one underestimates the critical temperature dramatically. This is shown in Fig. 4.8(a) for typical thermodynamic

parameters, where difference between the estimated and real critical temperature is as large as $T^* - T_c = 61\,\mathrm{K}$. The same underestimation is obtained when fitting the hysteresis versus inverse temperature curves with straight lines (see Fig. 4.8b).

4.3.5 *Determination of T_c for Non-Linear Pressure Data using Data Collapse*

This section describes a method for determining the critical temperature based on the assumption, a scaling law of the form indicated in Eq. (4.4) exists, i.e.

$$\text{hysteresis}\,(T, L) = \ln\left(\frac{p_{abs}\,(T, L)}{p_{des}\,(T, L)}\right) = f\left(\frac{T_c\,(L)}{T}\right). \tag{4.31}$$

It is important to stress that the procedure does not relay on any a priori assumptions about the function f except for $f\,(1) = 0$. As shown in the following lines, it is possible to determine the function f simply, by using the data of Bardhan *et al.* [69] for 4 different sizes of nanocubes. Equation (4.31) implies a connection for the hysteresis data of two particles of sizes L_1 and L_2. Data points of equal hysteresis satisfy

$$\begin{aligned} \text{hyst.}\,(T_1, L_1) &= f\left(\frac{T_c\,(L_1)}{T_1}\right) = \\ \text{hyst.}\,(T_2, L_2) &= f\left(\frac{T_c\,(L_2)}{T_2}\right). \end{aligned} \tag{4.32}$$

As the function f is single-valued this means that

$$\frac{T_c\,(L_1)}{T_1} = \frac{T_c\,(L_1)}{T_1} \rightarrow \frac{T_1}{T_2} = \frac{T_c\,(L_1)}{T_c\,(L_2)} = \text{const.} \tag{4.33}$$

Equation (4.33) allows to rescale the temperatures of every hysteresis data set to collapse them on one curve. In Fig. 4.9(a) this is applied

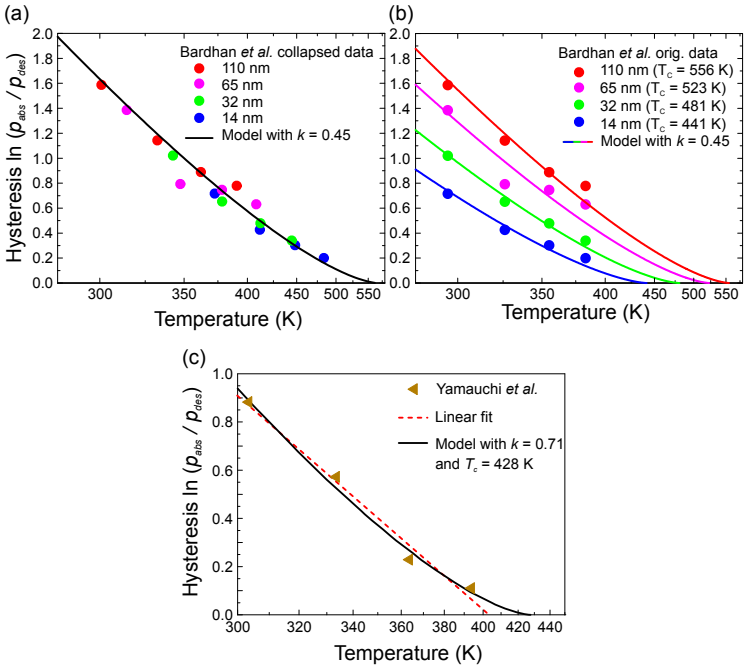

FIGURE 4.9. (a), Collapsed data of the temperature dependence of the hysteresis of 14 nm, 32 nm, 65 nm and 110 nm Pd nanocubes by Bardhan *et al.* [69] (the original values are taken from their Table S2) using the described procedure. The fit corresponds to the model described in Eq. (4.34) with $k = 0.45$. (b), The critical temperatures for the different nanocubes of Bardhan *et al.* [69] fitted with $k = 0.45$ are 441 K, 481 K, 523 K and 556 K. **c**. The Yamauchi *et al.* [68] hysteresis of their 7 nm nanoparticles fitted with a standard linear interpolation (red dotted line) and Eq. (4.34) with $k = 0.71$ resulting in $T_c = 428$ K instead of 403 K with the linear approximation. For all three panels the temperature scale is reciprocal.

to the data of Bardhan *et al.* [69], where the temperature of the data points for the 14 nm, 32 nm and 65 nm nanocubes are rescaled relative to the 110 nm cubes. The collapsed curve is well described by

$$\ln\left(\frac{p_{abs}}{p_{des}}\right) = k \cdot \left(8\frac{T_c}{T}z + 4\ln\left(\frac{1-z}{1+z}\right)\right) \tag{4.34}$$

with $k = 0.45$ and $T_c = 556\,\mathrm{K}$. As all data have been rescaled with respect to the 110 nm data, $T_c = 556\,\mathrm{K}$ is, thus, the critical temperature of the 110 nm nanocubes. The scaling factors, necessary for data collapse, allow to calculate the critical temperatures for the 14 nm, 32 nm and 65 nm nanocubes directly. Alternatively, one can fit Eq. (4.34) with $k = 0.45$ to the data sets of the individual nanocubes, resulting in $T_c\,(14\,\mathrm{nm}) = 441\,\mathrm{K}$, $T_c\,(32\,\mathrm{nm}) = 481\,\mathrm{K}$, and $T_c\,(65\,\mathrm{nm}) = 523\,\mathrm{K}$.

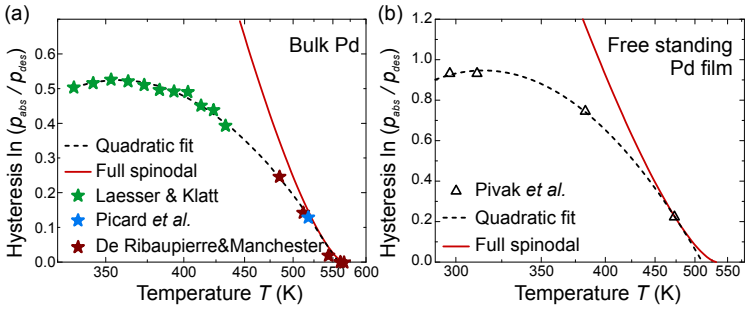

FIGURE 4.10. (a), Hysteresis of bulk palladium measured by Laesser and Klatt [87], Picard *et al.* [93] and de Ribaupierre & Manchester [94, 95], showing that for temperatures close to the critical temperature, the full spinodal hysteresis is obeyed. (b), Dataset of Pivak *et al.* [86] on 65 nm free standing palladium films exhibiting a similar behavior as bulk Pd. By fitting the full spinodal model to the points closest to the critical point, one finds $T_c = 532\,\mathrm{K}$.

In bulk palladium and thin films the hysteresis is much narrower than the full spinodal hysteresis. Therefore, the spinodal model is not applicable to determine the critical temperatures of such systems. However, as stated by de Ribaupierre and Manchester [94, 95], close to the critical point, even bulk-like systems exhibit hystereses close to the full spinodal hysteresis (see Fig. 4.10(a)). Hence, by fitting the full spinodal hysteresis model with $k = 1$ to measurement points close to the critical temperature, we are able to estimate the critical temperature for a free-standing Pd film that behaves bulk-like (Fig. 4.10(b)).

4.3.6 *Overview of Pd Nanoparticle Critical Temperatures*

The existing data about T_c are depicted in Fig. 4.11. The critical temperatures of Bardhan *et al.* [69] and Yamauchi *et al.* [68] are determined by the method described in Section 4.3.5 (Bardhan *et al.* [69] with $k = 0.45$ and Yamauchi *et al.* with $k = 0.71$). The temperature range of Wadells [73] data is very small. Therefore, it is not possible to apply a data collapse analysis to determine the function f experimentally, as done for the Bardhan *et al.* [69] data. In such a case, one can only estimate the critical temperatures roughly by means of Eq. (4.25). The corresponding T_c values are $T_c\,(22.5\,\text{nm}) = 443\,\text{K}$, $T_c\,(34.1\,\text{nm}) = 498\,\text{K}$, and $T_c\,(65.7\,\text{nm}) = 467\,\text{K}$.

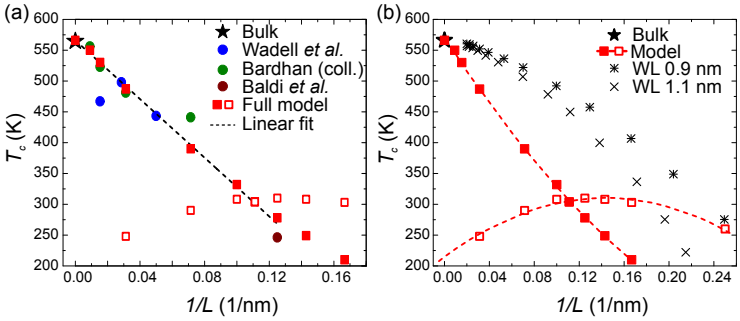

FIGURE 4.11. (a), Critical temperatures of Pd-H nanocubes as a function of their inverse size $1/L$. The references are Bardhan *et al.* [69], Wadell [73] , Baldi *et al.* [70] and bulk [87]. The mean-field model predicts two critical points (see Fig. 4.24). The open red squares correspond to the T_c associated with the surface-shell of the nanocube. The filled red squares indicate the critical temperature related to the core. The blue line $T_c = 566 - 2381/L$ is a linear fit to the experimental nanocube data with fixed intercept of 566 K at $1/L = 0$, as the critical temperature of bulk Pd-H is accurately known. (b). Comparison of our model critical temperatures to those calculated by Weissmüller and Lemier [96] (WL) for a somewhat comparable system, i.e. nanocrystalline materials made of nanosized grains separated by 0.9 or 1.1 nm grain boundaries. The dashed lines are guides to the eye.

The Pd nanoparticle critical temperature at 246 K (brown dot in Fig. 4.11(a)) is estimated from Baldi *et al.*'s [70] absorption and desorption data measured at 246 K for nanocubes in the range of 13 nm to 29 nm shown in Fig. 4.12. To determine an estimate for the nanocube size that would have a critical temperature of 246 K, their absorption pressures were fitted to a straight line. As the desorption pressures are increased by electron beam heating in an uncontrolled fashion, only the lowest lying points (corresponding to the 13 nm, 15 nm, 21 nm, 28 nm and 29 nm nanocubes) are used. The intersection of these two lines suggests a vanishing hysteresis at a nanocube size of approximately 8 nm. It is noteworthy, that the vanishing of hysteresis predicted by the mean-field model (described in details in Section 4.4) is actually around 7 nm, although the desorption data of Baldi or other literature values for nanoparticles this size did not enter the fitting procedure (see Fig. 4.17).

The data of Weissmüller and Lemier [96] are included for comparison, even though, they consider a related, but clearly different situation. They calculate the critical temperature of a nanocrystalline material consisting of nanosized grains separated by grain boundaries of various thickness (0.9 nm, 1 nm and 1.1 nm). They assume that there is no separation into α-PdH_x and β-PdH_x phases within the grain boundaries in which the concentration dependence of the chemical potential is assumed to be negligible. In the model developed in Section 4.4.2, both core and surface-shell, can exhibit α-PdH_x and β-PdH_x phases and the hydrogen concentration in the surface-shell is directly determined by the chemical potential of the surrounding hydrogen gas.

The size dependence of the critical temperature T_c (in degrees Kelvin) calculated with the mean-field model described in Section 4.4 is well represented by

$$T_c \approx 565.5 - \frac{2230}{L} \tag{4.35}$$

for nanocubes/nanoparticles with sizes $L > 10$ nm. For smaller nanostructures T_c remains within the range of 250 K and 310 K. The existence of two critical temperatures in Fig. 4.11 is a direct consequence of the core- and surface-shell structure assumed in our nanoparticle

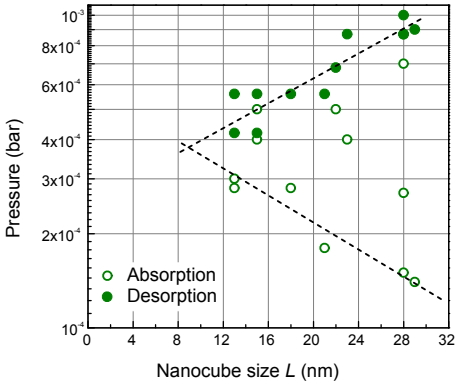

FIGURE 4.12. Absorption (dots) and desorption (open circles) plateau pressures measured by Baldi *et al.* [70] at 246 K for a series of nanocubes. As discussed by the authors only the absorption pressures can be measured reliably by EELS [70]. The dashed lines are linear fits to determine the nanocube size with T_c at 246 K.

model. The critical temperatures calculated by Weissmüller and Lemier [96] for a somewhat comparable system (nanocrystalline Pd-H with grain boundary thicknesses of 0.9 nm and 1.1 nm), exhibit a similar decrease of T_c with increasing $1/L$.

4.4 QUANTITATIVE MEAN-FIELD MODEL

The preceding conclusions are further substantiated by the quantitative comparison of experimental data and isotherms calculated by means of a mean-field model for the pressure-composition isotherms.

4.4.1 *Quantitative Model for the Pressure-Composition Isotherms of Bulk PdH_x*

We first start by introducing a PdH_x model, describing the well known bulk PdH pressure-composition isotherms. The model is a refined version of mean-field models introduced by Brodowsky [97], Wicke *et al.* [98], Wicke and Blaurock [88], Salomons *et al.* [99], Hemmes *et al.* [100] and Feenstra *et al.* [90]. It is based on the following expression for the pressure-composition isotherms of H in bulk Pd,

$$\frac{1}{2}\ln p = \ln\left(\frac{x}{1-x}\right) + \frac{\Delta H_\infty + H_{elast} + H_{el}}{RT} - \frac{\Delta S}{R}. \tag{4.36}$$

The enthalpy of solution (in J/mol_H) is

$$\Delta H_\infty = -14770 - 12.94 \times T, \tag{4.37}$$

where T is the absolute temperature in K. The expression in Eq. (4.37) is a linear representation of the experimental enthalpy data collected in the book of Manchester [47], summarizing the results published in 11 articles about the temperature variation of the enthalpy up to 920 K. The attractive elastic H-H interaction enthalpy is given by

$$H_{elast}(x) = -\int_0^x \frac{BV_H^2}{V} dx, \tag{4.38}$$

where B is the bulk modulus, V the molar volume of PdH_x , x the ratio of hydrogen to palladium atoms in PdH_x, and V_H the partial molar volume of H in PdH_x. Equation (4.38) can be expressed in polynomial form by [101]

$$H_{elast} = -63640x + 40170x^2 - 9740x^3. \tag{4.39}$$

The repulsive electronic H-H interaction is taken as

$$H_{el} = 7248x + \frac{87955x^4.1791}{\zeta + x^4} \tag{4.40}$$

with $\zeta = 1.0648$. It mainly depends on the hydrogen concentration dependence of the Fermi energy of PdH_x. The non-linear term arises

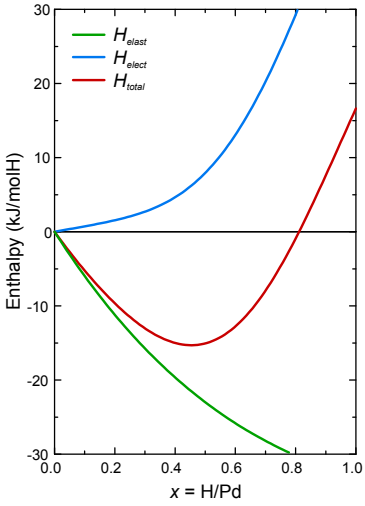

FIGURE 4.13. Elastic (green), electronic (blue) and total effective H-H interaction (red). The curves are calculated by means of Eqs. (4.39) and (4.40).

from the electronic d-band of Pd [90]. The compact analytical expression in Eq. (4.40) reproduces accurately the electronic contribution to the enthalpy shown in Fig. 2 of a publication by Hemmes *et al.* [100]. The total effective H-H interaction corresponding to the sum of H_{elast} and H_{el}, is depicted in Fig. 4.13.

The entropy is given by

$$\begin{aligned}\Delta S = &- 71.78 + 0.0702T - 6.88 \times 10^{-5}T^2 + 2.89 \times 10^{-8}T^3 \\ &- 29.23x + 9.15x^2 + 54.83x^3.\end{aligned} \tag{4.41}$$

The concentration x dependence of the entropy in Eq. (4.41) is taken from Eq. (6) in [101]. The temperature T dependence of the entropy is mainly due to the contribution of the optical phonons in PdH_x.

The pressure-composition isotherms calculated, by using Eqs. (4.37) and (4.39) to (4.41) together with Eq. (4.36), are shown in Fig. 4.14. They are in excellent agreement with the measured desorption isotherms of H in bulk Pd if one applies Maxwell's construction to determine the

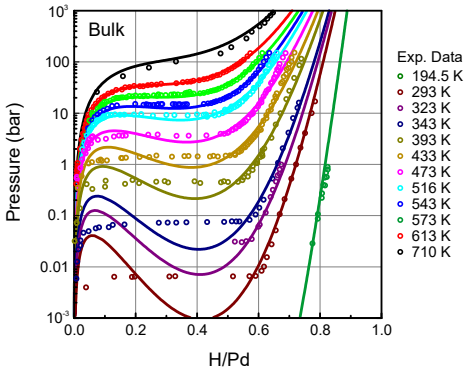

FIGURE 4.14. Pressure-composition (P-C) isotherms of bulk Pd compared to those calculated (colored lines) with the mean-field lattice gas model. The experimental data (colored circles) taken from Manchester *et al.* [47] are for hydrogen desorption.

incoherent desorption plateau pressures. This confirms the early conclusions of Wicke and Blaurock [88], that the desorption isotherms represent the true strain-free equilibrium; the absorption branches represent instead, an equilibrium under mechanical constraints.

4.4.2 *Quantitative Model for Nanoparticle Isotherms*

To describe the behavior of PdH_x nanoparticles one needs to introduce several changes compared to the bulk model described in Section 4.4.1. The basic assumptions are similar to that of Weissmüller and Lemier [96, 102] and Baldi *et al.* [70]. As proposed by Sachs *et al.* [83], hydrogen can be accommodated at subsurface sites in a surface-shell of thickness t and at sites in the core of a nanoparticle (see Fig. 4.15). The volume fraction g of surface-shell sites is defined as

$$g = \frac{V_{shell}}{V_{shell} + V_{core}} = 1 - \left(1 - \frac{2t}{L}\right)^3 \tag{4.42}$$

and the total concentration of hydrogen in the nanoparticle x_{total} is given by

$$x_{total} = (1-g)\, x_{core} + g x_{shell}, \tag{4.43}$$

where x_{shell} is the H concentration in the surface-shell of volume V_{shell} and x_{core} is the H concentration in the nanoparticle core of volume V_{core}.

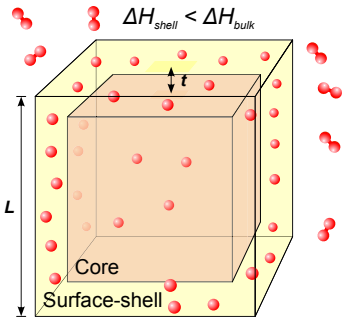

FIGURE 4.15. Nanocube configuration used for the mean-field calculations of the isotherms in Section 4.4.2.

During H absorption, the enthalpy of solution $\Delta H^{\infty}_{shell}$ for surface-shell sites is more negative than ΔH^{∞}_{core} for core sites [99, 102, 103] and the surface-shell H concentration x_{shell} is larger than x_{core}. This leads to H-dependent internal strains and, consequently, to H-dependent enthalpies in addition to the usual elastic and electronic effective H-H interactions, which are assumed to be the same as in bulk Pd. Surface tension [99, 104] and clamping contributions [105] to the enthalpy of hydride formation [106] are taken into account by the model, too.

The important additions to account for the size-dependence in the enthalpies, are the following:

- Adjustment of the enthalpy of H solution at the subsurface sites, with

$$\Delta H^{\infty}_{surf} < \Delta H^{\infty}_{core} \tag{4.44}$$

- A size-dependent surface tension enthalpy

$$H_{surf}(L) = \frac{u}{L} \tag{4.45}$$

  with the energy u depending essentially on the surace tension of Pd (see [105]).

- An adjusted elastic H-H interaction enthalpy, to allow for the influence of partial clamping by the substrate and/or an eventual surface contaminant or surfactant layers, and for an eventual difference of elastic properties between core and surface-shell. Thus, the attractive elastic H-H interaction enthalpy is allowed to be size dependent, such that

$$H_{elast}(L) = H^{bulk}_{elast} \cdot \left(1 - \frac{w}{L}\right), \tag{4.46}$$

  where w is an effective clamping thickness.

The repulsive electronic H-H interaction enthalpy H_{el} is assumed to be the same both for H in the core of the nanoparticle and in its surface-shell. Additionally, H_{el} shall not depend on the size of the nanoparticle. The same applies for the entropy.

4.4.3 *Elastic Coupling between Surface-shell and Core of the Nanoparticle*

As the enthalpy of H solutions at surface-shell sites is more negative than at core sites, the resulting larger surface H concentration leads to an expansion of the surface-shell, which expands also the inner part (i.e., the core) of the particle. The problem of elastic coupling between surface-shell and core of a nanoparticle has repeatedly been

considered in the past. Relevant is, here, the calculations of Pasquini *et al.* [107]. They considered the effect of elastic constraint on the thermodynamics of hydrogen absorption and desorption in composite core-surface-shell nanoparticles, where the core is a hydride forming metal and the surface-shell is made of a different material that does not absorb hydrogen. For a core containing a hydrogen concentration $x_{core} = H/Pd$ surrounded by a surface-shell without hydrogen they find that

$$\frac{\Delta V_{constr}}{V_{core}} = -\frac{x_{core} V_H}{V_{Pd}} \times \frac{2\eta\left(\rho^3 - 1\right)}{2\left(\frac{1-2\nu_{shell}}{1-2\nu_{core}}\right) + \rho^3\left(\frac{1+\nu_{shell}}{1-2\nu_{core}}\right) + 2\eta\left(\rho^3 - 1\right)}, \tag{4.47}$$

where $\Delta V_{constr}/V_{core}$ is the relative volume change of the hydride due to elastic constraint of the non-hydrogen-absorbing surface-shell and ρ is the ratio of the radius of the entire particle (i.e. core plus surface-shell) and the radius of the core, given by:

$$\rho = \frac{L/2}{L/2 - t} = \frac{1}{1 - 2t/L}. \tag{4.48}$$

η is the ratio of the surface-shell and core Young moduli

$$\eta = \frac{E_{shell}}{E_{core}}, \tag{4.49}$$

and ν_{core} and ν_{shell} are the Poisson ratios of the core and surface-shell, respectively.

For Pd nanoparticles, consisting of a core and a surface-shell, one expects at first approximation that the elastic constants of the surface-shell are the same as those of the core. This implies that $\eta = 1$ and $\nu_{core} = \nu_{shell}$ and consequently

$$\frac{\Delta V_{constr}}{V_{core}} = -\frac{x_{core} V_H}{V_{Pd}} \frac{2\left(\rho^3 - 1\right)}{2 + \rho^3\left(\frac{1+\nu}{1-2\nu}\right) + 2\left(\rho^3 - 1\right)}. \tag{4.50}$$

After a hydrogen concentration x_{core} has been added to the core, the overall relative volume change of the core is

$$\frac{\Delta V_{core}}{V_{core}} = -\frac{x_{core} V_H}{V_{Pd}} \left(1 - \frac{2\left(\rho^3 - 1\right)}{2 + \rho^3 \left(\frac{1+\nu}{1-2\nu}\right) + 2\left(\rho^3 - 1\right)} \right). \tag{4.51}$$

This relation takes a much simpler form, when expressed in terms of the parameter g defined in Eq. (4.42), as

$$g = 1 - \left(1 - \frac{2t}{L}\right)^3 = 1 - \frac{1}{\rho^3}. \tag{4.52}$$

Equation (4.51) reduces then simply to

$$\frac{\Delta V_{core}}{V_{core}} = \lambda x_{core} \left(1 - \gamma g\right). \tag{4.53}$$

with $\lambda = V_H / V_{Pd}$ and

$$\gamma = \frac{2}{3} \left(\frac{1 - 2\nu}{1 - \nu} \right). \tag{4.54}$$

The relation γ, including the Poission ratio ν, is well known from linear elasticity theory of a spherical particle [79]. For Pd, $\nu = 0.39$ and $\gamma = 0.24$. As discussed by Fukai [43] and Feenstra *et al.* [90], γ is not necessarily given by Eq. (4.54) and can in practice be as large as 1. For the model γ is considered as a free coupling parameter. The value in Eq. (4.54) corresponds to a perfect elastic coupling. A vanishing γ corresponds to a complete decoupling between *surface-shell* and *core*, and $\gamma = 1$ corresponds to an elastic enthalpy which depends essentially only on the total concentration x_{total}.

In a composite particle consisting of an inner core surrounded by a surface-shell, absorption of a hydrogen concentration x_{core} in the core and x_{shell} in the surface-shell leads to relative volume changes of the core and surface-shell that depends both on x_{core} and x_{shell}.

We denote these relative volume changes as

$$\frac{\Delta V_{core}}{V_{core}} \left(x_{core}, x_{shell} \right) \tag{4.55}$$

and

$$\frac{\Delta V_{shell}}{V_{shell}}\left(x_{core}, x_{shell}\right). \tag{4.56}$$

Hence, Eq. (4.53) corresponds to

$$\frac{\Delta V_{core}}{V_{core}}\left(x_{core}, x_{shell}=0\right) = \lambda x_{core}\left(1-\gamma g\right) \tag{4.57}$$

and the relative dilation of the surface-shell is

$$\frac{\Delta V_{shell}}{V_{shell}}\left(x_{core}, x_{shell}=0\right) = \lambda x_{core}\gamma\left(1-g\right). \tag{4.58}$$

Following the same approach as Pasquini *et al.* [107] it is straightforward to derive expressions for the case where hydrogen is only absorbed by the surface-shell while keeping the core free of hydrogen. Then, we have for the relative volume expansion of the core

$$\frac{\Delta V_{core}}{V_{core}}\left(x_{core}=0, x_{shell}\right) = \lambda x_{shell}\gamma g, \tag{4.59}$$

and for the surface-shell

$$\frac{\Delta V_{shell}}{V_{shell}}\left(x_{core}=0, x_{shell}\right) = \lambda x_{shell}\left(1-\gamma\left(1-g\right)\right). \tag{4.60}$$

In the general case with a hydrogen concentration $x_{core} > 0$ in the core and $x_{shell} > 0$ in the surface-shell we obtain

$$\frac{\Delta V_{core}}{V_{core}}\left(x_{core}, x_{shell}\right) = \lambda\left(x_{core} + \left(x_{shell} - x_{core}\right)\gamma g\right) \tag{4.61}$$

for the core, and

$$\frac{\Delta V_{shell}}{V_{shell}}\left(x_{core}, x_{shell}\right) = \lambda\left(x_{shell} + \left(x_{core} - x_{shell}\right)\gamma\left(1-g\right)\right) \tag{4.62}$$

for the surface-shell.

Exactly the same relations can be derived from the work of Rockenberger *et al.* [108]. The authors consider a situation where the core and

a surface-shell have different lattice spacings. As a result of epitaxial growth this lattice mismatch induces deformations of the core and the surface-shell governed by the shrink-fit condition stated in Eq. (A2) of Rockenberger *et al.* [108]. The isotropic strain inside the core of the same publication states (Eq. (A4))

$$\begin{aligned}\frac{\Delta V_{shrink-fit}}{V_{core}} =& 3\left(\frac{a_{shell}-a_{core}}{a}\right) \\ & \frac{2\delta\left(3+3\delta+\delta^2\right)}{3\left(1+\delta\right)^3}\left(\frac{1-2\nu}{1-\nu}\right)\end{aligned} \tag{4.63}$$

and the relative volume change in the surface-shell (Eqs. (A5) and (A6))

$$\begin{aligned}\frac{\Delta V_{shrink-fit}}{V_{shell}} =& \left(\frac{a_{shell}-a_{core}}{a}\right)\cdot\frac{2\left(1-2\nu\right)}{\left(1+\delta\right)^3} \\ & \left(\frac{-2\left(1-2\nu-3\left(1+\nu\right)\ln\left(1+\delta\right)\right)}{3\delta\left(1-\nu\right)\left(3+3\delta+\delta^2\right)}+\right. \\ & \left.\frac{-2\left(2-4\nu+3\left(1+\nu\right)\ln\left(1+\delta\right)\right)}{3\delta\left(1-\nu\right)\left(3+3\delta+\delta^2\right)}\right)\end{aligned} \tag{4.64}$$

$$\frac{\Delta V_{shrink-fit}}{V_{shell}} = -3\left(\frac{a_{shell}-a_{core}}{a}\right)\frac{2}{3\left(1+\delta\right)^3}\left(\frac{1-2\nu}{1-\nu}\right) \tag{4.65}$$

with δ being the ratio of surface-shell thickness t and the radius of the core $L/2-t$,

$$\delta = \frac{t}{L/2-t}. \tag{4.66}$$

These expressions take a much simpler form when expressed in terms of our volume fraction parameter g as

$$g = \frac{\delta}{\left(\delta+1\right)^3}\left(3+3\delta+\delta^2\right) \tag{4.67}$$

and

$$1 - g = \frac{1}{(\delta + 1)^3}. \tag{4.68}$$

Introducing these two relations together in Eqs. (4.63) and (4.65) gives

$$\frac{\Delta V_{shrink-fit}}{V_{core}} = 3\left(\frac{a_{shell} - a_{core}}{a}\right) g\gamma \tag{4.69}$$

and

$$\frac{\Delta V_{shrink-fit}}{V_{shell}} = -3\left(\frac{a_{shell} - a_{core}}{a}\right)(1 - g)\,\gamma. \tag{4.70}$$

To relate this to the situation where both core and surface-shell have different lattice spacings as a result of different hydrogen concentrations we need the following relations

$$\frac{\Delta V_{core}}{V_{core}}\left(x_{core}, x_{shell}\right) = \lambda x_{core} + \frac{\Delta V_{shrink-fit}}{V_{core}}, \tag{4.71}$$

$$\frac{\Delta V_{shell}}{V_{shell}}\left(x_{core}, x_{shell}\right) = \lambda x_{shell} + \frac{\Delta V_{shrink-fit}}{V_{shell}}, \tag{4.72}$$

and

$$3\frac{a_{shell} - a_{core}}{a} = \lambda\left(x_{shell} - x_{core}\right). \tag{4.73}$$

Introduction of Eqs. (4.69), (4.70) and (4.73) into Eqs. (4.71) and (4.72) leads exactly to the earlier derived Eqs. (4.61) and (4.62). These relations are mathematically simpler than those of Pasquini *et al.* [107] and Rockenberger *et al.* [108], since the volume fraction parameter g is restricted to $[0, 1]$ while $0 \leq \rho \leq \infty$ (see Eq. (4.48)) and $0 \leq \delta \leq \infty$ (see Eq. (4.66)) in their works. The relative volume change is, however, always finite.

The volume dependence of the enthalpy of hydride formation is [109]

$$\left.\frac{\partial \Delta H}{\partial \ln V}\right|_T = -BV_H, \tag{4.74}$$

with B as the bulk modulus and V_H, the partial molar volume of hydrogen in PdH_x (see Eq. (4.38)). Therefore, the volume strains in Eqs. (4.61) and (4.62) lead to

$$\begin{aligned}\Delta H_{core}\left(x_{core}, x_{shell}\right) =& \Delta H^{\infty}_{core} - \frac{BV_H^2}{V_{Pd}} x_{core} \\ & - \frac{BV_H^2}{V_{Pd}} \left(x_{shell} - x_{core}\right) \gamma g\end{aligned} \tag{4.75}$$

and

$$\begin{aligned}\Delta H_{shell}\left(x_{core}, x_{shell}\right) =& \Delta H^{\infty}_{shell} - \frac{BV_H^2}{V_{Pd}} x_{shell} \\ & - \frac{BV_H^2}{V_{Pd}} \left(x_{core} - x_{shell}\right) \gamma \left(1 - g\right).\end{aligned} \tag{4.76}$$

These two equations can be rewritten as

$$\begin{aligned}\Delta H_{core}\left(x_{core}, x_{shell}\right) =& \Delta H^{\infty}_{core} \\ & + \left(1 - \gamma g\right) H_{elast}\left(x_{core}, L\right) \\ & + \gamma g H_{elast}\left(x_{shell}, L\right)\end{aligned} \tag{4.77}$$

and

$$\begin{aligned}\Delta H_{shell}\left(x_{core}, x_{shell}\right) =& \Delta H^{\infty}_{shell} \\ & + \left(1 - \gamma g\right) H_{elast}\left(x_{shell}, L\right) \\ & + \gamma g H_{elast}\left(x_{core}, L\right),\end{aligned} \tag{4.78}$$

with $H_{elast}(x)$ defined as in Eq. (4.39).

4.4.4 *Pressure-Composition Isotherms*

Thermodynamic equilibrium between the surrounding hydrogen gas and H dissolved in the Pd lattice requires that the chemical potentials

in the core and surface-shell sites are equal to the one of gaseous hydrogen. Combining the results of the elastic theory with the conditions imposed in Section 4.4.2, we get

$$\begin{aligned}\frac{1}{2}\ln p = &\ln\left(\frac{x_{core}}{1-x_{core}}\right)\\ &+\frac{\Delta H_{core}\left(x_{core},x_{shell}\right)+H_{el}\left(x_{core}\right)+H_{surf}}{RT}\\ &-\frac{\Delta S\left(x_{core}\right)}{R}\end{aligned} \tag{4.79}$$

for H at core sites and

$$\begin{aligned}\frac{1}{2}\ln p = &\ln\left(\frac{x_{shell}}{1-x_{shell}}\right)\\ &+\frac{\Delta H_{shell}\left(x_{core},x_{shell}\right)+H_{el}\left(x_{shell}\right)+H_{surf}}{RT}\\ &-\frac{\Delta S\left(x_{shell}\right)}{R}\end{aligned} \tag{4.80}$$

at surface-shell sites. All enthalpies and entropies are given per mol H. The term H_{surf} accounts for the surface tension contribution to the enthalpy that depends only on the size L. To proceed, one needs to specify the variables determining H_{el} and ΔS.

- In a **non-local** model, H_{el} and ΔS depend only on the total H concentration x_{tot}

  $$x_{tot} = \left(1-g\right)x_{core} + g x_{shell} \tag{4.81}$$

  and Eqs. (4.79) and (4.80) together with Eqs. (4.77) and (4.78) lead to

  $$N_{core}\left(x_{core}\right) + \frac{\Delta H^{\infty}_{core}}{RT} = N_{shell}\left(x_{shell}\right) + \frac{\Delta H^{\infty}_{shell}}{RT} \tag{4.82}$$

  with

  $$N_j\left(x_j\right) = \ln\left(\frac{x_j}{1-x_j}\right) + \frac{\left(1-\gamma\right)H_{elast}\left(x_j\right)}{RT} \tag{4.83}$$

  and $j = core$ or $shell$.

- In a **local** model, H_{el} and ΔS depend on the local concentrations x_{shell} or x_{core}. The implicit relation in Eq. (4.82) is then replaced by

$$M_{core}\left(x_{core}\right) + \frac{\Delta H^{\infty}_{core}}{RT} = M_{shell}\left(x_{shell}\right) + \frac{\Delta H^{\infty}_{shell}}{RT} \quad (4.84)$$

with

$$M_j\left(x_j\right) = \ln\left(\frac{x_j}{1-x_j}\right) + \frac{\left(1-\gamma\right) H_{elast}\left(x_j\right) + H_{el}\left(x_j\right)}{RT} - \frac{\Delta S\left(x_j\right)}{R} \quad (4.85)$$

and $j = core$ or $shell$.

In both, the local and non-local cases, one obtains an implicit relation between the two concentrations x_{shell} and x_{core} which can be solved numerically.

4.4.5 *Local versus Non-Local Model*

All later results presented in Section 4.5 and all following sections are obtained with the local model (see Eqs. (4.84) and (4.85)). This is reasonable, as it is unlikely that the electronic term in Eqs. (4.79) and (4.80) depends on the total hydrogen concentration in a system where two spatially well separated regions (i.e., core and surface-shell) are present. It is important to note that the electronic term depends on the filling of the d-band. A difference in the work functions of separated regions can also lead to an electron transfer that influences the Fermi energy locally in addition to the band filling associated with hydrogen loading. This is in clear contrast with models for disordered alloys [110] where interstitial sites with different local chemical composition coexist within sub-nanometer distances. In such cases

the constancy of the Fermi energy together with a spatially averaged work function implies that the electronic repulsive H-H interaction would depend, essentially, on the average hydrogen concentration, leading to a non-local configuration.

4.5 APPLICATIONS OF THE NANOPARTICLE MEAN-FIELD MODEL

To evaluate the input parameters of the mean-field model described in the preceding sections (The enthalpy of solution of the surface-shell $\Delta H^{\infty}_{shell}$, the coupling parameter γ, the surface-shell thickness $t_{„}$ the surface tension energy u and the effective clamping thickness w from the adjusted elastic H-H interaction enthalpy), we use

- The pressure-composition isotherms of Bardhan *et al.* [69]
- The corresponding critical temperatures T_c, together with those of Wadell [73] (see Fig. 4.11)
- The pressure-composition isotherms of Wadell [73]
- The absorption plateau pressures of Baldi *et al.* [70]

After a fitting procedure we find that all the essential features of these experimental data are well reproduced with the values in Eq. (4.86).

$$\begin{aligned} \Delta H^{\infty}_{shell} &= -18\,000\,\mathrm{J/molH} \\ \gamma &= 0.5 \\ t &= 1\,\mathrm{nm} \\ u &= 10\,000\,\mathrm{nm} \times \mathrm{J/molH} \\ w &= 1.6\,\mathrm{nm} \end{aligned} \tag{4.86}$$

All these values can be related to known results about paladium:

- A surface-shell enthalpy of solution (i.e. $-18\,000\,\mathrm{nm} \times \mathrm{J/molH}$) that is more negative than the core value (given by Eq. (4.37)) is consistent with the values obtained by Dong *et al.* [103] (ΔH^{∞}_{subs} $= -18\,330\,\mathrm{nm} \times \mathrm{J/molH}$ for Pd{111}; $-17\,370\,\mathrm{nm} \times \mathrm{J/molH}$ for Pd{100} and $-19\,300\,\mathrm{J/molH}$ for Pd{110} surfaces).

- The coupling parameter $\gamma = 0.5$ falls within the interval $0.24 < \gamma < 1$ as mentioned in Section 4.4.3 [43].

- The surface-shell thickness $t = 1\,\mathrm{nm}$ is intermediate between the lattice spacing of Pd (0.389 nm) and 4 nm proposed by Wilde *et al.* [111] on basis of their depth-resolved measurements of subsurface H on Pd{100}. However, it is important to point out that $t = 4\,\mathrm{nm}$ is incompatible with the isotherms in Fig. 4.20(a) and (d) and Figs. 4.16 and 4.17. For the smaller cubes, it would lead to fully shell dominated isotherms and therefore, a very different result that is not visible in the experimental data.

- For a particle of size L the surface enthalpy is [99]

$$H_{surf} = \frac{u}{L} = 4\sigma\frac{V_H}{L}. \tag{4.87}$$

  With a H partial molar volume $V_H \approx 1.5 \times 10^{-6}\,\mathrm{m^3/molH}$ and a typical surface tension [112, 113] of $\sigma \approx 2\,\mathrm{J/m^2}$ we obtain $H_{surf} = 12,000/L$ with L expressed in nm. This would correspond to $u = 12\,000\,\mathrm{J} \times \mathrm{nm/molH}$, which is comparable to the fitted value $u = 10\,000\,\mathrm{J} \times \mathrm{nm/molH}$.

- The small effective clamping thickness $w = 1.6\,\mathrm{nm}$ implies that even in the smallest nanocubes investigated by Bardthan *et al.* and Baldi *et al.* [69, 70], i.e., 14 nm, the magnitude of the attractive H-H interaction is lowered by only $\sim 11\,\%$.

The pressure composition isotherms, calculated with these parameters for the four nanocube sizes of Bardhan *et al.* [69], are shown in Fig. 4.16. As the hydrogen concentrations are not accessible in the experiment, one can only compare the shape of the isotherms as well as the pressure values. In fact, the absorption *plateau* pressures are

close to the calculated upper spinodal pressure p_{us} while the desorption *plateau* pressures are close to the incoherent Maxwell pressure p_M (see Fig. 4.1).

The size dependence of absorption and desorption plateau pressures at 246 K are shown in Fig. 4.17. The fit to the measured absorption pressures is excellent. As expected, the measured desorption plateaus are much higher than the calculated ones. This is a result of the experimental difficulties with desorption measurements discussed by Baldi *et al.* [70].

The calculated hysteresis disappears for nanocubes of $\sim$ 8 nm. Interestingly, the calculated pressures p_M obtained with the Maxwell construction are almost size independent and close to the lowest measured desorption pressures. This can be regarded as further evidence for the true desorption pressures being close to p_M as is the case for all isotherms in Fig. 4.16. For all the nanocubes the model demonstrates that the ad hoc assumption in the model presented by Baldi *et al.* [70], i.e., that the surface-shell hydrogen concentration is constant and equal to 0.51 is reasonable for $0.05 < x_{core} < 0.5$ for all their nanocube sizes between 13 nm and 29 nm. This is explicitly shown in Fig. 4.18 for 13 nm, 21 nm and 29 nm nanocubes.

The assumption of a constant x_{shell} is, however, not well justified. Especially, since the applied H_2 gas pressure is varying by several orders of magnitude in their experiment. Besides, in a 15 nm Pd nanocube, $x_{shell} = 0.51$ in a surface-shell of thickness 1 nm would imply that $\approx$ 18 % of the hydrogen sits in this surface-shell.

As the isotherms in Fig. 4.20 do not exhibit the presence of this large amounts of hydrogen, one must conclude that their experimental method, EELS, with a beam diameter of $\approx$ 7 nm does not sense H in the surface-shell region for nanocubes with $L > 13$ nm. Although, Baldi *et al.* [70] obtained a nice agreement between their absorption plateau pressures and the calculated upper spinodal pressures p_{us}, their model predicts critical temperatures that are much higher than those determined from the data of Bardhan *et al.* [69]. This is explicitly shown in Fig. 4.19(b) for a 14 nm nanocube. The critical isotherm would be

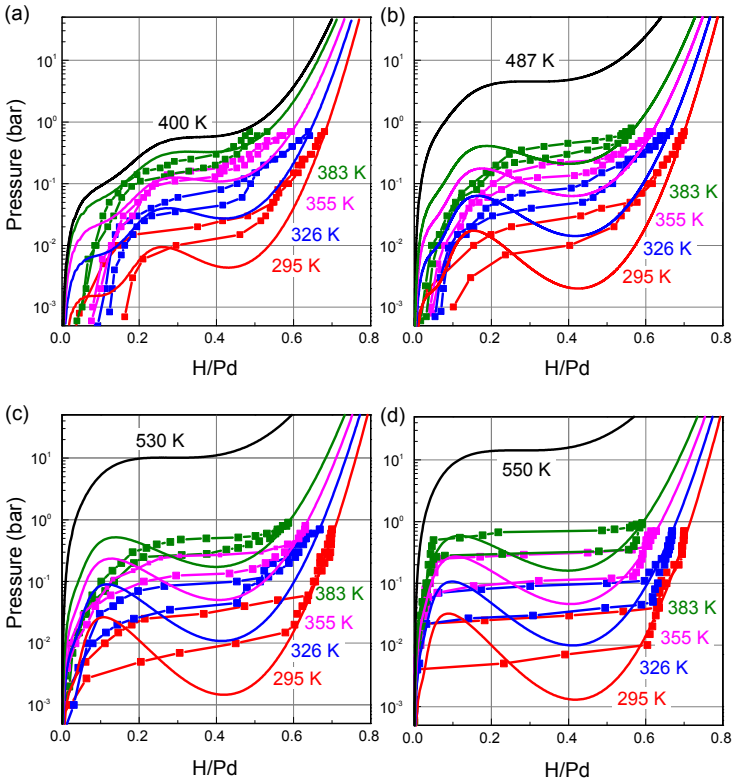

FIGURE 4.16. Pressure composition isotherms for 14 nm, 32 nm, 65 nm and 110 nm Pd nanocubes in panels (a), (b), (c), and (d), respectively. They are calculated with the parameters from Eq. (4.86) (coloured lines). that are also used for Fig. 4.20a to d. As the concentration for the isotherms (squares) could not be measured experimentally, Bardhan *et al.* [69] normalized it arbitrarily to unity. For a better comparison, the relative concentrations of the loading and unloading data of Bardhan *et al.* are rescaled by a constant factor, so that the endpoint of every experimental loading curve coincides with the concentration H/Pd obtained by the model at the same pressure. The black lines correspond to the models critical isotherms at 400 K, 487 K, 530 K and 550 K (see Fig. 4.11a).

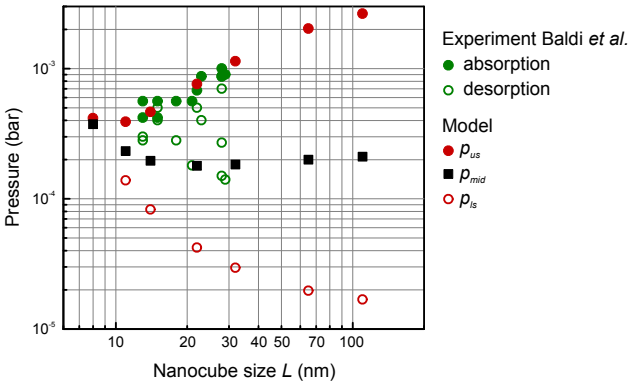

FIGURE 4.17. Size dependence of absorption and desorption plateau pressures at 246 K. Experimental absorption (green dots) and desorption (open green circles) data are taken from Baldi *et al.* [70]. The pressures are calculated using the parameters from Eq. (4.86), with the upper spinodal pressures (red dots), lower spinodal pressures (red circles) and plateau pressures obtained by means of the Maxwell construction (black squares).

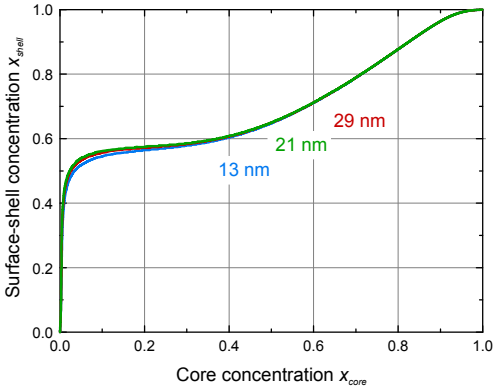

FIGURE 4.18. Surface-shell hydrogen concentration versus hydrogen concentration in the core of 13 nm, 21 nm and 29 nm nanocubes calculated with the parameters from Eq. (4.86). The size dependence is small and the three curves overlap at almost all concentrations.

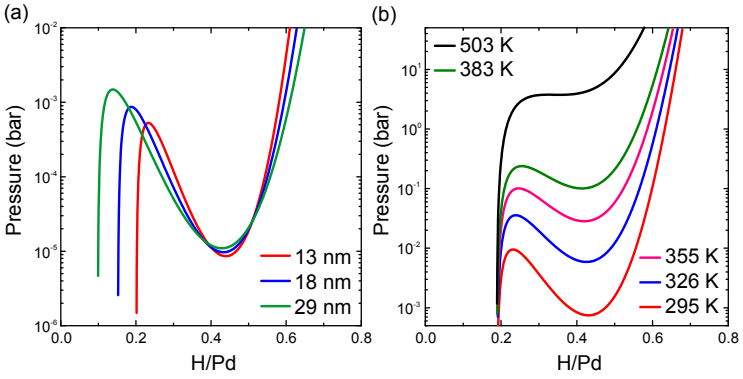

FIGURE 4.19. (a), Pressure-composition isotherms at 246 K according to the Baldi *et al.* model which is based only on Eq. (4.79) with $g = 0.24$ and $x_{shell} = 0.51$ in Eq. (4.81). In contrast with Fig. 4.20(c), the x-axis represents the total hydrogen concentration x_{tot} defined in Eq. (4.81). (b), Pressure composition isotherms of a 14 nm Pd nanocube as predicted by the Baldi *et al.* model using the same parameters as in (a).

at 503 K instead of $T_c \approx 441$ K, as found in Section 4.3.5. A common feature of the calculated isotherms in Fig. 4.20(a) to (c) and Fig. 4.16 is that the absorption plateau pressures are close to the upper spinodal pressure p_{us} while the desorption pressures are intermediate between the incoherent (i.e. Maxwell pressure p_M) and coherent desorption plateau pressures p_{ls}.

To conclude, Pd nanocubes of intermediate size ($\sim$ 13 to $\sim$ 110 nm) interact with hydrogen in a hybrid way.

- During H absorption the system remains in a supersaturated single phase up to a pressure close to the upper spinodal pressure is reached, after which it transforms coherently [80, 81] (i.e. without formation of dislocations) to the concentrated β-PdH$_x$ phase.

  Hydrogen absorption can thus be described by the theory of Schwarz and Khachaturyan [81].

- Hydrogen desorption, occurs as if some of the coherency stresses built up during absorption have been released.

Several hydrogen absorption-desorption scenarios are described in more detail in Section 4.6. In particular, they show that if during absorption, surface-shell-core coherency is maintained and no misfit dislocations are generated in the core, H desorption remains coherent (see Fig. 4.25) and the hysteresis is close to a full spinodal hysteresis.

For particles smaller than 50 nm no dislocations are generated in the core and a hysteresis smaller than the full spinodal hysteresis is realized, if the surface-shell-core elastic coupling is modified during absorption (see Fig. 4.26). Such a scenario is consistent with the prevervation crystallinity in the core of the nanocubes after several ab- and desorption cycles, investigated by Baldi *et al.* [70]. Especially, near the corners and edges of the nanocubes, we expect a stress release mechanism similar to that observed in epitaxial YH_x films [114, 115].

One possible modification might be that the larger lattice spacing of the hydrogen loaded surface-shell (compared to that in the core) is accommodated by allowing the surface-shell to generate protrusions along the edges of the nanocube in a way similar to the reversible edge generation observed in the already mentioned YH_x films [114, 115]. This is more likely to happen at the surface of a cube than of a sphere as the cube edges are clearly structurally different from the faces. Considering symmetry, such a degree of freedom does not exist on a sphere. It is important to note that these conclusions break down as soon as dislocations can be generated in the core of the nanocube. According to an estimate of Baldi *et al.* [70] this is expected to occur in nanocubes larger than $\sim$ 35 nm. However, this estimate is probably too low and the value is most likely temperature dependent, as we discuss in Section 4.6.3. A nice confirmation of the existence of a critical size follows from Fig. 4.22 in which the recent single nanocube data of Syrenova *et al.* [74] at 333 K are compared to the hysteresis calculated with our mean-field model.

Additionally, the model is consistent with the data of Wadell *et al.* [72] for very small nanoparticles. The isotherms calculated for

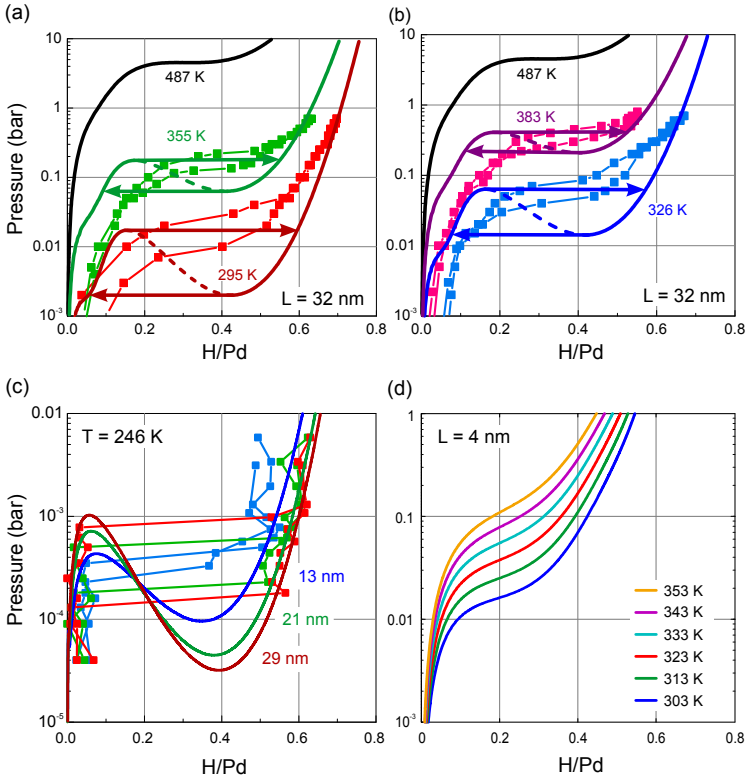

FIGURE 4.20. Model and experimental P-C isotherms of various Pd samples. (a) and (b), Experimental isotherms of Bardhan *et al.* [69] for a 32 nm Pd nanocubes compared to the mean-field model. The x-axes is scaled so that the endpoint of every experimental loading curve coincides with one obtained by the model. The black lines are the calculated critical isotherm at 487 K. (c), Three representative isotherms of Baldi *et al.* [70] compared to the calculated isotherms. For this the EELS energy shifts are converted to x_{core} as EELS measures predominantly the core of the Pd nanocube. (d), Pressure composition isotherms calculated for a 4 nm Pd nanocube for 303 K and 353 K. All calculations are performed wit the values from Eq. (4.86).

4 nm Pd nanoparticles at the temperatures investigated by Wadell *et al.* do not exhibit plateaus as the calculated critical temperature is

below the measurement temperature of 260 K (see Fig. 4.11(b)). This explains why the enthalpies and entropies measured on 2.7 nm and 5.3 nm nanocubes are found to be essentially the same for hydrogen absorption and desorption (see Fig. 4 in the publication of Wadell *et al.* [72]).

4.5.1 *Modeling Metal-Organic Framework coated Pd Nanocubes*

Electron transfer was recently invoked by Li *et al.* [71] to explain the enhanced hydrogen concentration in their *HKUST-1* coated 10 nm Pd nanocubes. Following this suggestion, one can calculate the pressure composition isotherms of a 10 nm nanocube. To compensate for the metal-organic framework (MOF) we use a larger ζ-parameter in the lattice gas term of the model (see Eq. (4.40)) Instead of $\zeta = 1.0648$ used for bulk Pd and for all other nanoparticle calculations presented in this thesis, we assume $\zeta = 2.1$. The higher value of the parameter ζ can be associated with a lowering of the Fermi energy in the core of the Pd nanocube. This would happen when electrons are extracted from Pd by the MOF coating.

This follows directly from the results of Feenstra *et al.* [90] on bulk PdH_x where it is shown that the repulsive electronic H-H interaction is related to the Fermi energy E_F

$$E_F(x) - E_F(0) = \frac{1}{\alpha_F} H_{elect}(x) \tag{4.88}$$

with the Fermi energy E_F given in eV and H_{elect} in J/mol(H). The parameter $\zeta = 29.62\,\mathrm{kJ/(mol\,(H)\ eV)}$ is the same for all transition metal hydrides [109]. A lowering of the Fermi energy by, for example, the MOF layer, implies that more hydrogen atoms need to be added to fill the d-band of palladium.

With a surface-shell site enthalpy of −14 000 J/mol(H) the calculated p-c isotherms reproduce the observed influence of the MOF layer on hydrogen absorption (see Fig. 4.21). As the reported value [71] H/Pd = 0.87 determined volumetrically at 1 bar is quite different from

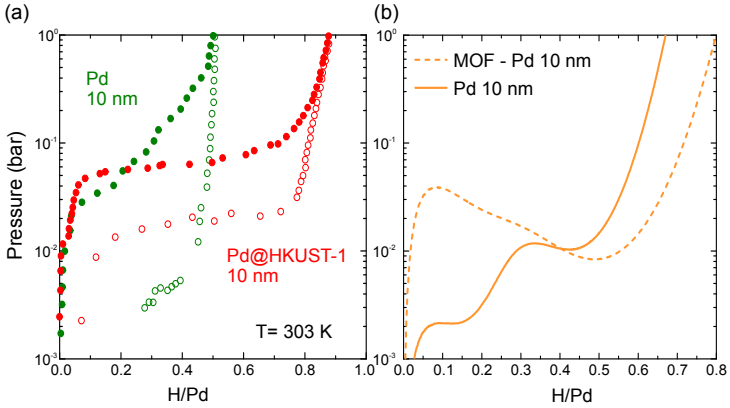

FIGURE 4.21. (a), Measured and (b) calculated pressure composition isotherms at 300 K for a 10 nm Pd nanocube (green dots and orange solid line, see also Fig. 4.24) and a 10 nm *HKUST-1* coated Pd nanocube (red dots and orange dashed line). For the uncoated Pd nanocube the parameters are taken from Eq. (4.86). For the MOF coated nanocube the enthalpy of solution of the surface-shell sites is −14 000 J/mol(H) and $\zeta = 2.1$ in Eq. (4.40). This leads to an increased hydrogen capacity.

H/Pd = 0.71 corresponding to the X-ray lattice spacing data an intermediate value, H/Pd = 0.8 at 1 bar is taken in the model pressure-composition isotherms. The MOF coating is probably the origin of the increase in the enthalpy of hydrogen solution at Pd surface-shell sites. The fundamental question that arises is, through which mechanism electrons can be extracted from the nanocube by the MOF coating.

4.5.2 *Comparison to the Syrenova et al. Data for Single Pd Nanoparticles*

In Fig. 4.7 the data of Wadell [73] and Syrenova *et al.* [74] are plotted by associating a critical temperature according to the empirical expression $T_c = 566 - 2831/L$ (see Eq. (4.35)). This is necessary, because on the one hand, no accurate values for the critical temperature T_c

could be derived from Wadell's data. On the other hand, Syrenova *et al.* measured absorption isotherms of 17 nm to 65 nm nanocubes at temperatures between 303 K and 333 K while desorption isotherms were only measured at 333 K.

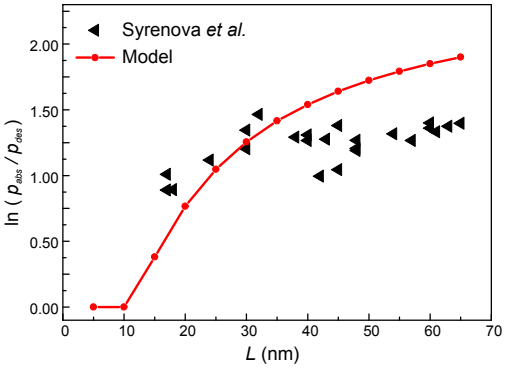

FIGURE 4.22. Comparison of experimental single particle hysteresis of Syrenove *et al.* [74] (black triangles) and hysteresis calculated with the mean-field model using the parameters in Eq. (4.86). The temperature is 333 K.

We can, however, compare their hysteresis data directly with the predictions of our mean-field model without need for T_c values. As depicted in Fig. 4.22 the measured hysteresis for nanocubes smaller than ≈ 35 nm is essentially equal to full-spinodal hysteresis while larger nanocubes have gradually smaller hystereses.

4.5.3 *Robustness of the Nanoparticle Model to Light-induced Temperature Variations*

Optical and EELS techniques used in recent works to measure hydrogen absorption in nanoparticles can induce local heating of the particles. Baldi *et el.* [70] discuss in great detail the impact of electron beam heating on their measurements and conclude that their desorption data are upper bounds of the actual desorption pressures. The

Wadell *et al.* directly compared isotherms measured by localized surface plasmon resonance (LSPR) sensing using light, with isotherms that ware measured gravimetrically by Quartz Crystal Microbalance with Dissipation Monitoring (QCM-D) and no light. They conclude that the effect of heating by light is negligible, since both methods lead to the same results [116]. This is also confirmed theoretically by Zhdanov *et al.* [117]. Since, Wadell *et al.* [72, 73] and Syrenova *et al.* [74] used the same experimental setup heating effects can be excluded in all their data.

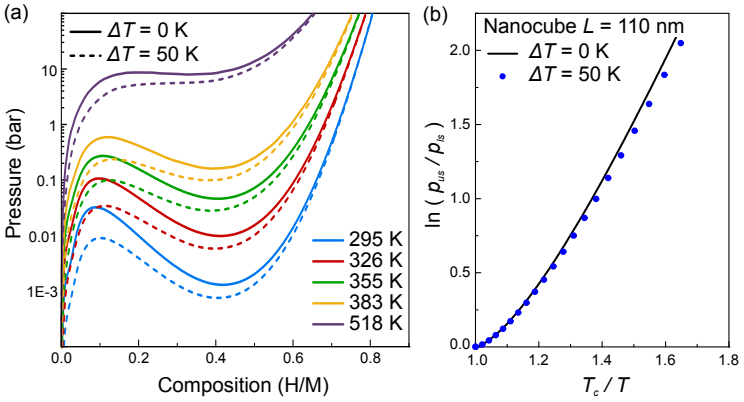

FIGURE 4.23. (a), Pressure-composition isotherms calculated with the mean-field model described in Section 4.4.2 for a 110 nm nanocube with a local heating ($\Delta T = 50$ K, dashed lines) and without local heating ($\Delta T = 0$ K, solid lines). The local heating decreases the critical temperature by 38 K. (b), Scaling-laws with and without local heating. All calculations are done with the parameters from Eq. (4.86).

For the Bardhan *et al.* [69] data the situation is less clear. The 5 mW laser beam focussed to a 2.5 µm spot can, in principle, heat up the nanocubes. A simple estimate using Eq. (2) in a publication by Baffou and Quidant [118] and the scattering cross-section, calculated by extended Mie theory for a spherical plasmonic particle (Eq. (5.19) in the book of Maier [32]) leads to an increase of about 50 K in a 110 nm nanoparticle. This would roughly decrease the critical temperature by 10 %. However, the T_c values of Bardhan *et al.* [69] are comparable to those

of Wadell [73]. This indicates that heating effects are not that serious. For the smaller nanocubes, the heating effects are small anyway. For a 30 nm particle the heating effect is less than 2 K.

Even in cases of lager structures, where local heating can be substantial, it is straightforward to demonstrate that the presented scaling law analysis and isotherm predictions still hold true. To prove the robustness of the scaling law towards heating effects, we consider an extreme case where a local heating effect (e.g. produced by a focused laser beam as in Bardhan *et al.*'s experiment) increases the temperature of a 110 nm nanoparticle by 50 K, while keeping the surrounding gas temperature constant. The calculated pressure-composition isotherms with and without local heating are depicted in Fig. 4.23(a). From these isotherms one calculates the full spinodal hysteresis and compares it to the one without local heating. Quite remarkably, the two curves are very close to each other. The origin of the robustness of the scaling-law is primarily that it depends on the ratio T_c/T which is only weakly influenced by a temperature offset, since the critical temperature rises in a similar fashion as the local temperature.

4.5.4 *Pressure-Composition Isotherms of very small Pd Clusters*

In 10 nm Pd nanocubes, the volume fraction g of surface-shell sites is as high aso.488. This implies that core and surface-shell contributions are almost equal.

In Fig. 4.24, the calculated isotherms clearly exhibit a double structure. For the 4 nm nanocubes the isotherms are dominated by the contribution of the surface-shell, while for 14 nm nanocubes the core contribution is more important. This switch from a surface-shell-dominated regime to a core-dominated regime at about 9.7 nm is responsible for the kink in the size dependence of the highest critical temperature in Fig. 4.11.

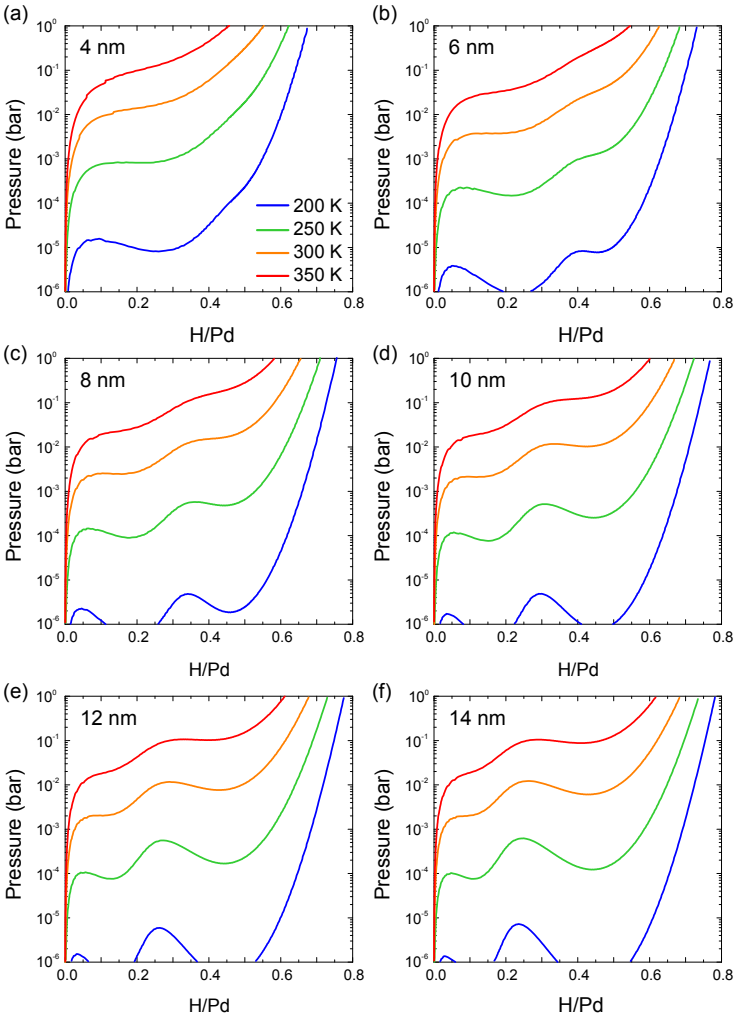

FIGURE 4.24. Pressure-composition isotherms at 200 K (blue), 250 K (green), 300 K (orange), and 350 K (red curves) for 4 nm (a) to 14 nm (f) nanocubes calculated with the parameters from Eq. (4.86). The existence of two critical temperatures in Fig. 4.11 is directly connected to the wavy shape of the isotherms.

4.6 SCENARIOS FOR HYDROGEN ABSORPTION AND DESORPTION IN PD NANOPARTICLES

The asymmetry between the absorption and desorption pressures in Fig. 4.5 together with the fact that most of the data points in hysteresis plot of Fig. 4.7 lay between the full- and 45 %-spinodal hysteresis indicate that, in nanocubes, the hydrogen absorption process can be different from the desorption process. Deviations from the full spinodal scaling curve are related to the generation of incoherency between core and surface-shell and/or the generation of misfit dislocations in the core of the nanoparticles. In this section we want to have a closer look on these two aspects and discuss possible scenarios for hydrogen absorption-desorption cycles.

4.6.1 ***Scenario I**: Fully coherent absorption-desorption cycle*

A fully coherent cycle in which the core-to-surface-shell elastic coupling remains intact and no misfit dislocations are generated in the core, can directly be calculated by means of our mean-field model described in Section 4.3.1. The concentration difference $x_{core} - x_{shell}$ is a measure of strains between surface-shell and core. Therefore, the hydrogen pressure dependence of the core and surface-shell concentrations, as well as the total concentration and the concentration differences are very interesting (see Fig. 4.25 for a nanocube of 32 nm at 295 K).

During hydrogen absorption starting at point ***A*** in Fig. 4.25(c) the concentration difference $x_{core} - x_{shell}$ reaches a maximum value close to 0.47 at the point ***C***. However, it remains below 0.25 during the entire desorption process. The maximum concentration difference is only very weakly dependent on the nanocube size. For the PdH_x system $x_{surf} - x_{core} = 0.47$ corresponds to a lattice mismatch of 2.8 %. This value is substantially smaller than the critical mismatch of about 5 % stated by Fan *et al.* [119] and Jin*et al.* [120]. They observed that epitaxial growth of heterogeneous core-surface-shell nanocrystals can

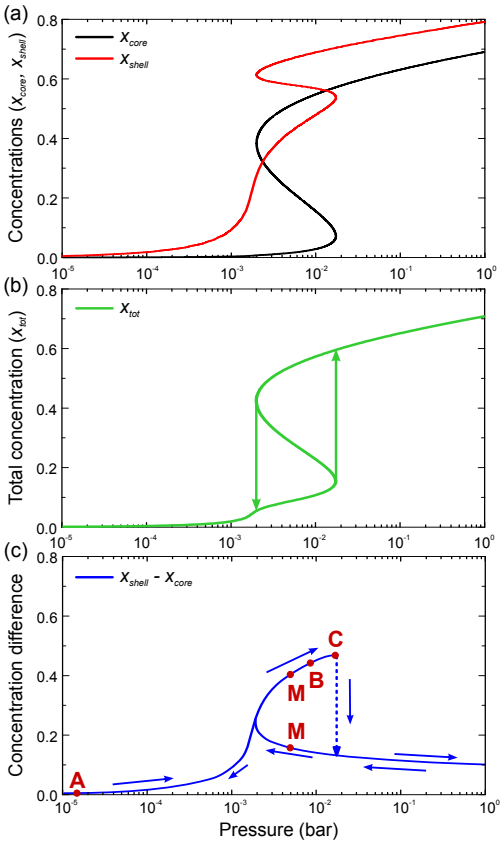

FIGURE 4.25. (a), Pressure dependence at 295 K of the core (black), and surface-shell (red) hydrogen concentrations in a 32 nm nanocube calculated with the parameters of Eq. (4.86). (b), Total H concentration in the nanocube (green curve). The green arrows indicate the upper (p_{us}) and lower (p_{ls}) spinodal pressures. (c), The concentration difference (blue curve). The blue arrows indicate the path followed in a fully coherent absorption-desorption cycle during which the core-surface-shell coupling remains intact and no misfit dislocations are generated (see Section 4.6.1). The red points are: **A**, start of absorption, **C**, maximum concentration difference, **B**, maximum difference, in incoherent absorption-desorption cycle, and **M** the values coresponding to the Maxwell plateaus.

occur when the lattice mismatch between core and surface-shell is smaller than about 5 %. On the basis of this argument one expects the hysteresis to be comparable to the full spinodal hysteresis, as core-surface-shell coherency is preserved during the entire cycle.

4.6.2 ***Scenario II***: *Incoherent absorption-desorption cycle without misfit dislocation generation in the core*

Another scenario can occur if during hydrogen absorption a certain critical value of strains is reached (at point ***B*** in Fig. 4.25(c). As an extreme case, we assume that core and surface-shell are then fully decoupled ($\gamma = 0$) and each of the subsystems continues to absorb hydrogen as if it was isolated. At high pressures (for the Pd system considered here, this occurs already at pressures above 1 bar), the hydrogen concentration in the surface-shell is only slightly larger than in the core. When the pressure is lowered, both core and surface-shell desorb hydrogen individually until they, again, naturally fit together at zero pressure.

The total concentration $x_{tot}^{incoherent}$ during desorption is described by the violet curve in Fig. 4.26. The surface-shell-core decoupling leads to a desorption plateau that is higher than the lower spinodal pressure. The net effect is a 20 % reduction of the hysteresis. This is consistent with the data of Wadell [73], Syrenova *et al.* [74] and Yamauchi *et al.* [68] in Fig. 4.7.

4.6.3 ***Scenario III***: *Absorption-desorption cycle with misfit dislocation generation in the core*

In Section 4.6.1 we considered a situation where point ***C*** in Fig. 4.25(c) has been reached without surface-shell-core decoupling, i.e. a situation in which the surface-shell-core coherency remains intact ($\gamma = 0.5$). As soon as the upper spinodal pressure is exceeded the nanoparticle absorbs spontaneously more hydrogen and forms a hydride

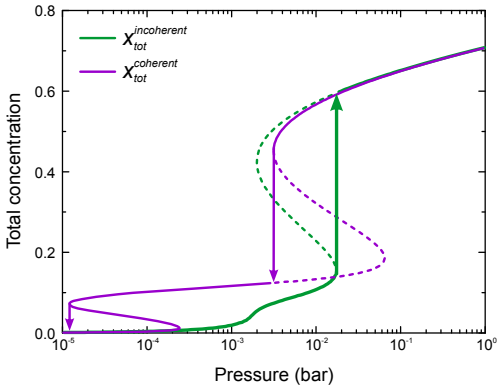

FIGURE 4.26. Simulation for a 32 nm Pd nanocube at 295 K of a scenario with coherent core-surface-shell hydrogen loading ($\gamma = 0.5$) and incoherent core-surface-shell unloading ($\gamma = 0.5$) but no misfit dislocation generation (see Section 4.6.2). The pressure dependence of the total concentration during coherent loading (green curve), $x_{tot}^{coherent}$, is calculated with the mean-field model using the parameters from Eq. (4.86). During desorption (magenta curve) all parameters are kept the same except for the elastic core-surface-shell parameter γ that is set equal to 0. The absorption curve is the same as in Fig. 4.25.

layer. Consequantly the sample consists out of three layers until the whole particles is filled with hydrogen. Outermost, th surface-shell layer of thickness t, then a β-hydride layer of thickness Δ and finally an inner sphere of essentially pure Pd. As explained by Schwarz and Khachaturyan [81], during this process, there is no equilibrium coexistence between the hydride layer and the inner Pd sphere.

There are, however, large coherency strains. To circumvent the corresponding large elastic energy, misfit dislocations are generated. Then the plateau pressure is effectively reduced to a value close to the Maxwell plateau that corresponds to points ***M*** in Fig. 4.25(c) and to the vertical dashed line in Fig. 4.27. The concentrations of the two coexisting phases are x_{α}^{core} and x_{β}^{core}.

According to Baldi *et al.* [70], the overall energy associated with the generation of a misfit dislocation (their Eqs. (2)-(5) of the supplementary information), is given by

$$\begin{aligned}\Delta E^{total} &= \Delta W^{loop} + \Delta W^{strain} \\ &= \frac{Gb^3}{2(1-\nu)}\left[l \cdot \ln(d) - d + 1\right. \\ &\left. + \frac{8}{9}(1+\nu)\, e^T (l-d)^2 \left(1 - \left(1 - \frac{d}{l}\right)^3\right)\right]\end{aligned} \tag{4.89}$$

with G, the shear modulus of Pd,

$$e^T = \frac{V_{Pd} - V_{PdH_x}}{V_{PdH_x}} \tag{4.90}$$

the fractional change in volume between PdH_x and Pd,

$$d = \frac{\Delta}{b} \tag{4.91}$$

and

$$l = \frac{L}{2b} \tag{4.92}$$

where b is the Burgers vector of the misfit dislocation.

It is favorable to generate dislocations when ΔE^{total} is negative. By taking $e^T = -0.1062$, which corresponds to the fractional volume change between α- and β-phase in bulk Pd at room temperature, Baldi *et al.* found that dislocations are not energetically favorable for particles smaller than 35 nm.

In fact, their upper size limit is likely to be too small since they assumed that $\Delta x = x_\beta^{core} - x_\alpha^{core} = 0.6$. From the calculated x_{core} (black curve in Fig. 4.27b) one can estimate the concentrations x_α^{core} and x_β^{core} of the α-PdH_x and β-PdH_x phases that would form in the core during an incoherent phase transition where a shell-structure of thickness Δ made of β-PdH_x phase is surrounding the sphere of α-PdH_x.

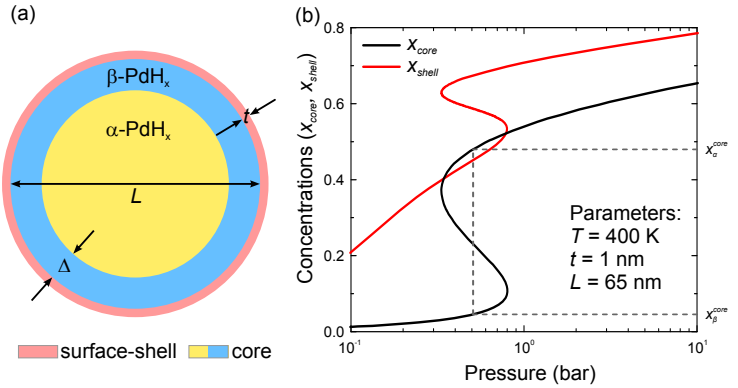

FIGURE 4.27. Pressure dependence of the calculated surface-shell and core concentrations. (a), Schematic hydrogen distribution during the spontaneous hydrogen absorption, which occurs when the applied hydrogen pressure exceeds the upper spinodal pressure. The core consists of a hydride layer of thickness Δ (blue shaded area) surrounding a sphere of essentially pure Pd (yellow area). The whole core (of diameter $(L - 2t)$) is surrounded by a thin surface-shell of thickness t. (b), Zoom into the pressure dependence of the calculated surface-shell and core concentrations for a 65 nm cube at 400 K. The surface-shell of thickness $t = 1$ nm is elastically coupled with the β-hydride shell of thickness Δ (inside the core). As the core concentration exhibits an *S-shape*, it can separate in an α- and β-phase. The difference $x_\beta^{core} - x_\alpha^{core}$ is used in the evaluation of the lattice mismatch parameter e^T of Baldi *et al.* [70] (see Eq. (4.90).

These values can then be used to calculate the lattice mismatch factor e^T and consequently the normalised total energy change associated with the generation of a misfit dislocation ΔE^{total}. For a 32 nm nanocube we find at 295 K, $\Delta x = 0.496$ and at 350 K, $\Delta x = 0.447$. For a 14 nm cube the temperature dependence is stronger and we find at 295 K, $\Delta x = 0.386$ and at 350 K, $\Delta x = 0.27$. These values are substantially smaller than the 0.6 assumed by Baldi *et al.* [70]. The normalized energy difference for 14 nm, 32 nm, 45 nm, 65 nm and 110 nm nanocubes at 295 K and 350 K is shown in Fig. 4.28. The conclusion is that 14 nm and 32 nm nanocubes should remain coherent during an entire absorption-desorption cycle for temperatures between 295 K and

350 K. This is, not the case for the 65 nm and 110 nm nanocubes. The 45 nm nanocube is somewhere in between and can be seen as the limiting case.

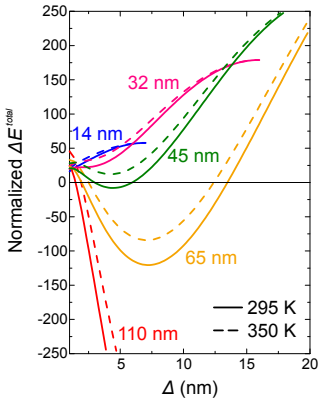

FIGURE 4.28. Normalized total energy change ΔE^{total} associated with the generation of misfit dislocations at 295 K and 350 K for various nanocube sizes. The β-PdH_x shell thickness Δ is necessarily smaller than the full core of diameter $(L - 2t)$.

It is insightful to explore the temperature dependence of ΔE^{total} for a given nanocube size (or to be exact a spherical nanoparticle diameter). As an example we take a particle with $L = 65$ nm (see Fig. 4.29). Below approximately 425 K we find that it is energetically favorable to generate a dislocation loop. However, above this temperature the transition should remain coherent. This suggests that above 425 K the hysteresis is large and equal to the full spinodal hysteresis while below 425 K the nucleation of a dislocation introduces incoherence and, consequently, stress release accompanied by a smaller hysteresis.

This explains the trend observed in the scaling-law plot in Fig. 4.7. At temperatures closer to the critical temperature, i.e. when T_c/T approaches 1, the hysteresis tends towards the full spinodal hysteresis. This tendency is even seen for bulk Pd where the deviation from a full spinodal hysteresis close to T_c decreases drastically with decreasing

temperature (see Fig. 4.10) and is also consistent with the suggestions by Flanagan and Oates [121].

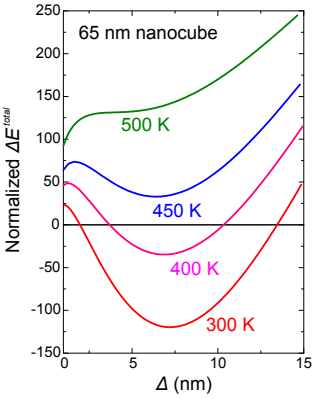

FIGURE 4.29. Temperature dependence of the total energy change ΔE^{total} associated with the presence of a misfit dislocation loop for a 65 nm nanoparticle obtained from Eq. (4.89) and concentration calculations similar to those presented in Fig. 4.26.

4.7 CONCLUSIONS

We conclude, the model described in our work is able to reproduce all the essential features of the thermodynamics of H in Pd nanoparticles over a wide range of sizes (from a few nm up to hundreds of nm) as long as no dislocations are generated in the core of the particles [122].

Finally, the results can be used to draw a technologically relevant conclusion concerning hydrogen storage in palladium nanoparticles. As palladium nanoparticles seem to yield higher absorption pressures and smaller isotherm plateau widths than bulk palladium, one needs to carefully consider whether the faster loading kinetics (due to the shorter diffusion lengths) in nanoparticles is sufficiently attractive

for hydrogen storage in such nano-geometries. The value of the present investigation is primarily fundamental in the sense that it provides a consistent interpretation of the existing (and, hopefully, of future) data on the thermodynamics of H in Pd nanoparticles in particular, and of hydrogen in nanoparticles in general. The theoretical framework is also essential for the understanding of the role of hydrogen in the newly discovered nanoparticle-systems (e.g., YH_x [30], MgH_x [67]) with tunable and active plasmonics. In Chapter 5 the thermodynamic studies are extended to larger sized nano- and microparticles.

5

PD AND PDH NANOPATCHES - A SIZE-DEPENDENT STUDY

In Chapter 3 we presented a theoretical model to determine the dielectric properties of nanosized materials, by only using the plasmonic resonance and the nanoparticle dimensions. In Chapter 4 we have investigated, how palladium (Pd) nanopatricles can behave differently than bulk material, when exposed to hydrogen. These changes alter thermodynamic properties and influence the geometrical expansion as well as the electronic and dielectric properties of Pd. In their experiments, Baldi *et al.* [70], Bardhan *et al.* [69] and Syrenova *et al.* [74] directly or indirectly used these changes to draw conclusions about the thermodynamic properties. Here, we want to show that the optical signal, more accurately the plasmonic resonance, can be used to learn more about the structural and dielectric changes that take place in Pd nano- and microstructures during hydrogen ab- and desorption. Of special interest is the size-dependent in-plane and out-of-plane expansion of Pd nanostructures that are placed on a substrate as well as the size-dependent variation of the hydrogen loading isotherms.

5.1 INTRODUCTION

Palladium-hydrogen is one of the best-studied metal-hydride systems in literature [14, 16, 43]. Nevertheless, many aspects of the interaction between palladium and hydrogen are either still unknown or strongly debated. Especially, the changes of the materials behavior are highly debated, going from bulk or thin films to structures that are truly nanosized in all three dimensions [28]. The vastly altered surface to volume ratio influences their thermodynamic behavior. Hydrogen is

absorbed differently in surface- and subsurface sites of Pd, since the enthalpy of solution at the surface sites is more negative than the one in bulk Pd.

In general, hydrogen ab- and desorption is accompanied by a change of the lattice parameter, leading to a molar volume increase of about 10.4 % when going from Pd to β-phase palladium hydride (PdH) [14]. The volume change is transferred to the macroscopic level anistropically, depending on the sample geometry. For extended thin films the volume expansion is directed almost exclusively out-of-plane, whereas small nanoparticles and nanocubes of sizes up to 100 nm expand isotropically [75].

Since direct measurements of nano- and microparticle volume-expansion are a challenging task, we developed an indirect optical method, using plasmonic resonances as a measure for geometrical changes in metal nanostructures. By the use of a model developed for metal square-patches of various sizes, we are able to separate optical changes induced by geometrical expansion and optical changes induced by changes in the the dielectric function. With this separation, it is possible to determine both the dielectric properties and the geometric expansion of Pd square-patches independently from each other.

An additional benefit of the plasmonic model is the possibility to obtain the dielectric properties of β-phase PdH (when not stated otherwise, from now on PdH is used as a synonym for β-phase PdH). Even though the dielectric properties of Pd and most other metal are unambiguously known and well measured [61], there is no complete and trusted picture for PdH, or metal hydrides in general. Several attempts have been made by Van Rottkay *et al.* [49], Isidorsson *et al.* [123] and Vargas *et al.* [124, 125] to measure the dielectric function of hydrogenated Pd films of various thickness (10 nm to 30 nm). However, comparing their results, no clear size-dependent trend is visible. Additionally, the measurement range covered by these groups only extends from about 200 nm to 1100 nm. Therefore, the extrapolation of their dielectric function models to the near- and mid-infrared comes at the expense of huge uncertainties (see Figs. 5.6 and 5.7).

We are using Pd square-patches with sizes between 200 nm and 3000 nm, covering a wavelength range between 900 nm and 8000 nm to directly determine the expansion behavior and the dielectric function in the infrared wavelength range.

5.2 PLASMONIC RESONANCE MODEL FOR THE PD TO PDH TRANSITION

The main result of the model developed in Chapter 3 is the relation between the plasmonic resonance wavelength λ_{res} and the dielectric function parameter E, stated in Eq. (3.53) for square-nanopatches:

$$E\left(\lambda, m, S, t, n\right) = 19.717 t S^{1.14} \left(\frac{mn}{\lambda}\right)^{2.14} - N\left(S, t\right). \tag{5.1}$$

Here, S and t are the side-length and height of the square-patch, n is the surrounding refractive index, m the geometric conversion factor relating the square-patch dimensions to an oblate spheroid (see Sections 3.3 and 3.3.2) and N the depolarization factor determined in Section 3.3.1.

The factor E can also be expressed as a combination of the surrounding refractive index n and the real and imaginary part of the dielectric function $\varepsilon = \varepsilon_1 + i\varepsilon_2$ (see Eq. (3.12)):

$$E\left(\lambda\right) = \frac{n^2\left(\varepsilon_1 - n^2\right)}{\left(\varepsilon_1 - n^2\right)^2 + \varepsilon_2^2}. \tag{5.2}$$

Therefore, it is independent of the particles geometry and thus, a general parameter describing the wavelength-dependent behavior of the material itself.

5.2.1 *Model for the In- and Out-of-Plane Expansion*

With help of the factor E, we first develop a model to determine the in- and out-of-plane expansion of Pd square-patches during hydrogen loading.

Similarly to the procedure to calculate m in Section 3.3.2, we choose a fixed λ_{res}^{PdH} for two different thicknesses t_i^{PdH} and t_j^{PdH}. As the parameter m is only related to geometry, we assume that it is the same for samples of Pd and PdH. Then

$$E\left(\lambda_{res}^{PdH}, mS_i^{PdH}, mt_i^{PdH}\right) = E\left(\lambda_{res}^{PdH}, mS_j^{PdH}, mt_j^{PdH}\right), \tag{5.3}$$

with

$$\begin{aligned} &E\left(\lambda_{res}^{PdH}, mS_i^{PdH}, mt_i^{PdH}\right) \\ &= 19.717 t_i^{PdH} \left(S_i^{PdH}\right)^{1.14} \left(\frac{mn}{\lambda_{res}^{PdH}}\right)^{2.14} - N_i^{PdH} \\ &= 19.717 t_i^{PdH} \left(S_i^{PdH}\right)^{1.14} \left(\frac{mn}{\lambda_{res}^{PdH}}\right)^{2.14} - \frac{1}{1.1\frac{S_i^{PdH}}{t_i^{PdH}} + 0.3}. \end{aligned} \tag{5.4}$$

It is important to note here that the actual sizes S_{PdH} and t_{PdH} of the hydrogen-loaded Pd samples are not accessible during the experiment. Therefore, we need a way to relate the measured PdH resonance wavelengths λ_{res}^{PdH} with the known sizes of the unloaded samples $\left(S_i^{Pd}, t_i^{Pd}\right)$, hence a function h so that

$$\lambda_{res}^{PdH} = h\left(S_i^{Pd}, t_i^{Pd}\right). \tag{5.5}$$

For a chosen couple S_i^{Pd}, t_i^{Pd} we determine D_j^{Pd} and D_k^{Pd}, as shown in Fig. 5.1 that obey the condition

$$\lambda_{res}^{PdH} = h\left(S_i^{Pd} = D_i^{Pd}, t_i^{Pd}\right) = h\left(D_j^{Pd}, t_j^{Pd}\right) = h\left(D_k^{Pd}, t_k^{Pd}\right). \tag{5.6}$$

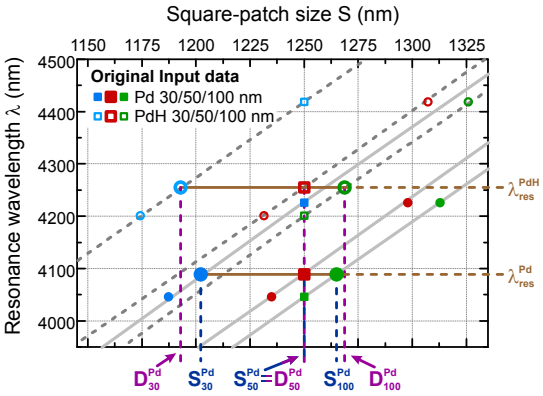

FIGURE 5.1. Construction of D_i^{Pd}, D_j^{Pd}, and D_k^{Pd} for PdH. The same technique as in Section 3.5.3 is applied, using the resonance wavelengths λ_{res}^{PdH} and one nominal Pd size ($S_i^{Pd} = S_{50}^{Pd} = D_{50}^{Pd}$), to calculate the other two nominal Pd sizes D_{30}^{Pd} and D_{100}^{Pd} at the same wavelength.

This is the same technique as in Section 3.5.3, but with the resonance wavelength data of the PdH samples. Important to note is that the D_j^{Pd} and D_k^{Pd} are different from the calculated S_j^{Pd} and S_k^{Pd} for the pure Pd samples, since they are determined from a different set of wavelengths $\lambda_{res}^{PdH} \neq \lambda_{res}^{Pd}$.

During hydrogenation the in-plane as well as the out-of-plane dimensions of the Pd square-nanopatches will change. So we can write

$$S_i^{PdH} = D_i^{Pd} \left(= S_i^{Pd}\right) \times (1+\sigma), \tag{5.7}$$

$$S_j^{PdH} = D_j^{Pd} \times (1+\sigma), \tag{5.8}$$

$$S_k^{PdH} = D_k^{Pd} \times (1+\sigma), \tag{5.9}$$

and

$$t_{i,j,k}^{PdH} = t_{i,j,k}^{Pd} \times (1+\tau). \tag{5.10}$$

The factors σ and τ are the in- and out-of-plane expansion factors that are related to the relative volume expansion ΔV_{PdH} of Pd through

$$\begin{aligned}\Delta V_{PdH} &= \left(V_{PdH} - V_{Pd}\right)/V_{Pd} = 2\sigma + \tau + O\left(\sigma^2, \sigma\tau\right) \\ &= 0.104\end{aligned} \tag{5.11}$$

The relative volume expansion from Pd to β-phase PdH (at atmospheric pressures and room temperature) is 0.104 [14]. It originates in the lattice expansion of the Pd (fcc) lattice from 0.3890 nm for pure Pd to 0.4025 nm for β-phase PdH in the β-phase [91]. It has been repeatedly shown in literature that the relative volume expansion is independent of the sample, no matter if it is bulk Pd [13], an extended thin film [126] or nanoscale Pd [127]. Thus, we assume that for all square-patches the overall relative volume expansion is constant, even though σ and τ are allowed to be size dependent.

Introducing Eq. (5.11) into Eq. (5.10) we obtain

$$t_{PdH} = t_{Pd} \times \left(1 + \Delta V_{PdH} - 2\sigma\right) = t_{Pd} \times (1.104 - 2\sigma)\,. \tag{5.12}$$

and, hence, eliminate τ from the above equation.

With the depolarization factor

$$\begin{aligned}N_i\left(S_{PdH}, t_{PdH}\right) &= \frac{1}{1.1\frac{S_i^{PdH}}{t_i^{PdH}} + 0.3} = \\ N_i\left(D_{Pd}, t_{Pd}, \sigma\right) &= \frac{1}{1.1\frac{D_i^{Pd}(1+\sigma)}{t_i^{Pd}(1.104-2\sigma)} + 0.3}\end{aligned} \tag{5.13}$$

and the size defining Eqs. (5.7) to (5.9) and (5.12), we can reformulate the condition Eq. (5.3) to obtain the general relation

$$\begin{aligned}&E\left(\lambda_{res}^{PdH}, mD_i^{Pd}\left(1+\sigma\right), mt_i^{Pd}\left(1.104-2\sigma\right)\right) \\ &\quad = E\left(\lambda_{res}^{PdH}, mD_j^{Pd}\left(1+\sigma\right), mt_j^{Pd}\left(1.104-2\sigma\right)\right).\end{aligned} \tag{5.14}$$

As all the parameters $\lambda_{res}^{PdH}, m, D_i^{Pd}, t_i^{Pd}, D_j^{Pd}$ and t_j^{Pd} in Eq. (5.14) are known, this equation determines the in-plane expansion parameter σ (and thus also the out-of-plane expansion factor $\tau = 1.104 - 2\sigma$) for square-patches with a certain resonance wavelength λ_{res}^{PdH}.

This method for determining σ (and with it the dielectric factor E) requires that $\sigma\left(S_i^{PdH}\right) \simeq \sigma\left(S_j^{PdH}\right)$ if $\lambda_{res}^{PdH}\left(S_i^{PdH}\right) = \lambda_{res}^{PdH}\left(S_j^{PdH}\right)$. Thus, it is only valid if σ is slowly varying with S and t.

Using Eq. (5.1) for E we explicitly have:

$$E\left(PdH\right) \simeq 19.717\,(mn)^{2.14}\, t_i^{Pd}\,(1.104-2\sigma)\left(D_i^{Pd}\right)^{1.14} \times (1+\sigma)^{1.14}\left(\frac{1}{\lambda_{res}^{PdH}}\right)^{2.14} - \frac{1}{1.1\frac{D_i^{Pd}(1+\sigma)}{t_i^{Pd}(1.104-2\sigma)} + 0.3}. \tag{5.15}$$

5.3 EXPERIMENTAL REALIZATION

We use different Pd samples with thicknesses $t_1 = 30\,\text{nm}$, $t_2 = 50\,\text{nm}$, $t_3 = 100\,\text{nm}$ to perform continuous hydrogen loading measurements. The square-patch fields of the samples are measured with a Fourier-transform infrared spectrometer (FTIR). With a square aperture of $50\,\mu\text{m} \times 50\,\mu\text{m}$ and averaging over 24 scans each, we have a measurement time of about 10 s per field. The samples are placed in a titanium vacuum-tight gas-flow cell that is hooked up to a computerized gas-mixing system consisting of Bronkhorst mass-flow controllers for hydrogen (H_2) and argon (Ar). An Ar 5.0 bottle (99.999 % pure Ar) and an Ar W5 (5 vol % H_2 in 95 % Ar) bottle are connected to the measurement setup. The gas-flow cell has two broadly transparent calcium fluoride (CaF_2) windows to perform the FTIR transmission measurements over the full spectral range. One side of the cell is connected to the gas mixing system , while the other is open to ensure atmospheric pressure in the cell (approx. 1013 mbar).

For proper normalization and to minimize influences due to molecular vibrations of the surrounding atmosphere every 10 measurements a reference measurement is performed (same conditions as the measurements on the fields, but using the pure CaF_2 substrate).

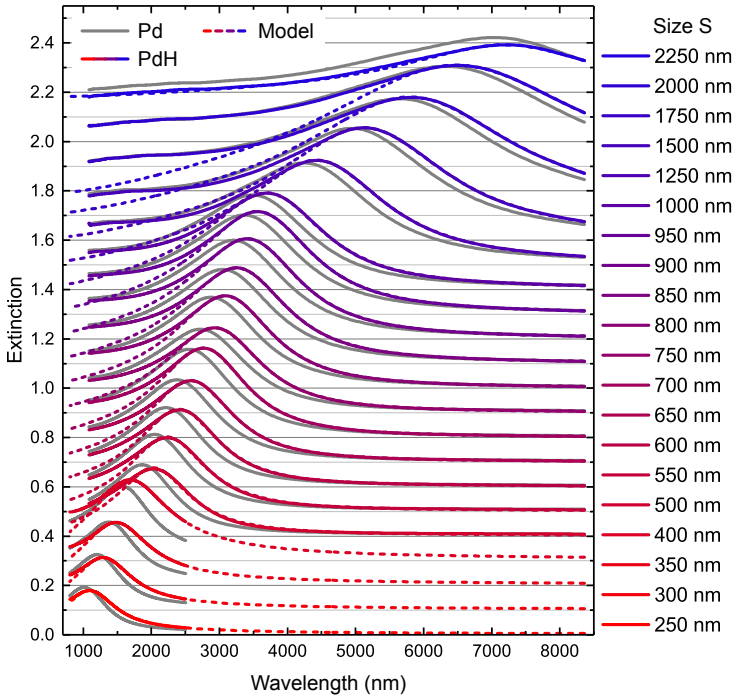

FIGURE 5.2. Extinction spectra for $t = 50\,\text{nm}$ and varying S, in the pure Pd state (grey curves) and the β-phase state (colored curves). For comparison the fitted model results (later used to determine F) are plotted as dashed colored lines.

All samples are measured consecutively with all three detectors (see Section 3.5.2) with an overall measurement time of 900 s for a full set of resonance data. Parallel to the FTIR measurements, the sample is exposed to a controlled gas-flow cycle. The cycle is designed to have a constant gas flow of 1 nl/min (1 norm-liter per minute) over the

sample, while the gas mixture is changed over time. Since, the measurement time for covering all fields is 900 s, all partial pressure steps are fitted to a multiple of this measurement time.

After the measurements, the dataset is processed to extract the important parameters, like the center-wavelengths and the loading and unloading times. The raw transmission spectra, that were recorded over a linear wavenumber scale, are cleaned, stitched and analyzed (see Section 3.5.2) and afterwards converted to a wavelengths scale. Figure 5.2 shows the resulting spectra for $t = 50\,\text{nm}$ and varying S, in the pure Pd state (grey curves) and the β-phase PdH state (colored curves).

5.3.1 *In- and Out-of-Plane Expansion of PdH Samples*

To reduce the large amount of data, we first analyze the measurement results for the two extreme states, the pure Pd and β-phase PdH samples. considering that we declare the median value of all measurements at 0 vol % H_2 in Ar as pure Pd and the median of all measurements at 5 vol % H_2 in Ar as PdH (knowing that we do not have fully loaded $PdH_{0.71}$. However, Fig. 5.9 shows that we are well in β-phase PdH).

Using the equality $E_i\left(\lambda\right) = E_j\left(\lambda\right)$ (see Eq. (5.14)) and the definition of E in Eq. (5.15), we can determine the in-plane-expansion going from Pd to PdH for the three combination $E_{30} = E_{50}, E_{30} = E_{100}, E_{50} = E_{100}$. Here the subscripts indicate the sample thickness t. The in-plane expansion coefficients, for all three combinations, are shown in Fig. 5.3.

Figure 5.3 depicts that σ decreases weakly from $\sigma \sim 0.08$ to ~ 0.02 when the patch size increases from 250 to 2500 nm. Isotropic expansion would correspond to $\sigma \simeq 0.104/3 \simeq 0.035$. This weak size dependence is fully consistent with the weak dependence of the plateau pressures shown in Fig. 5.9(d). The data suggest a further peak around 450 nm that is best visible in the blue line. From the measurements it

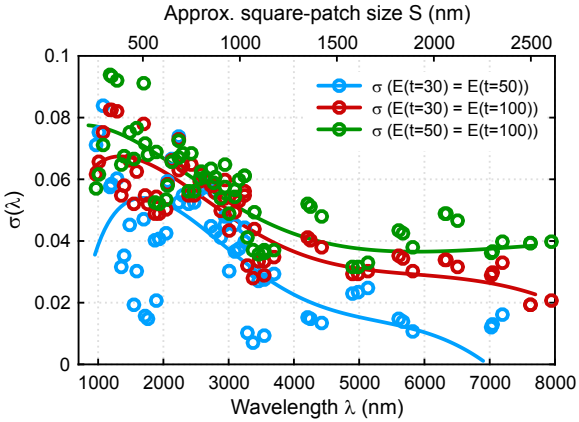

FIGURE 5.3. Calculated in-plane-expansion σ from Pd to PdH square-patches, using Eq. (5.14). The dots are calculated using the technique described in Section 3.5.3, whereas the lines are calculated using a 4th order polynomial fit through the resonance wavelengths $\lambda_{res}^{PdH}(S)$. There are clear differences in value between σ from $E_{30} = E_{50}$ (blue line/dots) and $E_{50} = E_{100}$ (green line/dots), probably originating from the very different aspect ratios for the $t = 30\,\text{nm}$ and $t = 100\,\text{nm}$ samples. However, the general monotonic decrease with size is visible for all samples. For better comparison the upper x-axis shows the corresponding approximate mean square-patch size for the wavelengths $\lambda_{res}^{PdH}(S)$.

is no fully clear, whether it is a real effect or just a numerical artifact. Nevertheless, if it is real, the data suggests that for very small sqaure-nanopatches the expansion tends towards an isotropic expansion. These findings are consistent with the data of Baldi *et al.* [70] on 13 nm to 29 nm sized Pd nanocubes that remain crystalline after repeated hydrogen loading and unloading.

It is, however, intriguing to see that the expansion coefficient σ is higher than $\Delta V_{PhD}/2 = 0.104/2 = 0.052$, and therefore correspond to $\tau < 0$. Wetting would lead to such a behavior. In analogy to water droplets, the nanoparticles seem to get flatter when their size increases due to hydrogen incorporation. In water droplets gravitational energies are responsible for the surface wetting. For Pd nanopatches

gravitation does not a role. However, for reducing the overall energy it seems that it still wants to wet the surface of the substrate. Only for very large patches the sticking to the substrate prevents in-plane expansion, leading to $\sigma \longrightarrow 0$.

The resulting in-plane expansion of the smaller size patches is contradictory to the known results of small scale single crystalline nanocubes expanding isotropically in all directions. Especially, the larger patches with about 3 µm side length should behave very similar to extended thin films with negligible in-plane expansion and thus $\sigma \approx 0$. This and the large quantitative difference between the three data sets hints that the initial condition that σ should be the same for all patches that have the same resonance wavelength was too simple. The blue line in Fig. 5.3 ($E_{30} = E_{50}$) is showing the smallest (and therefore most reasonable) values of σ. It also represents the smallest difference in t (with both thicknesses being in the range of only having one crystallite in z-direction). Therefore, the general trend of larger values for σ for the smaller patches and the decrease towards a constant (near-zero) value for larger patches, should be reliable and valid, even though the absolute values have large margins of error. If one subtracts a constant value of about 0.02 from the mean data-set (or just takes the σ_{30-50} values) the expected behavior is recovered.

Besides, it is important that $S_{PdH} = (1 + \sigma) S_{Pd}$ is evaluated by using wavelength differences of the plasmonic resonances and, therefore, only accounts for the size differences relevant for the plasmonic resonance. If, for example, the hydrogenation is leading to some non-isotropic expansion in the x-y-plane or generates special edge (or shell) states with a different plasmonic behavior, our model averages over these effects and generates some kind of effective side length S_{eff}^{PdH}. The results presented in Chapter 4 strongly suggest the assumption of such edge effects.

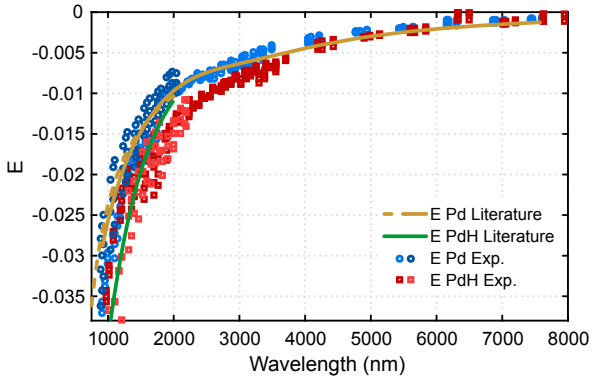

FIGURE 5.4. Calculated results for the dielectric factor E for Pd and PdH. The dark and light blue dots are calculated from our Pd nanosquare plasmonic measurements of two different sets of samples. The golden line is the E value calculated from literature values of ε [49, 61]. The red squares are calculated using the data from the fully hydrogenated Pd samples. For comparison, the best available literature values for ε_{PdH} are plotted, too (green line).

5.3.2 *Dielectric Function of Pd and PdH*

Even though, the calculated $\sigma(\lambda)$ and $\tau(\lambda)$ might not give the full picture concerning the in- and out-of-plane expansion of the Pd square patches, the basic assumption of having an equation separating size and electronic effects in plasmonic resonances still holds true. By using the calculated '*effective expansion factors*' σ and τ we can calculate the dielectric factor E for the hydrogen loaded Pd samples.

Figure 5.4 displays the calculated results both for Pd (blue dots) and PdH (red dots) measured for two different sets of samples (lighter and darker colors). The pure Pd data shows very good agreement with the corresponding literature values (golden line) as already discussed in Chapter 3. For PdH, there are only very limited literature data available. The green line in Fig. 5.4 represents the largest and mostly used set of dielectric data from Von Rottkay *et al.* [49, 124]. Unfortunately, it only covers wavelengths between 200 nm and 2000 nm and it is not

clear whether or not the authors corrected for the hydrogen induced lattice expansion when calculating the dielectric function from their ellipsometric measurements. Nevertheless, it shows the same qualitative behavior as our data, even though, the absolute agreement in the region between 1.5 and 2 µm is poor. In this region, the literature PdH data approaches the values for non-hydrogenated pure Pd whereas our data for E are markedly lower. Von Rottkay *et al.*s setup [49] approaches the edge of their measurement setup in this wavelength region. This could result in a strongly reduced signal-to-noise ratio and thus lead to a noise-phenomenon with all data approaching the same values. A similar issue can be observed in our setup at wavelengths above 10 µm (or below 1000 cm^{-1}).

Apart from the E-factor, we can also calculate the F factor from fitting the extinction model described in Section 3.3 to the experimental extinction data (see dashed lines in Fig. 5.2), by using the procedure described in Section 3.4.1. Figure 5.5 shows the wavelength dependent F factor for both Pd and β-phase PdH nanopatches together with the respective literature values. Both Pd and PdH are very close to each other with the tendency of $F\left(\mathrm{Pd}\right) < F\left(\mathrm{PdH}\right)$ below 2000 nm and $F\left(\mathrm{Pd}\right) > F\left(\mathrm{PdH}\right)$ for higher wavelength (especially between 2000 nm and 4000 nm). These results agree with the limited data available for PdH (grey dashed lines representing data of Vargas *et al.* [128] and Isidorsson *et al.* [123], see below for more details) in the way of showing very little difference to the Pd data. In fact, it is intriguing how diverse the literature curves measured on similar film systems are. This holds even true in the region below 1000 nm, where data were experimentally obtained. This verifies that it is of great importance to get broader and more accurate dielectric data of hydrided Pd samples.

The combination of E and F form the dielectric function $\varepsilon\left(\lambda\right)$ (using Eqs. (3.79) to (3.81)). Figures 5.6 to 5.8 depict the resulting $\varepsilon_1 = \mathrm{Re}\left(\varepsilon\right)$ and $\varepsilon_2 = \mathrm{Im}\left(\varepsilon\right)$. Since both, ε_1 and ε_2, involve quotients of E and F it is not surprising that the values are more scattered than the original values for E and F in Figs. 5.4 and 5.5. The graphs show a wide spread of the PdH literature dielectric functions from Vargas *et al.* [128] and Isidorsson *et al.* [123]. The real parts of the dielectric function of the

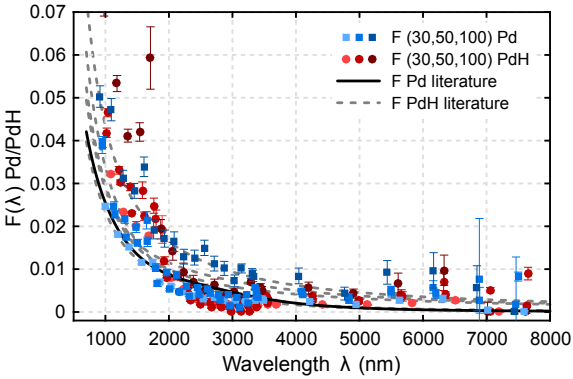

FIGURE 5.5. *F* factor for Pd and PdH nanopatches, derived from a fitting procedure of the experimental extinction spectra to Eq. (3.82). The blue squares are for the Pd data (light blue for $t = 30$ nm, blue for 50 nm and dark blue for 100 nm). The errorbars depict the standard deviation confidence interval from the fit, and the solid black line is the literaure value calculated from Rakic *et al.* [61]. The red dots depict the PdH data (bright to dark colors as for Pd). The comparison to the literature values (dashed lines) indicate a strong similarity between Pd and PdH values.

loaded (with 1 bar H_2) 10 nm film from Vargas *et al.* (solid green line) and the partially loaded (at 40 mbar H_2) 12 nm thick film from Isidorsson *et al.* (dashed yellow line) are very close to the literature value for pure Pd. Whereas the thicker Vargas *et al.* films (long and short dashed green lines) and the fully loaded Isidorsson *et al.* film (solid yellow line) show a qualitatively different behavior with markedly smaller absolute values for ε_1. This spread does not necessarily have anything to do with different behavior of thicker or thinner films, but could simply arise from the fact that the curves are generated using model parameters (Brendel-Bormann model for Vargas *et al.* and a Drude-Lorentz model for Isidorsson *et al.*) that were fitted in a different wavelength region (aprrox. 200 nm to 1100 nm).

Looking at the resulting ε_1 calculated from our experimental data, it seems that the larger negative literature values are closer to reality or at least to the behavior of our evaporated thin films (see red squares

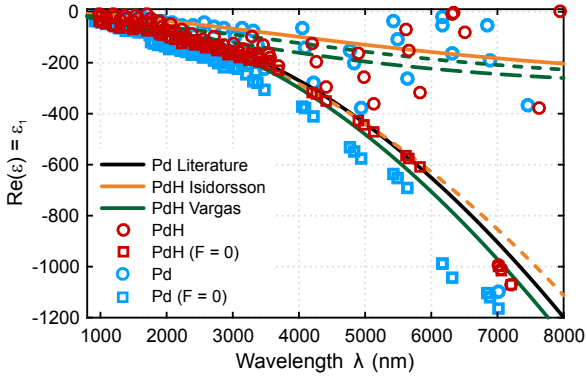

FIGURE 5.6. Real part of the dielectric function for Pd and PdH. The lines are literature dielectric data for pure Pd from Rakic *et al.* [61] (black line), for a 12 nm PdH film from Isidorsson *et al.* [123] (40 mbar H_2 yellow dashed line, 1 bar H_2 yellow solid line) and for PdH films of Vargas *et al.* [128] (10 nm film green solid line, 15 nm film green long dashed line, 30 nm film green short dashed line). The circles are the experimentally obtained values of Pd (blue) and β-phase PdH (red) using Eq. (3.79). The squares are calculated assuming $F \approx 0$ (Eq. (3.81)).

in Fig. 5.6). As discussed in Chapter 3 and also shown in Fig. 5.5, in the wavelength region above 5000 nm, F becomes very noisy. This leads to unrealistic values of ε_1 (and ε_2) when factored into the calculations (see blue and red circles in Fig. 5.6). Therefore, for wavelengths above 5000 nm one should use the approximate formula Eq. (3.81), setting $F = 0$ to obtain $\varepsilon_1(\lambda)$.

Taking these findings into account, one can say that the real part of ε_{PdH} is less negative than that of Pd. Otherwise it follows a similar curvature (as shown in Fig. 5.8). Since, the absolute value of ε_1 (when negative) is a measure for the conductance of a metal, the smaller absolute values of ε_1 (PdH) compared to ε_1 (Pd) confirm the literature knowledge about PdH, of being a worse conductor compared to Pd [14, 43]. The available literature dielectric functions show the same trend (except the 10 nm Vargas *et al.* film, where other effects as for example percolation could play a role).

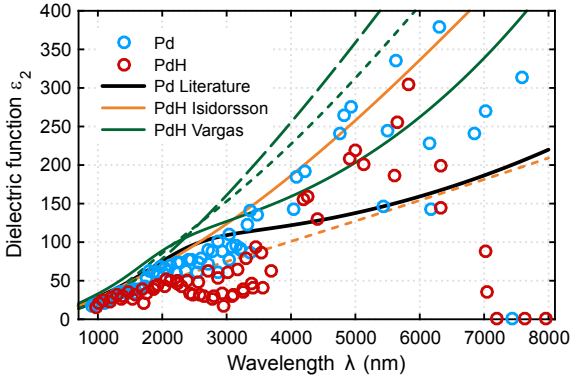

FIGURE 5.7. Imaginary part of the dielectric function for Pd and PdH. The lines are literature dielectric data for pure Pd from Rakic *et al.* [61] (black line), for a 12 nm PdH film from Isidorsson *et al.* [123] (40 mbar H_2 yellow dashed line, 1 bar H_2 yellow solid line) and for PdH films of Vargas *et al.* [128] (10 nm film green solid line, 15 nm film green long dashed line, 30 nm film green short dashed line). The circles are the experimentally obtained values of Pd (blue) and β-phase PdH (red) using Eq. (3.80).

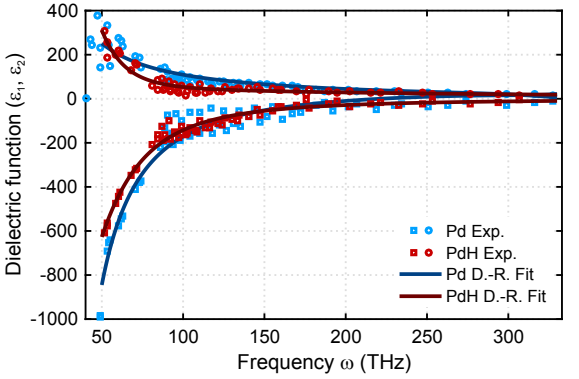

FIGURE 5.8. Dielectric functions of Pd (blue squares for ε_1 and dots for ε_2) and PdH (red squares for ε_1 and dots for ε_2) together with a higher order Drude-Lorentz fit using Eq. (5.16) with the fitting parameters stated in Table 5.1.

Interestingly, we see an opposite behavior in the imaginary part of the dielectric function (see Fig. 5.7 and dots in Fig. 5.8). Here, ε_2 (PdH) is showing a lower value than Pd (for wavelengths below 5000 nm). This effect can be translated to a lower damping, which is different from (most of) the calculated literature values. However, we need to stress, that the functions are fitted to wavelengths below 1000 nm. In this area our PdH and Pd values for ε_2 are very similar to each other (and even overlap between 900 nm and 1800 nm), similarly to the literature data. Between 2000 nm and 4000 nm the PdH data show the same qualitative behavior as the Pd data (almost linear increase till 2300 nm, then a bump with constant or decreasing values till 3100 nm and then again a monotonous increase). A similar behavior can be seen in the literature Pd data (black line) and the Vargas *et al.* 10 nm film, only shifted higher values of ε_2.

To be able to use the results for any further research, one needs to fit a generic Kramers-Kronig relations obeying model to these data sets [129]. One typical model, containing sums of real and complex pole functions (1st and 2nd order) that represents basically sums of Drude and Lorentz oscillators has the following form:

$$\varepsilon(\omega) = \varepsilon_\infty + \sum_n \frac{\beta_n}{\alpha_n + i\omega} + \sum_n \frac{\gamma_{0,n} + i\omega\gamma_{1,n}}{\delta_{0,n} + i\omega\delta_{1,n} - \omega^2}. \tag{5.16}$$

Using a standard least square fitting algorithm one obtains a 8th order model for Pd and 4th order model for PdH (see Table 5.1), displayed in Fig. 5.8.

These values provide further proof that distinct differences in dielectric properties between Pd and PdH exist (generally less negative ε_1 and smaller positive ε_2 values for PdH compared to Pd square-patches). Together with the size-dependent geometrical expansion shown in Section 5.3.1, we get a comprehensive picture of the processes influencing the optical properties in hydrogenated Pd nanostructures. These results can be used to predict the behavior of more complex nanoparticles geometries, since the obtained dielectric properties, together with the geometrical expansion factors, are sole variables of the wavelength, but do not depend on the particular geometry.

Pd dielectric data					
ε_∞	=	70.0155			
α_1	=	1.22×10^{14} Hz;	β_1	=	2.28×10^{18} Hz
α_2	=	3.27×10^{13} Hz;	β_2	=	3.44×10^{18} Hz
α_3	=	2.13×10^{15} Hz;	β_3	=	-6.51×10^{16} Hz
α_4	=	8.66×10^{13} Hz;	β_4	=	-5.61×10^{18} Hz
$\gamma_{0,1}$	=	-1.92×10^{31} Hz^2;	$\delta_{0,1}$	=	3.75×10^{28} Hz^2
$\gamma_{1,1}$	=	-4.37×10^{16} Hz;	$\delta_{1,1}$	=	1.30×10^{14} Hz
$\gamma_{0,2}$	=	-1.55×10^{31} Hz^2;	$\delta_{0,2}$	=	4.50×10^{30} Hz^2
$\gamma_{1,2}$	=	-5.43×10^{15} Hz;	$\delta_{1,2}$	=	4.73×10^{14} Hz
PdH dielectric data					
ε_∞	=	1			
α_1	=	2.42×10^{15} Hz;	β_1	=	-6.35×10^{15} Hz
α_2	=	1.35×10^{10} Hz;	β_2	=	4.43×10^{17} Hz
$\gamma_{0,1}$	=	-1.98×10^{32} Hz^2;	$\delta_{0,1}$	=	9.03×10^{28} Hz^2
$\gamma_{1,1}$	=	-3.98×10^{17} Hz;	$\delta_{1,1}$	=	5.89×10^{14} Hz

TABLE 5.1. Model values for Pd and PdH dielectric data, calculated using the complex model of Eq. (5.16).

5.4 CONTINUOUS LOADING EXPERIMENTS

To gain more insight on the dynamic behavior of the hydrogenation process of the Pd square-patches, we investigate in detail the loading isotherms of the different samples. Since all samples are measured simultaneously and under exactly the same conditions, it is possible to correlate the results quantitatively. The absolute accuracy concerning hydrogen pressure and H/Pd composition, using optical measurements together with a gas-flow cell, is not comparable with the one obtained by volumetric measurements in pressure-cells [68]. However, the used equipment together with the simultaneous measurements allow for a high relative accuracy.

First, the plasmonic resonance positions are correlated to the corresponding gas concentration. Since, the sample needs a certain concentration dependent timespan to reach equilibrium, all concentration steps span over at least two full measurement runs (in the α- and β-phase equilibrium is reached very fast, whereas, in the miscibility gap where α- and β-phase coexist, the response time till equilibrium is reached, can be quite long). In the analysis, the measurement data per concentration step are averaged through a weighted average, depending on the time difference to the closest past concentration change (to account for the loading times of the samples, the first run per concentration step (900 s) is always thrown away). The resulting loading and unloading isotherms are then converted from wavenumber to wavelength and normalized by setting the median of all measurements at 0 vol % H_2 in Ar to 0 and the median value of all measurements at 5 vol % H_2 to 1. To determine the plateau loading concentrations for the different fields and samples, the loading isotherms are interpolated to match the same x-axis (wavelength axis $\propto$ H/Pd-axis). Afterwards, the pressure value at the x-value of the minimal slope is taken to be the plateau loading pressure.

Figure 5.9 shows the resulting loading isotherms and plateau pressures for three different sample thicknesses t and square-patch sizes S between 200 nm and 2500 nm. The plateau pressure of all samples is between 16 mbar and 22 mbar, which is in good agreement to the literature results for Pd thin films (see Chapter 4). The isotherms and especially the plateau pressures seem to be independent of the sample thickness. The slightly enhanced values of the 50 nm thick sample are most probably due to slight differences in the measurement condition, namely slight temperature or overal pressure variation.

Since the conditions during the measrements are accurately controled, there is no doubt that the in-plane dimensions play a signifcant role, regarding the isotherm slope as well es the plateau pressures. Figures Fig. 5.9(a)-(d) show that the isotherm slope increases with particle size. It has been repeatedly shown in literature that the flatness and width of the isotherm plateau region strongly depend on defects [14, 130] and film clamping [131, 132]. Our Pd films are evaporated using electron gun evaporation (with a rate of 2 Å/s at a vacuum of

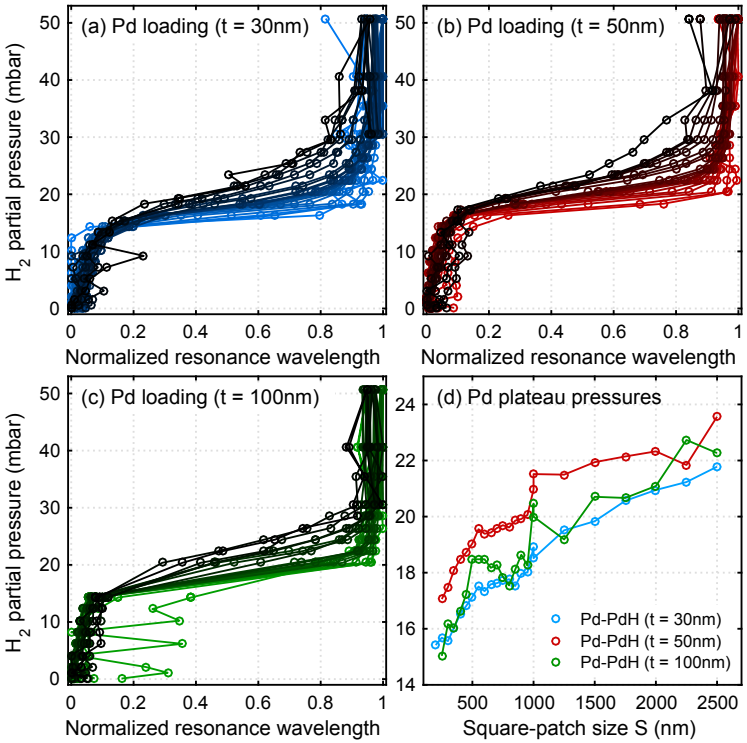

FIGURE 5.9. Loading isotherms of Pd square-patch samples. (a), Loading isotherms for a Pd sample with $t = 30$ nm varying S from 200 (lightest blue line) to 2500 nm (black line). (b), Loading isotherms for a sample with $t = 50$ nm and S varying from 250 (lightest red line) to 2500 nm (black line). (c), Same as in (b) with $t_{Pd} = 100$ nm. (d), Plateau pressures extracted from the measurements of (a)-(c), showing a small but characteristic increase with increasing square-patch size S, whereas there does not seem to be a significant dependence on the sample thickness t.

about 10^{-7} mbar), the metal forms a poly-crystalline film with crystallites sizes of about 20 nm to 50 nm. Therefore, larger square-patches that contain more crystallites and defects might show a higher loading pressure and sloping plateaus. The size-dependence of the loading pressures should be visible down to sizes of about 50 nm, where only one crystallite would form. Another explanation for the sloping plateaus is that large patches undergo drastic atomic displacements in order to expand predominantly out-of-plane. The increasingly sloping plateaus are therefore in agreement with the data for σ in Fig. 5.3, which show that σ decreases with increasing size S.

Additionally, the clamping to the substrate increases with patch-size. Even though, highly debated [133, 134], clamping of thin films to the substrate can increase the loading pressure compared to a bulk of freely movable Pd [77]. The clamping, in our case, can be supported additionally, by lattice spacing matching of the substrate. The used CaF_2 substrates form a basic cubic lattice and are cleaved along the 111 surface and thus have a molecular spacing of $x = a_{CaF_2} \times \sqrt{2} = 5.462\,\text{Å} \times \sqrt{2} = 7.724\,\text{Å}$ [135]. The unhydrogenated Pd forms a fcc lattice with lattice parameter $a_{Pd} = 3.889\,\text{Å}$ [14]. When taking two unit cells ($2 \times a_{Pd} = 7.778\,\text{Å}$), the Pd lattice almost perfectly fits onto the {111} CaF_2 surface with $x_{CaF_2} = 7.724\,\text{Å}$. This fit enhances the surface adhesion of the Pd, leading to an extra energy, necessary to form PdH with a markedly different lattice parameter ($a_{PdH} = 4.025\,\text{Å}$). Such a theory is also supported by the analysis of the in- and out-of-plane expansion in Fig. 5.3. It shows that the larger squares expand more out-of plane as the smaller squares, what could be supported by substrate adhesion effects. Here, our data proves the same trend of increasing plateau pressure ($\Delta p = 6\,\text{mbar}$), when going from $S = 250\,\text{nm}$ to $S = 2500\,\text{nm}$.

5.5 CONCLUSION

The extensive PdH square-patch studies show that even though polycrystalline and fairly large structures of sizes between 200 nm and 3000 nm were used, there are clear differences from bulk or thin film

behavior. We demonstrate for the first time that the in- and out-of-plane expansion of Pd square-patches change with size. Even though, the absolute values need to be confirmed using more direct methods, as for example, in-situ atomic force microscopy (AFM) or scanning near-field optical microscopy (SNOM) measurements, the trend going from in-plane to mostly out-of-plane expansion for increasing patch size, is well identified.

Besides the size-expansion, the change in the electronic properties of the Pd is the second large factor influencing the optical properties. We employed an analytical model for plasmon resonances of square patches to deduce these electronic properties, namely the dielectric function for hydrogenated Pd. One great advantage of our method is, that is does not rely on any assumptions about the form of the dielectric function. As a result we obtain, for the first time, reliable values for the optical properties of PdH in the infrared wavelength range going from 900 nm to 8000 nm.

The great advantage of our optical method is that it makes it possible to measure simultaneously room temperature isotherms for all the differently sized samples. These isotherms showed that the plateau loading pressure is situated between 16 mbar and 22 mbar with an almost linear increase with increasing side-lengths of the square patches. This interesting behavior shows that the energy necessary to overcome the miscibility gap and form the β-phase increases with increasing patch size. Such a size-dependent (partial) clamping of the Pd to the substrate is in agreement with the enhanced out-of-plane expansion observed for our larger squares.

Existing literature about palladium and hydrogen, deals with bulk and thin films on one hand, and with (mostly single crystalline) nanpoarticles of sizes between 2 nm and 100 nm one the other hand. For the intermediate region, our investigations are the first systematic approach to close the gap between nanocrystal and bulk behavior. To get a complete picture, more studies of this system are necessary. Temperature dependent loading and unloading measurements would provide a complete thermodynamic picture and in-situ AFM could verify the geometrical changes on the nanoscale.

6

HYBRID METAL NANOPARTICLE PLASMONIC SYSTEMS

In recent years, plasmonic hydrogen sensing schemes using complex hybrid Pd-Au nanostructures have attracted significant attention. However, most studies have focused on investigating the sensing performance of nanosensor geometries where the constituent materials are laterally coupled. In contrast to such planar hybrid systems, which often require complex multi-step fabrication approaches, devices where the materials are stacked directly on top of each other can be fabricated in a single step, enabling straightforward high-throughput processing. In this chapter, that was adapted from our publication in ref. [29], we introduce a novel hydrogen sensing scheme which incorporates complex hybrid plasmonic nanostructures consisting of stacked gold and palladium nanodisks. In particular, the influence of stacking order and geometry will be studied, experimentally and numerically, to find an optimal arrangement for a hydrogen sensor device. With an optimized sensing geometry - a stack of gold as lower and palladium as upper disk - spectral shifts as large as 30 nm at 4 vol % H_2 were obtained, which is a strong improvement compared to previous indirect sensing designs. The samples yield large signals and are fabricated by low-cost hole-mask colloidal lithography and therefore yield sample sizes over areas of 1 cm^2.

6.1 INTRODUCTION

Over the last decade, the concept of a hydrogen economy has emerged as a topical and highly debated candidate for replacing fossil fuels in large-scale energy production. However, this important development

is still hampered by a lack of cheap, reliable, safe and compact hydrogen sensors that can be used for monitoring all process steps of the hydrogen production and consumption chain, from energy plants to hydrogen-fueled cars.

Upto now, a variety of possible sensing concepts have been proposed and evaluated [22, 72]. Initial experiments focused mainly on plasmonic structures with large nanostructured areas, by employing geometries such as nanodisks, hole arrays, and perfect absorbers [19, 42, 136]. Moving from extended systems towards progressively lower detection volumes, single particle nanosensor geometries, such as nanostructured antennas [104] and chemically synthesized '*smart dust*' nano-probes [23, 25, 137, 138], were investigated. One important concept for high sensitivity palladium-based plasmonic hydrogen sensors is the integration of multiple materials into a single hybrid nanosensor geometry. Here, gold or silver nanostructures are commonly used to enhance the changes in other chemically reactive materials, since they yield the highest field enhancement and the narrowest plasmonic resonances in the visible and near-infrared wavelength region. There are some concepts involving alloyed nanostructures [139, 140] and also core-shell pillars forming a metasurface [24] that are used as plasmonic hydrogen detectors. However, most hybrid hydrogen sensing geometries investigated so far involve the lateral placement of palladium and gold antennas with surface-to-surface distances around 10 nm [41, 141, 142], the placement of gold and palladium disks on the sides of a nano-pyramiede [143], or the stacking of a palladium disk on top of a gold antenna with a dielectric spacer in between [144–146].

In all these geometries, one key unifying design goal is to place the two constituent materials at very close surface-to-surface distances while preventing direct contact. This is usually achieved either by complex two-layer lithography steps [41] or by introducing a spacer layer between the two materials [104]. In many earlier approaches, direct contact between the noble metal used for the antenna and the highly reactive but often strongly damped functional material, is assumed to be detrimental for the sensitivity of the full structure. Therefore, only very recently palladium on top of silver triangles have been studied in comparison to palladium-silver heterodimers [147].

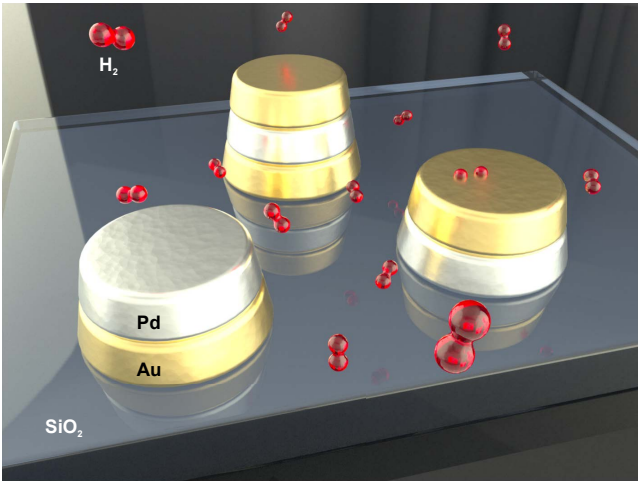

FIGURE 6.1. Schematic view of the different palladium-gold nanodisk systems under investigation. The stacking sequence of gold and palladium is varied.

Here, the sensing performance of hybrid plasmonic nanosensor geometries consisting of stacked gold and palladium nanodisks in direct contact is investigated. It is realized, by employing colloidal hole-mask lithography to fabricate the nanostacks [148], and performing hydrogen-dependent time-resolved transmittance measurements to investigate geometries with different material placement and number of constituent disks. Especially, we find that the order of materials in the nanostacks plays a crucial role for both, the sensitivity and the response time of the structures.

The resulting insight should ease the way to fabricate reliable, highly sensitive, low-cost hydrogen sensors with good temporal response that are ideally suited for technological applications.

6.2 THE PD-AU / AU-PD / AU-PD-AU NANOSTACK SYSTEMS

To conduct a thorough study on direct contact palladium gold nanodisk stacks, three alternating vertical arrangements of two or three nanodisks are investigated. Figure 6.1 shows a schematic view of the investigated designs. Each geometry was experimentally realized using hole-mask colloidal lithography, which produces disk stacks with high density, random placement and large-area coverage [149]. Therefore, this method is ideally suited for studying the plasmonic effects of such nanodisk stacks without the disturbance of grating effects [22] such as the Wood-anomaly [64]. An additional advantage of hole-mask colloidal lithography is the absence of any residual dielectric Poly(methyl methacrylate) (PMMA) resist from the fabrication process in contact with the disks.

Samples with different stacking geometries are characterized with a SEM as shown in the left column in Fig. 6.2, together with schematic views of the respective structures. All the Pd and Au disks have the same basic geometry, with a diameter of about 150 nm (lowest disk) and a thickness of about 20 nm. The cobweb-like structures around the disks in the SEM images arise from very small amounts of residual PMMA left over from the fabrication process. Still, the PMMA is sufficiently separated from the disk stacks to have no significant influence on their optical properties.

In the center column of Fig. 6.2, we show single particle scattering FEM simulations of the studied structures using tabulated constants for Au, Pd (blue curves) and PdH (red curves) [33, 49]. All systems exhibit a redshift and broadening of the plasmonic resonance, when using PdH dielectric data compared to Pd. The ensemble extinction spectra of fabricated large-area samples, which are measured in pure nitrogen atmosphere (blue curves) and with 4 vol % hydrogen in nitrogen carrier gas (red curves) using a white light transmission spectroscopy system, are shown in the right column in Fig. 6.2. The experimental results agree very well with the simulations, both considering the resonance width and position as well as the hydrogen

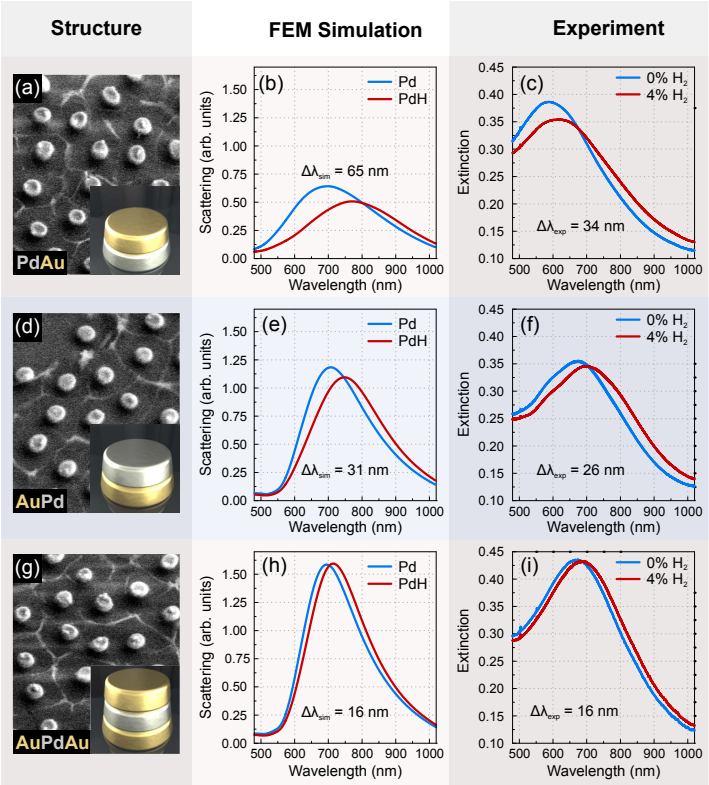

FIGURE 6.2. Simulated and measured spectra of the nanostack systems with (red curves) and without hydrogen (blue curves). (a), Exemplary scanning electron microscope (SEM) image of the Pd-Au system. (b), Single particle scattering finite element method (FEM) simulation of the Pd-Au system using tabulated Pd and PdH data. The spectra display a redshift and broadening when going from Pd to PdH. (c), Extinction measurements of the fabricated system showing the same qualitative behavior as the simulations. (d) - (i) SEM images, simulation and measurement data for the other two nanostack systems.

sensing performance, which manifests as a red-shift and broadening of the plasmonic resonance upon hydrogen exposure.

However, there are some visible differences between experiment and simulation. Particularly, in the case of the Pd-Au nanostack, the fabricated structures exhibit a plasmonic resonance at lower wavelengths when compared to the simulated structures. This can mostly be attributed to material defects or fabrication tolerances, which may result in a smaller gold disk in the second layer, compared to the design in simulation (due to the clogging effect from the hole-masks). It is challenging to determine the size difference, since SEM measurements cannot distinguish between palladium and gold, and element-resolved transmission electron microscope (TEM) methods cannot be easily applied to samples fabricated using hole-mask colloidal lithography.

The difference between the measured and numerically predicted resonance shifts in the Pd-Au system can be attributed in part to material defects and palladium-gold alloying, which are more significant when the palladium is placed below the gold disk. Apart from the resonance shift, all other properties such as the predicted hydrogen-induced changes in resonance amplitude and width are well reproduced in the experiment.

When focusing on the hydrogen sensing performance of our nanostack geometries, we find a clear difference between the fist (Pd-Au) and the remaining two systems (Au-Pd, Au-Pd-Au).

- The Pd-Au stack shows a relatively broad resonance which is blue-shifted compared to the other systems. However, the resonance change upon hydrogen exposure is relatively large (65 nm in simulation and about 34 nm in experiment). Thus, this system can be considered '*palladium-like*', due to the strong influence of the palladium disk on the overall plasmon resonance.

- The second category systems (Au-Pd, Au-Pd-Au) exhibit a relatively narrow resonance more similar to the one of a sole gold disk. Upon hydrogen exposure, there is a resonance red-shift with a relatively small decrease in resonance amplitude. Thus,

in contrast to the *palladium-like* stack, the gold disk is the main driver of the plasmonic resonance, rendering the whole system more '*gold-like*'. This becomes obvious when considering that the Au-Pd-Au system (which includes two gold disks, coupled through the palladium disk) exhibits the narrowest resonance with virtually no change in resonance amplitude upon H_2 exposure.

Synopsizing, the Au-Pd-Au system shows the strongest and narrowest resonance with a full width at half maximum (FWHM) of approx. 210 nm, but only a small wavelength shift of 16 nm upon hydrogenation. The Au-Pd stack with a somewhat larger FWHM of about 235 nm in the unhydrogenated state and 255 nm as Au-PdH, exhibits twice the hydrogen-induced wavelength shift of almost 30 nm. For the Pd-Au system we have a significantly larger resonance width, with a FWHM of about 310 nm. Nevertheless, in exchange, the system yields larger wavelength shifts upon hydrogenation.

6.3 TEMPORAL RESPONSE OF THE SYSTEMS

To evaluate the performance of a plasmonic geometry for hydrogen sensing applications, it is not only important to look at the final optical response at various hydrogen concentrations, but also to study the temporal behavior of such a device. For example, in the context of industrial hydrogen sensing, detector geometries with a large optical change upon hydrogen exposure are only useful if the change happens within a reasonable timescale. As a consequence, the hydrogen loading and unloading dynamics for various concentrations in all previously discussed stacking geometries have been investigated.

In the experiments, ensemble extinction spectra were recorded every 5 s while the samples were exposed to sequences of different hydrogen concentrations in nitrogen carrier gas at a constant gas flow-rate of 1 l/min. The concentration sequence starts with 200 s of 0.5 vol % H_2 in N_2, followed by 200 s of pure nitrogen, then 200 s at 1 vol % H_2 and so on, until a maximum H_2 concentration of 5 vol % H_2

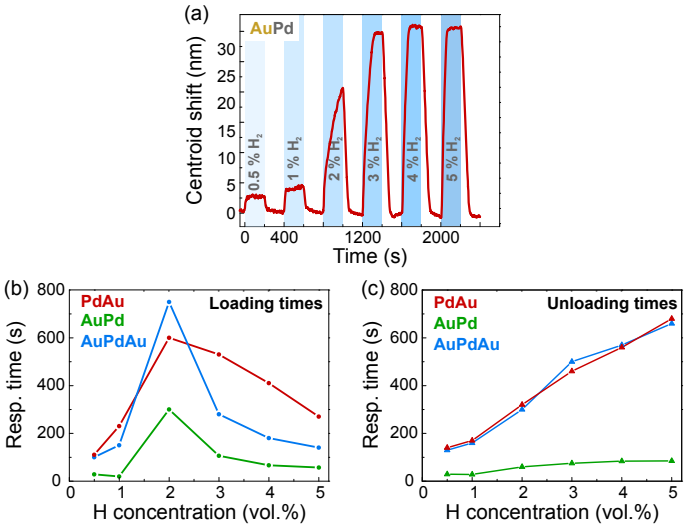

FIGURE 6.3. (a), Exemplary time trace of the centroid wavelength shifts upon a sequence of hydrogen gas exposure, going from 0.5 to 5 vol % H_2 in N_2 for the Au-Pd system. (b), Extracted loading times for different hydrogen concentrations for all three sensing geometries. Note, the exceptionally high loading time for 2 vol % H_2 observed in all systems is related to a phase transition from α- to β-phase in PdH_x. (c), Extracted unloading times for the same concentration steps as in (b) for all three sensing geometries. All systems show a distinct reaction to the different hydrogen concentrations, where the Au-Pd system performs the fastest in both loading and unloading times (< 100 s, except at 2 vol % H_2).

in N_2 is reached. Figure 6.3 shows the resulting time-dynamics of the plasmon-peak wavelength for the three geometries exposed to such a hydrogen sequence. The plasmon peak positions for the different stacks (exemplary shown for the Au-Pd stack in Fig. 6.3(a) and for the other systems in Fig. 6.4) are obtained by employing a centroid method that calculates the center of mass of the extinction peak. This method offers a very robust and reliable way of detecting even small peak-shifts independent of the peak shape and noise in the spectral data [138, 150]. As already mentioned, the two-layer stack with gold as

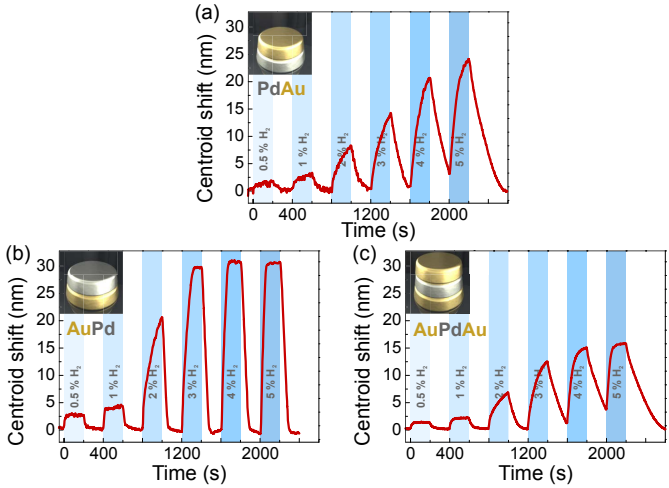

FIGURE 6.4. Time traces of the centroid wavelength shifts upon a representative cycle of hydrogen gas exposure, changing from 0.5 – 5 vol % hydrogen in nitrogen for (a) the Pd-Au system, (b) the Au-Pd system, and (c) the Au-Pd-Au system. All three systems exhibit a distinct reaction to the different hydrogen concentrations, where the Au-Pd system performs the fastest and exhibits the strongest reaction with a 30 nm redshift.

a lower disk gives a strong shift of about 30 nm. However, this geometry not only exhibits a large plasmon resonance shift, but also shows the fastest loading and unloading behavior with about 50 s to reach the maximum response for 5 vol % H_2 (see Fig. 6.3(a) and green lines in Fig. 6.3(b) and (c)).

The other two geometries with the palladium disk placed below the gold disk (Pd-Au, Au Pd Au) both show dramatically longer loading and unloading times (blue and red lines in Fig. 6.3(b) and (c)). At 5 vol % H_2, for example, unloading times above 200 s are observed for both cases as well as loading times of about 100 s (Au-Pd-Au) and even above 200 s for the Pd-Au case. Since, all samples were measured directly after fabrication and manufactured using the same materials under the same conditions, the strong differences in the temporal behavior cannot be attributed to material differences or sample degradation [21].

Since the open surface area of the palladium plays a crucial role for both the loading and unloading process, it is easy to understand that the geometry with the palladium disk on top and hence the highest relative open surface area, exhibits the fastest hydrogen ab- and desorption processes. In the other two systems (Pd-Au, Au-Pd-Au), the Pd disk is effectively buried between a gold disk and either another disk or the substrate. Therefore, only the sidewalls of the disks provide the needed catalytic surface for splitting and absorbing hydrogen molecules or in case of unloading the available surface area for hydrogen recombination. This leads to a strong increase in both loading and unloading times, since all hydrogen ions have to ab- and desorb through the bottleneck of the sidewalls. Concerning loading times, the three-disk Au-Pd-Au stack is still reacting slightly faster than the Pd-Au system. This is probably due to the fabrication process, which leads to strongly decreasing disk diameters for increasing stack heights. Therefore, the third disk is disproportionately smaller than the lower two disks, leading to a higher open surface for the middle disk and a accelerated reaction process.

All recorded time-traces show that no matter how fast any of the sensors reacts, the maximum centroid shift is only concentration dependent up to a value of about 3 vol % H_2 in N_2 (see Fig. 6.3(a)). For higher concentrations, only the reaction time changes, but not the shift amplitude. Additionally, the maximum shift per concentration shows a strong rise at about 2 vol % from less than 5 nm for lower concentration to over 10 nm shift for higher H_2 concentrations, accompanied with a strongly enlarged loading time at 2 vol % H_2 (see maxima in Fig. 6.3(b)).

This is a typical behavior for palladium nanostructures and relates to the occurrence of a phase transition between the so-called α- and β-phases in palladium hydride, where hydrogen ions are either interstitial (α-phase) or build in chemically as PdH_x (β-phase, with $0.2 < x < 0.7$)[14]. For bulk palladium, this phase transition sets in at about 15 to 20 mbar H_2 partial pressure (approx. 2 vol % H_2 in N_2 at room temperature and ambient pressures), leading to a saturation behavior for higher concentrations. As we have seen in Chapters 4 and 5, nanostructured Pd can have increased transition pressures compared

to bulk [28, 69, 70, 72]. To avoid the saturation effect in sensing applications at high partial hydrogen pressures, palladium can be alloyed with other metals such as Au, Ni, or Ag [21].

The time-resolved measurements in Fig. 6.3 clearly show that it is not only important to study the maximum optical response of any nanoplasmonic sensing scheme, but also take into account the relative '*free surface area*' of the system, which strongly alters its temporal response. Depending on the target application, both systems have specific advantages. If large wavelength shifts upon hydrogen exposure (hence large sensitivities) are required, *palladium-like* system such as the Pd-Au nanostacks are ideally suited. However, if the main focus is on fast reaction times, a system with a large Pd open surface area is advantageous, leading to fast loading and unloading times at the expense of smaller hydrogen-induced spectral shifts.

6.4 SINGLE PARTICLE SIMULATIONS

To further explore the origin of the strong differences in sensing performance for the various stacked hydrogen-sensing geometries, it is instructive to also examine the electric fields and current densities of the respective geometries in addition to the spectral shifts. Due to the challenges associated with mapping plasmonic near-fields experimentally, we concentrate on FEM simulations of our system.

To accurately represent the experimental geometries, we modeled truncated Au and Pd cones with a bottom diameter of 150 nm and a tapering angle of about 8.5°. The simulations were performed using the CST Microwave Studio (CST) 2014 FEM solver with single structures placed on an infinite SiO_2 substrate. Single particle simulations are required, since ensemble simulations using randomly placed structures are not possible with our simulation tool and any periodic assembly would give rise to grating effects [64].

The calculated single particle scattering spectra for the two two-disk stacks are shown in Fig. 6.5(a) (green and red curves), together

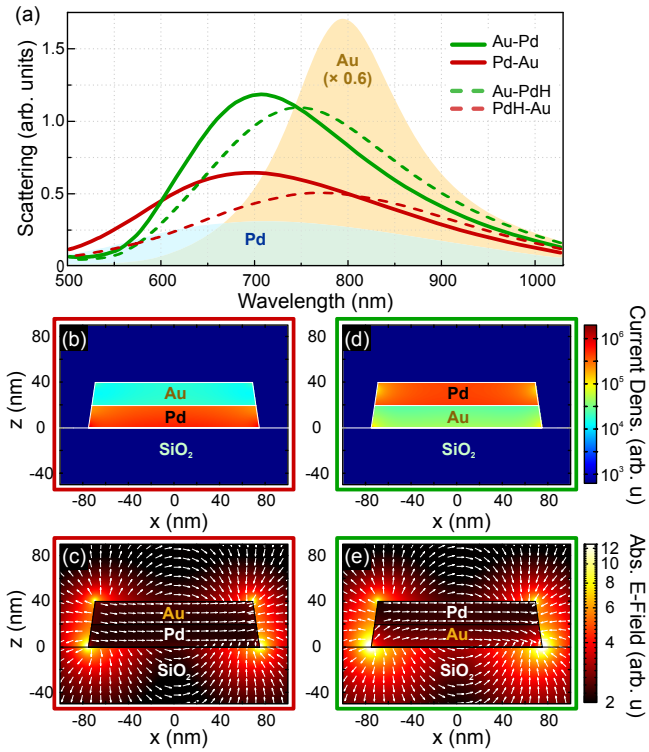

FIGURE 6.5. (a), Calculated single particle scattering spectra for the Au-Pd (green) and Pd-Au system (red) in the hydrogenated (dashed lines) and unhydrogenated states (solid lines). The Au-Pd system exhibits a stronger resonance and is blue-shifted compared to the Pd-Au system. Nevertheless, both systems show a red-shift and broadening of the resonance when going from Pd to PdH. Additional spectra for a sole Au (dark yellow shaded) and Pd disk (light blue shaded area) are included for comparison. (b), Calculated current densities for the Pd-Au system at the resonance frequency showing strong optical currents in the palladium nanodisk. (c), Calculated absolute electric fields together with the field vectors for the same geometry and frequency as in (b), depicting the strongest field at the bottom edge of the structure and in-phase oscillations in the Au and Pd disks. (d), Current densities and (e). Electric fields of the Au-Pd system which exhibit notably enhanced fields and currents in the Au disk, compared to the geometry in (b) and (c).

with the respective spectra for single Au and Pd disks on SiO_2 (yellow and blue shaded areas). Figure 6.5, panels (b) - (e) show the logarithmically plotted current densities and absolute values for the electric field on a cut-plane through the middle of the structures at the respective resonance frequencies. When considering the electric fields in the two- and three-disk stack geometries (Fig. 6.5(c), (e) and Fig. 6.6(b)), we observe a clear dipolar pattern for all systems. Importantly, the electric fields inside the disks are oriented in phase, indicating that the sandwich system can actually be considered as a single plasmonic resonator. This is mainly due to the fact that all disks are in direct conductive contact. Additionally, both the Au and Pd disk exhibit plasmonic resonances between 600 nm and 800 nm, resulting in spectral overlap and consequently similar resonant properties (see yellow and blue shaded areas in Fig. 6.5(a)).

For the Pd-Au structures (red curve in Fig. 6.5(a) and Fig. 6.5(b) and (c)) the plasmon resonance is broadened compared to the Au-Pd system. The reason for this can be understood again by examining the current densities in the metal nanodisks (Fig. 6.5(b) and (d)). Nearly all of the oscillating optical currents are located in the Pd-part of the disk-stack. This is for two reasons.

- First, palladium has a higher intrinsic electronic damping than gold ($\varepsilon_{2_{Pd}} > \varepsilon_{2_{Au}}$), which leads to higher Ohmic losses in the material and consequently higher optical currents in the relevant wavelength region ($\sigma_{opt} \propto \varepsilon_2$). Therefore, in that spectral region, the palladium structures always exhibit a higher current density than the gold, independent of the geometrical arrangement.

- Second, and more relevant for understanding the differences between the two systems in Fig. 6.5, the palladium disk is in contact with the substrate and hence to a material with a significantly higher refractive index compared to the air surrounding the upper gold disk. For nanostructures, contact to high refractive index materials leads to a concentration of energy close to the interface. The main reason for the different behavior of the Au-Pd and Pd-Au systems with- and without substrate is the

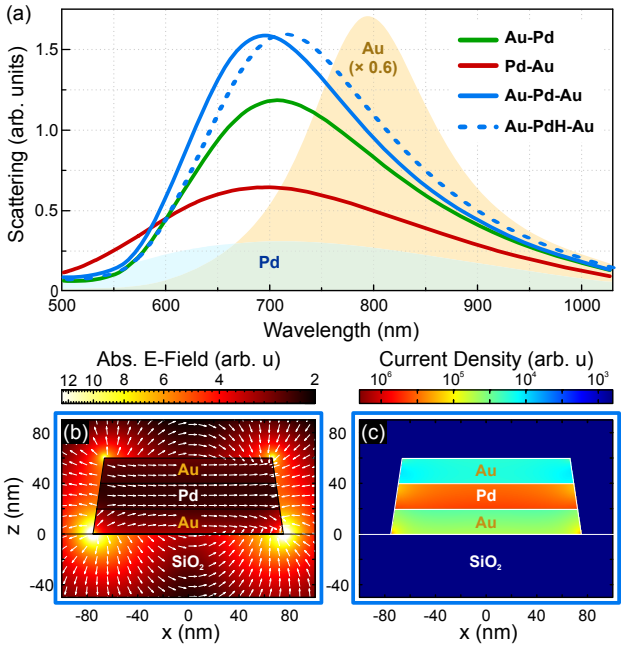

FIGURE 6.6. (a), Calculated single particle scattering spectra of the Au-Pd-Au disk stack in the unhydrogenated (blue solid line) and hydrogenated state (blue dashed line), demonstrating that the structure exhibits a blue-shift and signal increase compared to the respective two disk structure (Au-Pd). The spectra of the two disk stacks and single disks are also plotted (green and red lines) for comparison. (b), Calculated absolute electric fields together with the field vectors for the Au-Pd-Au structure on SiO_2. The field vectors show that, at resonance, the electric field oscillates in phase in all three disks, resulting in a collective resonance for all the particles. (c), Calculated current densities for the same structure.

break of symmetry. Otherwise, both systems would essentially give the same field and spectral results (see Fig. 6.7).

Taking into account the substrate effect and the fact that the disk-stack can be treated as one resonator, we find that the collective electron oscillations in the Pd-Au stack lead to a more damped resonance

in the blue wavelength region that can be seen as more *palladium-like*. However, in the Au-Pd case, we have a narrower, stronger and red-shifted resonance that acts more *gold-like*. This is supported by the stronger electric fields and the higher optical currents in the gold disk (see Fig. 6.5(b) and (d)).

When moving from the two-disk stacks to the more complex Au-Pd-Au sandwiches, which are displayed in Fig. 6.6, further insight can be gained. The two gold antennas enhance the oscillator strength to induce the strongest resonance of all systems, as shown in the unhydrogenated spectra (blue solid line in Fig. 6.6(a)). The spectra are blue-shifted, with higher scattering amplitudes, compared to the Au-Pd two-disk stack (green line). However, the resonances of both systems are still very similar, since the addition of another (gold) disk on top (and therefore farther away from the substrate) has little effect on the Au-Pd-Au system that exhibits a *gold-like* resonance similar to the Au-Pd stack. The field-plot in Fig. 6.6(b) and the current densities in Fig. 6.6(c), draw further evidence for the collective oscillations of all three disks. The strongest fields occur at the edges of the lowest disk while the strongest currents are situated in the gold.

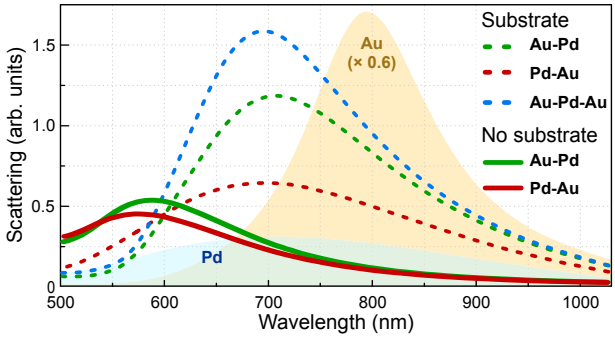

FIGURE 6.7. Comparison between the calculated scattering spectra for nanodisk stacks with substrate (colored dashed lines) and without substrate (green and red solid line). Without substrate the two systems Au-Pd and Pd-Au only differ slightly, due to the differences in disk-size between upper and lower disk. Only the introduction of a substrate renders the Au-Pd system *gold-like* and the Pd-Au system *palladium-like*.

The blue-shifted resonance wavelength of the Au-Pd-Au system compared to the Au-Pd stack results from the increase in total height of the combined system, which leads to a blue-shift of the plasmonic resonance as long as the other dimensions remain constant [151]. Intuitively, an additional gold-disk should produce increased oscillator strength, near-field enhancement, and consequently the largest hydrogen-induced changes. However, the Au-PdH-Au spectra plotted in Fig. 6.6(a) exhibit the smallest wavelength shifts of all investigated geometries.

These results become obvious, when examining the electric near-fields in Fig. 6.6(b). In fact, the addition of a top Au disk moves the hotspots of the electric field away from the Pd disk, resulting in lower sensitivity. This is supported by the current densities in the Pd disk (Fig. 6.6(c)), which are significantly lower than in the two-disk cases.

6.5 CONCLUSIONS

I have shown - theoretically and experimentally – the plasmonic behavior as well as the hydrogen sensing performance of different stacked direct contact palladium and gold nanodisks. Moving towards a different direction in comparison to the majority of indirect sensing schemes in the literature, where direct contact between materials was considered detrimental, we find that the direct-contact palladium-gold disk nanostacks show very good sensing results and are easily implemented.

One intriguing aspect of the direct contact scheme is that, despite the stacks being comprised of individual gold and palladium nanostructures, they form one collective plasmonic mode. This mode can behave more *gold-* or *palladium-like*, depending on the stacking order. We find that the material directly adjacent to the substrate determines the character of plasmonic response of the complete system. Consequently, if one is looking for the system that shows the best sensitivity while being less demanding concerning the reaction times, it is best to use a *palladium-like* structure. In case, the application focuses mainly

on the temporal sensing performance, it is most useful to consider a direct contact scheme with palladium on top, such as the investigated Au-Pd stack.

Overall, the investigations show a promising path towards low-cost, large-area, easy to fabricate direct contact hydrogen sensors. Variations in size and form of the antennas can be considered to further optimize the resonance quality and sensing performance of the systems. Our geometries can easily be implemented in many of the optical sensing devices that have been developed [11, 21], since the nanostructures yield high signal modulation over large areas and have no restrictive demands on the substrate materials.

7

SWITCHABLE PLASMONICS USING YTTRIUM NANOANTENNAS

A key challenge for the development of active plasmonic nanodevices is the lack of materials with fully controllable plasmonic properties. In this chapter that was adapted from our publication in ref. [30], we show that plasmonic resonances in top-down nanofabricated yttrium antennas can be completely and reversibly turned on and off using hydrogen exposure. We fabricated arrays of yttrium nanorods and optically observed the hydrogen-induced phase transition between the metallic yttrium dihydride and the insulating trihydride. Whereas the yttrium dihydride nanostructures exhibit a pronounced particle plasmon resonance, the transition to yttrium trihydride leads to a complete vanishing of the resonant behavior. The plasmonic resonance in the dihydride state can be tuned over a wide wavelength range by simply varying the size of the nanostructures. Furthermore, an analytical diffusion model is developed, that is able to explain the temporal behaviour of the hydrogen loading and unloading process observed in experiments and gain information about the thermodynamics of the device. Thus, the investigated nanorod system serves as a versatile basic building block for active plasmonic devices ranging from switchable perfect absorbers to active local heating control elements.

7.1 INTRODUCTION

Plasmonics has evolved into a broad and important field of nanooptics that enables a variety of new applications [32, 152, 153]. By creating

local hotspots of the electric field on the nanometer scale, it is possible to develop very sensitive chemical and biological sensor devices and locally initiate and control chemical processes [154, 155]. In recent years, plasmonics has expanded towards active nanophotonic devices, that can be reconfigured using external stimuli such as laser pulses [156], mechanical strain [157–160], heat [161], or electrical currents [162, 163]. Furthermore, the realization of active plasmonic devices requires a move from widely used but passive metals such as silver or gold towards novel materials systems [164]. This allows additional degrees of freedom in device design and enables external control over the optical response of a plasmonic nanostructure without having to directly modify its geometry [165, 166].

Phase change materials provide an ideal toolkit for the realization of active nanodevices. Several materials with heating- or laser-induced switching behavior, such as vanadium-dioxide (VO_2) [161, 167–169], gallium lanthanum sulphide (GLS) [170] or germanium antimony telluride (GST) [171–173] have already been investigated in the context of plasmonics.

In 1996, Huiberts *et al.* [174] discovered a switchable mirror effect in thin films of yttrium when exposed to hydrogen gas. They demonstrated that a fully reflecting metallic yttrium mirror becomes dielectric and almost completely transparent after absorbing a sufficient amount of hydrogen. This work was expanded to the field of nanoparticles by Stepanov *et al.* [175, 176], who showed that hydrogenated spherical yttrium nanoparticles under ultrahigh vacuum conditions can have switchable Mie resonances.

Here, reconfigurable YH_x nanoantennas are introduced. They are fabricated via electron beam lithography and exhibit a pronounced plasmonic resonance in their metallic YH_2 state. The resonance wavelength and width can be widely tuned by variation of the antenna dimensions. Compared to the very small, bottom-up produced nanoparticles from Stepanov, Bour, and Gartz *et al.* [175, 176], we demonstrate antennas and antenna assemblies with large oscillator strength and varying size, showing custom-designed plasmonic properties in the near- and mid-IR spectral regions. The transition between metallic

and dielectric yttrium hydride antennas is induced by simple hydrogen exposure from the gas phase or from electrolysis under ambient atmospheric conditions and shows a drastic change of the spectral response.

Compared to other promising phase change materials used in plasmonic devices, yttrium dihydride has the advantage of comparatively low intrinsic damping and can therefore support plasmonic resonances itself. Whereas, the metallic phases of VO_2, GST, or GLS are known to exhibit only a weak plasmonic response, if any. Despite the advantage of much faster switching times, they can often be only used in hybrid plasmonic systems, i.e., in combination with gold or other good plasmonic metals. However, the use of hybrid systems drastically lowers the switching contrast, since only the dielectric environment of the resonant material changes but not the antenna itself.

Therefore, yttrium dihydride is a highly relevant and very promising alternative for plasmonic applications that require a high switching contrast and are less dependent on ultrashort switching times. Furthermore, as a metal, yttrium and its hydrides can be structured easily using standard nanofabrication techniques.

During hydrogen absorption, metallic yttrium (Y) transforms first into yttrium dihydride (YH_2, Fig. 7.1a), which even has a higher electrical conductivity than pure yttrium. This phase change from a metal in *hcp* configuration into a *fcc* metal is non-reversible under normal conditions. Through further exposure to hydrogen, it undergoes a second, reversible, phase change into yttrium trihydride (YH_3,Fig. 7.1b), a transparent semiconductor with *hcp* structure. However, it is important to note that under normal hydrogen partial pressures (i.e., less than 1 bar near room temperature) full stoichiometric YH_3 cannot be realized [177], and the final state of the system reaches only $YH_{3-\delta}$, where δ is in the range of 0.1 to 0.3 (Under very high pressure $\delta = 0.01$ can be reached [178]). For simplicity, we will refer to this final state as yttrium trihydride (YH_3).

The transition from YH_2 to YH_3 induces strong and reversible changes in the dielectric properties that can be triggered at low partial

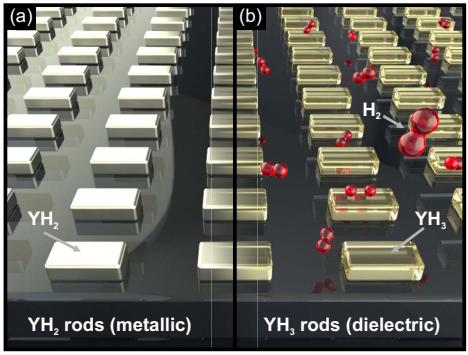

FIGURE 7.1. Schematic drawing of (a), a metallic yttrium dihydride (YH_2) nanorod array on a fused silica substrate in hydrogen-free environment and (b), the formation of dielectric yttrium trihydride (YH_3) nanorods under hydrogen exposure.

pressures of hydrogen. Even though yttrium hydride thin films exhibit a large hysteresis effect [179], the ability to switch reversibly (in the sense that after a full hysteresis loop it returns to the original dihydride phase) from metal to a transparent semiconductor upon hydrogen absorption makes yttrium an attractive candidate for active plasmonic applications. Moreover, due to the drastic change from metal to insulator, the plasmonic response vanishes completely when the yttrium is in the trihydride phase and recovers when switched back into the yttrium dihydride phase.

7.2 SPECTRAL CHANGES SWITCHING FROM YTTRIUM DIHYDRIDE TO YTTRIUM TRIHYDRIDE NANOPARTICLES

To demonstrate the functionality of such a switchable plasmonic system, we fabricate arrays of yttrium nanorods (Fig. 7.2). We choose nanorods as a model system because they exhibit a strong plasmonic

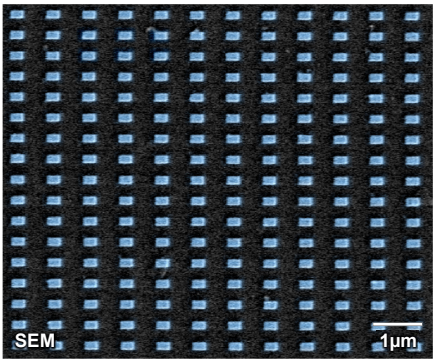

FIGURE 7.2. Exemplary (colored) SEM image of the fabricated YH_2 nanorods.

response and approximately dipole-like behavior. Therefore they constitute an ideal development platform for new plasmonic materials such as yttrium dihydride.

For the experimental realization, we prepare PMMA masks on a fused silica substrates using a standard electron beam lithography process [180]. Afterwards, yttrium and platinum are evaporated onto the developed PMMA mask via electron beam assisted evaporation. Platinum on top of the yttrium rods serves as catalytic layer to dissociate the H_2 molecules into atomic hydrogen. Hydrogen can then be incorporated into the yttrium lattice to form the hydride states. Catalytic materials such as platinum or palladium next to yttrium are necessary because yttrium itself is not able to catalytically dissociate H_2 molecules into atomic hydrogen. Additionally, the platinum cover prevents oxidation at the top surface of the yttrium rods. Such oxidation is common in transition metals like yttrium, which easily form an oxide layer (Y_2O_3) of several nanometers when exposed to oxygen [176]. This impedes hydrogen from penetrating into the particle volume. Although the thin layer of platinum introduces some additional damping to our system, the overall influence on the plasmonic response is weak.

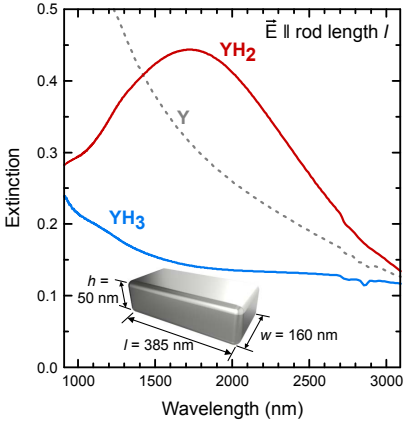

FIGURE 7.3. Extinction spectra of yttrium, YH_2 and YH_3 nanorods. The metallic YH_2 rods (red line) show a distinct particle plasmon resonance at 1720 nm. In contrast, the YH_3 rods (blue line) are almost transparent in the same spectral region. The increased extinction in Y nanorods (grey dotted line) towards lower wavelengths can be attributed to the tail of a broad electronic transition in yttrium occurring at around 400 nm what makes them unsuitable for plasmonic applications.

Figure 7.3 shows typical extinction spectra of the different hydrogenation states of yttrium nanoantennas measured with a commercial Fourier transform infrared spectroscopy system (Bruker Vertex 80 FTIR + Bruker Hyperion). The incident light is focused using a Cassegrain objective (15x) with numerical aperture NA = 0.4, and the transmitted intensities are detected with both, a Si and a InGaAs diode. The incident polarization is set along the long axis of the nanorods with infrared polarizers. The measured transmittance spectra I_T are normalized with respect to the substrate signal I_S and converted into extinction values via $I_{ext} = -\ln(I_T/I_S)$. The displayed rods in Fig. 7.3 have lateral dimensions of 385 nm × 160 nm and a height of 50 nm yttrium plus 6 nm platinum.

Pure yttrium is a metal with relatively low electrical conductivity [181, 182]. Therefore, Y nanoantennas do not exhibit a distinct plasmonic response in the visible and near-IR spectral region (grey

dotted line in Fig. 7.3). The decrease in extinction towards longer wavelengths can be attributed to the tail of a very strong and broad electronic resonance at about 3.1 eV (400 nm) [183]. In contrast to Y, YH_2 is a good metal with a markedly different atomic and electronic structure [176, 184, 185]. To transform the yttrium into YH_2, we expose our sample to 4 vol.% hydrogen in nitrogen for 10 min. According to literature, this is more than sufficient to reach the dihydride and even the trihydride state [186]. However, the transition between yttrium and YH_2 is non-reversible at room temperature, whereas the second transition between YH_2 and YH_3 is fully reversible. Therefore, the rods automatically settle in the YH_2 state after the hydrogen is turned off and equilibrium is reached.

The red line in Fig. 7.3 shows an extinction spectrum of such a hydrogenated rod array in the YH_2 state. The YH_2 rods have a clear extinction maximum at approximately 1720 nm that can be attributed to a localized surface plasmon resonance. This YH_2 state can be seen as the ground state of our switchable plasmonic structure, because the system will not return to the unhydrided state without extremely harsh and destructive measures such as strong heating and ultra-high vacuum. Therefore the yttrium nanostructure can only be switched reversibly between the dihydride and trihydride phase. This is not a disadvantage, as there is a large contrast in extinction between YH_2 and YH_3 (see Fig. 7.3).

When continuously exposed to hydrogen (in this case 5 vol.% H_2 in N_2 at room temperature), the yttrium nanostructures switch into the trihydride phase within seconds. This dramatic change from a metal to a Mott-insulator leads to a drastic change in the extinction spectrum. In fact, yttrium hydride is one of the few strongly correlated systems with a continuous Mott-Hubbard metal-insulator transition [187, 188].

The particle plasmon resonance fully vanishes and the extinction spectrum becomes almost flat, as shown by the blue line in Fig. 7.3. This proves that it is possible to turn off the plasmon resonance completely, by introducing only small and safe amounts of hydrogen into the system. The switching results in a relative extinction change at

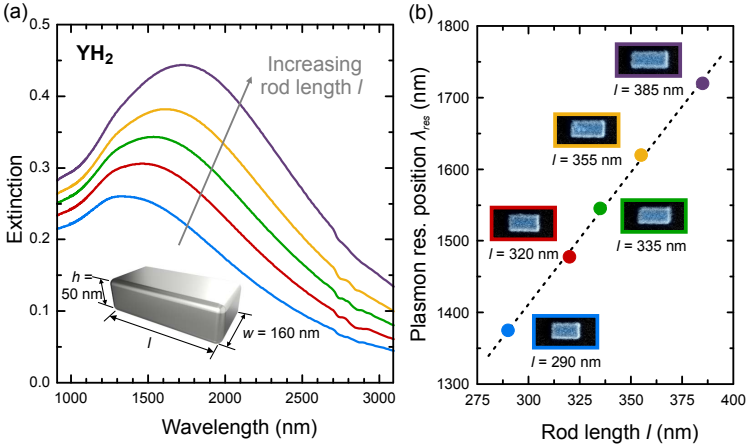

FIGURE 7.4. (a), YH_2 extinction spectra for various rod lengths l and constant width $w = 160$ nm and height $h = 50$ nm, showing a red-shift and increase in amplitude of the resonance for increasing rod lengths. (b), the extracted particle plasmon peak positions (colored dots) that scale linearly with rod length ($\lambda_{res} = 4.2 \cdot l + 115$ nm), as indicated by the black dashed line.

the peak wavelength (1720 nm) of almost 70 %, which translates to an absolute change in transmittance of 23 % that can easily be observed by the naked eye.

To incorporate yttrium nanostructures into switchable plasmonic devices, the ability to tune the plasmon resonance over a wide spectral range is needed. Here, the simplest approach is to vary the length of the plasmonic nanorods while leaving width and height constant.

Consequently, we fabricated yttrium rod arrays with constant width w of 160 nm and height h of 50 nm yttrium covered with 6 nm platinum, while varying the length from 290 nm to 385 nm. Figure 7.4 shows the change of the plasmon resonance for increasing rod length. For longer rods, we observe an enhanced extinction as well as a red-shift of the resonance wavelength. The increasing extinction can be attributed to the enhanced dipole strength that is caused by the increase in nanoparticle volume. Furthermore, the increased filling factor

of the arrays adds to the enlarged extinction, since the periodicity ($p_x = 700\,\text{nm}$ and $p_y = 400\,\text{nm}$) was keept unchanged, for all rod lengths. The red-shift of about 400 nm is a clear indication of a particle plasmon resonance that is highly correlated with particles dimension and shape.We find a linear relation between rod length l and plasmon resonance wavelength λ_{res}, shown in the inset of Fig. 7.4, which is in excellent agreement with theoretical and experimental knowledge about plasmon resonances in metal nanoantennas [189, 190]. The tuning range of our reconfigurable antennas is mainly limited at lower wavelengths due to a broad electronic transition at around 400 nm. At longer wavelengths, the YH_2 dielectric function follows a Drude-like behaviour and thus enables full tunability of the plasmonic resonance.

7.3 SWITCHING BEHAVIOR

To investigate the switching behaviour in our nanoantenna system in more detail, we study the temporal behavior of the extinction during hydrogen exposure. Figures 7.5 and 7.6 show the H_2 loading and the unloading process of an yttrium rod array with rod parameters $l = 290\,\text{nm}$, $w = 160\,\text{nm}$, $h_Y = 50\,\text{nm}$, $h_{Pt} = 6\,\text{nm}$ and a periodicity $p_{(x,y)} = 400\,\text{nm}$, measured at room temperature. We start in the YH_2 phase and a strong resonance at 1580 nm (red line, Fig. 7.5(a)). After exposing the system to hydrogen (5 vol.% H_2 in N_2), the resonance immediately flattens and continuously approaches the YH_3 spectrum where it saturates after approximately 50 seconds (blue line). The spectra in Fig. 7.5(a) show a typical set of FTIR measurements recorded during hydrogen uptake with one measurement every 4 seconds. In Fig. 7.5(b) the extinction time trace at 1580 nm (position of the YH_2 plasmon resonance) is displayed (green line), demonstrating an almost instantaneous reaction to hydrogen exposure. Within a few seconds, the extinction starts to drop from 0.62 with an almost constant slope of 2 % per second. This large change together with the reasonable response time makes the system well suited for active plasmonic devices. Moreover, the switching time from the dihydride to the trihydride phase

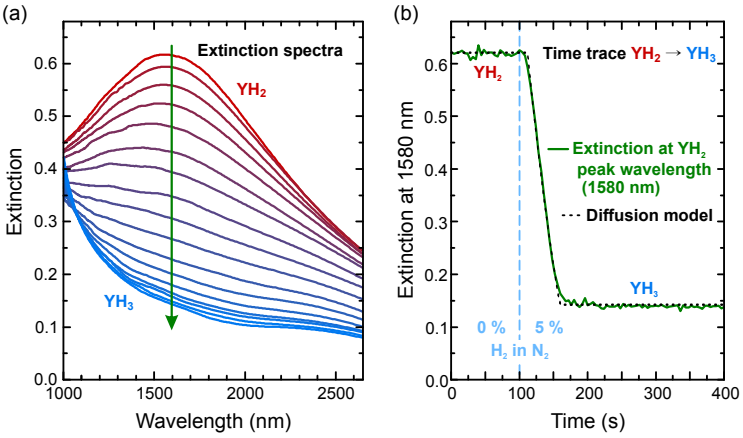

FIGURE 7.5. In situ hydrogenation loading dynamics of the yttrium nanorods at room temperature. (a), Extinction spectra taken every 4 s during hydrogen exposure. The phase transition from the metallic YH_2 (red lines) to the dielectric YH_3 (blue lines) can be clearly observed. (b), Full time trace of the measured extinction at a wavelength of 1580 nm. After 100 s the sample is exposed to 5 vol % hydrogen in nitrogen at constant pressure of 1 bar. The system almost instantly reacts and switches to the dielectric YH_3 state. The complete phase transition is completed within less than 50 s. The black dashed line shows the fit to our diffusion model.

increases monotonically with the hydrogen pressure as shown and explained by the diffusion model below.

Figure 7.6(b) shows the back reaction, moving from YH_3 to YH_2. This takes approximately 3 hours, which is significantly slower than the absorption reaction. There are several factors that lead to this slow transition. The key reason is the reduced out-diffusion of hydrogen due to the platinum capping layer and the oxidized sidewalls of the nanoantennas.

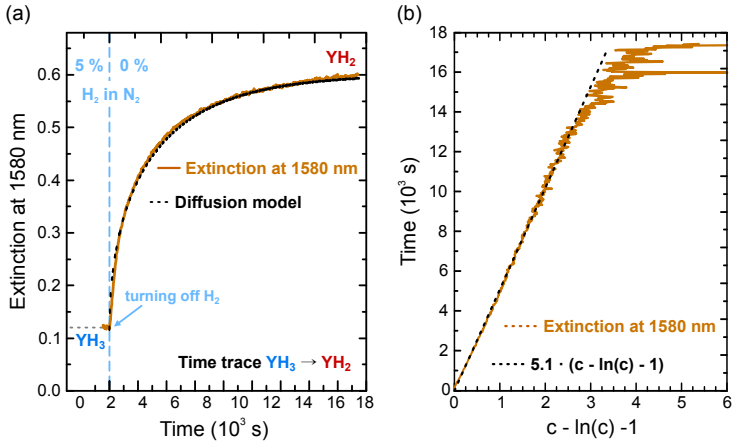

FIGURE 7.6. In situ hydrogenation unloading dynamics of the yttrium nanorods at room temperature. (a), Full unloading time trace of the measured extinction at a wavelength of 1580 nm. After the sample was exposed to 5 vol % hydrogen in nitrogen the system relaxes back into the metallic YH_2 state (orange line) being kept in a nitrogen atmosphere. The black dashed line shows the fit to our diffusion model. (b), Time trace of (a) renormalized to a range between 0 and 1 (named c for concentration) and then plotted as time versus $(c - 1 - \ln c)$ (orange line). The resulting straight line demonstrates the validity of our analytical diffusion model. The slope (5100 s) of the best fit straight line (black dashed line) yields the fitting parameter τ/f (see Eq. (7.23)).

7.4 ANALYTICAL DIFFUSION MODEL

In order to explain this asymmetry in the behavior of our system we developed an analytical one-dimensional diffusion model, following the ideas of Pasturel *et al.* [191]. The assumption of a 1D system is valid, since the oxidized side-walls of the nanorods channel the hydrogen flow through the platinum capping layer in and out of the yttrium-hydride nanostructures. The model incorporates the diffusion of atomic hydrogen through the caplayer and into the Y nanoantenna (see Fig. 7.7). Soon after exposition to hydrogen gas at pressure p_{H_2}, a stationary state is established with a linear concentration gradient in the

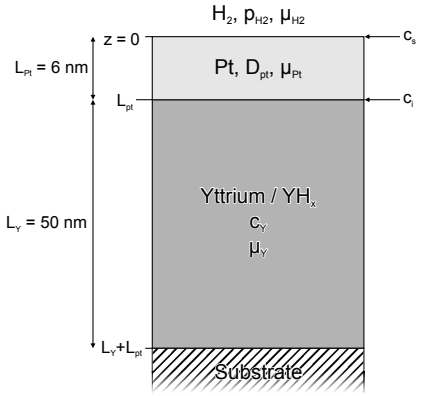

FIGURE 7.7. Sketch of a cut through an yttrium antenna, illustrating the important quantities of the one-dimensional diffusion model.

caplayer. The H current through the caplayer is then equal to the diffusion current j_{diff} into the Y antennas and we have

$$j_{diff} = \frac{D_{Pt}}{V_{Pt}} \cdot \frac{c_s - c_i}{L_{Pt}} = \frac{L_Y}{V_Y} \cdot \frac{dc_Y}{dt}, \tag{7.1}$$

where L_{Pt} is the thickness of the Pt caplayer, D_{Pt} the diffusion coefficient of H in Pt, L_Y the thickness of Y, and V_{Pt} and V_Y the molar volumes of Pt and Y, respectively. The H concentrations in the Pt layer are c_s at the surface and c_i at the Pt-Y interface. The H concentration in Y is c_Y.

To be able to solve Eq. (7.1),one needs to link the hydrogen concentrations at the surface of the caplayer c_s and at the interface c_i to the concentration in the Yttrium/YH_x layer c_Y. At the surface, thermodynamic equilibrium implies that the chemical potential of molecular H_2 is related to the chemical potential of H in Pt, through

$$\frac{1}{2}\mu_{H_2} = \mu_{Pt}, \tag{7.2}$$

as hydrogen dissolves atomically into Pt. The chemical potential of gaseous H_2 can be written as

$$\mu_{H_2} = RT \ln p_{H_2} + H_{H_2} - TS_{H_2} \tag{7.3}$$

with $S_{H_2} = 130.77$ J/(K mol(H2)), the standard molar entropy at 1 bar. The enthalpy H_{H_2} is essentially given by $7/2 \cdot RT$ where R is the ideal gas constant. The chemical potential of H at the surface of the cap-layer is

$$\mu_{Pt}\big|_{z=0} = RT \ln c_s + H_{Pt} - TS_{Pt} \tag{7.4}$$

The solubility of H in Pt is very low due to the positive enthalpy of H solution in Pt ($c_s \ll 1$).

Substituting Eqs. (7.3) and (7.4) into Eq. (7.2), we obtain

$$\frac{1}{2} RT \ln p_{H_2} = RT \ln c_s + \Delta H_{Pt} - T\Delta S_{Pt}, \tag{7.5}$$

where

$$\Delta H_{Pt} = H_{Pt} - \frac{1}{2} H_{H_2} \tag{7.6}$$

and

$$\Delta S_{Pt} = S_{Pt} - \frac{1}{2} S_{H_2} \cong -\frac{1}{2} S_{H_2} \tag{7.7}$$

are the enthalpy and entropy of hydride formation. The approximation on the right-hand-side of Eq. (7.7) is valid, as the entropy of hydrogen in a metal lattice is small compared to the one of gaseous hydrogen.

Solving Eq. (7.5) for c_s leads to

$$c_s = g \cdot \sqrt{p_{H_2}} \tag{7.8}$$

with

$$g = \exp\left(-\frac{\Delta H_{Pt} + 1/2\, T\Delta S_{H_2}}{RT} \right). \tag{7.9}$$

To obtain a relation between the hydrogen concentration c_Y in the Y layer and the concentration c_i at the Pt-Y interface, we use the continuity of the chemical potential at the interface between the two layers. Thus, with

$$\mu_{Pt}\big|_{z=L_{Pt}} = RT \ln c_i + H_{Pt} - TS_{Pt} \tag{7.10}$$

at the Pt-Y interface, and

$$\mu_Y = RT \ln \frac{c_Y}{1 - c_Y} + H_Y - TS_Y \tag{7.11}$$

for the chemical potential of H in the Y layer. The continuity of the chemical potentials at the Pt-Y interface

$$\mu_{Pt}\big|_{z=L_{Pt}} = \mu_Y\big|_{z=L_{Pt}} \tag{7.12}$$

leads to

$$c_i = f \cdot \frac{c_Y}{1 - c_Y} \tag{7.13}$$

width

$$f = \exp\left(\frac{\Delta H_Y - \Delta H_{Pt}}{RT}\right) \tag{7.14}$$

as S_{H_2} is much larger than S_Y and S_{Pt}.

Substituting Eqs. (7.8) and (7.13) into Eq. (7.1) leads to a differential equation describing both the diffusion in and out of our system

$$\frac{dc_Y}{dt} = \frac{m}{\tau}\left(g\sqrt{p_{H_2}} - f\frac{c_Y}{1 - c_Y}\right), \tag{7.15}$$

width

$$\tau = \frac{L_{Pt}L_Y}{D_{Pt}} \tag{7.16}$$

and

$$m = \frac{V_Y}{V_{Pt}} \tag{7.17}$$

During hydrogen loading at a given pressure p_{H_2}, we need to solve the full differential equation. This can be carried out by integrating the inverse function

$$t\left(c_Y\right) = \frac{\tau}{mf}\left(\frac{c_Y}{k+1} + \frac{1}{\left(k+1\right)^2} \cdot \ln\frac{1}{1 - c_Y\left(1 + 1/k\right)}\right) \tag{7.18}$$

with

$$k = \frac{g}{f}\sqrt{p_{H_2}}. \tag{7.19}$$

In the case of hydrogen loading and low concentrations c_Y, Eq. (7.18) can be approximated by a simple straight line

$$c_Y\left(t\right) \cong \frac{m\,g}{\tau}\sqrt{p_{H_2}} \cdot t \tag{7.20}$$

with slope

$$\frac{dc_Y}{dt} = \frac{m\,g\sqrt{p_{H_2}}}{\tau} \tag{7.21}$$

as shown in Fig. 7.8(a).

The measured loading curve in Fig. 7.6b resembles this linear behavior very well. By normalizing the measured extinction values to the interval $[0, 1]$, one finds $mg\sqrt{p_{H_2}}/\tau \approx 1/46$.Since, $p_{H_2} = 0.05\,\text{bar}$ during the loading process, we have $mg/\tau = 0.097/\text{bar}$.

To validate the assumptions of a square root pressure dependency for the loading process, we performed loading measurements with various partial pressures of hydrogen on a new nanorod array sample. We used loading pressures of 0.05 bar, 0.1 bar and 0.2 bar H_2 gas (in nitrogen gas) and performed extinction measurements, taking a spectrum every 2 seconds. The time traces of the extinction maxima (particle plasmon resonance) for the three loading pressures are renormalized to the interval $[0, 1]$ and plotted in Fig. 7.8(b). By fitting straight lines to the three curves, we can extract the slope from

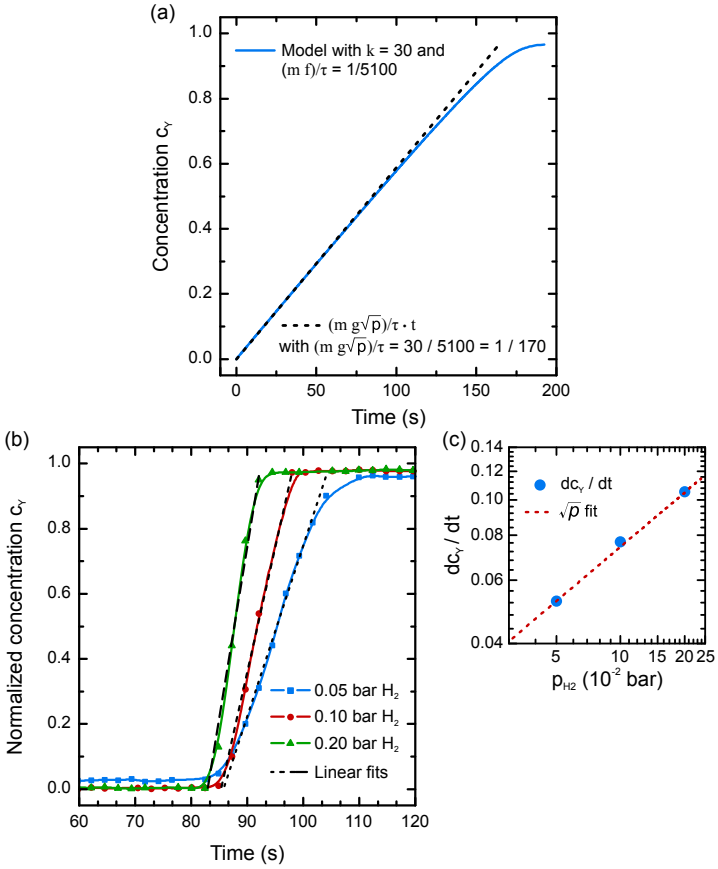

FIGURE 7.8. (a), Comparison between full solution of the diffusion model and a straight line with slope $\left(m\,g\sqrt{p}\right)/\tau$. (b), Time trace of hydrogen loading measurements with hydrogen pressures of 0.05 bar, 0.1 bar and 0.2 bar H_2, extracted from extinction measurements and renormalized to $[0, 1]$. (c), The slopes of the three curves with the expected hydrogen pressure dependence of $\sqrt{p}$ derived in the model.

Eq. (7.21) for all three pressures p_{H_2}. These values nicely resemble the square root dependency on the pressure as predicted by the model (see the log-log plot in the inset of Fig. 7.8b). The deviations between the slopes from Fig. 7.5(b) and Fig. 7.8(b) can be explained by fabrication differences between the two samples and the different age and quality of the platinum caplayer.

For the hydrogen unloading process the derived differential equation Eq. (7.15) reduces to

$$\frac{dc_Y}{dt} = -\frac{mf}{\tau}\left(\frac{c_Y}{1-c_Y}\right). \tag{7.22}$$

As the external hydrogen pressure p_{H_2} is zero, this equation can be solved again using the inverse function and subsequent integration to give

$$t\left(c_Y\right) = -\frac{\tau}{mf}\left(c_Y - c_\infty + \ln\frac{c_\infty}{c_Y}\right). \tag{7.23}$$

Under the chosen experimental conditions we expect c_∞ to be close to unity. A plot of time versus $\left(c_Y - \ln c_Y - 1\right)$, thus, is a straight line with slope $\tau/\left(mf\right)$. Figure 7.6(b) shows the measured unloading data from Fig. 7.6(a) normalized to the range from 1 to 0 (orange line) plotted over $\left(c - \ln c - 1\right)$. The measured data points follow a straight line with slope $\tau/\left(mf\right) = 5100\,\mathrm{s}$. Deviations at higher times (for c close to 0) are merely due to noise in the measurement data. The excellent agreement between model and experimental data for both hydrogen loading and unloading, strongly supports the validity of the assumptions made in its derivation. As

$$m = \frac{V_Y}{V_{Pt}} = \frac{19.88}{9.09} = 2.19 \tag{7.24}$$

we find $f/\tau = 9\times10^{-5}\,\mathrm{s}^{-1}$.

With $D_{Pt} = 3\times10^{-7}\,\mathrm{cm}^2/\mathrm{s}$ derived from an extrapolation of Katsuta and McLellan diffusity data [192] to room temperature, we find

$$\tau = \frac{L_{Pt}L_Y}{D_{Pt}} = 1\times10^{-5}\,\mathrm{s} \tag{7.25}$$

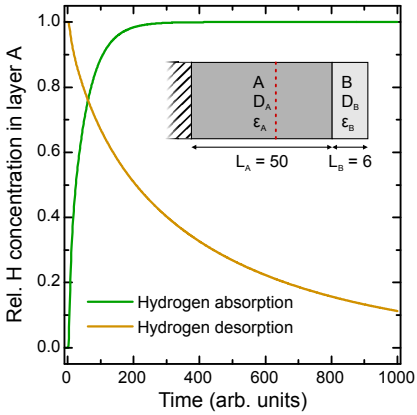

FIGURE 7.9. Diffusion time trace calculated at 30 nm distance from the substrate (red dotted line) for both the absorption (green line) and desorption process (yellow line) of hydrogen, using the numerical diffusion model of Pasturel *et al* [191]. The inputs used for the simulation were the diffusion parameters $D_A = 50$, $D_B = 20$ and the dimensionless energy parameters $\varepsilon_A = 8.2$ and $\varepsilon_B = -4.6$.

and thus $f = 9 \times 10^{-10}$.

From the definition of f and $\Delta H_Y \cong -40\,\mathrm{kJ/mol\,(H)}$ from van Gogh *et al.* [181] we find $\Delta H_{Pt} \cong 8\,\mathrm{kJ/mol\,(H)}$ for the enthalpy of hydrogen solution for the platinum layer. The value is smaller than $\Delta H_{Pt} \cong 35\,\mathrm{kJ/mol\,(H)}$ for bulk Pt [92]. This might be due to partial alloying of platinum with the underlying yttrium rod (supported by the fact that the enthalpy of a Y-Pt alloy is very negative $\Delta H_{Y-Pt} = -247\,\mathrm{kJ/mol\,(H)}$ [193]). Additionally, the surface roughness of the thin caplayer ($L_{Pt} = 6\,\mathrm{nm}$) could play an important role, especially if taking into account the large lattice expansions occurred during the initial loading of the antenna from pure Y to dihydride YH_2.

At this point it is worth investigating whether the large asymmetry between loading and unloading times is due to a particular choice of parameters. It is in fact easy to show that it is a robust property only related to the low solubility of H in the caplayer. From Eq. (7.1)

follows that, at half loading, i.e. when $c_Y = 0.5$, ($c_i = f$ according to Eq. (7.13)) the H particle current is proportional to $(c_s - c_i)$. During unloading the driving gradient is $(c_s - c_i) = -c_i = -f$ as the surface concentration is at best 0. During loading, however, relatively large values of the surface concentration can be set up so that $(c_s - f) \ll f$. For metals with a low solubility f is very small (for Pt, $f = 2 \times 10^{-9}$, see above) and $c_s \ll 2f$ is already satisfied at relatively low pressures (in our case, for $p > 0.01$ bar).

We see that the asymmetry between the loading and unloading times can be explained by the high (and in this case even positive) solution enthalpy of platinum. This conclusion is also supported by a simple 1D diffusion calculation using the numerical model of Pasturel *et al.* [191] and typical parameters for yttrium and platinum (see Fig. 7.9 that shows how differences in solution enthalpies lead to a strong asymmetry between absorption and desorption times, e.g. with the choosen realistic parameters, the desorption is 10 times slower than the absorption).

Since the enthalpy of solution depends on the nanoscale structure and thickness of the platinum, it will be of interest to conduct further studies on the optimal thickness and material of the capping layer in order to obtain shorter switching times without interfering with the plasmonic properties of the system. Even without such optimizations both the diffusion limited absorption and desorption process can be accelerated by heating the sample.

7.5 NUMERICAL SIMULATIONS

Good agreement between experimental results and theoretical/numerical predictions is crucial for the efficient and robust design of switchable devices. To verify this for our yttrium nanoantenna system, we perform numerical simulations of the optical response using a commercial FEM solver (CST® Microwave Studio) and periodic boundary conditions (unit cell $700 \times 400\,\mathrm{nm}^2$). The optical constants of yttrium and the different hydrides are taken from literature [181, 194].

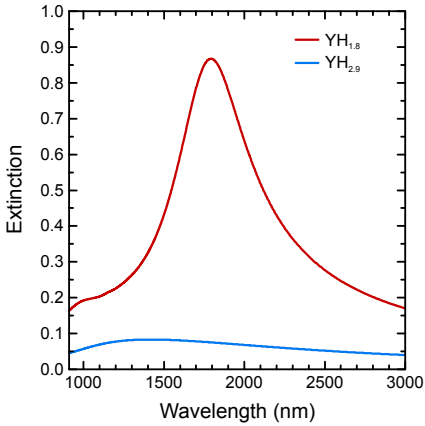

FIGURE 7.10. Calculated extinction spectra, using tabulated dielectric data from van Gogh *et al.* [181]. The metallic yttrium dihydride exhibits a plasmonic resonance at 1800 nm (red line) whereas the dielectric trihydride has a negligible extinction signal (blue line).

Here, the dielectric functions of $YH_{1.8}$ and $YH_{2.9}$ from van Gogh *et al.* [181] provide the closest match to the yttrium hydride states that were investigated in our measurements and identified as YH_2 and YH_3, respectively. The numerical results for such YH1.8 and YH2.9 nanorod arrays rod antenna dimensions $380 \times 160 \times 50\,nm^3$ on a glass substrate ($n_{SiO_2} = 1.5$) are shown in Fig. 7.10.

Whereas the $YH_{2.9}$ results are in good agreement with the measured data (almost flat response), the $YH_{1.8}$ spectra require closer attention. Figure 7.11 shows the numerical results for a YH_2 + Pt nanorod array on a fused silica substrate as a green dotted line. In this simulation we use the complex dielectric function of $YH_{1.8}$ from van Gogh *et al.* [181], and Pt from Weaver [195], respectively. The rods are assumed to have dimensions of $380 \times 160 \times 56\,nm^3$ and periodicities of $700 \times 400\,nm^2$ in accordance with SEM measurements on the fabricated structures. The measured spectrum is shown as a solid black line in Fig. 7.11. Comparing the black solid and green dotted line, we can observe significant differences. The numerical extinction peak is

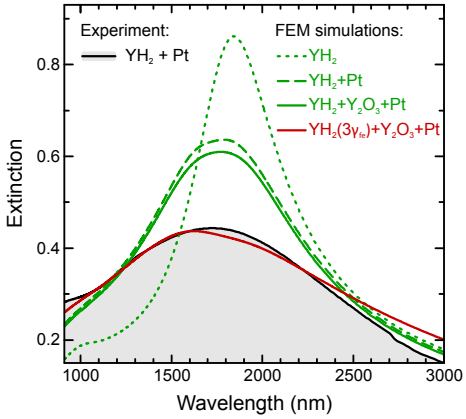

FIGURE 7.11. Comparing the experiment to FEM simulations of the yttrium rod system. The black line shows the experimental spectrum of a YH_2 nanorod array with parameters $l = 380\,\text{nm}$; $w = 160\,\text{nm}$; $h_{YH_2} = 50\,\text{nm}$; $h_{Pt} = 6\,\text{nm}$. The green lines show simulated data for the same system using tabulated dielectric data. However, the simulated spectra for YH_2 rods with platinum cover (green dotted line) show a resonance, which is much narrower and slightly red-shifted compared to the experimental data. This mismatch cannot be compensated by simply introducing a surrounding yttrium oxide shell (dashed green line) into the simulation. Only an additional increase of the free electron damping γ_{fe} in the YH_2 dielectric function by a factor of three is able to fully reproduce the experimental data (red line).

much narrower, higher in amplitude and red-shifted compared to the measured one.

Since, both experiment and simulation, return absolute values for the extinction, the reason for the significant quantitative deviation has to be found in the modeling of the simulated nanorod system itself. One major deviation between the model and the experimental system is the yttrium oxide (Y_2O_3) layer that forms at all yttrium surfaces, which are not protected from oxygen. This layer has a thickness of a few nanometers [176, 182] and forms at the side walls of the yttrium rods, since, they are not protected by either the substrate or the platinum cover layer. If we assume an oxide thickness of 3 nm and

replace the outermost 3 nm in our model's sidewalls with dielectric Y_2O_3, using a constant refractive index of $n = 1.93$ [196], we obtain the dashed green line in Fig. 7.11. Even though the discrepancy between simulation and experiment is slightly reduced, there is still a key ingredient missing to match the experimental data. In our previous calculations, we have used a dielectric function of $YH_{1.8}$ measured on extended thin films with thicknesses in the 300 nm range, prepared and characterized under ultra-high vacuum conditions [181]. However, the nano-structuring process (PMMA masking, electron-beam assisted evaporation) can introduce impurities and defects into our nanorod system. Combined with the higher reactivity of yttrium and its desire to form yttrium oxide, this leads to a deterioration of the plasmonic properties. The effect becomes especially pronounced, when moving from extended films to nanoparticle structures. One way of measuring the impact of the nanostructuring on the yttrium dielectric function quantitatively would be to perform ellipsometry on such a nanorod array. However, this is not feasible due to the low reflectance of the arrays at glancing angles.

In general, surface modifications as well as impurities in a plasmonic material lead to a decreased free electron life time τ_{fe} compared to the film that was used in [181]. Therefore, there is an enhanced free electron damping $\gamma_{fe} = 1/\tau_{fe}$ in our system.

To modify the dielectric function of yttrium dihydride with this assumption, we first fit a Drude model together with a harmonic oscillator to the YH_2 dielectric data following the approach of Gartz *et al.* for unhydrided yttrium [183].

Gartz *et al.* [183] have shown that it is possible to describe the dielectric function of yttrium by

$$\varepsilon(\omega) = \varepsilon_\infty + \frac{S_{osc} \cdot \omega_{osc}^2}{\omega_{osc}^2 - \omega^2 - i\omega\gamma_{osc}} - \frac{\omega_p^2}{\omega^2 + i\omega\gamma_{fe}}. \tag{7.26}$$

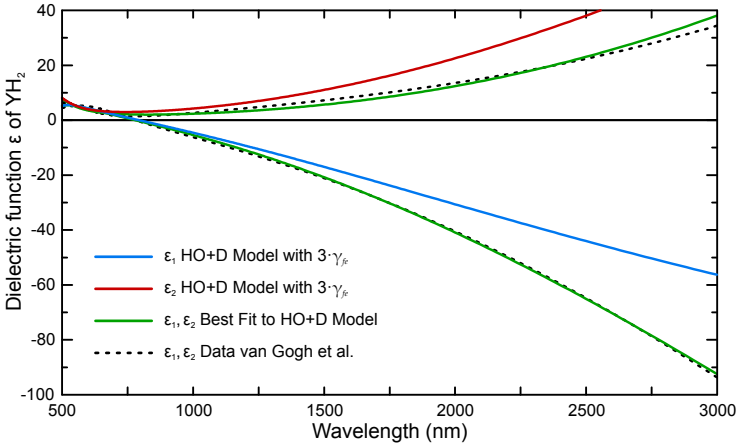

FIGURE 7.12. Dielectric function of YH_2 in the visible and NIR range. The black dashed lines shows the measured dielectric function ($YH_{1.8}$) by van Gogh *et al.* [181] on a continuous yttrium film. The green lines represent the best fit to the van Gogh *et al.* data using a combined harmonic oscillator and Drude (HO+D) model. The blue and the red curve show the real (ε_1) and imaginary part (ε_2) of the modified dielectric function that describes well the present nanoantenna data. The dielectric function is calculated with the HO+D model and a 3 times enhanced $\gamma^*_{fe} = 3 \cdot \gamma_{fe}$ compared to the green line.

Here, the first part represents a standard harmonic oscillator with oscillator strength S_{osc}, oscillator frequency ω_{osc} and a damping constant γ_{osc}. The second term represents the Drude theory for metals including the plasma frequency ω_p and the free electron damping γ_{fe}.

The model is quite general and can be used to describe many metals [62]. Therefore, we used it as basis to fit the dielectric function of YH_2 (see Fig. 7.12) and found the following parameters:

$$\begin{aligned} S_{osc} &= 3.41 \\ \omega_{osc} &= 4.2 \times 10^{15}\ \mathrm{s}^{-1} \\ \gamma_{osc} &= 1.4 \times 10^{15}\ \mathrm{s}^{-1} \\ \omega_p &= 6.7 \times 10^{15}\ \mathrm{s}^{-1} \\ \gamma_{fe} &= 2.4 \times 10^{14}\ \mathrm{s}^{-1} \end{aligned} \tag{7.27}$$

Except for some small deviations, the model reproduces the experimental values of van Gogh *et al.* [181]. The harmonic oscillator part is only significant between 500 nm and 1000 nm (Fig. 7.12). Therefore, changing the oscillator damping will not affect the plasmonic resonance situated around 2 µm. Hence, the Drude part of the model and in particular the free electron damping needs to be adjusted to explain our experimental data. The red and blue lines in Fig. 7.12 show how changing the free electron damping affects the real and imaginary part of the dielectric function.

If we want to incorporate the previously discussed impurities and defects into our simulation, we can increase the free electron damping in the dielectric function without changing other parameters. Increasing the damping constant γ_{fe} by a factor of three is reasonable, since the nanofabrication process strongly alters the structure of the yttrium compared to yttrium films used for ellipsometry measurements in literature. Hence, we get

$$\gamma_{fe}^{*} = 3 \cdot \gamma_{fe} = 7.2 \times 10^{14}\ \mathrm{s}^{-1}. \tag{7.28}$$

With all influences included (platinum cover, yttrium oxide layer, enhanced intrinsic damping), we obtain excellent agreement with the measured data, as exemplified by the red line in Fig. 7.11, verifying the hypothesis of an increased intrinsic damping in our samples.

7.6 CONCLUSIONS

It was shown that yttrium nanostructures offer an exciting new pathway for the design of active plasmonic devices by utilizing hydrogen-induced metal insulator transitions. I have demonstrated that YH_2 nanorods exhibit a pronounced particle plasmon resonance in the NIR spectra region which can be tuned over a wide spectral range. The resonance can be switched off within several seconds by introducing hydrogen into the system, transforming the nanorods into dielectric YH_3. After the hydrogen exposure is stopped, the plasmonic

resonance slowly returns to its original form, demonstrating the full reversibility of the transition.

In addition, we found a way to model the corresponding diffusion process analytically and gain knowledge about the thermodynamic quantities of our system. The model gives us the ability to further improve the material system in the future, aiming for a fast and reliable switching device. Consequently, we also modeled the dielectric properties and the plasmonic behavior of our YH_2 nanoantennas. The resulting adjustments provide a powerful tool to predict the behavior of any yttrium based plasmonic nanodevice. They even allow us to make quantitative predictions about the resonance width and position of more complex nanostructures.

In the future, yttrium nanostructures can form a crucial building block in the realization of a variety of plasmonic switching schemes. Possible applications include switchable plasmonic EIT [197] or switchable plasmonic perfect absorber devices [19], where the hydrogen concentration can be adjusted by changing the voltage in a simple electrochemical cell setup [198]. Furthermore, the system can be used as a hydrogen detector through monitoring the slope of the YH_2 to YH_3 phase transition. Another interesting application could be the local control over chemical processes that require a certain activation energy. This energy can then be provided by the enhanced local electric fields, generated by the plasmonic resonance. Throug adjusting the surrounding hydrogen/proton concentration one can influcene the amount of energy provided.

Due to its high refractive index, YH_3 can even act as high-index nanophotonic material ($n \approx 2.8$ at 600 nm [181, 199]), which supports electric and magnetic Mie resonances [200, 201] that can be switched on and off using hydrogen. Other transition metals, such as vanadium [202] or scandium, and also transition metal alloys like Mg-Y, Mg-La, Mg-Sc, and Mg-Gd, may provide even faster response times [203–206]. Complete blackness and thus highest switching contrast is expected using nickel-metal-hydrides (such as Mg_2MeH_x, with

Me = Ni, Co, Fe) [207]. Finally, studies of the Mott-Hubbard metal-to-insulator phase transition in rare earth and lanthanide hydride nanostructures as function of structure size, morphology, etc., can enable a whole family of intriguing experiments.

8

CONCLUSIONS AND OUTLOOK

8.1 CONCLUSIONS

This thesis covered many different aspects of metal hydrogen interaction. Through the use of plasmonics, the knowledge about the interplay between hydrogen, palladium and yttrium nanostructures was extended and new routes to applications have been shown.

In Chapter 2, we first reviewed the basic principles plasmonics. Plasmons are electron gas oscillation in metal nanostructures. Their resonances depend on the electronic properties of the material, the geometry of the nanostructure and on the dielectric environment. These properties render it a powerful metrology tool for measuring intrinsic and extrinsic properties of nanomaterials.

In Chapter 3 we developed an analytical description of plasmonic resonances in oblate spheroidal nanoparticle. We demonstrated using some reasonable simplifications and assumption that it is possible to separate the geometrical contributions from the dielectric contributions and linking both to the plasmon resonance frequency. In doing so, we determine the dielectric properties of a nanosized material (to be exact the factor E that is a combination of the real and imaginary part of the dielectric function, see Section 3.4), when knowing the size, dielectric environment and plasmonic resonance frequency of a nanoparticle. Analyzing the shape of the resonance, the additional factor F could be retrieved, too, enabling us to restore the full dielectric functions for gold and palladium nanosquares. The developed model and experimental setting was used in Chapter 5 to study the transition from palladium to palladium hydride and calculate the dielectric function of palladium hydride over a wavelength range of 800 nm to

8000 nm. These calculations are of special interest, since determining the dielectric properties of (three dimensionally) nanostructured materials over a large wavelength range have not been demonstrated so far.

The transition from palladium to palladium hydride was also the main topic in Chapter 4. In this chapter, a model for the ab- and desorption dynamics in palladium nanostructures based on literature experimental data was developed. The model reveals that the hydrogen absorption process in Pd nanoparticles can occur coherently, whereas the desorption process is happening incoherently. In a fully coherent process the whole particle is loaded in the α-phase and then transforms coherently into the β-phase. It involves elevated loading plateau pressures, since not stress-releasing dislocations can be formed. A fully incoherent process implies that the particles can form domains of β-phase early on, lowering the loading plateau pressure and leading to a small loading-unloading hysteresis. In bulk palladium both the ab- and desorption process are realized incoherently. Therefore, the possibility of coherent loading thermodynamically distinguishes nanoparticles from bulk. The fully coherent absorption process is only obeyed by nanoparticles small enough to withstand the coherency stress induced by loading the full particle in α-phase without forming stress-releasing dislocations and β-phase domains. The critical size is temperature dependent and seems to be somewhere around 35 nm at room temperature.

The thermodynamical and optical models of the two previous chapters were used to study palladium square patches in Chapter 5.We gained information about the size-dependent loading pressures, the in- and out-of-plane nanoparticle expansion and the dielectric properties of palladium hydride. The results that were obtained through experimentally measured plasmon resonances of various sized square patches. We could demonstrate that polycrystalline palladium nanostructures followed an almost linear increase in loading plateau pressures from 16 mbar to 22 mbar, when increasing the in-plane size of the square-patches from 200 nm to 2500 nm. This increase in loading pressure is probably closely related to the decreasing in-plane expansion that was observed at the same time. Surface energy reduction

mechanisms and partial clamping to the substrate and are found to be responsible for these effects. These results locate the measured square patches in the intermediate region between the single crystalline nanoparticles studied in Chapter 4 and bulk palladium.

We have seen that plasmonics can assist in retrieving thermodynamic and dielectric properties of metal hydride nanostructures. However, it can also be employed to monitor the hydrogen pressures impinging on the nanostructures. The search for the optimal sensing geometry was the topic of Chapter 6. Here, the known method of combining palladium sturctures with gold nanoantennas was used to introduce a new and easy-to-produces Au+Pd disk stack hydrogen sensor. By comparing the sensitivity and temporal response of Au-Pd, Pd-Au, and Au-Pd-Au nanostacks, it was possible to identify the optimal system for a given application. Interestingly, all three systems plasmonically act as one *"super"*-disk with in phase current oscillations spanning over the whole stack. The fastest sensor was an Au-Pd stack that has the largest free surface area, accelerating the hydrogen uptake and release. However, due to the substrate, the largest part of the oscillating currents are located in the disk closest to the substrate. Therefore, the Pd-Au nanostack offers the highest sensitivity to hydrogen with resonance wavelength shifts up to 34 nm.

Palladium is a great hydrogen sensor material, due to the reversible and monotonous change in dielectric and geometric properties. Nevertheless, other metals, like lanthanum, magnesium or yttrium show more dramatic reactions to hydrogen, rendering them more suited for other hydrogen-related applications. Yttrium, for example, was already used in the mid 90's as a switchable mirror and as base material for hydrogenography. These applications are based on the fact that yttrium (after being converted to yttrium dihydride) undergoes a huge phase change from metal to transparent dielectric, when exposed to hydrogen. This reversible phase change is the base of the studies conducted in Chapter 7. We used the yttrium material system to realize, for the first time, a plasmonic switch, with plasmonic resonances (extinction maxima) that can be fully switched off (and on again) through controlled hydrogen exposure. By electron beam lithography and evaporation, we fabricated yttrium nanorods of various sizes and

demonstrated their size-dependent plasmonic resonances spanning over the full near-infrared wavelength range. These resonances were fully switches off using small hydrogen pressures below 50 mbar, realizing a wavelength-specific optical switch. The dynamic switching behavior was studied experimentally and perfectly modeled using an analytical one-dimensional two-layer diffusion model. A fast hydrogen loading ($\sim$ 20 s for *on* $\rightarrow$ *off*) and slow unloading ($\sim 10 \times 10^3$ s for *off* $\rightarrow$ *on*) was observed and explained with the limiting bottleneck of the necessary platinum cover layer. However, further optimization of the geometry and the use of thinner palladium cover layers promises unloading times in the range of seconds, opening up applications as switching devices in telecommunications or radar technology.

8.2 OUTLOOK

In the future, energy storage and the related research will be even more important. Therefore, unanswered questions on how hysteresis and defect formation in battery materials like nickel metal hydrides ($NiMeH_x$), other metal hydrides or even lithium (for lithium ion batteries) will still trigger a lot of research. Even though, our model for palladium nanoparticles hints first answers on how nanostructures of such hydrides behave, there are still many open questions left, from the influences of nanoparticle packing to the role of crystallinity. When going from palladium to other more complex materials and alloys, a whole new category of research topics opens up. We have already done a first step into this direction, by studying magnesium nanoparticles and their hydrogenisation [67]. We have seen that, similar to yttrium, magnesium undergoes a phase transition from a metal to a dielectric (MgH_2). However, the transition back to pure magnesium requires the use of oxygen (if performed at room temperature) and is not yet fully understood. The need of oxygen (and in some geometries even elevated temperatures) can also be used to '*freeze*' the particles in a particular state. Therefore, it is possible to do snapshots of the hydrogensiation and dehydrogenisation of magnesium particles using scanning near-field optical microscopy (SNOM) with sub

50 nm spacial resolution and the ability to see single domains developing inside a particle [208]. Further steps are the investigation of thermodynamic properties, like the the critical temperature, the absorption isotherms and the size-dependent transition pressure. Studying these properties is inevitable if one wants to find better hydrogen storage solutions. To perform these tasks new technologies have been established, enabling the direct observation and visualization of hydrogen absorption, diffusion and desorption processes. Narayan *et al.* [76] showed that an environmental transmission electron microscope (TEM) can be employed to visualize the dynamics of α- and β-phase domains in palladium (Pd) nanocubes. Ulvestad *et al.* [209] employed coherent X-ray diffraction imaging to investigate and visualize hydrogen induced strain formation in Pd nanocubes. These techniques, together with atomic force microscopy (AFM), SNOM and plasmonics are great ways to investigate and improve metal hydride nanoparticles on the nanometer level. Especially plasmonics is able to transfer microscopic optical, electronic and structural properties into the farfield, allowing for non-invasive in-situ studies of active metal hydrogen systems.

BIBLIOGRAPHY

[1] World Health Organization:
Review of evidence on health aspects of air pollution - REVIHAAP Project,
Tech. rep.,
2013,
P. 309.
Cit. on p. 1.

[2] The International Energy Agency:
Energy and Air Pollution - World Energy Outlook Special Report,
Tech. rep.,
2016,
P. 262.
Cit. on p. 1.

[3] W. McDowall and M. Eames: *Forecasts, scenarios, visions, backcasts and roadmaps to the hydrogen economy: A review of the hydrogen futures literature.* Energy Policy **34**, 1236–1250 (2006).
DOI 10.1016/j.enpol.2005.12.006, cit. on p. 1.

[4] G. Marbán and T. Valdés-Solís: *Towards the hydrogen economy?* Int. J. Hydrogen Energy **32**, 1625–1637 (2007).
DOI 10.1016/j.ijhydene.2006.12.017, cit. on p. 1.

[5] M. Armand and J.-M. Tarascon: *Building better batteries.* Nature **451**, 652–657 (2008).
DOI 10.1038/451652a, cit. on pp. 1, 65.

[6] D. Unruh, K. Pabst, and G. Schaub: *Fischer-Tropsch Synfuels from Biomass: Maximizing Carbon Efficiency and Hydrocarbon Yield.* Energy & Fuels **24**, 2634–2641 (2010).
DOI 10.1021/ef9009185, cit. on p. 1.

[7] L. Schlapbach: *Technology: Hydrogen-fuelled vehicles.* Nature **460**, 809–811 (2009).
DOI 10.1038/460809a, cit. on p. 1.

[8] B. Sakintuna, F. Lamari-Darkrim, and M. Hirscher: *Metal hydride materials for solid hydrogen storage: A review.* Int. J. Hydrogen Energy **32**, 1121–1140 (2007).
DOI 10.1016/j.ijhydene.2006.11.022, cit. on p. 2.

[9] L. Klebanoff and J. Keller: *5 Years of hydrogen storage research in the U.S. DOE Metal Hydride Center of Excellence (MHCoE).* Int. J. Hydrogen Energy **38**, 4533–4576 (2013).
DOI 10.1016/j.ijhydene.2013.01.051, cit. on p. 2.

[10] L. Boon-Brett, J. Bousek, G. Black, P. Moretto, P. Castello, T. Hübert, and U. Banach: *Identifying performance gaps in hydrogen safety sensor technology for automotive and stationary applications.* Int. J. Hydrogen Energy **35**, 373–384 (2010).
DOI 10.1016/j.ijhydene.2009.10.064, cit. on p. 3.

[11] T. Hübert, L. Boon-Brett, G. Black, and U. Banach: *Hydrogen sensors - A review.* Sensors Actuators B Chem. **157**, 329–352 (2011).
DOI 10.1016/j.snb.2011.04.070, cit. on pp. 3, 4, 167.

[12] U.S. DRIVE Partnership. (Driving Research and Innovation for Vehicle efficiency and Energy sustainability): *Hydrogen Storage Technologies Technical Team Roadmap Roadmap*,
Tech. rep. June,
2013.
Cit. on p. 3.

[13] F. A. Lewis: *The Palladium Hydrogen System*, 1 edition, Academic Press Inc. (London), 1967.
Cit. on pp. 4, 23, 134.

[14] T. B. Flanagan: *The Palladium-Hydrogen System.* Annu. Rev. Mater. Sci. **21**, 269–304 (1991).
DOI 10.1146/annurev.matsci.21.1.269, cit. on pp. 4, 129, 130, 134, 143, 147, 149, 160.

[15] R. Krishna, E. Titus, M. Salimian, O. Okhay, S. Rajendran, A. Rajkumar, J. M. G. Sousa, A. L. C. Ferreira, J. Campos, and J. Gracio: *Hydrogen Storage for Energy Application.* In: Hydrog. Storage, InTech (Rijeka, Croatia), 2012. ISBN 9789533070520, cit. on p. 4.

[16] B. D. Adams and A. Chen: *The role of palladium in a hydrogen economy.* Mater. Today **14**, 282–289 (2011). DOI 10.1016/S1369-7021(11)70143-2, cit. on pp. 4, 21, 129.

[17] B. Chadwick and M. Gal: *Enhanced optical detection of hydrogen using the excitation of surface plasmons in palladium.* Appl. Surf. Sci. **68**, 135–138 (1993). DOI 10.1016/0169-4332(93)90222-W, cit. on p. 4.

[18] C. Langhammer, E. M. Larsson, B. Kasemo, and I. Zorić: *Indirect Nanoplasmonic Sensing: Ultrasensitive Experimental Platform for Nanomaterials Science and Optical Nanocalorimetry.* Nano Lett. **10**, 3529–3538 (2010). DOI 10.1021/nl101727b, cit. on p. 4.

[19] A. Tittl, P. Mai, R. Taubert, D. Dregely, N. Liu, and H. Giessen: *Palladium-based plasmonic perfect absorber in the visible and its applications to hydrogen sensing.* Nano Lett. **11**, 4366–4369 (2011). DOI 10.1021/nl202489g, cit. on pp. 4, 152, 193.

[20] B. Xie, S. Zhang, F. Liu, X. Peng, F. Song, G. Wang, and M. Han: *Response behavior of a palladium nanoparticle array based hydrogen sensor in hydrogen-nitrogen mixture.* Sensors Actuators A Phys. **181**, 20–24 (2012). DOI 10.1016/j.sna.2012.04.036, cit. on p. 4.

[21] N. Strohfeldt, A. Tittl, and H. Giessen: *Long-term stability of capped and buffered palladium-nickel thin films and nanostructures for plasmonic hydrogen sensing applications.* Opt. Mater. Express **3**, 194 (2013). DOI 10.1364/OME.3.000194, cit. on pp. 4, 159, 161, 167.

[22] A. Tittl, H. Giessen, and N. Liu: *Plasmonic gas and chemical sensing.* Nanophotonics **3**, 157–180 (2014). DOI 10.1515/nanoph-2014-0002, cit. on pp. 4, 152, 154.

[23] N. Li, A. Tittl, S. Yue, H. Giessen, C. Song, B. Ding, and N. Liu: *DNA-assembled bimetallic plasmonic nanosensors.* Light Sci. Appl. **3**, 226 (2014).
DOI 10.1038/lsa.2014.107, cit. on pp. 4, 152.

[24] M. E. Nasir, W. Dickson, G. a. Wurtz, W. P. Wardley, and A. V. Zayats: *Hydrogen detected by the naked eye: Optical hydrogen gas sensors based on core/shell plasmonic nanorod metamaterials.* Adv. Mater. **26**, 3532–3537 (2014).
DOI 10.1002/adma.201305958, cit. on pp. 4, 152.

[25] R. Jiang, F. Qin, Q. Ruan, J. Wang, and C. Jin: *Ultrasensitive Plasmonic Response of Bimetallic Au/Pd Nanostructures to Hydrogen.* Adv. Funct. Mater. **24**, 7328–7337 (2014).
DOI 10.1002/adfm.201402091, cit. on pp. 4, 152.

[26] C. Wadell, S. Syrenova, and C. Langhammer: *Plasmonic Hydrogen Sensing with Nanostructured Metal Hydrides.* ACS Nano **8**, 11925–11940 (2014).
DOI 10.1021/nn505804f, cit. on p. 4.

[27] S. Bagheri, N. Strohfeldt, F. Sterl, A. Berrier, A. Tittl, and H. Giessen: *Large-Area Low-Cost Plasmonic Perfect Absorber Chemical Sensor Fabricated by Laser Interference Lithography.* ACS Sensors **1**, 1148–1154 (2016).
DOI 10.1021/acssensors.6b00444, cit. on p. 4.

[28] R. Griessen, N. Strohfeldt, and H. Giessen: *Thermodynamics of the hybrid interaction of hydrogen with palladium nanoparticles.* Nature Mater. **15**, 311–317 (2016).
DOI 10.1038/nmat4480, cit. on pp. 5, 65, 129, 161.

[29] N. Strohfeldt, J. Zhao, A. Tittl, and H. Giessen: *Sensitivity engineering in direct contact palladium-gold nano-sandwich hydrogen sensors [Invited].* Opt. Mater. Express **5**, 2525 (2015).
DOI 10.1364/OME.5.002525, cit. on pp. 5, 151.

[30] N. Strohfeldt, A. Tittl, M. Schäferling, F. Neubrech, U. Kreibig, R. Griessen, and H. Giessen: *Yttrium Hydride Nanoantennas for Active Plasmonics.* Nano Lett. **14**, 1140–7 (2014).
DOI 10.1021/nl403643v, cit. on pp. 6, 64, 128, 169.

[31] N. Strohfeldt: *Nanoplasmonic gas-sensing: Hydrogen sensors based on palladium nanoparticles*. Diploma thesis, University of Stuttgart, 2012.
Cit. on p. 7.

[32] S. A. Maier: *Plasmonics: Fundamentals and Applications*, 1 edition, Springer (New York), 2007.
ISBN 9780387331508, cit. on pp. 7, 11–13, 15, 117, 169.

[33] P. B. Johnson and R. W. Christy: *Optical Constants of the Noble Metals*, 1972,
DOI: 10.1103/PhysRevB.6.4370.
Cit. on pp. 11, 42, 154.

[34] P. Drude: *Zur Elektronentheorie der Metalle.* Ann. Phys. **306**, 566–613 (1900).
DOI 10.1002/andp.19003060312, cit. on p. 11.

[35] E. Kretschmann: *Die Bestimmung optischer Konstanten von Metallen durch Anregung von Oberflaechenplasmaschwingungen.* Zeitschrift fuer Phys. **241**, 313–324 (1971).
DOI 10.1007/BF01395428, cit. on p. 12.

[36] J. Homola, S. S. Yee, and G. Gauglitz: *Surface plasmon resonance sensors: review.* Sensors Actuators B Chem. **54**, 3–15 (1999).
DOI 10.1016/S0925-4005(98)00321-9, cit. on p. 13.

[37] C. F. Bohren and D. R. Huffman: *Absorption and Scattering of Light by Small Particles*, Wiley-VCH Verlag GmbH (Weinheim, Germany), 1998.
ISBN 9783527618156, cit. on p. 17.

[38] S. Link, M. B. Mohamed, and M. A. El-Sayed: *Simulation of the Optical Absorption Spectra of Gold Nanorods as a Function of Their Aspect Ratio and the Effect of the Medium Dielectric Constant.* J. Phys. Chem. B **103**, 3073–3077 (1999).
DOI 10.1021/jp990183f, cit. on p. 18.

[39] J. N. Anker, W. P. Hall, O. Lyandres, N. C. Shah, J. Zhao, and R. P. Van Duyne: *Biosensing with plasmonic nanosensors.* Nature Mater. **7**, 442–53 (2008).
DOI 10.1038/nmat2162, cit. on p. 19.

[40] E. R. Peck and S. Huang: *Refractivity and dispersion of hydrogen in the visible and near infrared.* J. Opt. Soc. Am. **67**, 1550 (1977).
DOI 10.1364/JOSA.67.001550, cit. on p. 19.

[41] N. Liu, M. L. Tang, M. Hentschel, H. Giessen, and A. P. Alivisatos: *Nanoantenna-enhanced gas sensing in a single tailored nanofocus.* Nature Mater. **10**, 631–636 (2011).
DOI 10.1038/nmat3029, cit. on pp. 19, 152.

[42] C. Langhammer, I. Zorić, B. Kasemo, and B. M. Clemens: *Hydrogen storage in Pd nanodisks characterized with a novel nanoplasmonic sensing scheme.* Nano Lett. **7**, 3122–7 (2007).
DOI 10.1021/nl071664a, cit. on pp. 19, 152.

[43] Y. Fukai: *The Metal-Hydrogen System Basic Bulk Properties.* Springer series in materials science, 2 edition, Springer-Verlag (Berlin Heidelberg), 2005.
ISBN 3-540-00494-7, cit. on pp. 20, 21, 99, 107, 129, 143.

[44] P. Patnaik: *A comprehensive guide to the hazardous properties of chemical substances*, 3 edition, John Wiley & Sons (), 2007.
ISBN 9780471714583, cit. on p. 20.

[45] H. Dambeck: *http://www.spiegel.de/wissenschaft/technik/energiewende-dank-wasserstoff-wind-im-tank-a-793840.html*, 2011.
Cit. on p. 20.

[46] N. N. Greenwood and A. Earnshaw: *Chemistry of the elements*, 1. ed., re edition, Pergamon Press (Oxford [u.a.]), 1986.
ISBN 0-08-022056-8, cit. on pp. 21, 24.

[47] F. D. Manchester: *Phase Diagrams of Binary Hydrogen Alloys*, Monograph edition, ASM International (), 2000.
ISBN 0-87170-587-7, cit. on pp. 22, 67, 69, 71, 74, 78, 93, 95.

[48] M. Khanuja, B. R. Mehta, P. Agar, P. K. Kulriya, and D. K. Avasthi: *Hydrogen induced lattice expansion and crystallinity degradation in palladium nanoparticles: Effect of hydrogen concentration, pressure, and temperature.* J. Appl. Phys. **106**, 093515 (2009).
DOI 10.1063/1.3253733, cit. on p. 23.

[49] K. Von Rottkay, M. Rubin, and P. A. Duine: *Refractive index changes of Pd-coated magnesium lanthanide switchable mirrors upon hydrogen insertion.* J. Appl. Phys. **85**, 408 (1999).
Cit. on pp. 23, 130, 140, 141, 154.

[50] H. Tompkins and E. A. Irene: *Handbook of ellipsometry*, William Andrew (), 2005.
Cit. on p. 26.

[51] A. R. Forouhi and I. Bloomer: *Optical dispersion relations for amorphous semiconductors and amorphous dielectrics.* Phys. Rev. B **34**, 7018–7026 (1986).
DOI 10.1103/PhysRevB.34.7018, cit. on p. 26.

[52] A. R. Forouhi and I. Bloomer: *Optical properties of crystalline semiconductors and dielectrics.* Phys. Rev. B **38**, 1865–1874 (1988).
DOI 10.1103/PhysRevB.38.1865, cit. on p. 26.

[53] C. F. Bohren and D. R. Huffman: *Particles Small Compared with the Wavelength.* In: Absorption and Scattering of Light by Small Particles, Wiley-VCH Verlag GmbH (Weinheim, Germany), 1983.
ISBN 9783527618156, cit. on pp. 28, 30.

[54] A. Sihvola: *Advanced mixing principles.* In: Electromagnatic Mixing Formulas and Applications, IET (The Institution of Engineering and Technology, Michael Faraday House, UK), 1999.
ISBN 9780852967720, cit. on p. 28.

[55] O. D. Kellogg: *Potentials as Solutions of Laplace's Equation; Electrostatics.* In: Foundations of Potential Theory, Springer Berlin Heidelberg (Berlin, Heidelberg), 1967.
ISBN 978-3-642-86748-4, cit. on p. 28.

[56] L. Landau and E. Lifshitz: *Static Magnetic Field*. In: Electrodynamics of Continous Media, Elsevier (Amsterdam, The Netherlands), 1984.
ISBN 9780080302751, cit. on p. 28.

[57] E. J. Zeman and G. C. Schatz: *An Accurate Electromagnetic Theory Study of Surface Enhancement Factors for Ag, Au, Cu, Li, Na, AI, Ga, In, Zn, and Cd*. J. Phys. Chem. **91**, 634–643 (1987).
DOI 10.1021/j100287a028, cit. on p. 29.

[58] W.-H. Yang, G. C. Schatz, and R. P. Van Duyne: *Discrete dipole approximation for calculating extinction and Raman intensities for small particles with arbitrary shapes*. J. Chem. Phys. **103**, 869 (1995).
DOI 10.1063/1.469787, cit. on p. 29.

[59] T. Jensen, K. L. Kelly, A. Lazarides, and G. C. Schatz: *Electrodynamics of noble metal nanoparticles and nanoparticle clusters*. J. Clust. Sci. **10**, 295–317 (1999).
DOI 10.1023/A:1021977613319, cit. on p. 29.

[60] I. Zorić, M. Zäch, B. Kasemo, and C. Langhammer: *Gold, platinum, and aluminum nanodisk plasmons: Material independence, subradiance, and damping mechanisms*. ACS Nano **5**, 2535–2546 (2011).
DOI 10.1021/nn102166t, cit. on p. 29.

[61] A. D. Rakic, A. B. Djurisic, J. M. Elazar, and M. L. Majewski: *Optical properties of metallic films for vertical-cavity optoelectronic devices*. Appl. Opt. **37**, 5271–83 (1998).
Cit. on pp. 33, 42, 47, 48, 59, 61–63, 130, 140, 142–144.

[62] M. Quinten: *Optical Properties of Nanoparticle Systems: Mie and Beyond*, 4 edition, John Wiley & Sons (Weinheim, Germany), 2010.
ISBN 3527633154, cit. on pp. 41, 191.

[63] U. Kreibig and M. Vollmer: *Optical Properties of Metal Clusters*. Springer Series in Materials Science, Springer Berlin Heidelberg (), 2013.
ISBN 9783662091098, cit. on p. 41.

[64] R. Wood: *XLII. On a remarkable case of uneven distribution of light in a diffraction grating spectrum.* Philos. Mag. Ser. 6 **4**, 396–402 (1902).
DOI 10.1080/14786440209462857, cit. on pp. 50, 154, 161.

[65] P. H. C. Eilers: *A perfect smoother.* Anal. Chem. **75**, 3631–3636 (2003).
DOI 10.1021/ac034173t, cit. on p. 52.

[66] M. W. Knight, N. S. King, L. Liu, H. O. Everitt, P. Nordlander, and N. J. Halas: *Aluminum for Plasmonics.* ACS Nano **8**, 834–840 (2014).
DOI 10.1021/nn405495q, cit. on p. 64.

[67] F. Sterl, N. Strohfeldt, R. Walter, R. Griessen, A. Tittl, and H. Giessen: *Magnesium as Novel Material for Active Plasmonics in the Visible Wavelength Range.* Nano Lett. **15**, 7949–7955 (2015).
DOI 10.1021/acs.nanolett.5b03029, cit. on pp. 64, 128, 198.

[68] M. Yamauchi, R. Ikeda, H. Kitagawa, and M. Takata: *Nanosize Effects on Hydrogen Storage in Palladium.* J. Phys. Chem. C **112**, 3294–3299 (2008).
DOI 10.1021/jp710447j, cit. on pp. 65, 69–72, 74, 75, 78, 80, 88, 90, 122, 146.

[69] R. Bardhan, L. O. Hedges, C. L. Pint, A. Javey, S. Whitelam, and J. J. Urban: *Uncovering the intrinsic size dependence of hydriding phase transformations in nanocrystals.* Nature Mater. **12**, 905–912 (2013).
DOI 10.1038/nmat3716, cit. on pp. 65, 68–72, 74–78, 80, 87, 88, 90, 106–109, 113, 117, 129, 161.

[70] A. Baldi, T. C. Narayan, A. L. Koh, and J. a. Dionne: *In situ detection of hydrogen-induced phase transitions in individual palladium nanocrystals.* Nature Mater. **13**, 1143–1148 (2014).
DOI 10.1038/nmat4086, cit. on pp. 65, 68–70, 75, 90–92, 95, 106–108, 110, 112, 113, 116, 124, 125, 129, 138, 161.

[71] G. Li, H. Kobayashi, J. M. Taylor, R. Ikeda, Y. Kubota, K. Kato, M. Takata, T. Yamamoto, S. Toh, S. Matsumura, and H. Kitagawa: *Hydrogen storage in Pd nanocrystals covered with a metal-organic framework.* Nature Mater. **13**, 802–806 (2014).
DOI 10.1038/nmat4030, cit. on pp. 65, 68, 69, 114.

[72] C. Wadell, T. Pingel, E. Olsson, I. Zorić, V. P. Zhdanov, and C. Langhammer: *Thermodynamics of hydride formation and decomposition in supported sub-10nm Pd nanoparticles of different sizes.* Chem. Phys. Lett. **603**, 75–81 (2014).
DOI 10.1016/j.cplett.2014.04.036, cit. on pp. 65, 68–72, 80, 112, 114, 117, 152, 161.

[73] C. Wadell: *Plasmonic Nanostructures for Optical Absorption Engineering and Hydrogen Sensing.* PhD thesis, Chalmers University of Technology, 2015.
Cit. on pp. 65, 68–75, 78, 80, 90, 106, 115, 117, 118, 122.

[74] S. Syrenova, C. Wadell, F. A. A. Nugroho, T. a. Gschneidtner, Y. a. Diaz Fernandez, G. Nalin, D. Świtlik, F. Westerlund, T. J. Antosiewicz, V. P. Zhdanov, K. Moth-Poulsen, and C. Langhammer: *Hydride formation thermodynamics and hysteresis in individual Pd nanocrystals with different size and shape.* Nature Mater. **14**, 1236–1244 (2015).
DOI 10.1038/nmat4409, cit. on pp. 65, 68–73, 78, 112, 115–117, 122, 129.

[75] T. C. Narayan, A. Baldi, A. L. Koh, R. Sinclair, and J. A. Dionne: *Reconstructing solute-induced phase transformations within individual nanocrystals.* Nature Mater. (2016).
DOI 10.1038/nmat4620, cit. on pp. 65, 130.

[76] T. C. Narayan, F. Hayee, A. Baldi, A. Leen Koh, R. Sinclair, and J. A. Dionne: *Direct visualization of hydrogen absorption dynamics in individual palladium nanoparticles.* Nature Communications **8**, 14020 (2017).
DOI 10.1038/ncomms14020, cit. on pp. 65, 68, 70, 199.

[77] A. Pundt: *Hydrogen in Nano-sized Metals.* Adv. Eng. Mater. **6**, 11–21 (2004).
DOI 10.1002/adem.200300557, cit. on pp. 65, 149.

[78] R. Griessen and R. Feenstra: *Volume changes during hydrogen absorption in metals.* J. Phys. F Met. Phys. **15**, 1013–1019 (1985).
DOI 10.1088/0305-4608/15/4/024, cit. on p. 66.

[79] G. Alefeld: *Phase transitions of hydrogen in metals due to elastic interaction.* Berichte der Bunsengesellschaft für Phys. Chemie **76**, 746–755 (1972).
DOI 10.1002/bbpc.19720760809, cit. on pp. 66, 99.

[80] R. B. Schwarz and A. G. Khachaturyan: *Thermodynamics of Open Two-Phase Systems with Coherent Interfaces.* Phys. Rev. Lett. **74**, 2523–2526 (1995).
DOI 10.1103/PhysRevLett.74.2523, cit. on pp. 66, 67, 70, 80, 111.

[81] R. B. Schwarz and A. G. Khachaturyan: *Thermodynamics of open two-phase systems with coherent interfaces: Application to metal-hydrogen systems.* Acta Mater. **54**, 313–323 (2006).
DOI 10.1016/j.actamat.2005.08.044, cit. on pp. 66, 67, 70, 80, 111, 123.

[82] J. C. Maxwell: *On the Dynamical Evidence of the Molecular Constitution of Bodies.* Nature **11**, 357–359 (1875).
DOI 10.1038/011357a0, cit. on pp. 67, 80, 83.

[83] C. Sachs, A. Pundt, R. Kirchheim, M. Winter, M. Reetz, and D. Fritsch: *Solubility of hydrogen in single-sized palladium clusters.* Phys. Rev. B **64**, 075408 (2001).
DOI 10.1103/PhysRevB.64.075408, cit. on pp. 69, 70, 74, 75, 80, 95.

[84] A. Züttel, C. Nützenadel, G. Schmid, C. Emmenegger, P. Sudan, and L. Schlapbach: *Thermodynamic aspects of the interaction of hydrogen with Pd clusters.* Appl. Surf. Sci. **162**, 571–575 (2000).
DOI 10.1016/S0169-4332(00)00252-X, cit. on pp. 69, 70, 75.

[85] A. Pundt and R. Kirchheim: *HYDROGEN IN METALS: Microstructural Aspects.* Annu. Rev. Mater. Res. **36**, 555–608 (2006).
DOI 10.1146/annurev.matsci.36.090804.094451, cit. on pp. 70, 76.

[86] Y. Pivak, R. Gremaud, K. Gross, M. Gonzalez-Silveira, A. Walton, D. Book, H. Schreuders, B. Dam, R. Griessen, M. Gonzalez-Silveira, and A. Walton: *Effect of the substrate on the thermodynamic properties of PdHx films studied by hydrogenography*. Scr. Mater. **60**, 348–351 (2009). DOI 10.1016/j.scriptamat.2008.11.012, cit. on pp. 71, 74, 77, 78, 89.

[87] R. Lässer and K. H. Klatt: *Solubility of hydrogen isotopes in palladium*. Phys. Rev. B **28**, 748–758 (1983). DOI 10.1103/PhysRevB.28.748, cit. on pp. 71, 74, 75, 77, 78, 89, 90.

[88] E. Wicke and J. Blaurock: *New experiments on and interpretations of hysteresis effects of Pd-D2 and Pd-H2*. J. Less Common Met. **130**, 351–363 (1987). DOI 10.1016/0022-5088(87)90129-9, cit. on pp. 75, 80, 93, 95.

[89] P. Haasen and B. L. Mordike: *Physical Metallurgy*, Cambridge University Press (), 1996. ISBN 9781316139257, cit. on p. 76.

[90] R. Feenstra, R. Griessen, and D. G. De Groot: *Hydrogen induced lattice expansion and effective H-H interaction in single phase PdH*. J. Phys. F Met. Phys **16**, 1933–1952 (1986). DOI 10.1088/0305-4608/16/12/008, cit. on pp. 77, 78, 93, 94, 99, 114.

[91] G. Alefeld, B. Baranowski, H. Brodowsky, T. Schober, B. Stritzkr, H. Wenzl, C. . Wert, E. Wicke, H. Wipf, R. Wiswall, and H. Wühl: *Hydrogen in Metals II*. In: Hydrog. Met. II Appl. Prop. Topics in Applied Physics, ed. by G. Alefeld and J. Völkl, Springer Berlin Heidelberg (), 1978. ISBN 3540087052, 9783540087052, cit. on pp. 78, 134.

[92] R. Griessen and T. Riesterer: *Heat of formation models*. In: Hydrog. Intermet. Compd. I, Topics in Applied Physics, ed. by L. Schlapbach, Springer Berlin Heidelberg (), 1988. ISBN 3540546685, cit. on pp. 78, 186.

[93] C. Picard, O. J. Kleppa, and G. Boureau: *A thermodynamic study of the palladium-hydrogen system at 245-352 °C and at pressures up to 34 atm.* J. Chem. Phys. **69**, 5549 (1978).
DOI 10.1063/1.436550, cit. on p. 89.

[94] Y. de Ribaupierre and F. D. Manchester: *Experimental study of the critical-point behaviour of the hydrogen in palladium system. I. Lattice gas aspects.* J. Phys. C Solid State Phys. **7**, 2126–2139 (1974).
DOI 10.1088/0022-3719/7/12/006, cit. on p. 89.

[95] Y. D. Ribaupierre and F. D. Manchester: *Experimental study of the critical-point behaviour of the hydrogen in palladium system. III. Spinodal curves and isotherm relations.* J. Phys. C Solid State Phys. **8**, 1339–1348 (1975).
DOI 10.1088/0022-3719/8/9/004, cit. on p. 89.

[96] J. Weissmüller and C. Lemier: *On the size dependence of the critical point of nanoscale interstitial solid solutions.* Philos. Mag. Lett. **80**, 411–418 (2000).
DOI 10.1080/095008300403558, cit. on pp. 90–92, 95.

[97] H. Brodowsky: *On the non-ideal solution behavior of hydrogen in metals.* Berichte der Bunsengesellschaft für Phys. Chemie **76**, 740–746 (1972).
DOI 10.1002/bbpc.19720760808, cit. on p. 93.

[98] E. Wicke, H. Brodowsky, and H. Züchner: *Hydrogen in palladium and palladium alloys.* In: Hydrog. Met. II SE - 3, Topics in Applied Physics, ed. by G. Alefeld and J. Völkl, Springer Berlin Heidelberg (), 1978.
ISBN 978-3-540-08883-7, cit. on p. 93.

[99] E. Salomons, R. Griessen, D. G. De Groot, and A. Magerl: *Surface Tension and Subsurface Sites of Metallic Nanocrystals Determined from H-Absorption.* Europhys. Lett. **5**, 449–454 (1988).
DOI 10.1209/0295-5075/5/5/012, cit. on pp. 93, 96, 107.

[100] H. Hemmes, E. Salomons, R. Griessen, P. Sänger, and A. Driessen: *Lattice-gas model for the formation of palladium-silver hydrides at pressures up to 100 GPa.* Phys. Rev. B **39**, 10606–10613 (1989).
DOI 10.1103/PhysRevB.39.10606, cit. on pp. 93, 94.

[101] E. Salomons, H. Hemmes, and R. Griessen: *Hydrogen spectroscopy of Pd 1-y Ag y and Pd 1-y Cu y alloys.* J. Phys. Condens. Matter **2**, 817–834 (1990).
DOI 10.1088/0953-8984/2/4/004, cit. on pp. 93, 94.

[102] C. Lemier and J. Weissmüller: *Grain boundary segregation, stress and stretch: Effects on hydrogen absorption in nanocrystalline palladium.* Acta Mater. **55**, 1241–1254 (2007).
DOI 10.1016/j.actamat.2006.09.030, cit. on pp. 95, 96.

[103] W. Dong, V. Ledentu, P. Sautet, A. Eichler, and J. Hafner: *Hydrogen adsorption on palladium: a comparative theoretical study of different surfaces.* Surf. Sci. **411**, 123–136 (1998).
DOI 10.1016/S0039-6028(98)00354-9, cit. on pp. 96, 107.

[104] C. Langhammer, V. P. Zhdanov, I. Zorić, and B. Kasemo: *Size-dependent kinetics of hydriding and dehydriding of Pd nanoparticles.* Phys. Rev. Lett. **104**, 135502 (2010).
DOI 10.1103/PhysRevLett.104.135502, cit. on pp. 96, 152.

[105] A. Baldi, M. Gonzalez-Silveira, V. Palmisano, B. Dam, and R. Griessen: *Destabilization of the Mg-H system through elastic constraints.* Phys. Rev. Lett. **102**, 226102 (2009).
DOI 10.1103/PhysRevLett.102.226102, cit. on pp. 96, 97.

[106] V. Bérubé, G. Radtke, M. Dresselhaus, and G. Chen: *Size effects on the hydrogen storage properties of nanostructured metal hydrides: A review.* Int. J. Energy Res. **31**, 637–663 (2007).
DOI 10.1002/er.1284, cit. on p. 96.

[107] L. Pasquini, M. Sacchi, M. Brighi, C. Boelsma, S. Bals, T. Perkisas, and B. Dam: *Hydride destabilization in core-shell nanoparticles.* Int. J. Hydrogen Energy **39**, 2115–2123 (2014).
DOI 10.1016/j.ijhydene.2013.11.085, cit. on pp. 98, 100, 102.

[108] J. Rockenberger, L. Troger, A. L. Rogach, M. Tischer, M. Grundmann, A. Eychmuller, and H. Weller: *The contribution of particle core and surface to strain, disorder and vibrations in thiolcapped CdTe nanocrystals.* J. Chem. Phys. **108**, 7807–7815 (1998).
DOI 10.1063/1.476216, cit. on pp. 100–102.

[109] R. Griessen and A. Driessen: *Heat of formation and band structure of binary and ternary metal hydrides*. Phys. Rev. B **30**, 4372–4381 (1984).
DOI 10.1103/PhysRevB.30.4372, cit. on pp. 102, 114.

[110] R. Gremaud, A. Baldi, M. Gonzalez-Silveira, B. Dam, and R. Griessen: *Chemical short-range order and lattice deformations in Mgy Ti1-y Hx thin films probed by hydrogenography*. Phys. Rev. B **77**, 1–10 (2008).
DOI 10.1103/PhysRevB.77.144204, cit. on p. 105.

[111] M. Wilde, M. Matsumoto, K. Fukutani, and T. Aruga: *Depth-resolved analysis of subsurface hydrogen absorbed by Pd(100)*. Surf. Sci. **482-485**, 346–352 (2001).
DOI 10.1016/S0039-6028(01)00727-0, cit. on p. 107.

[112] A. R. Miedema: *Surface energies of solid metals*. Zeitschrift für Met. **69**, 287 (1978).
Cit. on p. 107.

[113] W. Tyson and W. Miller: *Surface free energies of solid metals: Estimation from liquid surface tension measurements*. Surf. Sci. **62**, 267–276 (1977).
DOI 10.1016/0039-6028(77)90442-3, cit. on p. 107.

[114] J. W. J. Kerssemakers, S. J. Van der Molen, N. J. Koeman, R. Günther, and R. Griessen: *Pixel switching of epitaxial Pd/YHx/CaF2 switchable mirrors*. Nature **406**, 489–91 (2000).
DOI 10.1038/35020024, cit. on p. 112.

[115] J. W. J. Kerssemakers, S. J. Van der Molen, R. Günther, B. Dam, and R. Griessen: *Local switching in epitaxial YHx switchable mirrors*. Phys. Rev. B **65**, 1–8 (2002).
DOI 10.1103/PhysRevB.65.075417, cit. on p. 112.

[116] I. Zorić, E. M. Larsson, B. Kasemo, and C. Langhammer: *Localized Surface Plasmons Shed Light on Nanoscale Metal Hydrides*. Adv. Mater. **22**, 4628–4633 (2010).
DOI 10.1002/adma.201000973, cit. on p. 117.

[117] V. P. Zhdanov, I. Zorić, and B. Kasemo: *Plasmonics: Heat transfer between metal nanoparticles and supporting nanolayers*. Phys. E Low-Dimensional Syst. Nanostructures **46**, 113–118 (2012).
DOI 10.1016/j.physe.2012.09.004, cit. on p. 117.

[118] G. Baffou and R. Quidant: *Nanoplasmonics for chemistry*. Chem. Soc. Rev. **43**, 3898–907 (2014).
DOI 10.1039/c3cs60364d, cit. on p. 117.

[119] F. R. Fan, D. Y. Liu, Y. F. Wu, S. Duan, Z. X. Xie, Z. Y. Jiang, and Z. Q. Tian: *Epitaxial growth of heterogeneous metal nanocrystals: From gold nano-octahedra to palladium and silver nanocubes*. J. Am. Chem. Soc. **130**, 6949–6951 (2008).
DOI 10.1021/ja801566d, cit. on p. 120.

[120] M. Jin, H. Zhang, J. Wang, X. Zhong, N. Lu, Z. Li, Z. Xie, M. J. Kim, and Y. Xia: *Copper can still be epitaxially deposited on palladium nanocrystals to generate core-shell nanocubes despite their large lattice mismatch*. ACS Nano **6**, 2566–2573 (2012).
DOI 10.1021/nn2050278, cit. on p. 120.

[121] T. B. Flanagan and W. Oates: *The effect of hysteresis on the phase diagram of Pd-H*. J. Less Common Met. **92**, 131–142 (1983).
DOI 10.1016/0022-5088(83)90234-5, cit. on p. 127.

[122] K. Nörthemann and A. Pundt: *Coherent-to-semi-coherent transition of precipitates in niobium-hydrogen thin films*. Phys. Rev. B **78**, 1–9 (2008).
DOI 10.1103/PhysRevB.78.014105, cit. on p. 127.

[123] J. Isidorsson, I. A. M. E. Giebels, H. Arwin, and R. Griessen: *Optical properties of MgH2 measured in situ by ellipsometry and spectrophotometry*. Phys. Rev. B **68**, 115112 (2003).
DOI 10.1103/PhysRevB.68.115112, cit. on pp. 130, 141, 143, 144.

[124] W. E. Vargas, I. Rojas, D. Azofeifa, and N. Clark: *Optical and electrical properties of hydrided palladium thin films studied by an inversion approach from transmittance measurements*. Thin Solid Films **496**, 189–196 (2006).
DOI 10.1016/j.tsf.2005.08.346, cit. on pp. 130, 140.

[125] W. E. Vargas, D. E. Azofeifa, N. Clark, H. Solis, F. Montealegre, and M. Cambronero: *Parametric formulation of the dielectric function of palladium and palladium hydride thin films.* Appl. Opt. **53**, 5294 (2014).
DOI 10.1364/AO.53.005294, cit. on p. 130.

[126] U. Laudahn, S. Fahler, H. U. Krebs, A. Pundt, M. Bicker, U. Hülsen, U. Geyer, and R. Kirchheim: *Determination of elastic constants in thin films using hydrogen loading.* Appl. Phys. Lett. **74**, 647–649 (1999).
DOI 10.1063/1.123028, cit. on p. 134.

[127] S. Nazarpour, C. Zamani, and A. Cirera: *Fracture force analysis at the interface of Pd and SrTiO3.* Appl. Surf. Sci. **255**, 6048–6053 (2009).
DOI 10.1016/j.apsusc.2009.01.071, cit. on p. 134.

[128] W. Vargas, D. Azofeifa, N. Clark, H. Solis, F. Montealegre, and M. Cambronero: *Parametric Formulation of the Dielectric Function of Palladium and Palladium Hydride Thin Films.* Appl. Opt. (2014).
DOI 10.1364/AO.53.005294, cit. on pp. 141, 143, 144.

[129] J. S. Toll: *Causality and the Dispersion Relation: Logical Foundations.* Phys. Rev. **104**, 1760–1770 (1956).
DOI 10.1103/PhysRev.104.1760, cit. on p. 145.

[130] T. B. Flanagan and J. Lynch: *The effect of lattice defects on Hydrogen solubility in palladium.* J. Less Common Met. **49**, 25–35 (1976).
DOI 10.1016/0022-5088(76)90023-0, cit. on p. 147.

[131] J. Kürschner, S. Wagner, and A. Pundt: *Delamination-supported growth of hydrides in Pd thin films studied by electrochemical hydrogenography.* J. Alloys Compd. **593**, 87–92 (2014).
DOI 10.1016/j.jallcom.2014.01.026, cit. on p. 147.

[132] J. Čížek, O. Melikhova, M. Vlček, F. Lukáč, M. Vlach, P. Dobron, I. Procházka, W. Anwand, G. Brauer, S. Wagner, H. Uchida, R. Gemma, and A. Pundt: *Hydrogen Interaction with Defects in Nanocrystalline, Polycrystalline and Epitaxial Pd Films.* J. Nano Res. **26**, 123–133 (2013). DOI 10.4028/www.scientific.net/JNanoR.26.123, cit. on p. 147.

[133] S. Kishimoto, M. Inoue, N. Yoshida, and T. B. Flanagan: *Solution of hydrogen in thin palladium films.* J. Chem. Soc. Faraday Trans. 1 Phys. Chem. Condens. Phases **82**, 2175 (1986). DOI 10.1039/f19868202175, cit. on p. 149.

[134] E. Salomons, R. Feenstra, D. de Groot, J. Rector, and R. Griessen: *Pressure-composition isotherms of thin PdHc films.* J. Less Common Met. **130**, 415–420 (1987). DOI 10.1016/0022-5088(87)90136-6, cit. on p. 149.

[135] F. J. Giessibl and M. Reichling: *Investigating atomic details of the CaF 2 (111) surface with a qPlus sensor.* Nanotechnology **16**, S118 (2005). Cit. on p. 149.

[136] E. Maeda, S. Mikuriya, K. Endo, I. Yamada, A. Suda, and J.-J. J. Delaunay: *Optical hydrogen detection with periodic subwavelength palladium hole arrays.* Appl. Phys. Lett. **95**, 1–4 (2009). DOI 10.1063/1.3224890, cit. on p. 152.

[137] M. L. Tang, N. Liu, J. a. Dionne, and a. P. Alivisatos: *Observations of shape-dependent hydrogen uptake trajectories from single nanocrystals.* J. Am. Chem. Soc. **133**, 13220–3 (2011). DOI 10.1021/ja203215b, cit. on p. 152.

[138] A. Tittl, X. Yin, H. Giessen, X.-D. Tian, Z.-Q. Tian, C. Kremers, D. N. Chigrin, and N. Liu: *Plasmonic Smart Dust for Probing Local Chemical Reactions.* Nano Lett. **13**, 1816–1821 (2013). DOI 10.1021/nl4005089, cit. on pp. 152, 158.

[139] F. Gu, H. Zeng, Y. B. Zhu, Q. Yang, L. K. Ang, and S. Zhuang: *Single-crystal Pd and its alloy nanowires for plasmon propagation and highly sensitive hydrogen detection.* Adv. Opt. Mater. **2**, 189–196 (2014).
DOI 10.1002/adom.201300413, cit. on p. 152.

[140] F. Gu, G. Wu, and H. Zeng: *Hybrid photon-plasmon Mach-Zehnder interferometers for highly sensitive hydrogen sensing*. Nanoscale **7**, 924–929 (2015).
DOI 10.1039/C4NR06642A, cit. on p. 152.

[141] T. Shegai, P. Johansson, C. Langhammer, and M. Käll: *Directional Scattering and Hydrogen Sensing by Bimetallic Pd-Au Nanoantennas*. Nano Lett. **12**, 2464–9 (2012).
DOI 10.1021/nl300558h, cit. on p. 152.

[142] S. Syrenova, C. Wadell, and C. Langhammer: *Shrinking-hole colloidal lithography: self-aligned nanofabrication of complex plasmonic nanoantennas.* Nano Lett. **14**, 2655–63 (2014).
DOI 10.1021/nl500514y, cit. on p. 152.

[143] A. Yang, M. D. Huntington, M. F. Cardinal, S. S. Masango, R. P. Van Duyne, and T. W. Odom: *Hetero-oligomer Nanoparticle Arrays for Plasmon-Enhanced Hydrogen Sensing.* ACS Nano **8**, 7639–47 (2014).
DOI 10.1021/nn502502r, cit. on p. 152.

[144] T. J. Antosiewicz, S. P. Apell, C. Wadell, and C. Langhammer: *Absorption Enhancement in Lossy Transition Metal Elements of Plasmonic Nanosandwiches.* J. Phys. Chem. C **116**, 120917140315004 (2012).
DOI 10.1021/jp306541n, cit. on p. 152.

[145] T. Shegai and C. Langhammer: *Hydride Formation in Single Palladium and Magnesium Nanoparticles Studied By Nanoplasmonic Dark-Field Scattering Spectroscopy.* Adv. Mater. **23**, 4409–4414 (2011).
DOI 10.1002/adma.201101976, cit. on p. 152.

[146] C. Wadell, T. J. Antosiewicz, and C. Langhammer: *Optical Absorption Engineering in Stacked Plasmonic Au-SiO(2)-Pd Nanoantennas.* Nano Lett. **12**, 4784–90 (2012).
DOI 10.1021/nl3022187, cit. on p. 152.

[147] K. Ikeda, S. Uchiyama, M. Takase, and K. Murakoshi: *Hydrogen-Induced Tuning of Plasmon Resonance in Palladium-Silver Layered Nanodimer Arrays.* ACS Photonics **2**, 66–72 (2015).
DOI 10.1021/ph500242c, cit. on p. 152.

[148] S. Cataldo, J. Zhao, F. Neubrech, B. Frank, C. Zhang, P. V. Braun, and H. Giessen: *Hole-mask colloidal nanolithography for large-area low-cost metamaterials and antenna-assisted surface-enhanced infrared absorption substrates.* ACS Nano **6**, 979–85 (2012).
DOI 10.1021/nn2047982, cit. on p. 153.

[149] J. Zhao, B. Frank, F. Neubrech, C. Zhang, P. V. Braun, and H. Giessen: *Hole-mask colloidal nanolithography combined with tilted-angle-rotation evaporation: A versatile method for fabrication of low-cost and large-area complex plasmonic nanostructures and metamaterials.* Beilstein J. Nanotechnol. **5**, 577–586 (2014).
DOI 10.3762/bjnano.5.68, cit. on p. 154.

[150] A. B. Dahlin, J. O. Tegenfeldt, and F. Höök: *Improving the instrumental resolution of sensors based on localized surface plasmon resonance.* Anal. Chem. **78**, 4416–23 (2006).
DOI 10.1021/ac0601967, cit. on p. 158.

[151] K. M. Mayer and J. H. Hafner: *Localized surface plasmon resonance sensors.* Chem. Rev. **111**, 3828–57 (2011).
DOI 10.1021/cr100313v, cit. on p. 166.

[152] N. J. Halas, S. Lal, W.-S. Chang, S. Link, and P. Nordlander: *Plasmons in strongly coupled metallic nanostructures.* Chem. Rev. **111**, 3913–61 (2011).
DOI 10.1021/cr200061k, cit. on p. 169.

[153] V. Giannini, A. I. Fernández-Domínguez, S. C. Heck, and S. A. Maier: *Plasmonic nanoantennas: fundamentals and their use in controlling the radiative properties of nanoemitters.* Chem. Rev. **111**, 3888–912 (2011).
DOI 10.1021/cr1002672, cit. on p. 169.

[154] P. Christopher, H. Xin, A. Marimuthu, and S. Linic: *Singular characteristics and unique chemical bond activation mechanisms of photocatalytic reactions on plasmonic nanostructures.* Nature Mater. **11**, 1–7 (2012).
DOI 10.1038/nmat3454, cit. on p. 170.

[155] S. Lal, S. Link, and N. J. Halas: *Nano-optics from sensing to waveguiding.* Nature Photonics **1**, 641–648 (2007).
DOI 10.1038/nphoton.2007.223, cit. on p. 170.

[156] D. Traviss, R. Bruck, B. Mills, M. Abb, and O. L. Muskens: *Ultrafast plasmonics using transparent conductive oxide hybrids in the epsilon-near-zero regime.* Appl. Phys. Lett. **102**, 121112 (2013).
DOI 10.1063/1.4798833, cit. on p. 170.

[157] X. Zhu, L. Shi, X. Liu, J. Zi, and Z. Wang: *A mechanically tunable plasmonic structure composed of a monolayer array of metal-capped colloidal spheres on an elastomeric substrate.* Nano Res. **3**, 807–812 (2010).
DOI 10.1007/s12274-010-0048-y, cit. on p. 170.

[158] I. M. Pryce, K. Aydin, Y. A. Kelaita, R. M. Briggs, and H. A. Atwater: *Highly strained compliant optical metamaterials with large frequency tunability.* Nano Lett. **10**, 4222–7 (2010).
DOI 10.1021/nl102684x, cit. on p. 170.

[159] X. Qian and H. S. Park: *The influence of mechanical strain on the optical properties of spherical gold nanoparticles.* J. Mech. Phys. Solids **58**, 330–345 (2010).
DOI 10.1016/j.jmps.2009.12.001, cit. on p. 170.

[160] S. Olcum, A. Kocabas, G. Ertas, A. Atalar, and A. Aydinli: *Tunable surface plasmon resonance on an elastomeric substrate.* Opt. Express **17**, 8542–7 (2009).
Cit. on p. 170.

[161] K. Appavoo, D. Y. Lei, Y. Sonnefraud, B. Wang, S. T. Pantelides, S. A. Maier, and R. F. Haglund: *Role of defects in the phase transition of VO2 nanoparticles probed by plasmon resonance spectroscopy.* Nano Lett. **12**, 780–6 (2012).
DOI 10.1021/nl203782y, cit. on p. 170.

[162] N. K. Emani, T.-F. Chung, X. Ni, A. V. Kildishev, Y. P. Chen, and A. Boltasseva: *Electrically tunable damping of plasmonic resonances with graphene.* Nano Lett. **12**, 5202–6 (2012). DOI 10.1021/nl302322t, cit. on p. 170.

[163] J.-Y. Ou, E. Plum, J. Zhang, and N. I. Zheludev: *An electromechanically reconfigurable plasmonic metamaterial operating in the near-infrared.* Nature Nanotechnol. **8**, 252–5 (2013). DOI 10.1038/nnano.2013.25, cit. on p. 170.

[164] G. V. Naik, V. M. Shalaev, and A. Boltasseva: *Alternative plasmonic materials: beyond gold and silver.* Adv. Mater. **25**, 3264–94 (2013). DOI 10.1002/adma.201205076, cit. on p. 170.

[165] S. R. C. Vivekchand, C. J. Engel, S. M. Lubin, M. G. Blaber, W. Zhou, J. Y. Suh, G. C. Schatz, and T. W. Odom: *Liquid Plasmonics: Manipulating Surface Plasmon Polaritons via Phase Transitions.* Nano Lett. **12**, 4324–4328 (2012). DOI 10.1021/nl302053g, cit. on p. 170.

[166] B. Soares, F. Jonsson, and N. I. Zheludev: *All-Optical Phase-Change Memory in a Single Gallium Nanoparticle.* Phys. Rev. Lett. **98**, 153905 (2007). DOI 10.1103/PhysRevLett.98.153905, cit. on p. 170.

[167] T. Driscoll, S. Palit, M. M. Qazilbash, M. Brehm, F. Keilmann, B.-G. Chae, S.-J. Yun, H.-T. Kim, S. Y. Cho, N. M. Jokerst, D. R. Smith, and D. N. Basov: *Dynamic tuning of an infrared hybrid-metamaterial resonance using vanadium dioxide.* Appl. Phys. Lett. **93**, 024101 (2008). DOI 10.1063/1.2956675, cit. on p. 170.

[168] M. J. Dicken, K. Aydin, I. M. Pryce, L. A. Sweatlock, E. M. Boyd, S. Walavalkar, J. Ma, and H. A. Atwater: *Frequency tunable near-infrared metamaterials based on VO2 phase transition.* Opt. Express **17**, 18330–9 (2009). Cit. on p. 170.

[169] D. Y. Lei, K. Appavoo, Y. Sonnefraud, R. F. Haglund, and S. A. Maier: *Single-particle plasmon resonance spectroscopy of phase transition in vanadium dioxide.* Opt. Lett. **35**, 3988–90 (2010).
Cit. on p. 170.

[170] Z. L. Sámson, K. F. MacDonald, F. De Angelis, B. Gholipour, K. Knight, C. C. Huang, E. Di Fabrizio, D. W. Hewak, and N. I. Zheludev: *Metamaterial electro-optic switch of nanoscale thickness.* Appl. Phys. Lett. **96**, 143105 (2010).
DOI 10.1063/1.3355544, cit. on p. 170.

[171] Y. Chen, T. Kao, B. Ng, and X. Li: *Hybrid phase-change plasmonic crystals for active tuning of lattice resonances.* Opt. Express **21**, 1566–1569 (2013).
DOI 10.1364/OE.21.013691, cit. on p. 170.

[172] B. Gholipour, J. Zhang, K. F. MacDonald, D. W. Hewak, and N. I. Zheludev: *An all-optical, non-volatile, bidirectional, phase-change meta-switch.* Adv. Mater. **25**, 3050–4 (2013).
DOI 10.1002/adma.201300588, cit. on p. 170.

[173] A.-K. U. Michel, D. N. Chigrin, T. W. W. Maß, K. Schönauer, M. Salinga, M. Wuttig, and T. Taubner: *Using Low-Loss Phase-Change Materials for Mid-Infrared Antenna Resonance Tuning.* Nano Lett. **13**, 3470–3475 (2013).
DOI 10.1021/nl4006194, cit. on p. 170.

[174] J. N. Huiberts, R. Griessen, J. H. Rector, R. J. Wijngaarden, J. P. Dekker, D. G. de Groot, and N. J. Koeman: *Yttrium and lanthanum hydride films with switchable optical properties.* Nature **380**, 231–234 (1996).
DOI 10.1038/380231a0, cit. on p. 170.

[175] A. L. Stepanov, G. Bour, A. Reinholdt, and U. Kreibig: *The formation of hydrogenated yttrium nanoparticles.* Tech. Phys. Lett. **28**, 642–644 (2002).
DOI 10.1134/1.1505537, cit. on p. 170.

[176] A. L. Stepanov, G. Bour, M. Gartz, Y. Osin, A. Reinholdt, and U. Kreibig: *Synthesis of yttrium clusters.* Vacuum **64**, 9–14 (2001).
DOI 10.1016/S0042-207X(01)00359-1, cit. on pp. 170, 173, 175, 189.

[177] E. S. Kooij, A. T. M. van Gogh, D. G. Nagengast, N. J. Koeman, and R. Griessen: *Hysteresis and the single-phase metal-insulator transition in switchable YHx films*. Phys. Rev. B **62**, 10088–10100 (2000). DOI 10.1103/PhysRevB.62.10088, cit. on p. 171.

[178] J. N. Huiberts, R. Griessen, R. J. Wijngaarden, M. Kremers, and C. Van Haesendonck: *Logarithmic Divergence of the Electrical Resistivity in the Metal Hydride YH3-δ*. Phys. Rev. Lett. **79**, 3724–3727 (1997). DOI 10.1103/PhysRevLett.79.3724, cit. on p. 171.

[179] A. Remhof, S. J. Van der Molen, A. Antosik, A. Dobrowolska, N. Koeman, and R. Griessen: *Switchable mirrors for visualization and control of hydrogen diffusion in transition metals*. Phys. Rev. B **66**, 020101 (2002). DOI 10.1103/PhysRevB.66.020101, cit. on p. 172.

[180] M. Hentschel, T. Weiss, S. Bagheri, and H. Giessen: *Babinet to the Half: Coupling of Solid and Inverse Plasmonic Structures.* Nano Lett. (2013). DOI 10.1021/nl402269h, cit. on p. 173.

[181] A. T. M. Van Gogh, D. Nagengast, E. S. Kooij, N. Koeman, J. Rector, R. Griessen, C. Flipse, and R. Smeets: *Structural, electrical, and optical properties of $La_zY_zH_x$ switchable mirrors*. Phys. Rev. B **63**, 195105 (2001). DOI 10.1103/PhysRevB.63.195105, cit. on pp. 174, 186–188, 190–193.

[182] G. Bour, A. Reinholdt, A. L. Stepanov, C. Keutgen, and U. Kreibig: *Optical and electrical properties of hydrogenated yttrium nanoparticles*. Eur. Phys. J. D **16**, 219–223 (2001). DOI 10.1007/s100530170096, cit. on pp. 174, 189.

[183] M. Gartz and M. Quinten: *Broadening of resonances in yttrium nanoparticle optical spectra.* Appl. Phys. B Lasers Opt. **73**, 327–332 (2001). DOI 10.1007/s003400100702, cit. on pp. 175, 190.

[184] P. Vajda: *Hydrogen in rare-earth metals, including RH_2+x phases*. In: Handb. Phys. Chem. Rare Earths Vol. 20, ed. by K. A. Gschneidner, J. Eyring, and LeRoy, Elsevier (), 1995. ISBN 9780444820143, cit. on p. 175.

[185] I. Aruna, L. K. Malhotra, and B. R. Mehta: *Switchable Metal Hydride Films*. In: Handb. Phys. Chem. Rare Earths, ed. by K. A. Gschneidner, J.-C. G. Bunzli, and V. K. Pecharsky, Elsevier (), 2006.
ISBN 0168-1273, cit. on p. 175.

[186] E. S. Kooij, A. T. M. van Gogh, and R. Griessen: *In Situ Resistivity Measurements and Optical Transmission and Reflection Spectroscopy of Electrochemically Loaded Switchable YH[sub x] Films*. J. Electrochem. Soc. **146**, 2990 (1999).
DOI 10.1149/1.1392040, cit. on p. 175.

[187] A. F. T. Hoekstra, A. S. Roy, and T. F. Rosenbaum: *Scaling at the Mott Hubbard metal insulator transition in yttrium hydride*. J. Phys. Condens. Matter **15**, 1405–1413 (2003).
DOI 10.1088/0953-8984/15/9/304, cit. on p. 175.

[188] A. F. T. Hoekstra, A. Roy, T. Rosenbaum, R. Griessen, R. J. Wijngaarden, and N. Koeman: *Light-Induced Metal-Insulator Transition in a Switchable Mirror*. Phys. Rev. Lett. **86**, 5349–5352 (2001).
DOI 10.1103/PhysRevLett.86.5349, cit. on p. 175.

[189] G. W. Bryant, F. J. García de Abajo, and J. Aizpurua: *Mapping the plasmon resonances of metallic nanoantennas*. Nano Lett. **8**, 631–6 (2008).
DOI 10.1021/nl073042v, cit. on p. 177.

[190] T. Dattoma, M. Grande, R. Marani, G. Morea, V. Marrocco, and A. D'Orazio: *Resonance wavelength dependance and mode formation in gold nanorod optical antennas with finite thickness*. Prog. Electromagn. Res. B **30**, 337–353 (2011).
DOI 10.2528/PIERB11042107, cit. on p. 177.

[191] M. Pasturel, R. J. Wijngaarden, W. Lohstroh, H. Schreuders, M. Slaman, B. Dam, and R. Griessen: *Influence of the Chemical Potential on the Hydrogen Sorption Kinetics of Mg 2 Ni/TM/Pd (TM = transition metal) Trilayers*. Chem. Mater. **19**, 624–633 (2007).
DOI 10.1021/cm062157h, cit. on pp. 179, 186, 187.

[192] H. Katsuta and R. B. McLellan: *Diffusivity permeability and solubility of hydrogen in platinum.* J. Phys. Chem. Solids **40**, 697–699 (1979).
DOI 10.1016/0022-3697(79)90182-3, cit. on p. 185.

[193] K. H. J. Buschow, P. C. P. Bouten, and A. R. Miedema: *Hydrides formed from intermetallic compounds of two transition metals: a special class of ternary alloys.* Reports Prog. Phys. **45**, 937–1039 (1982).
DOI 10.1088/0034-4885/45/9/001, cit. on p. 186.

[194] J. Weaver and C. Olson: *Optical absorption of hcp yttrium.* Phys. Rev. B **15**, 590–594 (1977).
DOI 10.1103/PhysRevB.15.590, cit. on p. 187.

[195] J. Weaver: *Optical properties of Rh, Pd, Ir, and Pt.* Phys. Rev. B **11**, 1416–1425 (1975).
DOI 10.1103/PhysRevB.11.1416, cit. on p. 188.

[196] M. Bass, C. DeCusatis, J. Enoch, V. Lakshminarayanan, G. Li, C. MacDonald, V. Mahajan, and E. Van Stryland: *Handbook of Optics, Third Edition Volume IV: Optical Properties of Materials, Nonlinear Optics, Quantum Optics (set).* Handbook of Optics, Mcgraw-hill (), 2009.
ISBN 9780071498920, cit. on p. 190.

[197] N. Liu, T. Weiss, M. Mesch, L. Langguth, U. Eigenthaler, M. Hirscher, C. Sönnichsen, and H. Giessen: *Planar metamaterial analogue of electromagnetically induced transparency for plasmonic sensing.* Nano Lett. **10**, 1103–1107 (2010).
DOI 10.1021/nl902621d, cit. on p. 193.

[198] R. Griessen, I. A. M. E. Giebels, and B. Dam: *Optical properties of metal-hydrides: switchable mirrors.* In: Hydrog. as a Futur. Energy Carr. Vol. June, ed. by A. Zttel, A. Borgschulte, and L. Schlapbach, Wiley-VCH Verlag GmbH & Co. KGaA (Weinheim, Germany), 2008.
ISBN 9783527622894, cit. on p. 193.

[199] M. W. Lee and W. P. Shin: *Optical properties of the γ-phase yttrium trihydride $YH_{3-\delta}$.* J. Appl. Phys. **86**, 6798 (1999).
DOI 10.1063/1.371754, cit. on p. 193.

[200] Y. H. Fu, A. I. Kuznetsov, A. E. Miroshnichenko, Y. F. Yu, and B. Luk'yanchuk: *Directional visible light scattering by silicon nanoparticles.* Nature Commun. **4**, 1527 (2013).
DOI 10.1038/ncomms2538, cit. on p. 193.

[201] A. I. Kuznetsov, A. E. Miroshnichenko, u. H. Fu, J. Zhang, and B. Luk'yanchuk: *Magnetic light.* Sci. Rep. **2**, 492 (2012).
DOI 10.1038/srep00492, cit. on p. 193.

[202] D. Azofeifa, N. Clark, W. E. Vargas, H. Solís, G. K. Pálsson, and B. Hjörvarsson: *Hydrogen induced changes in the optical properties of Pd capped V thin films.* J. Alloys Compd. **580**, 114 (2013).
DOI 10.1016/j.jallcom.2013.03.146, cit. on p. 193.

[203] T. Messina, C. Miller, and J. Markert: *Steric quenching of the switchable mirror effect.* Phys. Rev. B **75**, 104109 (2007).
DOI 10.1103/PhysRevB.75.104109, cit. on p. 193.

[204] T. J. Richardson, J. L. Slack, R. D. Armitage, R. Kostecki, B. Farangis, and M. D. Rubin: *Switchable mirrors based on nickel-magnesium films.* Appl. Phys. Lett. **78**, 3047 (2001).
DOI 10.1063/1.1371959, cit. on p. 193.

[205] F. J. A. D. Broeder, S. J. Van der Molen, M. Kremers, J. N. Huiberts, D. G. Nagengast, A. T. M. Van Gogh, W. H. Huisman, N. J. Koeman, B. Dam, J. H. Rector, S. Plota, M. Haaksma, R. M. N. Hanzen, R. M. Jungblut, P. A. Duine, and R. Griessen: *Visualization of hydrogen migration in solids using switchable mirrors.* Nature **394**, 26–28 (1998).
DOI 10.1038/29250, cit. on p. 193.

[206] R. Griessen, J. N. Huiberts, M. Kremers, A. T. M. van Gogh, N. J. Koeman, J. P. Dekker, and P. H. L. Notten: *Yttrium and lanthanum hydride films with switchable optical properties.* J. Alloys Compd. **253-254**, 44–50 (1997).
DOI 10.1016/S0925-8388(96)02891-5, cit. on p. 193.

[207] W. Lohstroh, R. J. Westerwaal, B. Noheda, S. Enache, I. A. M. E. Giebels, B. Dam, and R. Griessen: *Self-Organized Layered Hydrogenation in Black Mg2NiHx Switchable Mirrors.* Phys. Rev. Lett. **93**, 197404 (2004).
DOI 10.1103/PhysRevLett.93.197404, cit. on p. 194.

[208] F. Sterl, H. Linnenbank, T. Steinle, F. Mörz, N. Strohfeldt, and H. Giessen:
"Nanoscale hydrogenography of individual magnesium nanoparticles,"
2017.
Cit. on p. 199.

[209] a. Ulvestad, M. J. Welland, S. S. E. Collins, R. Harder, E. Maxey, J. Wingert, A. Singer, S. Hy, P. Mulvaney, P. Zapol, and O. G. Shpyrko: *Avalanching strain dynamics during the hydriding phase transformation in individual palladium nanoparticles*. Nature Commun. **6**, 10092 (2015).
DOI 10.1038/ncomms10092, cit. on p. 199.

ACKNOWLEDGMENTS

Looking back on five amazing years of doing my PhD at the 4th Physics Institute at the University of Stuttgart, I am simply grateful for all the people who contributed to the success of my work, scientifically or otherwise.

Especially, I would like to thank:

- Prof. Dr. Harald Giessen for giving me the opportunity to work in his group and on such an interesting topic. Also for his constant encouragement and support, and for all the opportunities and ideas he has provided over the years.
- Prof. Dr. Sebastian Loth for agreeing to be my second adviser on such a short notice and for taking the time and effort to examine my thesis.
- Prof. Dr. Na Liu for many great scientific discussions and taking the time to be on my examination committee.
- Prof. Dr. Christian Holm for kindly agreeing to review my thesis and being head of the examination board.
- Prof. Dr. Ronald Griessen for his ideas, for fruitful collaborations on several projects and for a great friendship.
- Dr. Christine von Rekowski for being great help with all administrative matters and being the place to go for everything else concerning university.
- Mario Hentschel, Monika Ubl and Ramon Walter for all their help and guidance in the clean room.

- Andreas Tittl, for being my office mate for a long time and good friend, for all the shared projects, and for always lightening the mood in the face of paper rejections and other troubles.

- Florian Sterl, for being a great colleague and friend, for sharing many projects and many good laughs in the lab or after work.

- Shahin Bagheri, for being my office mate in the last two years, always having a sympathetic ear if needed, and for having great collaborations together.

- Martin Schäferling, Martin Mesch, Mario Hentschel, Heiko Linnenbank, Richard Taubert, Frank Neubrech, Xinghui Yin, Tobi Steinle, and Bernd Metzger for making life at the institute and after work enjoyable.

- All my colleagues at the 4th Physics Institute, who made the last years not only interesting, but also incredibly fun.

I also want to thank all my friends outside the institute for bearing with me through all the good and bad times during my work. Especially, *the physicists*, Hannes[2], Kai, Roland, Martina and Alex.

Finally, my deepest thanks go to my proud and supporting father, who tragically passed away this spring, my family and to my girlfriend. Without their constant support, encouragement and patience this thesis and also much of the studies preceding it would not have been possible.

CURRICULUM VITÆ

NAME	Nikolai-Sven Strohfeldt,
BORN	1984/11/04 in Waiblingen,
CITIZENSHIP	German,
CIVIL STATUS	Single,
ADDRESS	Senefelderstr. 99, 70176 Stuttgart, Germany,
PHONE	+49 711 47707813,
E-MAIL	NikolaiStr@web.de

1995–2005	Gymnasium Bildungszentrum Weissacher Tal, *Allgemeine Hochschulreife, Grade: 1.5*
2005–2012	Studies of physics: University of Stuttgart, Germany, *Degree: Dipl. Phys., Grade: 1.2*
2008–2009	Studies of physics: University of Oregon, Eugene, USA, *Degree: Master of Science*
2011–2012	Diploma thesis: *'Nanoplasmonic gas-sensing: Hydrogen sensors based on palladium nanoparticles'*, University of Stuttgart, advisor: Prof. Dr. Harald Giessen
2012	Research stay (3 months): National University of Singapore and A*STAR Research Institute IMRE, advisor: Prof. Dr. Minghui Hong (NUS) and Dr. Joel Yang (IMRE)
2012–2017	Ph.D. thesis: *'Hydrogen in metal nanoparticles – Understanding and applying thermodynamic properties of metal-hydrogen nanostructures'*, University of Stuttgart, advisor: Prof. Dr. Harald Giessen

COLOPHON

This thesis was typeset with LaTeX 2_ε using Robert Slimbach's Minion Pro font. The style was inspired by Robert Bringhurst's "*The Elements of Typographic Style*". It is available for LaTeX via CTAN as CLASSICTHESIS.